



THE UNIVERSITY  
*of* ADELAIDE

**Noble Metal Catalysts for Electrocatalytic Water Splitting in  
Acidic Environments**

**Jieqiong Shan**

A thesis submitted for the degree of Doctor of Philosophy

School of Chemical Engineering and Advanced Materials

The University of Adelaide

January 2021



## Table of contents

<b>Abstract.....</b>	<b>1</b>
<b>Thesis Declaration.....</b>	<b>3</b>
<b>Acknowledgments .....</b>	<b>4</b>
<b>Chapter 1 Introduction.....</b>	<b>6</b>
1.1. Background .....	6
1.2. Aim and Objectives .....	6
1.3. Thesis Layout.....	7
<b>Chapter 2 Literature Review .....</b>	<b>9</b>
2.1. Introduction.....	9
2.2. Regulating electrocatalysts via surface/interface engineering for acidic oxygen evolution .....	9
<b>Chapter 3 Charge-Redistribution-Enhanced Nanocrystalline Ru@IrO<sub>x</sub> Electrocatalysts for Oxygen Evolution in Acidic Media.....</b>	<b>24</b>
3.1. Introduction and Significance.....	24
3.2. Charge-redistribution-enhanced nanocrystalline Ru@IrO <sub>x</sub> electrocatalysts for oxygen evolution in acidic media .....	25
<b>Chapter 4 Transition-Metal-Doped RuIr Bifunctional Nanocrystals for Overall Water Splitting in Acidic Environments.....</b>	<b>60</b>
4.1. Introduction and Significance.....	60
4.2. Transition-metal-doped RuIr bifunctional nanocrystals for overall water splitting in acidic environments.....	61
<b>Chapter 5 Short-Range Ordered Iridium Single Atoms Integrated into Cobalt Oxide Spinel Structure for Highly Efficient Electrocatalytic Water Oxidation.....</b>	<b>84</b>
5.1. Introduction and Significance.....	84
5.2. Short-Range Ordered Iridium Single Atoms Integrated into Cobalt Oxide Spinel Structure for Highly Efficient Electrocatalytic Water Oxidation .....	85

<b>Chapter 6 Spatial Structure Tuning of Correlated Single-Atom Platinum Sites for Acidic Hydrogen Evolution and Oxidation Electrocatalysis .....</b>	<b>131</b>
6.1. Introduction and Significance.....	131
6.2. Spatial structure tuning of correlated single-atom platinum sites for acidic hydrogen evolution and oxidation electrocatalysis.....	132
<b>Chapter 7 Conclusions and perspectives .....</b>	<b>175</b>
<b>Appendix: Publications during Ph.D. Candidature.....</b>	<b>178</b>

## Abstract

This thesis aims to design electrocatalysts with high activity, long-term stability and cost-efficiency for proton exchange membrane (PEM) water electrolyzers. This technique is of vital importance for fast hydrogen fuel generation, but the catalysts generally suffer from rapid degradation due to the harsh acidic and oxidative conditions.

Firstly, a rational design strategy is reported for the fabrication of heterostructured oxygen evolution reaction (OER) electrocatalyst (Ru@IrO<sub>x</sub>), in which a strong charge redistribution exists between highly strained ruthenium core and partially oxidized iridium shell across the metal-metal oxide heterojunction. The increased valence of iridium shell and decreased valence of ruthenium core activate a synergistic electronic and structural interaction, resulting in the simultaneously enhanced activity and stability of the catalyst as compared to most of the state-of-the-art Ru- and Ir-based materials.

The electrocatalysts with bifunctionality for efficient OER and hydrogen evolution reaction (HER) in acidic environments towards PEM water electrolyzers have been further investigated. A bifunctional electrocatalyst (M-RuIr, M = Co, Ni, Fe) is designed by doping RuIr alloy nanocrystals with transition metals that modify electronic structure and binding strength of reaction intermediates. Applying the Co-RuIr as the catalyst for overall water splitting, a very small cell voltage of 1.52 V is required to achieve current density of 10 mA cm<sup>-2</sup>. More importantly, the catalytic activity is correlated with the chemical/valence states of catalysts and a novel composition-activity relationship is established.

Although noble metals exhibit potential towards energy conversion reactions in acidic environments, the wide application of noble metals is unfortunately restricted by high cost and

limited choice of geometric structures spanning single atoms, clusters, nanoparticles, and bulk crystals. Therefore, it is proposed to overcome this limitation by integrating noble metal atoms with the lattice of transition metal oxides to create a new type of hybrid structure. The third study shows that various kinds of noble metal atoms can be accommodated into the cationic sites of cobalt spinel oxide with short-range order and an identical spatial correlation with the host lattice. Among them, the iridium-incorporated hybrid exhibits higher electrocatalytic activity than the parent oxide by two orders of magnitude and significantly improved corrosion resistance towards the challenging OER under acidic conditions. This strategy can be extended to other oxide systems and would greatly diversify the topologies of noble metal structures for a variety of applications.

To further explore the effect of spatial structure of noble metal substitutions on their catalytic performance, a series of Pt-substituted Co spinel oxide catalysts with different amounts of Pt substitutions are synthesized. It is shown that the catalyst with optimized spatial correlation of Pt substitutions outperforms the commercial Pt/C catalyst towards HER and hydrogen oxidation reaction (HOR) in acidic environments by over one order of magnitude.

These systematic works open a new horizon for developing efficient electrocatalysts towards a wide range of applications in acidic environments by rational promotion of the chemical composition, interfacial structure and atomic spatial structure of noble metals to achieve a balance among activity, stability and cost of catalysts.

## **Thesis Declaration**

I certify that this work contains no material which has been accepted for the award of any other degree or diploma in my name, in any university or other tertiary institution and, to the best of my knowledge and belief, contains no material previously published or written by another person, except where due reference has been made in the text. In addition, I certify that no part of this work will, in the future, be used in a submission in my name, for any other degree or diploma in any university or other tertiary institution without the prior approval of the University of Adelaide and where applicable, any partner institution responsible for the joint-award of this degree.

I acknowledge that copyright of published works contained within this thesis resides with the copyright holder(s) of those works.

I also give permission for the digital version of my thesis to be made available on the web, via the University's digital research repository, the Library Search and also through web search engines, unless permission has been granted by the University to restrict access for a period of time.

I acknowledge the support I have received for my research through the provision of an Australian Government Research Training Program Scholarship.

Signature: \_\_\_\_\_

Date: 25/01/2021

## **Acknowledgments**

First and foremost, I would like to express my sincere gratitude to my principal supervisor Prof. Shi-Zhang Qiao and co-supervisor Dr. Yao Zheng for their careful guidance during my four-year candidature and the great efforts they spent in my thesis. Prof. Qiao has deeply inspired me to complete my study by his immense knowledge, diligent working, passion for research and rigorous approach to science. His encouragement has motivated me to improve my research ability and critical reasoning throughout my Ph.D. study. Dr. Zheng has provided invaluable help and support for my thesis with his impressive wisdom, keen interest in research and enlightening discussions. Without their continuous guidance and insightful suggestions, this thesis would hardly have been completed.

I really appreciate the support I have received in the accomplishment of my thesis and would like to extend my deepest gratefulness to: Prof. Chunxian Guo, who has helped me with inspiring ideas and various characterization techniques; Prof. Yihan Zhu, who has provided strong support in HRTEM imaging and extensive structure investigations; Dr. Yan Jiao, who has helped with expert scientific knowledge in theoretical computations; Dr. Chao Ye, who has conducted fundamental theoretical investigations and provided enlightening ideas to improve my work; Dr. Anthony Vasileff, who has made great contribution with technological assistance and enlightening discussions; Prof. Bo You, who has shared valuable experiences and insightful suggestions; Prof. Tao Ling, who has given wise advice in experimental techniques; Prof. Shuangming Chen and Prof. Li Song, who have helped to perform NEXAFS and EXAFS characterizations; Prof. Mietek Jaroniec, who has made many valuable comments to improve my writing of research paper; Dr. Kenneth Davey, who has provided rigorous suggestions to



my manuscripts.

I am very grateful to Dr. Qihong Hu her strong support in analytical techniques and kind help in my work. Special thanks go to Ms. Michelle Fitton, Ms. Sue Earle, Dr. Ay Ching Hee, Mr. Tom Wilson Mr. Philip Schmidt and Mr. Jason Peak for their administrative and technical help. I would also like to acknowledge the help of Dr. Ashley Slattery, Dr. Sarah Gilbert and Mr. Ken Neubauer from Adelaide Microscopy and Dr. Bruce Cowie, Dr. Lars Thomsen and Dr. Anton Tadich from Australian Synchrotron for their technical support.

I am also greatly thankful to the other colleagues in the University of Adelaide: Dr. Jingjing Duan, Dr. Dongliang Chao, Dr. Jingrun Ran, Dr. Jinlong Liu, Dr. Dongdong Zhu, Dr. Cheng Tang, Dr. Fangxi Xie, Dr. Yongqiang Zhao, Dr. Huanyu Jin, Dr. Chaochen Xu, Mr. Xin Liu, Ms. Xing Zhi, Mr. Laiquan Li, Mr. Bingquan Xia, Mr. Xianlong Zhou, Mr. Huan Li, Mr. Dazhi Yao, Ms. Xin Xu, Mr. Yanzhao Zhang, for their technological assistance in my work and help in my life.

I would like to thank China Scholarship Council, Australia Research Council and University of Adelaide for their financial support.

Last but most importantly, I am most grateful to my family for their strong support, ever-present care and unconditional love throughout all these years. I really appreciate the accompany, suggestions and encouragement that I received from my precious friends Dr. Biting Yu and Mr. Peter McMillan. Finally, I would like to give deep thanks to my husband Chao for his support in my work, love in my life and companion and encouragement for every step I have made towards a better tomorrow.

## **Chapter 1 Introduction**

### **1.1. Background**

The investigation of materials with high activity, long-term stability and reasonable cost is a primary goal of electrocatalyst design<sup>1</sup>. As a significant resolution to produce clean hydrogen energy, PEM water electrolyzers possess strong merits over traditional alkaline electrolyzers, and these include high voltage efficiency, low ohmic losses, and compact system design<sup>2</sup>. Nevertheless, the highly oxidative environment for anodic oxygen evolution reaction and harsh operation conditions set high standards for electrocatalysts<sup>3</sup>. Noble metals manifest themselves with high corrosion resistance, unique electronic structures and irreplaceable electrochemical properties towards a wide range of electrocatalytic applications, especially those working in acidic environments<sup>4</sup>. However, elaborate design is required to reach the balance among activity, stability and cost due to the scarcity and high cost of noble metals. Recently, it has been adopted as effective strategies to design and fabricate highly active and stable noble metal electrocatalysts by modifying their chemical composition, surface/interface structure and spatial atomic arrangements<sup>5,6</sup>. These strategies are expected to effectively adjust electronic properties of electrocatalysts towards energy conversion reactions including OER, HER and HOR in acidic environments, therefore provide promising solutions for generation and usage of clean hydrogen energy.

### **1.2. Aim and Objectives**

This thesis aims to achieve high activity, long-term stability and cost-efficiency in PEM electrolyzers for fast hydrogen fuel generation. The specific objectives are as follows.

(1) To promote catalytic activity and stability by developing advanced noble metal catalysts

for acidic HER/OER using surface/interface engineering strategies;

- (2) To establish Ru@IrO<sub>x</sub> core-shell structure to simultaneously enhance the activity and stability of the catalyst towards acidic OER;
- (3) To introduce surface heteroatom dopants in RuIr alloy and facilitate bifunctionality towards overall water splitting in acidic environments;
- (4) To explore a new topology of noble metals by integrating noble metal atoms in the framework of transition metal oxides;
- (5) To investigate the effect of spatial correlation of isolated noble metal sites on the catalytic performance;
- (6) To establish the relationship among physical structural properties, chemisorption behavior and catalytic performance;

### **1.3. Thesis Layout**

This thesis contains seven chapters. Chapter 1 introduces the significance and objectives of the thesis. Chapter 2 reviews the recent achievements in surface and interface engineering in acidic OER electrocatalysts from both experimental and theoretical perspectives. Chapter 3 presents the rational design of a heterostructured OER electrocatalyst (Ru@IrO<sub>x</sub>) that has unique physicochemical properties induced by strong charge redistribution across the metal-metal oxide heterojunction. Chapter 4 studies the catalytic activity dependence at fundamental level on the chemical/valence states of a series of M-RuIr (M = Co, Ni, Fe) catalysts. Chapter 5 investigates the integration of noble metal atoms in the cationic sites of cobalt spinel oxide with short-range order towards significantly improved OER catalytic performance under acidic conditions. Chapter 6 explores the effect of spatial structure of correlated Pt substitutions in

cobalt spinel oxide lattice on their catalytic performance. Chapter 7 summarizes the overall conclusions of this thesis and provides perspectives for future work in the design and development of noble metal electrocatalysts.

## References

1. Seh, Z. W. *et al.* Combining theory and experiment in electrocatalysis: Insights into materials design. *Science* **355**, eaad4998 (2017).
2. Reier, T. *et al.* Electrocatalytic Oxygen Evolution Reaction in Acidic Environments - Reaction Mechanisms and Catalysts. *Adv. Energy Mater.* **7**, 1601275 (2017).
3. Spori, C. *et al.* The Stability Challenges of Oxygen Evolving Catalysts: Towards a Common Fundamental Understanding and Mitigation of Catalyst Degradation. *Angew. Chem. Int. Ed.* **56**, 5994-6021 (2017).
4. Shi, Q., Zhu, C., Du, D. & Lin, Y. Robust noble metal-based electrocatalysts for oxygen evolution reaction. *Chem. Soc. Rev.* **48**, 3181-3192 (2019).
5. Xie, C. *et al.* Surface and Interface Control in Nanoparticle Catalysis. *Chem. Rev.* **120**, 1184-1249 (2020).
6. Yang, Y. *et al.* Metal Surface and Interface Energy Electrocatalysis: Fundamentals, Performance Engineering, and Opportunities. *Chem* **4**, 2054-2083 (2018).

## **Chapter 2 Literature Review**

### **2.1. Introduction**

Although PEM-based water electrolyzers are the key to generation of clean hydrogen fuel from solar and wind energy, in acidic environments the corresponding anodic OER remains to be a bottleneck and prohibits large-scale application. However, because the properties of electrocatalysts are heavily dependent on physicochemical makeup, surface/interface engineering offers a practical way to boost performance of catalysts. This chapter reviews these advances in surface/interface regulation for acidic OER electrocatalysts and explores the structure-property relationship. Specifically, three parts are included: 1. Prevailing OER mechanisms in acid from both a theoretical computational view and experimental findings; 2. The relationship between catalyst design, electronic structure and catalytic performance; 3. The correlation between the OER mechanism and the electronic structure of a catalyst.

### **2.2 Regulating electrocatalysts via surface/interface engineering for acidic oxygen evolution**

This chapter is included as a published perspective article by Jieqiong Shan, Yao Zheng, Bingyang Shi, Kenneth Davey and Shi-Zhang Qiao, Regulating electrocatalysts via surface/interface engineering for acidic oxygen evolution, *ACS Energy Lett.* 2019, 4, 2719–2730.

# Statement of Authorship

Title of Paper	Regulating electrocatalysts via surface/interface engineering for acidic oxygen evolution		
Publication Status	<input checked="" type="checkbox"/> Published	<input type="checkbox"/> Accepted for Publication	
	<input type="checkbox"/> Submitted for Publication	<input type="checkbox"/> Unpublished and Unsubmitted work written in manuscript style	
Publication Details	Shan, J., Zheng, Y., Shi, B., Davey, K. and Qiao, S. Z. (2019). Regulating electrocatalysts via surface and interface engineering for acidic water electrooxidation. <i>ACS Energy Letters</i> , 4(11), 2719-2730.		

## Principal Author

Name of Principal Author (Candidate)	Jieqiong Shan		
Contribution to the Paper	Jieqiong Shan prepared the manuscript.		
Overall percentage (%)	70%		
Certification:	This paper reports on original research I conducted during the period of my Higher Degree by Research candidature and is not subject to any obligations or contractual agreements with a third party that would constrain its inclusion in this thesis. I am the primary author of this paper.		
Signature		Date	20 Jan 2021

## Co-Author Contributions

By signing the Statement of Authorship, each author certifies that:

- i. the candidate's stated contribution to the publication is accurate (as detailed above);
- ii. permission is granted for the candidate to include the publication in the thesis; and
- iii. the sum of all co-author contributions is equal to 100% less the candidate's stated contribution.

Name of Co-Author	Yao Zheng		
Contribution to the Paper	Dr. Yao Zheng gave comments and revised the paper.		
Signature		Date	20 Jan 2021

Name of Co-Author	Bingyang Shi		
Contribution to the Paper	Prof. Bingyang Shi contributed to this work in an advisory capacity and revised the paper.		
Signature		Date	21 Jan 2021

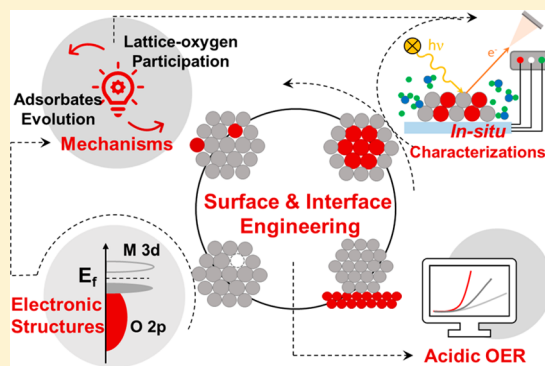
Name of Co-Author	Kenneth Davey		
Contribution to the Paper	Dr. Kenneth Davey contributed to this work in an advisory capacity and revised the paper.		
Signature		Date	25 Jan 2021

Name of Co-Author	Shi-Zhang Qiao		
Contribution to the Paper	Prof. Shi-Zhang Qiao contributed to this work in an advisory capacity and revised the paper.		
Signature		Date	21 Jan 2021

# Regulating Electrocatalysts via Surface and Interface Engineering for Acidic Water Electrooxidation

Jieqiong Shan,<sup>†,§</sup> Yao Zheng,<sup>\*,†,§</sup> Bingyang Shi,<sup>#</sup> Kenneth Davey,<sup>†,§</sup> and Shi-Zhang Qiao<sup>\*,†,§</sup><sup>†</sup>School of Chemical Engineering & Advanced Materials, The University of Adelaide, Adelaide, SA 5005, Australia<sup>§</sup>Centre for Materials in Energy and Catalysis, The University of Adelaide, Adelaide, SA 5005, Australia<sup>#</sup>Henan-Macquarie University Joint Centre for Biomedical Innovation, School of Life Sciences, Henan University, Kaifeng, Henan 475004, China

**ABSTRACT:** Although proton exchange membrane (PEM) water electrolyzers offer a promising means for generation of hydrogen fuel from solar and wind energy, in acidic environments the corresponding anodic oxygen evolution reaction (OER) remains a bottleneck. Because the activity and stability of electrocatalysts depend significantly on physicochemical properties, material surface and interface engineering can offer a practical way to boost performance. To date, significant advances have been made using a judicious combination of advanced theoretical computations and spectroscopic characterizations. To provide a critical assessment of this field, we focus on the establishment of material property–catalytic activity relationships. We start with a detailed exploration of prevailing OER mechanisms in acid solution through evaluating the role of catalyst lattice oxygen. We then critically review advances in surface and interface engineering in acidic OER electrocatalysts from both experimental and theoretical perspectives. Finally, a few promising research orientations are proposed to inspire future investigation of high-performance PEM catalysts.



Clean hydrogen energy is widely considered a promising substitute for dwindling supplies of traditional fossil fuels and the environmental pollution caused through the continued burning of these.<sup>1–3</sup> An ideal means to produce hydrogen is using electrical energy from renewable sources via water electrolysis. This involves two electrochemical reactions in an electrolyzer, namely, oxygen evolution reaction (OER) at the anode and hydrogen evolution reaction (HER) at the cathode.<sup>2,4</sup> As one of the most critical electron-donating counter reactions,<sup>5</sup> the four-electron transferred OER ( $2\text{H}_2\text{O} \rightarrow \text{O}_2 + 4\text{H}^+ + 4\text{e}^-$ ) however exhibits sluggish kinetics. Compared with the two-electron transferred HER, OER dominates the applied voltage of devices for overall water electrolysis.<sup>6,7</sup> Additionally, when compared with alkaline electrolyzers, acidic proton exchange membrane (PEM) water electrolyzers offer significant advantages, including greater voltage efficiency and gas purity.<sup>5</sup> Although HER benefits from fast kinetics in acids, OER in acidic electrolytes remains a significant research and practical challenge because of the corrosive conditions and sluggish kinetics.<sup>3,8</sup>

Ruthenium (Ru) and iridium (Ir) oxides have been extensively investigated as OER electrocatalysts in acidic environments because of inherent advantageous electronic

properties.<sup>9–14</sup> However, although Ru oxides exhibit significant catalytic activity, they generally suffer from poor stability due to the formation of soluble high-oxidation state  $\text{RuO}_4$  during OER.<sup>15,16</sup> In contrast to Ru-based materials, Ir oxides exhibit a relatively high stability but, generally, a lower catalytic activity.<sup>9,17</sup> A few strategies in catalyst design have been adopted to address the requirement for high activity together with long-term stability. One in particular is based on modification of catalyst composition. For example, Ru–Ir bimetallic oxides ( $\text{Ru}_x\text{Ir}_{1-x}\text{O}_2$ ) exhibit a better stability over monometallic Ru oxides based on activity as a function of concentration of Ru.<sup>12,14</sup> Another focuses on regulation of catalyst structure. For example, establishing a Ru@ $\text{IrO}_x$  core–shell nanostructure with strained active Ru core and protective stable  $\text{IrO}_x$  shell can achieve simultaneous high activity together with long-term stability.<sup>18</sup>

As a four-electron transferred reaction, the OER mechanism involves multiple electrochemical steps including the breaking of H–O bonds and the formation of O–O bonds. Therefore,

Received: August 13, 2019

Accepted: October 8, 2019

Published: October 8, 2019



the adsorption strength of a series of reaction intermediates on the surface of the electrocatalyst determines the reaction energy barriers in overall OER kinetics.<sup>19</sup> According to the Sabatier principle, a moderate binding energy of intermediates assures optimal activity of a catalyst.<sup>20</sup> According to the fundamental understanding at present, the adsorption strength of intermediates is closely related to the electronic structure of a catalyst, including density of states (DOS), spin ordering, and charge distribution. A number of studies highlight the dependence of OER catalytic activity on metal–oxygen bond covalency, which indicates an interaction between the d-band of the metal active sites and the O 2p band of the reaction intermediates.<sup>21–23</sup> In addition, Shao-Horn et al. established a simplified parameter of orbit electron filling ( $e_g$ ) to describe the OER activity on perovskites and observed an optimal activity at around  $e_g = 1$ .<sup>24</sup> The regulation of the electronic structure of catalysts therefore offers a promising means to boost OER. Recent significant developments in theoretical calculations and in situ spectroscopy characterizations appear promising means to an enhanced understanding of the OER mechanism. As a result, in recent years a number of strategies have been developed for surfacial and interfacial engineering in material design, including regulation of components (e.g., defect and heteroatom-doping), atomic arrangement (facet and morphology), reconstruction, strain effect, and metal (oxide)-support.<sup>25,26</sup>

Here we provide a critical perspective of fundamental progress in material surface and interface engineering toward improved performance of acidic OER electrocatalysis. A key issue addressed here is the discussion of the two most plausible acidic OER mechanisms, namely, adsorbates evolution mechanism (AEM) and lattice-oxygen participation mechanism (LOM). Of additional interest is to correlate the recent advances in surface and interface engineering with the favorable electronic structure of acidic OER catalysts. We focus on establishing a material property–catalytic activity relationship for a range of OER catalysts. Based on this knowledge, an outline of the existing challenges and opportunities is provided to pave the way for future research.

**OER Mechanisms.** To date, a number of OER mechanisms in acid environments have been proposed based on density functional theory (DFT) calculations.<sup>5</sup> Two of these, i.e., AEM and LOM, are widely discussed by considering the origin of generated oxygen molecules, triggering a series of experimental contributions. AEM postulates that electrocatalytic oxygen product molecules are derived from the water in electrolytes.<sup>27</sup> This contrasts with LOM which proposes that oxygen molecules are partially from lattice oxygen in the catalyst.

AEM and LOM are widely discussed by considering the origin of generated oxygen molecules, triggering a series of experimental contributions.

As is seen in Figure 1a for AEM at pH 0, the first step on a metal oxide ( $\text{MO}_2$ ) surface is postulated to be the formation of adsorbed  $\text{OH}^*$  species on M site (eq A1). The  $\text{OH}^*$  subsequently undergoes proton coupling and electron removal to  $\text{O}^*$  species (eq A2). A nucleophilic attack occurs at  $\text{O}^*$  and forms a hydroperoxide intermediate  $\text{OOH}^*$  (eq A3) that can release an  $\text{O}_2$  molecule to give a clean M active site (eq

A4).<sup>5,27</sup> Each elementary step exhibits specific reaction-free energy as a function of binding energies of the corresponding intermediates ( $\text{O}^*$ ,  $\text{OH}^*$ ,  $\text{OOH}^*$ ). The step with the greatest free energy difference determines the theoretical overpotential ( $\eta_{\text{theory}}$ ) of the reaction. In most cases, the rate-determining step (RDS) is either the oxidation of  $\text{OH}^*$  to  $\text{O}^*$  or the formation of  $\text{OOH}^*$ .<sup>28</sup> Nilsson and co-workers reported an in situ X-ray photoelectron spectroscopy (XPS) study that provided experimental evidence for the DFT-predicted OER mechanism.<sup>29</sup> They observed a decrease in  $\text{IrO}_2$  surface hydroxide species as the electrode was cycled into the OER region. They concluded this was evidence that OER took place via converting hydroxide into oxide on the surface of the catalyst. In addition, a potential-dependent change from  $\text{Ir}^{\text{VI}}$  to  $\text{Ir}^{\text{V}}$  was observed. This was attributed to the formation of the  $\text{OOH}^*$  intermediate that was essential to OER.

At this point, a few issues in AEM on Ir oxides should be discussed. First, the valence states of Ir undergo meaningful change during OER. Specifically, the valence states of Ir were found to increase from +3 to above +4, while the surface  $\text{OH}^*$  species change to  $\text{O}^*$  and  $\text{OOH}^*$ . With subsequent release of an oxygen molecule, the Ir site returns to its initial state ( $\text{Ir}^{3+}$ ) and exhibits excellent cycle stability.<sup>30</sup> Another issue is the structural evolution of Ir oxides in water oxidation, which can be investigated by in situ Raman spectroscopy. As was demonstrated by Pavlovic et al.,<sup>31</sup> in the potential range 0.8–1.2 V (vs. RHE) the iridium oxide undergoes first-stage oxidation from  $\text{Ir}^{3+}$  to  $\text{Ir}^{4+}$ , with decreased Ir–O  $\delta$  stretching vibrations (linked to  $\text{Ir}^{3+}$ ) and increased Ir–O  $\gamma$  (and  $\epsilon$ ) stretching vibrations (linked to  $\text{Ir}^{4+}$ ). As the potential is increased to  $\sim 1.4$  V, the  $\text{Ir}^{4+}$  is oxidized to  $\text{Ir}^{5+}$  with only slight redshift of  $\gamma$  (and  $\epsilon$ ) peaks. When greater potentials are applied, the Ir oxides exhibit no further potential-dependent movement of  $\gamma$  (and  $\epsilon$ ) signals and begin to oxidize water. Additionally, the impact of the pH of the electrolyte solutions is an important consideration in OER. According to AEM, the proton and electron transfer are coupled in every step. This coupled proton–electron-transfer thesis is supported by Nakagawa et al., who found that OER overpotentials of a heterogeneous Ir oxide catalyst have no dependencies on pH value.<sup>32</sup>

It was demonstrated that the adsorption free energies ( $\Delta G$ ) of different intermediates are strongly correlated via a linear relationship, for example,  $\Delta G_{\text{OOH}^*} (\text{eV}) = \Delta G_{\text{OH}^*} + 3.2$ , as can be seen in Figure 1b. Based on this so-called scaling relation, the difference between  $\Delta G_{\text{OH}^*}$  and  $\Delta G_{\text{O}^*}$  was introduced to describe OER overpotential on metal oxide surfaces. A volcano plot can be established to give a general universal principle for activity at pH 0.<sup>33</sup> It should be noted that this scaling relation limits the further optimization of OER overpotential because  $\Delta G$  for each intermediate cannot be modified independently. With the best values of  $\Delta G_{\text{O}^*}$  and  $\Delta G_{\text{OH}^*}$ , a minimum  $\eta_{\text{theory}} = \sim 0.37$  V can be achieved, which imposes a fundamental limitation for PEM electrolyzers.<sup>27,33</sup> A significant research effort in OER is therefore required to break (or bypass) this scaling relation and to realize substantial enhancement in OER catalytic activity.<sup>34</sup> For example, it is reported that the incorporation of Ni and Co into  $\text{RuO}_2$  can reduce OER catalytic overpotential by inducing a proton donor–acceptor effect in a 0.1 M  $\text{HClO}_4$  solution.<sup>35</sup> Based on theoretical model predictions, if a Ni/Co site is located in the surface bridge site, the oxygen atom on top of it will be activated so as to adsorb hydrogen from  $\text{OH}^*$  and  $\text{OOH}^*$  species adsorbed on

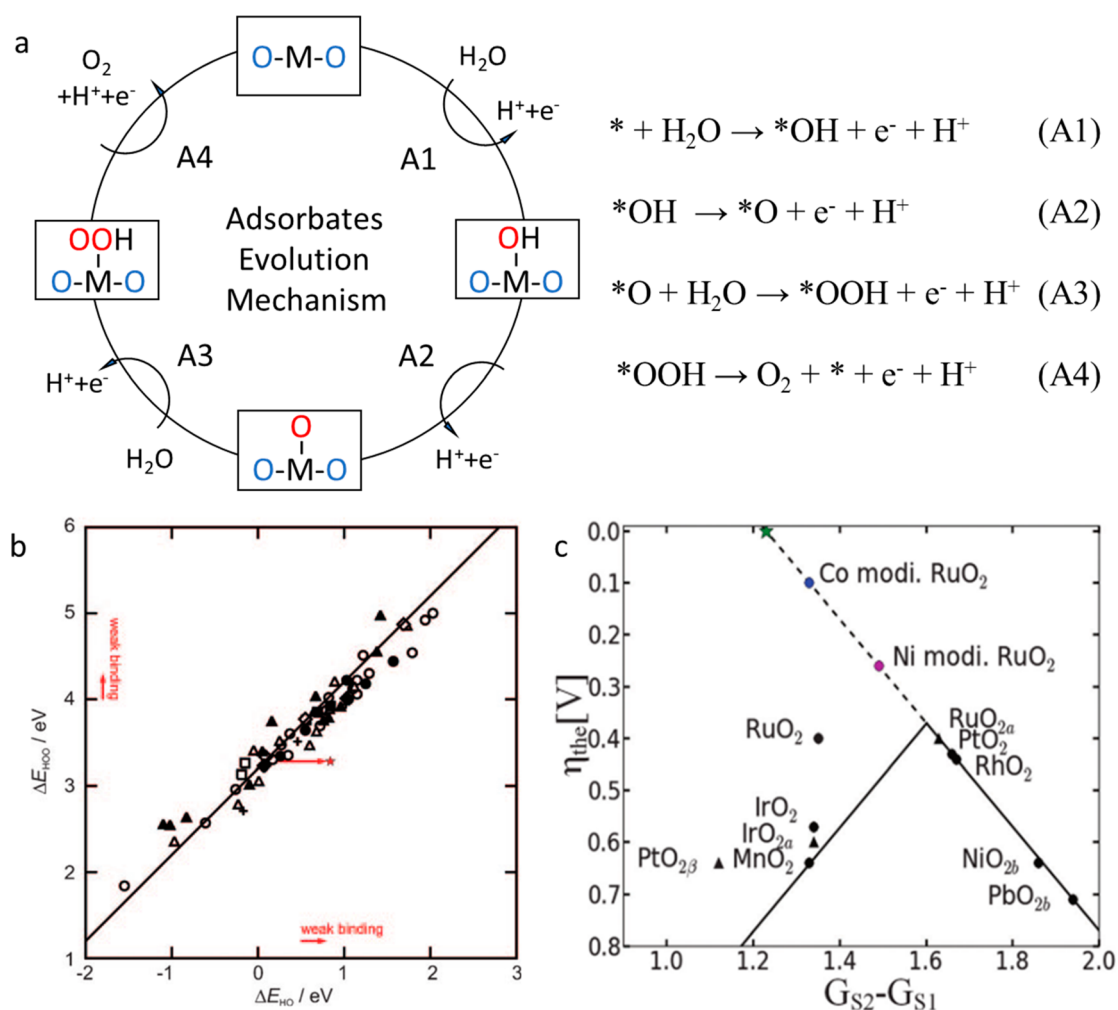


**Figure 1.** (a) Proposed AEM for OER in an acidic environment. (b) Adsorption energy of HOO\* plotted against adsorption energy of HO\* for different oxides. Reprinted with permission from ref 33. Copyright 2011 John Wiley Sons, Inc. (c) Volcano curve of theoretical overpotential for OER using the second charge-transfer reaction as a descriptor. Reprinted with permission from ref 35. Copyright 2014 Royal Society of Chemistry.

neighboring Ru sites. An additional tunable parameter was then introduced to describe this donor–acceptor effect. Through incorporating different dopants, this additional parameter can be optimized independently of the conventional descriptor. In this way an improved OER activity was achieved and the scaling relation based on a conventional descriptor can be overcome (Figure 1c).

By way of contrast to AEM, the LOM mechanism postulates that the evolution of oxygen molecules is derived from the lattice oxygen with a key step of direct O–O coupling.<sup>36</sup> As is illustrated in Figure 2a (pH 0), the first two steps (eqs L1 and L2) can be seen to be similar to those with AEM. For the third step, however, the adsorbed \*O species couple with the lattice oxygen ( $\text{O}_\text{L}$ ) to release one oxygen molecule and to leave a surface oxygen vacancy ( $\text{V}_\text{O}$ ) in the lattice (eq L3). The  $\text{V}_\text{O}$  sites are replenished by water dissociation products to generate adsorbed \*H species (eq L4). In a final mechanism step, the adsorbed \*H is removed to give a clean M site (eq L5). Tarascon and co-workers demonstrated LOM to be pH-dependent with a sequential proton and electron transfer on  $\text{La}_2\text{LiIrO}_6$ .<sup>37</sup> This pH dependence is attributed to the mismatch between the electron-transfer kinetics and hydroxide affinity at the catalyst/electrolyte interface and reflects

nonconcerted proton–electron-transfer behavior.<sup>38</sup> Shao-Horn et al. reported direct experimental evidence of LOM in perovskites for alkaline OER. By performing in situ mass spectrometry they measured the weight of the oxygen molecules produced in OER electrocatalysis on  $^{18}\text{O}$ -labeled perovskites.<sup>39</sup> They found that lattice oxygen participated in OER on certain perovskites. By combining these experimental findings with theoretical computations, the authors further proposed the origin of the LOM as the increase of metal–oxygen bond covalency that activate lattice-oxygen oxidation to trigger nonconcerted proton–electron transfers during OER (Figure 2b). Importantly, it was suggested that LOM bypasses the scaling relation and that it has a lower reaction barrier.

Yoo et al. investigated a series of perovskites and compared theoretical performance through AEM and LOM.<sup>36</sup> As is illustrated in Figure 2c the LOM volcano overlapped that of AEM with a higher peak, which indicates that some electrocatalysts with LOM have lower overpotentials compared with the minimum  $\eta_{\text{theory}}$  defined in AEM. This is attributed to the favorable interaction with \*OH to form oxygen vacancies and \*OO on some surfaces, depending on the A cation sites in the  $\text{ABO}_3$  cell. Additionally, recent studies with Ir-based oxide electrocatalysts indicate direct participation of surface oxygen

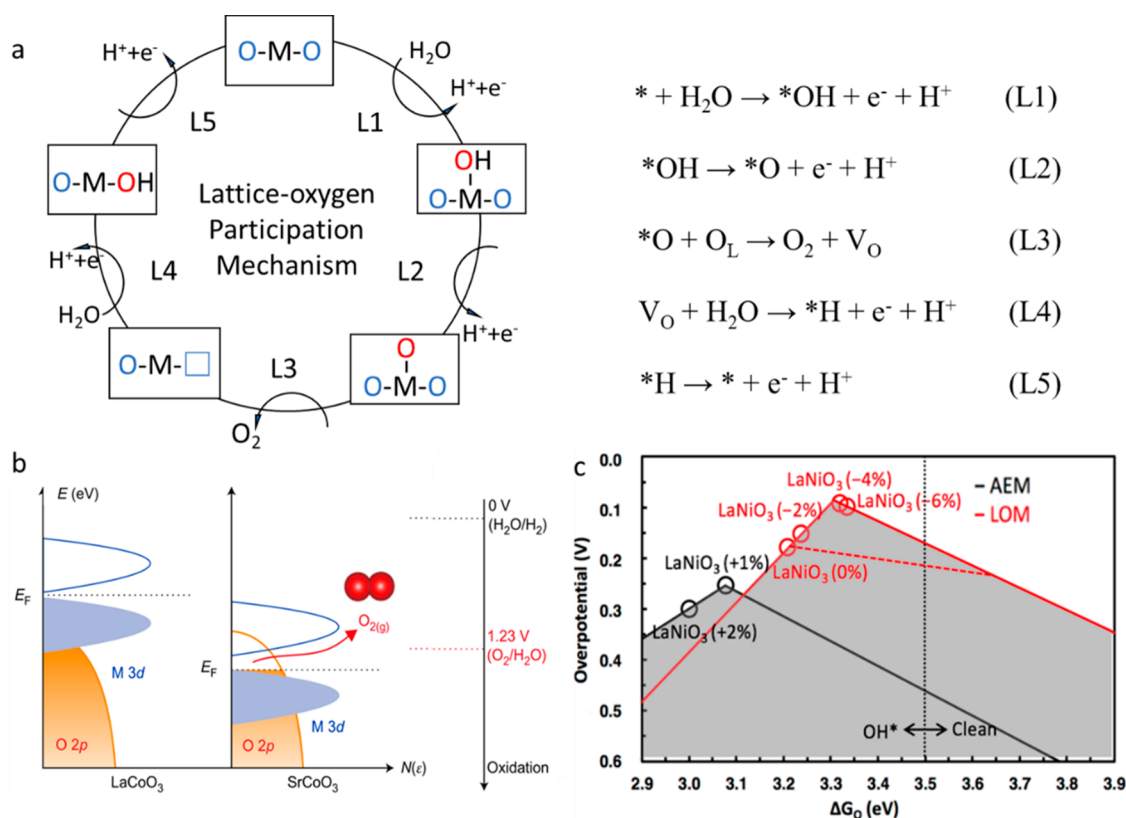


**Figure 2.** (a) Proposed LOM for OER in an acidic environment. The empty square represents the oxygen vacancy. (b) Schematic rigid band diagrams for  $\text{LaCoO}_3$  and  $\text{SrCoO}_3$ . Reprinted with permission from ref 39. Copyright 2017 Nature Publishing Group. (c) Overall OER volcano that takes into account both AEM (black) and LOM (red) for perovskites. Reprinted from ref 36. Copyright 2018 American Chemical Society.

species in acidic OER.<sup>40,41</sup> Ni leaching in IrNi oxide alloy under OER in acid transformed inert surface lattice oxygen into loosely bound surface OH groups that can be directly involved in the reaction.<sup>40</sup> However, other researchers state that LOM can lead to increased dissolution of metal active sites and thereby limit the stability of catalysts.<sup>42</sup> This is because the critical step in reversible formation of oxygen vacancy on the surface of a catalyst can also result in significant insertion and removal of oxygen in and out of its lattice.<sup>36</sup> The current situation points to the fact that a more precise in situ characterization and in-depth understanding of LOM needs to be realized.

A crucial consideration with acidic OER electrocatalysis is long-term stability. This sets a high practical requirement for the catalysts because of strong acidic and oxidative operating conditions. Generally, a chronopotentiometric hold with a constant current density of  $10 \text{ mA cm}^{-2}$  for up to 50 h, or a cyclic voltammetry (CV) test in the OER potential range under scan rates of 50 or  $100 \text{ mV s}^{-1}$  for up to 10 000 cycles, is used as the long-term stability measurement. However, a slowly increased, or even unchanged potential does not necessarily indicate a stable OER electrocatalyst without loss or decay of active sites. The partial dissolution of surface sites might increase the number of exposed active sites. This helps to compensate intrinsic activity decay of each site and can result in an (almost) unchanged apparent performance.<sup>43</sup> Therefore, it is appealed that the catalyst loading should be controlled in long-term stability testing because large amount of catalysts can be gradually corroded and result in an overestimation of working-life. A more objective view of long-

term stability could therefore be obtained from the monitoring of dissolved catalyst ions in electrolytes.<sup>19</sup> In addition, some electrocatalysts can undergo change in structural or surface components in OER. This leads to a mismatch between the fresh-prepared catalysts and the actual catalysts in reactions.<sup>44</sup> In such cases careful characterization must be undertaken to obviate potentially misleading conclusions.

*Surface Engineering for Electronic Structure Modification.* Recent studies have highlighted effective strategies for modification of electronic structure and catalytic performance of electrocatalysts through surface engineering. These include tailored modification of surface composition, surface atomic arrangement regulation, and surface reconstruction.

Modification of surface composition is illustrated in Figure 3a (left), which is generally achieved by introducing structural defects or incorporating heteroatom dopants. This strategy offers a versatile pathway to tune electrocatalytic properties of materials through creation of increased number of active sites, an increased electronic conductivity, and optimized adsorption of reaction intermediates. For example, it has been suggested that surface anion defects like oxygen vacancies can increase electronic conductivity of the catalyst material and boost the rate of charge transfer during electrocatalysis.<sup>47</sup> Cation vacancies on the other hand can induce a lattice distortion and change the local electron distribution, therefore resulting in a tailored intermediate adsorption behavior.<sup>48</sup> For metal oxides, the existence of surface vacancies is generally accompanied by a modified oxygen ligand environment, which associates with the LOM mechanism.<sup>49</sup> For example, in a  $\text{Y}_2[\text{Ru}_{1.6}\text{Y}_{0.4}]\text{O}_{7-\delta}$  electrocatalyst, the partial substitution of

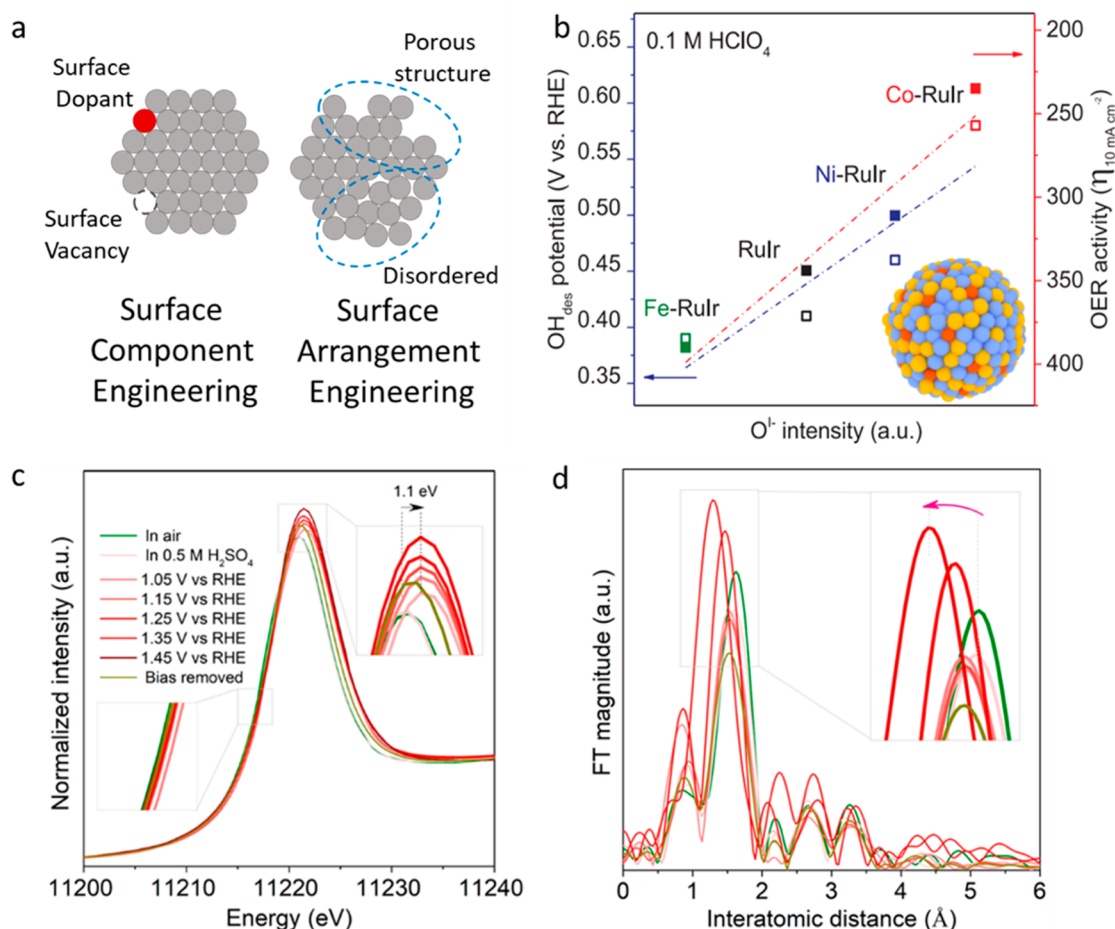


**Figure 3.** (a) Schematic of surface engineering strategies for component and arrangement engineering. (b) Relationship between  $\text{O}^{1-}$  species concentration and  $\text{OH}$  desorption potential and that for OER on various electrocatalysts. Reprinted with permission from ref 45. Copyright 2019 John Wiley Sons, Inc. (c) In situ Ir- $L_3$  XANES and (d) EXAFS spectra recorded under different applied potentials on Li incorporated  $\text{IrO}_x$ . As is shown in the legend of panel c, the curves with darker red color represent spectra achieved through applying greater potentials. Reprinted from ref 46. Copyright 2019 American Chemical Society.

$\text{Ru}^{4+}$  with  $\text{Y}^{3+}$  cations results in a lattice oxygen vacancy and mixed valence states of Ru sites. The oxygen-deficient pyrochlore structure exhibits a lower Ru d-band center and strengthened covalency between Ru 4d and O 2p bands. These two factors together lead to an enhanced OER activity via a LOM pathway.<sup>50</sup> We have reported a Co-doped RuIr alloy electrocatalyst for overall water splitting in acidic environments.<sup>45</sup> Under OER conditions the leaching of less stable Co species in acid resulted in the formation of cation vacancies and increased concentration of surface reactive  $\text{O}^{1-}$  species. The generated electrophilic  $\text{O}^{1-}$  species were highly active in OER because they were vulnerable to nucleophilic attack from water molecules, or hydroxyl species.<sup>41</sup> When coupled with electrochemical investigation on a series of transition metal-doped RuIr, a double-linear relationship can be demonstrated for both oxygen intermediate adsorption ability and OER activity with intensity of  $\text{O}^{1-}$  species (Figure 3b). In another system the depletion of surface Ni in  $\text{IrNiO}_x$  resulted in the formation of  $\text{IrNi}@\text{IrO}_x$  core-shell nanoparticles and gave rise to lattice vacancies in the  $\text{IrO}_x$  shell, as was evidenced by in situ X-ray near-edge structure analysis (XANES).<sup>51</sup> The vacancies produced a significant number of d-band holes that referred to unoccupied d-band states on surface Ir centers, resulting in

increased Ir oxidation states and an enhanced electrophilic characteristic of the surface oxygen ligand. Because of activation of electrophilic oxygen, an energetically favorable O–O bond formation is realized by nucleophilic attack by water or hydroxyl ligands at reduced kinetic barriers that ultimately contribute to improved OER activity.

Heteroatom doping is an effective means to tailor the electronic structure of catalysts.<sup>52</sup> The d-band theory suggests that the introduction of heteroatom dopants moves a metal d-band center relative to the Fermi level and modifies the adsorption ability of reaction intermediates.<sup>53</sup> A systematic study of different transition metal-substituted rutile  $\text{TiO}_2(110)$  surfaces was conducted for OER electrocatalysis. It was predicted that in the case of most dopants, especially for example, Cr, Mo, Mn, and Ir, the doped  $\text{TiO}_2$  surfaces would exhibit boosted OER due to enhanced adsorption of intermediate species.<sup>54</sup> In addition, heteroatom dopants in the crystalline lattice can tailor the local coordination environment. Su et al. designed a Cu-doped  $\text{RuO}_2$  hollow porous polyhedron with a significant OER activity. XPS investigation and DFT calculations demonstrated that charge redistribution around Cu dopants, together with the formation

of neighboring coordinatively unsaturated Ru sites (CUSs), is responsible for the boosted activity.<sup>55</sup>

In addition to surface composition optimization, an effective strategy to alter electrocatalytic properties of a catalyst material

In addition to surface composition optimization, an effective strategy to alter electrocatalytic properties of a catalyst material is structural regulation.

is structural regulation. Within this, surface atomic arrangement has attracted wide research interest. Surface atomic arrangement can be practically realized through the adjustment of surface orientation, surface morphology, and degree of order (Figure 3a, right). For example, Shao-Horn et al. examined OER kinetics on a single-crystal  $\text{RuO}_2(110)$  surface.<sup>56</sup> With a combination of DFT calculations and in situ surface diffraction measurements that monitored atomic structural changes, it was confirmed that Ru CUS sites were in fact the active sites for OER. Then a modified AEM pathway was proposed that RDS was the stabilization of  $-\text{OO}$  species on Ru CUS active sites. A consistent finding was reported also for  $\text{RuO}_2(110)$ , (100), (101), and (111) orientations, where a positive trend was established between density of CUS sites and OER catalytic

activity.<sup>57</sup> In addition, morphology control has been investigated as a structural regulation strategy to boost OER performance through increasing the number of active sites, or through enhancing electronic conductivity. For example, 2D mesoporous metallic Ir nanosheets were reported to exhibit a significantly improved OER activity as a benefit from the greater availability of chemically active sites.<sup>58</sup> In comparison with nanoparticle counterparts, the nanoporous architecture provided an electron transport channel with comparatively lower resistance and was responsible for the increased catalytic activity.<sup>59</sup>

The order degree of catalyst surfaces has recently been considered as a significant parameter impacting OER activity; that is, there is an observed greater activity on amorphous  $\text{IrO}_x$  in comparison with that for crystalline counterparts.<sup>41,60</sup> For example, in a  $\text{Li}-\text{IrO}_x$  system, X-ray absorption spectroscopy (XAS) results denoted that the long-range order of rutile  $\text{IrO}_2$  was broken because of incorporation of lithium and that an amorphous  $\text{Li}-\text{IrO}_x$  structure with disordered  $[\text{IrO}_6]$  octahedrons can be generated.<sup>46</sup> As the applied potential was increased, a constant increase in the absorption peak energy in the Ir  $L_3$ -edge XANES spectra (Figure 3c) and a shrinkage of the Ir–O distance in the Ir  $L_3$ -edge extended X-ray absorption fine structure (EXAFS) spectra (Figure 3d) were observed. This enhanced activity of amorphous  $\text{Li}-\text{IrO}_x$  can be interpreted, therefore, as resulting from the ready oxidation

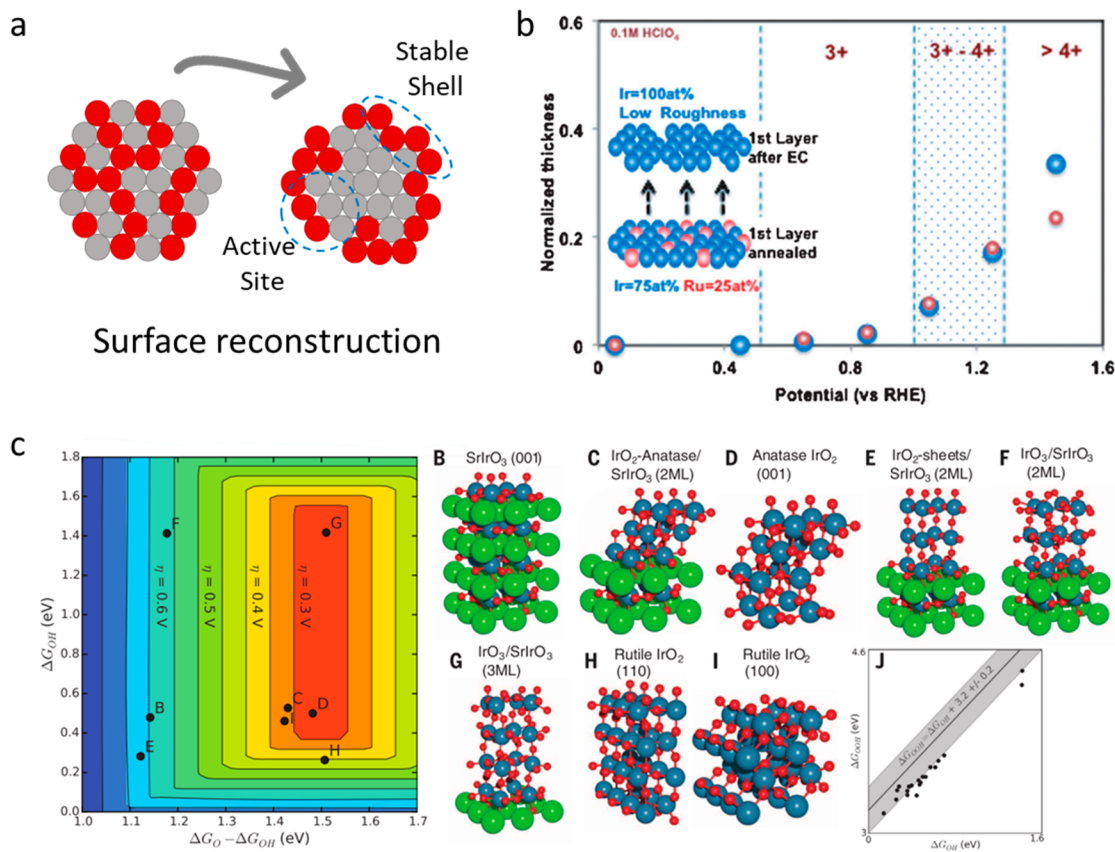
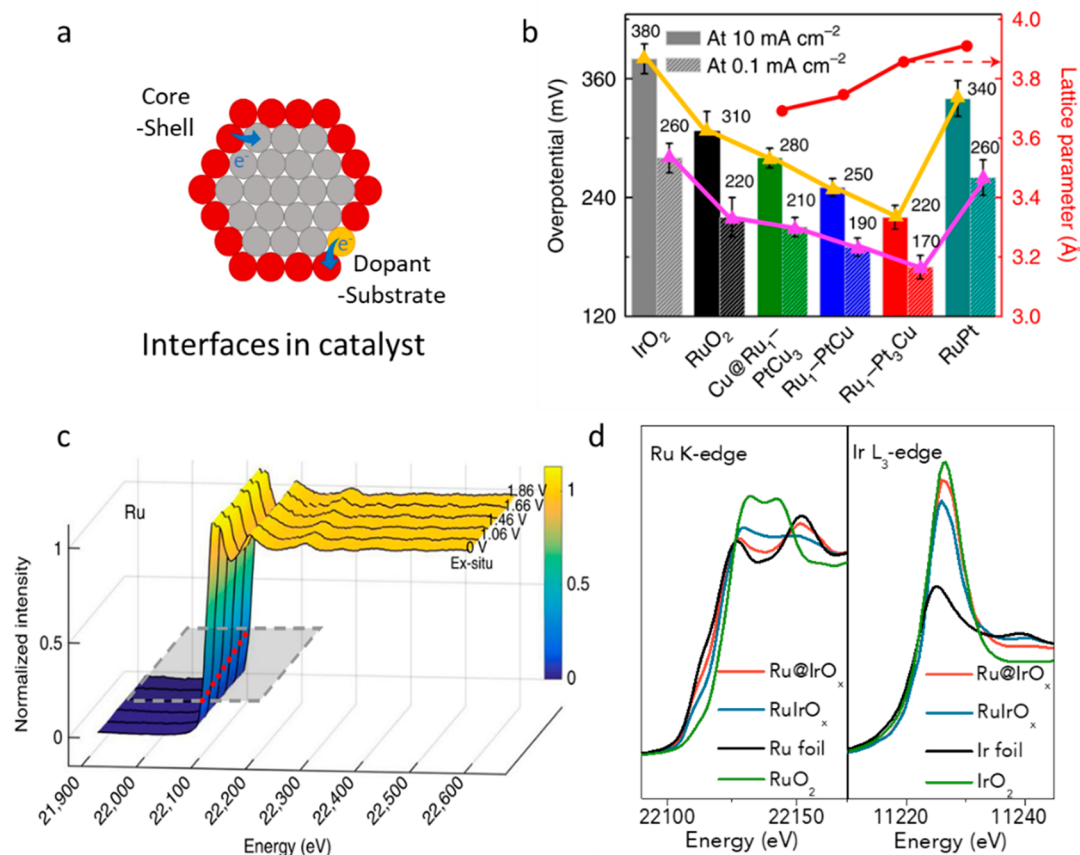


Figure 4. (a) Schematic of surface reconstruction under OER conditions. (b) Relationship between the surface oxidation state of annealed  $\text{Ru}_{0.5}\text{Ir}_{0.5}$  with Ir skeleton formation during OER. Reprinted with permission from ref 62. Copyright 2014 John Wiley Sons, Inc. (c) Theoretical overpotential volcano plot with  $\text{O}^*$  and  $\text{OH}^*$  binding energies as descriptors. The data marked as B–I refer to corresponding visual representation of  $\text{IrO}_x$  and  $\text{SrIrO}_3$  surfaces shown in the right (strontium, green; iridium, blue; oxygen, red). Reprinted with permission from ref 63. Copyright 2016 American Association for the Advancement of Science.



**Figure 5.** (a) Schematic of interfaces in catalyst systems. (b) Overpotential to reach 0.1 and 10 mA cm<sup>-2</sup> for Ru<sub>1-x</sub>PtCu and lattice parameter dependence on composition of different Pt/Cu catalysts. (c) In situ XAS spectra for Ru K-edge during the OER. Reprinted with permission from ref 68. Copyright 2019 Nature Publishing Group. (d) XANES spectra of Ru@IrO<sub>x</sub> core-shell nanocrystals. Reprinted with permission from ref 18. Copyright 2019 Elsevier.

of Ir sites during OER and from shrinkage of the Ir–O bond that promotes hydroxyl oxidation and O–O bond formation.

There is increasing research awareness that many catalyst surfaces can undergo structural reconstruction in catalysis. This is particularly true for OER in acid because of the corrosive and oxidative environment.<sup>44</sup> Surface reconstruction raises a difficulty in identifying the active sites. However, it could be advantageously utilized to boost catalytic performance. One of the most commonly reported surface reconstruction observations is dealloying of multicomponent alloys during electrocatalysis. Typically, the less-noble components undergo selective dissolution under electrochemical environments and leave the segregation of more-noble components in the near-surface domain (Figure 4a).<sup>61</sup> In a well-established acidic OER electrocatalyst of RuIr bimetallic alloys, a Ru<sub>0.5</sub>Ir<sub>0.5</sub> alloy was reported as a model for investigation of the surface segregation phenomenon of Ir. An in situ XANES analysis was conducted on sputtered and annealed Ru<sub>0.5</sub>Ir<sub>0.5</sub> alloy surfaces. Results indicated that a protective Ir skeleton was formed on the latter via rapid dissolution of less-stable Ru (Figure 4b). As a result, it was possible to balance the near-surface composition to form an annealed surface with the segregation-induced enrichment of Ir. This exhibited a four times-enhanced stability without compromising any OER activity.<sup>62</sup>

Additionally, surface reconstruction offers an opportunity to balance the activity and stability of electrocatalysts, thereby making it practical to optimize catalytic performance. In an Ir

core@nanoporous IrO<sub>2</sub> shell (dtf-Ir<sub>25</sub>Os<sub>75</sub>) system synthesized through selective etching of Os in Ir<sub>25</sub>Os<sub>75</sub> precursors, because of successful surface rearrangement, dtf-Ir<sub>25</sub>Os<sub>75</sub> exhibited a 30-fold increase in activity-stability in comparison with the Ir oxide catalyst.<sup>59</sup> Apart from multimetallic alloys, metal oxides have also been demonstrated to undergo surface rearrangement during acidic OER. In a catalyst of IrO<sub>x</sub>/SrIrO<sub>3</sub> derived from bulk SrIrO<sub>3</sub>, the less-stable Sr leached from surface layers during OER electrocatalysis in acid and simultaneously formed a highly active IrO<sub>x</sub> surface layer.<sup>63</sup> An initial activity improvement was observed in continuous electrocatalysis tests that was attributed to the in situ formation of highly active sites through the leaching of Sr. To explore the evolution of active sites during surface reconstruction, DFT calculations were conducted for a series of possible motifs (Figure 4c). Through evaluation of theoretical overpotentials, IrO<sub>3</sub> and anatase IrO<sub>2</sub> motifs were identified as being responsible for the experimentally demonstrated greater activity.

**Interface Engineering for Electronic Structural Modification.** Electrocatalysis is strongly associated with the properties of electrochemical interfaces in a catalyst system, including both the catalyst itself and the structure of the electrocatalyst–electrolyte double layer.<sup>64</sup> Notably the latter is rarely discussed in the general field of acidic OER.<sup>65</sup> Therefore, we focus mainly on interfacial engineering of electrocatalysts. This is achieved through investigation of inner boundaries among

different components of the catalysts and interfaces between catalyst and substrate materials (Figure 5a).

It is a common strategy to tune the catalytic property of metals by alloying with other elements, which leads not only to the adjustment of surface composition but also to the induction of lattice strain among the different components with different lattice parameters. The lattice strain together with lattice mismatch or lattice defects can be used to tailor the electronic structure of catalysts.<sup>66</sup> For example, it is reported that a significant quantity of oxygen vacancies can be generated when a tensile strain is introduced on the outermost surface of CoO nanorods.<sup>67</sup> These oxygen vacancies result in facilitated water dissociation kinetics and a well-modified electronic structure that leads to an optimized catalytic performance. Further, the d-band center can be up-shifted by tensile lattice strain to cause an increased interaction with adsorbates. Alternatively, it can be down-shifted by compressive strain and weaken the interactions.<sup>69</sup> Recently, a series of Pt–Cu alloys with atomically embedded Ru atoms in the Pt-rich shell were used as efficient OER electrocatalysts in acid (Figure 5b).<sup>68</sup> On one hand, the Pt shell exerted a compressive strain on Ru sites, inducing an up-shifted d-band center with optimized intermediate binding energies. On the other hand, in situ XANES studies showed that along with the applied potential, the Pt L<sub>3</sub>-edge underwent an increase in white-line intensity while the Ru K-edge spectra exhibited no change. This finding suggests an increased valence state of Pt and stable oxidation state of Ru in OER (Figure 5c). It is concluded these results imply a charge compensation of Ru from Pt, which acted as an electron reservoir to donate electrons and helped prevent an overoxidation and subsequent dissolution of Ru.<sup>68</sup> Through capture of the OOH\* intermediate on the catalyst surface using in situ attenuated total reflection infrared spectrum, it was confirmed that the dominant OER mechanism on Ru<sub>1</sub>–Pt<sub>3</sub>Cu was AEM rather than LOM, which contributed to its cycling stability.

In addition to modulation of band structure, facilitated charge transfer can also be achieved at the interfaces among

In addition to modulation of band structure, facilitated charge transfer can also be achieved at the interfaces among the different components, leading to modified valence states of the active sites.

the different components, leading to modified valence states of the active sites. For example, a strong charge redistribution can be generated in a well-established Ru@IrO<sub>x</sub> core–shell catalyst with a highly disordered Ru core and a partially oxidized Ir shell.<sup>18</sup> As underscored by XANES, the charge redistribution across the metal–metal oxide heterojunction resulted in a decreased valence for Ru and an increased valence for Ir (Figure 5d). These favorable valence states were reckoned to be responsible for the boosted OER catalytic activity. More importantly, compared with conventional RuIr alloy, the core–shell nanostructure simultaneously exhibited significantly improved structural stability—as well as a more effective protection for inner sites.

The introduction of a support material into the catalyst system offers opportunity to increase dispersion and to reduce

the agglomeration of the active electrocatalysts (Figure 6a). Carbon-based materials are frequently adopted as substrates because of inherent large surface area and high conductivity.<sup>70,71</sup> These can however be oxidized to CO<sub>2</sub> under OER potentials and are therefore not practically appropriate as support materials in PEM electrolyzers.<sup>5</sup> Consequently, other materials have recently been used to trigger electronic effects across the catalyst–substrate interface. For example, Ng et al. introduced an underlying gold–metal support in a Ce-doped Ni oxide catalyst. It was suggested that the Au support increases accessibility of Ni sites during electrocatalysis via geometric effects or high conductivity, contributing to optimized value of OER activity descriptor (Figure 6b).<sup>72</sup> Moreover, complex oxides including pyrochlore oxides have recently been utilized as support materials in alkaline OER applications. The adopted support materials are proposed to assist to expel generated electrons and to reduce the energy barrier of intermediate formation.<sup>73</sup> However, it remains unresolved whether similar approaches will be successful with acidic OER; only a few stable and conductive oxides, including Sn-, In-, W-, and Ti-based oxides, have been used. For example, through using Nb-doped TiO<sub>2</sub> as a support, both mass-based activity and stability of IrO<sub>2</sub> displayed meaningful improvement.<sup>74</sup>

To reveal connections between electrochemical stability and electronic structure of supported catalysts, Strasser et al. developed electrochemically oxidized IrO<sub>x</sub> nanoparticles on mesoporous antimony-doped tin oxide (ATO) and on carbon.<sup>75</sup> They found that, in contrast to carbon, ATO exhibited evident interaction with the IrO<sub>x</sub> catalyst that they inferred as metal–metal oxide support interaction (MMOSI) effects (Figure 6c). As a result of this MMOSI effect, IrO<sub>x</sub>/ATO exhibited a low Ir mass loss (28.3%) in a long-term stability test, substantially outperforming that of the IrO<sub>x</sub>/C counterpart (97.1%). According to XANES analysis, the MMOSI effect can also tailor the electronic structure of Ir (Figure 6d). Ir species exhibited a lower average oxidation state in IrO<sub>x</sub>/ATO (Ir<sup>3.2+</sup>) as compared with those in IrO<sub>x</sub>/C (Ir<sup>4+</sup>). Because of the sacrifice of stability in the formation of high valent Ir oxide layer, it is suggested that the MMOSI effect facilitates a thinner surface oxide layer thickness in the IrO<sub>x</sub>/ATO and assists in stabilizing the Ir species in IrO<sub>x</sub>.

**Challenges and Outlook.** Through a judicious combination of experimental methodologies and advanced characterization techniques, significant progress has been made in research understanding of acidic OER. However, a number of fundamental challenges remain, including the following:

(1) The use of highly scarce iridium in acidic OER electrocatalysts is a bottleneck in the scaling-up of PEM electrolyzers.<sup>19</sup> Therefore, increasing the efficiency of these catalysts through either reducing the use of noble metals or development of earth-abundant alternatives is needed.<sup>6,76</sup> Additionally, although Ir and Ru are the present best OER electrocatalysts, substantial overpotentials are still required, which have slowed development of active OER catalysts. As no significant advances have been reported over the past decades, future research should therefore aim to break the scaling relation to result in reduced overpotentials.

(2) To quantitatively compare the performance of different electrocatalysts, agreed upon standards are needed. For example, mass activity and turnover frequency (TOF) more accurately reflect intrinsic catalyst activity than that based on geometric area. In addition, a significant challenge with acidic

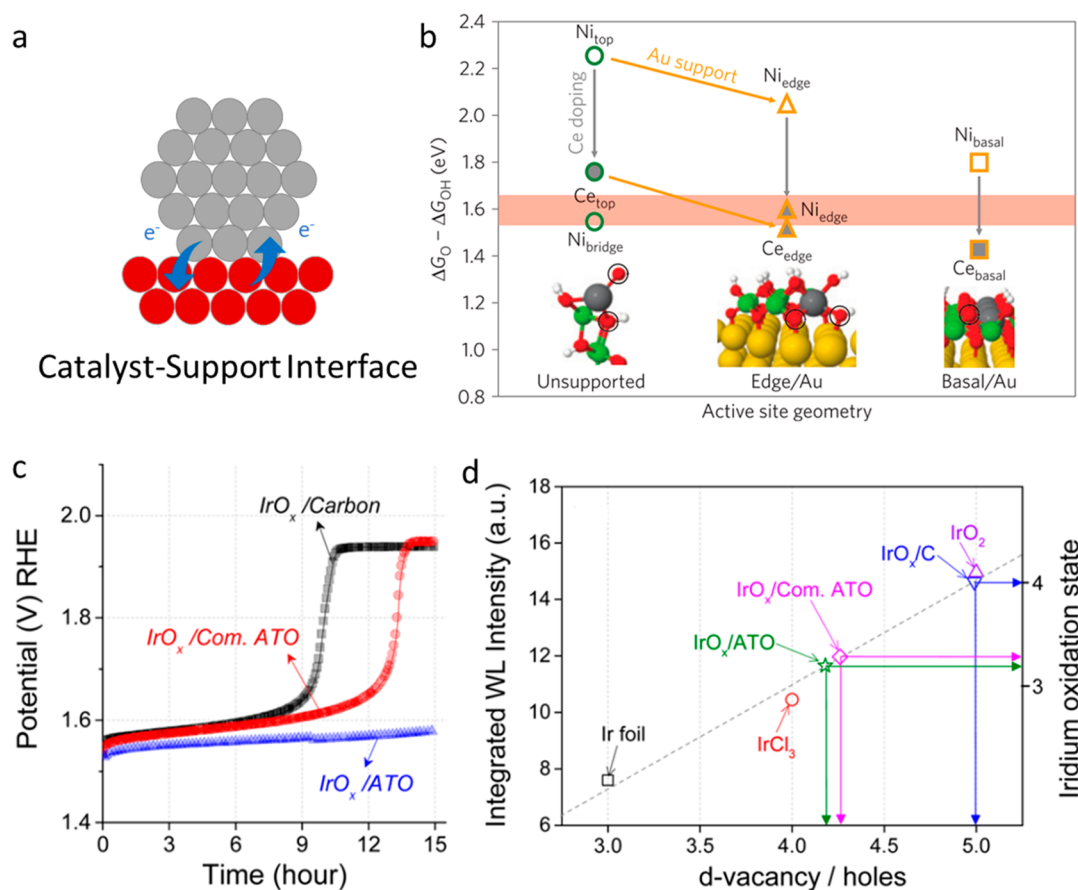


**Figure 6.** (a) Schematic of catalyst–support interface. (b) Deconvolution of various effects modifying OER performance of NiCeO<sub>x</sub>-Au based on DFT calculations. The region shaded in red indicates ideal binding energy of intermediates. Reprinted with permission from ref 72. Copyright 2016 Nature Publishing Group. (c) Constant current stability test of IrO<sub>x</sub>/ATO electrocatalysts for OER. (d) Determination of Ir oxidation states for IrO<sub>x</sub>/ATO and references according to Ir L<sub>3</sub>-edge XANES data. Reprinted from ref 75. Copyright 2016 American Chemical Society.

OER electrocatalysis is long-term stability in the strong acidic and oxidative operating conditions. Developments in understanding of catalytic stability have often been overlooked because of a major emphasis on catalytic activity. Greater in-depth experimental and theoretical study is therefore needed to reveal the origin of stability fading and the structure–stability relationship. Further, it would practically guide the future design of catalysts if a quantitative descriptor dealing with the catalyst stability could be raised.

Greater in-depth experimental and theoretical study is needed to reveal the origin of stability fading and the structure–stability relationship.

(3) Catalyst surfaces are changed dynamically under acidic OER electrocatalysis, mainly because of oxidized potential and acid corrosion. The result is to impede the precise identification of active sites and the exploration of mechanisms based on ex situ characterizations. Therefore, advanced in situ analytical techniques, operando theoretical computations, and microscopy should be utilized to develop understanding of the more well-established catalysts. In situ XAS is a powerful research tool to detect chemical and electronic structures of electrocatalysts during electrocatalysis, including surface

species and structural transformations dependent on applied potential. Resulting information will be of significant value in determining reaction mechanisms and in guiding design of electrocatalysts.<sup>77</sup>

Up to this point, we could expect the establishment of structure–activity/stability relationship as well as more in-depth insights of the reaction mechanism based on a combination of advanced characterizations and controlled electrochemical experiments. The fundamental understanding of electronic structural modification will facilitate design in not only electrocatalysis but also environmental science and energy conversions.

## ■ AUTHOR INFORMATION

### Corresponding Authors

\*E-mail: yao.zheng01@adelaide.edu.au.

\*E-mail: s.qiao@adelaide.edu.au.

### ORCID

Jieqiong Shan: 0000-0003-4308-5027

Yao Zheng: 0000-0002-2411-8041

Shi-Zhang Qiao: 0000-0002-4568-8422

### Notes

The authors declare no competing financial interest.



## Biographies

**Jieqiong Shan** received her M.E. from Shanghai Jiao Tong University in 2016. She is currently a Ph.D. candidate at the School of Chemical Engineering and Advanced Materials of the University of Adelaide under the supervision of Prof. Shi-Zhang Qiao. Her research focuses on electrocatalyst design for water electrolysis.

**Dr. Yao Zheng** received his Ph.D. from the University of Queensland in 2014. Currently he is a Senior Research Fellow in the University of Adelaide, working with Prof. Shi-Zhang Qiao. His research focuses on fundamental studies of key electrocatalysis processes such as oxygen reduction, hydrogen evolution, and CO<sub>2</sub> reduction reactions.

**Dr. Bingyang Shi** received his Ph.D. degree from the University of Adelaide in 2013. He is currently the executive director of International Joint Center for Biomedical Innovations (JCBI). Dr. Shi's research focuses on the development of nanobiotechnology and advanced multifunctional bionanosystems for cancer and neurodegenerative disease diagnosis and therapy.

**Dr. Kenneth Davey** received his Ph.D. degree from Melbourne University. He is currently a Senior Research Scientist in the University of Adelaide. He is an interdisciplinary researcher in chemical engineering, with applications to development of new risk assessments for improved efficiencies, reliability and safety, and energy conversions.

**Dr. Shi-Zhang Qiao** is currently a Chair Professor and Australian Laureate Fellow at the University of Adelaide. His research expertise is in nanomaterials for electrocatalysis, photocatalysis, and energy storage and conversion technologies. His group page is <https://chemeng.adelaide.edu.au/qiao/>.

## ACKNOWLEDGMENTS

This work was financially supported by the Australian Research Council through the Discovery Project programs (FL170100154, DP160104866, and DP170104464) and the Discovery Early Career Researcher Award (DE160101163). J.S. was supported by the Chinese CSC Scholarship Program.

## REFERENCES

- (1) Dunn, S. Hydrogen Futures: Toward a Sustainable Energy System. *Int. J. Hydrogen Energy* **2002**, *27*, 235–264.
- (2) Momirlan, M.; Veziroglu, T. The Properties of Hydrogen as Fuel Tomorrow in Sustainable Energy System for a Cleaner Planet. *Int. J. Hydrogen Energy* **2005**, *30*, 795–802.
- (3) Seh, Z. W.; Kibsgaard, J.; Dickens, C. F.; Chorkendorff, I.; Nørskov, J. K.; Jaramillo, T. F. Combining Theory and Experiment in Electrocatalysis: Insights into Materials Design. *Science* **2017**, *355*, No. eaad4998.
- (4) Jiao, Y.; Zheng, Y.; Jaroniec, M.; Qiao, S. Z. Design of Electrocatalysts for Oxygen- and Hydrogen-Involving Energy Conversion Reactions. *Chem. Soc. Rev.* **2015**, *44*, 2060–2086.
- (5) Reier, T.; Nong, H. N.; Teschner, D.; Schlögl, R.; Strasser, P. Electrocatalytic Oxygen Evolution Reaction in Acidic Environments - Reaction Mechanisms and Catalysts. *Adv. Energy Mater.* **2017**, *7*, 1601275.
- (6) Feng, J.; Lv, F.; Zhang, W.; Li, P.; Wang, K.; Yang, C.; Wang, B.; Yang, Y.; Zhou, J.; Lin, F.; et al. Iridium-Based Multimetallic Porous Hollow Nanocrystals for Efficient Overall-Water-Splitting Catalysis. *Adv. Mater.* **2017**, *29*, 1703798.
- (7) Huynh, M.; Bediako, D. K.; Nocera, D. G. A Functionally Stable Manganese Oxide Oxygen Evolution Catalyst in Acid. *J. Am. Chem. Soc.* **2014**, *136*, 6002–6010.
- (8) Lebedev, D.; Povia, M.; Waltar, K.; Abdala, P. M.; Castelli, I. E.; Fabbri, E.; Blanco, M. V.; Fedorov, A.; Copéret, C.; Marzari, N.; et al. Highly Active and Stable Iridium Pyrochlores for Oxygen Evolution Reaction. *Chem. Mater.* **2017**, *29*, 5182–5191.
- (9) Lee, Y.; Suntivich, J.; May, K. J.; Perry, E. E.; Shao-Horn, Y. Synthesis and Activities of Rutile IrO<sub>2</sub> and RuO<sub>2</sub> Nanoparticles for Oxygen Evolution in Acid and Alkaline Solutions. *J. Phys. Chem. Lett.* **2012**, *3*, 399–404.
- (10) Pedersen, A. F.; Escudero-Escribano, M.; Sebok, B.; Bodin, A.; Paoli, E.; Frydendal, R.; Friebel, D.; Stephens, I. E. L.; Rossmeisl, J.; Chorkendorff, I.; et al. Operando XAS Study of the Surface Oxidation State on a Monolayer IrOx on RuOx and Ru Oxide Based Nanoparticles for Oxygen Evolution in Acidic Media. *J. Phys. Chem. B* **2018**, *122*, 878–887.
- (11) Escudero-Escribano, M.; Pedersen, A. F.; Paoli, E. A.; Frydendal, R.; Friebel, D.; Malacrida, P.; Rossmeisl, J.; Stephens, I. E. L.; Chorkendorff, I. Importance of Surface IrOx in Stabilizing RuO<sub>2</sub> for Oxygen Evolution. *J. Phys. Chem. B* **2018**, *122*, 947–955.
- (12) Cheng, J.; Zhang, H.; Chen, G.; Zhang, Y. Study of IrxRuy-xO<sub>2</sub> Oxides as Anodic Electrocatalysts for Solid Polymer Electrolyte Water Electrolysis. *Electrochim. Acta* **2009**, *54*, 6250–6256.
- (13) Sardar, K.; Petrucco, E.; Hiley, C. I.; Sharman, J. D.; Wells, P. P.; Russell, A. E.; Kashtiban, R. J.; Sloan, J.; Walton, R. I. Water-Splitting Electrocatalysis in Acid Conditions Using Ruthenate-Iridate Pyrochlores. *Angew. Chem., Int. Ed.* **2014**, *53*, 10960–10964.
- (14) Kötz, R.; Stucki, S. Stabilization of RuO<sub>2</sub> by IrO<sub>2</sub> for Anodic Oxygen Evolution in Acid Media. *Electrochim. Acta* **1986**, *31*, 1311–1316.
- (15) Kötz, R.; Stucki, S.; Scherson, D.; Kolb, D. M. In-Situ Identification of RuO<sub>4</sub> as the Corrosion Product During Oxygen Evolution on Ruthenium in Acid Media. *J. Electroanal. Chem. Interfacial Electrochem.* **1984**, *172*, 211–219.
- (16) Wohlfahrt-Mehrens, M.; Heitbaum, J. Oxygen Evolution on Ru and RuO<sub>2</sub> Electrodes Studied Using Isotope Labelling and On-Line Mass Spectrometry. *J. Electroanal. Chem. Interfacial Electrochem.* **1987**, *237*, 251–260.
- (17) Danilovic, N.; Subbaraman, R.; Chang, K. C.; Chang, S. H.; Kang, Y. J.; Snyder, J.; Paulikas, A. P.; Strmcnik, D.; Kim, Y. T.; Myers, D.; et al. Activity-Stability Trends for the Oxygen Evolution Reaction on Monometallic Oxides in Acidic Environments. *J. Phys. Chem. Lett.* **2014**, *5*, 2474–2478.
- (18) Shan, J.; Guo, C.; Zhu, Y.; Chen, S.; Song, L.; Jaroniec, M.; Zheng, Y.; Qiao, S.-Z. Charge-Redistribution-Enhanced Nanocrystalline Ru@IrOx Electrocatalysts for Oxygen Evolution in Acidic Media. *Chem.* **2019**, *5*, 445–459.
- (19) Kibsgaard, J.; Chorkendorff, I. Considerations for the Scaling-up of Water Splitting Catalysts. *Nat. Energy* **2019**, *4*, 430–433.
- (20) Katsounaros, I.; Cherevko, S.; Zeradjanin, A. R.; Mayrhofer, K. J. Oxygen Electrochemistry as a Cornerstone for Sustainable Energy Conversion. *Angew. Chem., Int. Ed.* **2014**, *53*, 102–121.
- (21) Shang, C.; Cao, C.; Yu, D.; Yan, Y.; Lin, Y.; Li, H.; Zheng, T.; Yan, X.; Yu, W.; Zhou, S.; et al. Electron Correlations Engineer Catalytic Activity of Pyrochlore Iridates for Acidic Water Oxidation. *Adv. Mater.* **2018**, *31*, 1805104.
- (22) Sun, S.; Sun, Y.; Zhou, Y.; Xi, S.; Ren, X.; Huang, B.; Liao, H.; Wang, L. P.; Du, Y.; Xu, Z. Shifting Oxygen Charge Towards Octahedral Metal: A Way to Promote Water Oxidation on Cobalt Spinell Oxides. *Angew. Chem., Int. Ed.* **2019**, *58*, 6042–6047.
- (23) Grimaud, A.; May, K. J.; Carlton, C. E.; Lee, Y. L.; Risch, M.; Hong, W. T.; Zhou, J.; Shao-Horn, Y. Double Perovskites as a Family of Highly Active Catalysts for Oxygen Evolution in Alkaline Solution. *Nat. Commun.* **2013**, *4*, 2439.
- (24) Suntivich, J.; May, K. J.; Gasteiger, H. A.; Goodenough, J. B.; Shao-Horn, Y. A Perovskite Oxide Optimized for Oxygen Evolution Catalysis from Molecular Orbital Principles. *Science* **2011**, *334*, 1383–1385.
- (25) Jiao, Y.; Zheng, Y.; Chen, P.; Jaroniec, M.; Qiao, S. Z. Molecular Scaffolding Strategy with Synergistic Active Centers to Facilitate Electrocatalytic CO<sub>2</sub> Reduction to Hydrocarbon/Alcohol. *J. Am. Chem. Soc.* **2017**, *139*, 18093–18100.

- (26) Vasileff, A.; Xu, C.; Jiao, Y.; Zheng, Y.; Qiao, S.-Z. Surface and Interface Engineering in Copper-Based Bimetallic Materials for Selective CO<sub>2</sub> Electroreduction. *Chem.* **2018**, *4*, 1809–1831.
- (27) Rossmeisl, J.; Qu, Z. W.; Zhu, H.; Kroes, G. J.; Nørskov, J. K. Electrolysis of Water on Oxide Surfaces. *J. Electroanal. Chem.* **2007**, *607*, 83–89.
- (28) Montoya, J. H.; Seitz, L. C.; Chakthranont, P.; Vojvodic, A.; Jaramillo, T. F.; Nørskov, J. K. Materials for Solar Fuels and Chemicals. *Nat. Mater.* **2017**, *16*, 70–81.
- (29) Sanchez Casalongue, H. G.; Ng, M. L.; Kaya, S.; Friebel, D.; Ogasawara, H.; Nilsson, A. In Situ Observation of Surface Species on Iridium Oxide Nanoparticles During the Oxygen Evolution Reaction. *Angew. Chem.* **2014**, *126* (28), 7297–7300.
- (30) Cheng, J.; Yang, J.; Kitano, S.; Juhasz, G.; Higashi, M.; Sadakiyo, M.; Kato, K.; Yoshioka, S.; Sugiyama, T.; Yamauchi, M.; et al. Impact of Ir-Valence Control and Surface Nanostructure on Oxygen Evolution Reaction over a Highly Efficient Ir–TiO<sub>2</sub> Nanorod Catalyst. *ACS Catal.* **2019**, *9*, 6974–6986.
- (31) Pavlovic, Z.; Ranjan, C.; Gao, Q.; van Gastel, M.; Schlögl, R. Probing the Structure of a Water-Oxidizing Anodic Iridium Oxide Catalyst using Raman Spectroscopy. *ACS Catal.* **2016**, *6*, 8098–8105.
- (32) Nakagawa, T.; Beasley, C. A.; Murray, R. W. Efficient Electro-oxidation of Water near Its Reversible Potential by a Mesoporous IrOx Nanoparticle Film. *J. Phys. Chem. C* **2009**, *113*, 12958–12961.
- (33) Man, I. C.; Su, H.-Y.; Calle-Vallejo, F.; Hansen, H. A.; Martínez, J. I.; Inoglu, N. G.; Kitchin, J.; Jaramillo, T. F.; Nørskov, J. K.; Rossmeisl, J. Universality in Oxygen Evolution Electrocatalysis on Oxide Surfaces. *ChemCatChem* **2011**, *3*, 1159–1165.
- (34) Busch, M.; Halck, N. B.; Kramm, U. I.; Siahrostami, S.; Krtil, P.; Rossmeisl, J. Beyond the Top of The Volcano? – A Unified Approach to Electrocatalytic Oxygen Reduction and Oxygen Evolution. *Nano Energy* **2016**, *29*, 126–135.
- (35) Halck, N. B.; Petrykin, V.; Krtil, P.; Rossmeisl, J. Beyond the Volcano Limitations in Electrocatalysis-Oxygen Evolution Reaction. *Phys. Chem. Chem. Phys.* **2014**, *16*, 13682–13688.
- (36) Yoo, J. S.; Rong, X.; Liu, Y.; Kolpak, A. M. Role of Lattice Oxygen Participation in Understanding Trends in the Oxygen Evolution Reaction on Perovskites. *ACS Catal.* **2018**, *8*, 4628–4636.
- (37) Grimaud, A.; Demortière, A.; Saubanère, M.; Dachraoui, W.; Duchamp, M.; Doublet, M.-L.; Tarascon, J.-M. Activation of Surface Oxygen Sites on an Iridium-based Model Catalyst for the Oxygen Evolution Reaction. *Nat. Energy* **2017**, *2*, 16189.
- (38) Huang, Z.-F.; Song, J.; Du, Y.; Xi, S.; Dou, S.; Nsanzimana, J. M. V.; Wang, C.; Xu, Z. J.; Wang, X. Chemical and Structural Origin of Lattice Oxygen Oxidation in Co–Zn Oxyhydroxide Oxygen Evolution Electrocatalysts. *Nat. Energy* **2019**, *4*, 329–338.
- (39) Grimaud, A.; Diaz-Morales, O.; Han, B.; Hong, W. T.; Lee, Y. L.; Giordano, L.; Stoerzinger, K. A.; Koper, M. T. M.; Shao-Horn, Y. Activating Lattice Oxygen Redox Reactions in Metal Oxides to Catalyze Oxygen Evolution. *Nat. Chem.* **2017**, *9*, 457–465.
- (40) Reier, T.; Pawolek, Z.; Cherevko, S.; Bruns, M.; Jones, T.; Teschner, D.; Selve, S.; Bergmann, A.; Nong, H. N.; Schlögl, R.; et al. Molecular Insight in Structure and Activity of Highly Efficient, Low-Ir Ir-Ni Oxide Catalysts for Electrochemical Water Splitting (OER). *J. Am. Chem. Soc.* **2015**, *137*, 13031–13040.
- (41) Pfeifer, V.; Jones, T. E.; Velasco Velez, J. J.; Arrigo, R.; Piccinin, S.; Havecker, M.; Knop-Gericke, A.; Schlögl, R. In Situ Observation of Reactive Oxygen Species Forming on Oxygen-Evolving Iridium Surfaces. *Chem. Sci.* **2017**, *8*, 2143–2149.
- (42) Rong, X.; Parolin, J.; Kolpak, A. M. A Fundamental Relationship between Reaction Mechanism and Stability in Metal Oxide Catalysts for Oxygen Evolution. *ACS Catal.* **2016**, *6*, 1153–1158.
- (43) Spori, C.; Kwan, J. T. H.; Bonakdarpour, A.; Wilkinson, D. P.; Strasser, P. The Stability Challenges of Oxygen Evolving Catalysts: Towards a Common Fundamental Understanding and Mitigation of Catalyst Degradation. *Angew. Chem., Int. Ed.* **2017**, *56*, 5994–6021.
- (44) Jiang, H.; He, Q.; Zhang, Y.; Song, L. Structural Self-Reconstruction of Catalysts in Electrocatalysis. *Acc. Chem. Res.* **2018**, *51*, 2968–2977.
- (45) Shan, J.; Ling, T.; Davey, K.; Zheng, Y.; Qiao, S. Z. Transition-Metal-Doped RuIr Bifunctional Nanocrystals for Overall Water Splitting in Acidic Environments. *Adv. Mater.* **2019**, *31*, 1900510.
- (46) Gao, J.; Xu, C. Q.; Hung, S. F.; Liu, W.; Cai, W.; Zeng, Z.; Jia, C.; Chen, H. M.; Xiao, H.; Li, J.; et al. Breaking Long-Range Order in Iridium Oxide by Alkali Ion for Efficient Water Oxidation. *J. Am. Chem. Soc.* **2019**, *141*, 3014–3023.
- (47) Chen, P.; Tong, Y.; Wu, C.; Xie, Y. Surface/Interfacial Engineering of Inorganic Low-Dimensional Electrode Materials for Electrocatalysis. *Acc. Chem. Res.* **2018**, *51*, 2857–2866.
- (48) Cheng, W.; Zhang, H.; Zhao, X.; Su, H.; Tang, F.; Tian, J.; Liu, Q. A Metal-Vacancy-Solid-Solution NiAlP Nanowall Array Bifunctional Electrocatalyst for Exceptional All-pH Overall Water Splitting. *J. Mater. Chem. A* **2018**, *6*, 9420–9427.
- (49) Mefford, J. T.; Rong, X.; Abakumov, A. M.; Hardin, W. G.; Dai, S.; Kolpak, A. M.; Johnston, K. P.; Stevenson, K. J. Water Electrolysis on La(1-x)Sr(x)CoO(3-delta) Perovskite Electrocatalysts. *Nat. Commun.* **2016**, *7*, 11053.
- (50) Kim, J.; Shih, P. C.; Qin, Y.; Al-Bardan, Z.; Sun, C. J.; Yang, H. A Porous Pyrochlore Y<sub>2</sub>[Ru<sub>1.6</sub>Y<sub>0.4</sub>]O<sub>7-delta</sub> Electrocatalyst for Enhanced Performance towards the Oxygen Evolution Reaction in Acidic Media. *Angew. Chem., Int. Ed.* **2018**, *57*, 13877–13881.
- (51) Nong, H. N.; Reier, T.; Oh, H.-S.; Gliech, M.; Paciok, P.; Vu, T. H. T.; Teschner, D.; Heggen, M.; Petkov, V.; Schlögl, R.; et al. A Unique Oxygen Ligand Environment Facilitates Water Oxidation in Hole-doped IrNiOx Core-shell Electrocatalysts. *Nat. Catal.* **2018**, *1*, 841–851.
- (52) Bayatsarmadi, B.; Zheng, Y.; Tang, Y.; Jaroniec, M.; Qiao, S. Z. Significant Enhancement of Water Splitting Activity of N-Carbon Electrocatalyst by Trace Level Co Doping. *Small* **2016**, *12*, 3703–3711.
- (53) Zheng, Y.; Jiao, Y.; Zhu, Y.; Cai, Q.; Vasileff, A.; Li, L. H.; Han, Y.; Chen, Y.; Qiao, S. Z. Molecule-Level g-C<sub>3</sub>N<sub>4</sub> Coordinated Transition Metals as a New Class of Electrocatalysts for Oxygen Electrode Reactions. *J. Am. Chem. Soc.* **2017**, *139*, 3336–3339.
- (54) García-Mota, M.; Vojvodic, A.; Metiu, H.; Man, I. C.; Su, H.-Y.; Rossmeisl, J.; Nørskov, J. K. Tailoring the Activity for Oxygen Evolution Electrocatalysis on Rutile TiO<sub>2</sub>(110) by Transition-Metal Substitution. *ChemCatChem* **2011**, *3*, 1607–1611.
- (55) Su, J.; Ge, R.; Jiang, K.; Dong, Y.; Hao, F.; Tian, Z.; Chen, G.; Chen, L. Assembling Ultrasmall Copper-Doped Ruthenium Oxide Nanocrystals into Hollow Porous Polyhedra: Highly Robust Electrocatalysts for Oxygen Evolution in Acidic Media. *Adv. Mater.* **2018**, *30*, 1801351.
- (56) Rao, R. R.; Kolb, M. J.; Halck, N. B.; Pedersen, A. F.; Mehta, A.; You, H.; Stoerzinger, K. A.; Feng, Z.; Hansen, H. A.; Zhou, H.; et al. Towards Identifying the Active Sites on RuO<sub>2</sub>(110) in Catalyzing Oxygen Evolution. *Energy Environ. Sci.* **2017**, *10*, 2626–2637.
- (57) Stoerzinger, K. A.; Diaz-Morales, O.; Kolb, M.; Rao, R. R.; Frydendal, R.; Qiao, L.; Wang, X. R.; Halck, N. B.; Rossmeisl, J.; Hansen, H. A.; et al. Orientation-Dependent Oxygen Evolution on RuO<sub>2</sub> without Lattice Exchange. *ACS Energy Lett.* **2017**, *2*, 876–881.
- (58) Jiang, B.; Guo, Y.; Kim, J.; Whitten, A. E.; Wood, K.; Kani, K.; Rowan, A. E.; Henzie, J.; Yamauchi, Y. Mesoporous Metallic Iridium Nanosheets. *J. Am. Chem. Soc.* **2018**, *140*, 12434–12441.
- (59) Kim, Y. T.; Lopes, P. P.; Park, S. A.; Lee, A. Y.; Lim, J.; Lee, H.; Back, S.; Jung, Y.; Danilovic, N.; Stamenkovic, V.; et al. Balancing Activity, Stability and Conductivity of Nanoporous Core-Shell Iridium/Iridium Oxide Oxygen Evolution Catalysts. *Nat. Commun.* **2017**, *8*, 1449.
- (60) Pfeifer, V.; Jones, T. E.; Velasco Velez, J. J.; Massué, C.; Arrigo, R.; Teschner, D.; Girgsdies, F.; Scherzer, M.; Greiner, M. T.; Allan, J.; et al. The Electronic Structure of Iridium and Its Oxides. *Surf. Interface Anal.* **2016**, *48*, 261–273.

(61) Strasser, P. Free Electrons to Molecular Bonds and Back: Closing the Energetic Oxygen Reduction (ORR)-Oxygen Evolution (OER) Cycle Using Core-Shell Nanoelectrocatalysts. *Acc. Chem. Res.* **2016**, *49*, 2658–2668.

(62) Danilovic, N.; Subbaraman, R.; Chang, K. C.; Chang, S. H.; Kang, Y.; Snyder, J.; Paulikas, A. P.; Strmcnik, D.; Kim, Y. T.; Myers, D.; et al. Using Surface Segregation to Design Stable Ru-Ir Oxides for the Oxygen Evolution Reaction in Acidic Environments. *Angew. Chem., Int. Ed.* **2014**, *53*, 14016–14021.

(63) Seitz, L. C.; Dickens, C. F.; Nishio, K.; Hikita, Y.; Montoya, J.; Doyle, A.; Kirk, C.; Vojvodic, A.; Hwang, H. Y.; Nørskov, J. K.; et al. A Highly Active and Stable IrO<sub>x</sub>/SrIrO<sub>3</sub> Catalyst for the Oxygen Evolution Reaction. *Science* **2016**, *353*, 1011–1014.

(64) Stamenkovic, V. R.; Strmcnik, D.; Lopes, P. P.; Markovic, N. M. Energy and Fuels from Electrochemical Interfaces. *Nat. Mater.* **2017**, *16*, 57–69.

(65) Wu, C. H.; Weatherup, R. S.; Salmeron, M. B. Probing Electrode/Electrolyte Interfaces In Situ by X-ray Spectroscopies: Old Methods, New Tricks. *Phys. Chem. Chem. Phys.* **2015**, *17*, 30229–30239.

(66) Guo, C.; Zheng, Y.; Ran, J.; Xie, F.; Jaroniec, M.; Qiao, S. Z. Engineering High-Energy Interfacial Structures for High-Performance Oxygen-Involving Electrocatalysis. *Angew. Chem., Int. Ed.* **2017**, *56*, 8539–8543.

(67) Ling, T.; Yan, D. Y.; Wang, H.; Jiao, Y.; Hu, Z.; Zheng, Y.; Zheng, L.; Mao, J.; Liu, H.; Du, X. W.; et al. Activating Cobalt(II) Oxide Nanorods for Efficient Electrocatalysis by Strain Engineering. *Nat. Commun.* **2017**, *8*, 1509.

(68) Yao, Y.; Hu, S.; Chen, W.; Huang, Z.-Q.; Wei, W.; Yao, T.; Liu, R.; Zang, K.; Wang, X.; Wu, G.; et al. Engineering the Electronic Structure of Single Atom Ru Sites via Compressive Strain Boosts Acidic Water Oxidation Electrocatalysis. *Nat. Catal.* **2019**, *2*, 304–313.

(69) Mavrikakis, M.; Hammer, B.; Nørskov, J. K. Effect of Strain on the Reactivity of Metal Surfaces. *Phys. Rev. Lett.* **1998**, *81*, 2819–2822.

(70) Duan, H.; Li, D.; Tang, Y.; He, Y.; Ji, S.; Wang, R.; Lv, H.; Lopes, P. P.; Paulikas, A. P.; Li, H.; et al. High-Performance Rh<sub>2</sub>P Electrocatalyst for Efficient Water Splitting. *J. Am. Chem. Soc.* **2017**, *139*, 5494–5502.

(71) Najafi, L.; Bellani, S.; Oropesa-Nunez, R.; Prato, M.; Martin-Garcia, B.; Brescia, R.; Bonaccorso, F. Carbon Nanotube-Supported MoSe<sub>2</sub> Holey Flake: Mo<sub>2</sub>C Ball Hybrids for Bifunctional pH-Universal Water Splitting. *ACS Nano* **2019**, *13*, 3162–3176.

(72) Ng, J. W. D.; Garcia-Melchor, M.; Bajdich, M.; Chakhranont, P.; Kirk, C.; Vojvodic, A.; Jaramillo, T. F. Gold-Supported Cerium-Doped NiO<sub>x</sub> Catalysts for Water Oxidation. *Nat. Energy* **2016**, *1*, 16053.

(73) Kim, M.; Lee, B.; Ju, H.; Lee, S. W.; Kim, J. Reducing the Barrier Energy of Self-Reconstruction for Anchored Cobalt Nanoparticles as Highly Active Oxygen Evolution Electrocatalyst. *Adv. Mater.* **2019**, *31*, 1901977.

(74) Hu, W.; Chen, S.; Xia, Q. IrO<sub>2</sub>/Nb–TiO<sub>2</sub> Electrocatalyst for Oxygen Evolution Reaction in Acidic Medium. *Int. J. Hydrogen Energy* **2014**, *39*, 6967–6976.

(75) Oh, H. S.; Nong, H. N.; Reier, T.; Bergmann, A.; Gliech, M.; Ferreira de Araujo, J.; Willinger, E.; Schlogl, R.; Teschner, D.; Strasser, P. Electrochemical Catalyst-Support Effects and Their Stabilizing Role for IrO<sub>x</sub> Nanoparticle Catalysts During the Oxygen Evolution Reaction. *J. Am. Chem. Soc.* **2016**, *138*, 12552–12563.

(76) Pi, Y.; Shao, Q.; Wang, P.; Guo, J.; Huang, X. General Formation of Monodisperse IrM (M = Ni, Co, Fe) Bimetallic Nanoclusters as Bifunctional Electrocatalysts for Acidic Overall Water Splitting. *Adv. Funct. Mater.* **2017**, *27*, 1700886.

(77) Yang, Y.; Luo, M.; Zhang, W.; Sun, Y.; Chen, X.; Guo, S. Metal Surface and Interface Energy Electrocatalysis: Fundamentals, Performance Engineering, and Opportunities. *Chem.* **2018**, *4*, 2054–2083.

## **Chapter 3 Charge-Redistribution-Enhanced Nanocrystalline Ru@IrO<sub>x</sub> Electrocatalysts**

### **for Oxygen Evolution in Acidic Media**

#### **3.1. Introduction and Significance**

Electrochemical OER in acidic media is of great importance in PEM-based water electrolyzers for clean hydrogen fuel generation but largely hindered by serious catalyst degradation due to harsh corrosive and oxidative operation conditions of this process. So far, however, not only the highly active and stable OER electrocatalysts are still lacking, but the rational catalyst design fulfilling the OER requirement of simultaneously optimizing activity and stability is rarely elucidated. This chapter aims to present a new strategy of inducing “charge redistribution across heterojunction” to achieve unique physicochemical properties on nanocrystalline Ru@IrO<sub>x</sub> electrocatalysts, where the OER catalytic activity and stability are simultaneously enhanced. In this chapter, atomic imaging and advanced spectroscopy techniques, including HAADF-STEM and synchrotron-based XAFS have been used to identify the existence of highly strained and distorted Ru cores and partially oxidized Ir shells in Ru@IrO<sub>x</sub> nanocrystals. A strong charge redistribution occurred across the Ru metal-Ir oxide heterojunction, resulting in an increased valence of iridium shell and a decreased valence of ruthenium core, which bring a synergistic electronic and structural interaction for enhanced activity and stability. Significantly, the newly developed Ru@IrO<sub>x</sub> exceeds the most known active RuO<sub>2</sub> catalyst in the activity and simultaneously surpasses the most known stable IrO<sub>2</sub> in the stability.

### **3.2. Charge Redistribution-Enhanced Nanocrystalline Ru@IrO<sub>x</sub> Electrocatalysts for Oxygen Evolution in Acidic Media**

This section is included as a published article by Jieqiong Shan, Chunxian Guo, Yihan Zhu, Shuangming Chen, Li Song, Mietek Jaroniec, Yao Zheng and Shi-Zhang Qiao, Charge Redistribution-Enhanced Nanocrystalline Ru@IrO<sub>x</sub> Electrocatalysts for Oxygen Evolution in Acidic Media, *Chem* 2019, 5, 445–459.

# Statement of Authorship

Title of Paper	Charge-Redistribution-Enhanced Nanocrystalline Ru@IrO <sub>x</sub> Electrocatalysts for Oxygen Evolution in Acidic Media
Publication Status	<input checked="" type="checkbox"/> Published <input type="checkbox"/> Accepted for Publication <input type="checkbox"/> Submitted for Publication <input type="checkbox"/> Unpublished and Unsubmitted work written in manuscript style
Publication Details	Shan, J., Guo, C., Zhu, Y., Chen, S., Song, L., Jaroniec, M., Zheng, Y. and Qiao, S. Z. (2019). Charge-redistribution-enhanced nanocrystalline Ru@ IrO <sub>x</sub> electrocatalysts for oxygen evolution in acidic media. <i>Chem</i> , 5(2), 445-459.

## Principal Author

Name of Principal Author (Candidate)	Jieqiong Shan
Contribution to the Paper	Jieqiong Shan synthesized the materials, conducted physical characterizations and electrocatalytic experiments and wrote the paper.
Overall percentage (%)	60%
Certification:	This paper reports on original research I conducted during the period of my Higher Degree by Research candidature and is not subject to any obligations or contractual agreements with a third party that would constrain its inclusion in this thesis. I am the primary author of this paper.
Signature	Date 20 Jan 2021

## Co-Author Contributions

By signing the Statement of Authorship, each author certifies that:

- i. the candidate's stated contribution to the publication is accurate (as detailed above);
- ii. permission is granted for the candidate to include the publication in the thesis; and
- iii. the sum of all co-author contributions is equal to 100% less the candidate's stated contribution.

Name of Co-Author	Chunxian Guo
Contribution to the Paper	Prof. Chunxian Guo conducted the XPS characterization and contributed to writing the paper.
Signature	Date 20 Jan 2021

Name of Co-Author	Yihan Zhu
Contribution to the Paper	Prof. Yihan Zhu conducted the HAADF-STEM analysis and contributed to writing the paper.
Signature	Date 20 Jan 2021

Name of Co-Author	Shuangming Chen		
Contribution to the Paper	Prof. Shuangming Chen conducted the XAS characterization.		
Signature		Date	20 Jan 2021

Name of Co-Author	Li Song		
Contribution to the Paper	Prof. Li Song conducted the XAS characterization.		
Signature		Date	21 Jan 2021

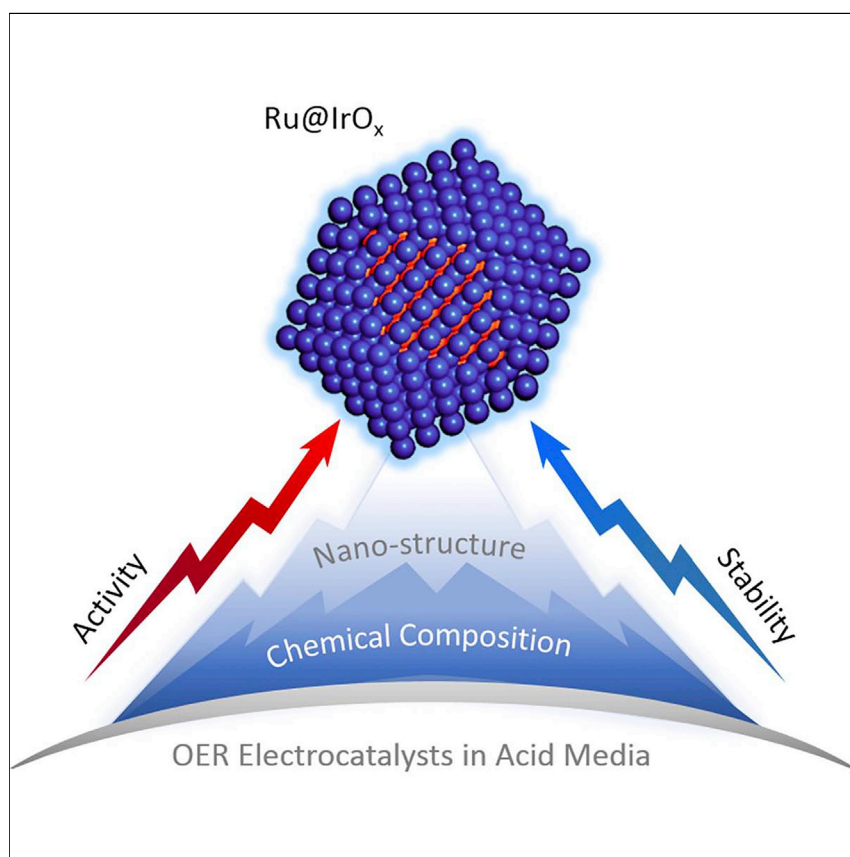
Name of Co-Author	Mietek Jaroniec		
Contribution to the Paper	Prof. Mietek Jaroniec contributed to this work in an advisory capacity and revised the paper.		
Signature		Date	20 Jan 2021

Name of Co-Author	Yao Zheng		
Contribution to the Paper	Dr. Yao Zheng designed the experiments and contributed to writing the paper.		
Signature		Date	20 Jan 2021

Name of Co-Author	Shi-Zhang Qiao		
Contribution to the Paper	Prof. Shi-Zhang Qiao designed the experiments and contributed to writing the paper.		
Signature		Date	21 Jan 2021

## Article

# Charge-Redistribution-Enhanced Nanocrystalline Ru@IrO<sub>x</sub> Electrocatalysts for Oxygen Evolution in Acidic Media



A core-shell Ru@IrO<sub>x</sub> heterostructured nanocrystal was designed and constructed to be OER electrocatalyst in acidic media. Enhanced by strong charge redistribution across the core-shell heterojunction, this catalyst not only breaks the activity and stability limits of RuO<sub>2</sub> and IrO<sub>2</sub> simultaneously but also outperforms most of the known acidic OER electrocatalysts. This project offers a new idea to simultaneously enhance electrocatalytic activity and stability by inducing charge redistribution within heterostructured electrocatalysts.

Jieqiong Shan, Chunxian Guo, Yihan Zhu, ..., Mietek Jaroniec, Yao Zheng, Shi-Zhang Qiao

yao.zheng01@adelaide.edu.au (Y.Z.)  
s.qiao@adelaide.edu.au (S.-Z.Q.)

#### HIGHLIGHTS

The Ru@IrO<sub>x</sub> catalyst shows superb acidic OER activity and long-term stability

Ru@IrO<sub>x</sub> breaks the activity and stability limits of RuO<sub>2</sub> and IrO<sub>2</sub> simultaneously

Charge redistribution in Ru@IrO<sub>x</sub> facilitates its catalytic performance



Shan et al., Chem 5, 445–459  
February 14, 2019 © 2018 Elsevier Inc.  
<https://doi.org/10.1016/j.chempr.2018.11.010>





## Article

# Charge-Redistribution-Enhanced Nanocrystalline Ru@IrO<sub>x</sub> Electrocatalysts for Oxygen Evolution in Acidic Media

Jieqiong Shan,<sup>1,5</sup> Chunxian Guo,<sup>1,5</sup> Yihan Zhu,<sup>2,5</sup> Shuangming Chen,<sup>3</sup> Li Song,<sup>3</sup> Mietek Jaroniec,<sup>4</sup> Yao Zheng,<sup>1,\*</sup> and Shi-Zhang Qiao<sup>1,6,\*</sup>

## SUMMARY

Achieving high activity and long-term stability is a major challenge in the design of catalysts. In particular, the oxygen evolution reaction (OER) in acidic media, which plays a key role in proton exchange membrane electrolyzers for fast hydrogen fuel generation, seriously suffers from rapid degradation of catalysts as a result of the harsh acidic and oxidative conditions. Here, we report a rational design strategy for the fabrication of a heterostructured OER electrocatalyst (Ru@IrO<sub>x</sub>) that has unique physicochemical properties and in which a strong charge redistribution exists between a highly strained ruthenium core and a partially oxidized iridium shell across the metal-metal oxide heterojunction. The increased valence of the iridium shell and the decreased valence of the ruthenium core activate a synergistic electronic and structural interaction, which results in the enhanced activity and stability of the catalyst compared with the majority of the state-of-the-art ruthenium- and iridium-based materials.

## INTRODUCTION

Exploration of catalysts with enhanced activity and long-term operation durability is the ultimate goal in the design of materials.<sup>1–5</sup> It is a great challenge to simultaneously achieve these two properties because often they are inversely correlated: usually an enhancement in the activity of a catalyst sacrifices its stability, and vice versa.<sup>6,7</sup> For example, platinum (Pt) catalysts after reducing their particle sizes exhibit an improved catalytic activity toward hydrolysis of ammonia borane, which simultaneously decreases their stability due to the agglomeration of the resulting particles.<sup>8</sup> On the other hand, the adoption of stabilizers, e.g., polymers, can improve the stability of palladium (Pd) catalytic particles in the Suzuki reaction, although at the same time this strategy reduces their catalytic activity.<sup>9</sup>

The same dilemma also exists in the case of the electrocatalytic oxygen evolution reaction (OER), which is one of the most critical electron-donating reactions for renewable energy conversion processes such as water electrolysis.<sup>10,11</sup> Compared with the two-electron hydrogen evolution reaction proceeding at the cathode, the kinetics of four-electron anodic OER is more sluggish, and dominates the applied voltage in the overall water electrolysis devices.<sup>12,13</sup> Over conventional alkaline electrolyzers, the advanced proton exchange membrane electrolyzers possess strong merits attributable to their faster and higher current density for hydrogen generation.<sup>10,14</sup> Nevertheless, acidic electrolytes always create a strong oxidation environment, which sets high standards for robust electrocatalysts.<sup>15,16</sup> In particular, the aforementioned opposite trends of a catalyst's activity and stability are more significant for OER in

## The Bigger Picture

The investigation of materials with both activity and stability is a primary goal of electrocatalyst design. As a significant resolution to produce clean hydrogen energy, proton-exchange-membrane water electrolyzers possess strong merits over traditional alkaline electrolyzers, and these include high voltage efficiency, low ohmic losses, and compact system design. Nevertheless, the anodic oxygen evolution reaction suffers from slow reaction kinetics and harsh operation conditions, which sets high standards for electrocatalysts. Here, on the basis of the state-of-the-art ruthenium (Ru) and iridium (Ir) oxide nanocrystals, we report a core-shell Ru@IrO<sub>x</sub> nanocrystal with charge redistribution across the interface. Benefiting from the favorable valence states and stable nanostructure, Ru@IrO<sub>x</sub> exhibits simultaneously enhanced activity and stability. This work opens a new horizon for developing efficient electrocatalysts by rational promotion of charge redistribution within heterostructures.



acidic electrolytes.<sup>7,17</sup> As has been shown previously, the more active noble metal oxides with high surface energy tend to be less stable during electrocatalytic oxygen evolution processes.<sup>7,18,19</sup>

For decades, only ruthenium (Ru) and iridium (Ir) and their derivatives have been intensively investigated as OER electrocatalysts in acidic media because of their inherent electronic properties and relatively high stability.<sup>20–25</sup> Ru oxides (e.g., RuO<sub>2</sub>) exhibit high catalytic activity but normally suffer from poor stability due to the formation of soluble high oxidation state Ru oxides (e.g., RuO<sub>4</sub>) during the OER process.<sup>26,27</sup> In contrast, Ir oxides (e.g., IrO<sub>2</sub>) show a relatively high stability but always exhibit lower catalytic activity than Ru-based materials.<sup>7,20</sup> Correspondingly, one of the possible strategies for the activity-stability optimization is based on the exploration of bimetallic Ru and Ir materials.<sup>12,23,25,28–30</sup> For example, RuO<sub>2</sub>-IrO<sub>2</sub> mixed oxides initially exhibit an improved activity in comparison with that of Ir monometallic oxide, but their activity drops significantly as a result of the loss of Ru sites during the reaction.<sup>16,31</sup> On the other hand, RuIr bimetallic oxides (Ru<sub>x</sub>Ir<sub>1-x</sub>O<sub>2</sub>) show better stability than RuO<sub>2</sub>, but their activity cannot exceed that of RuO<sub>2</sub>.<sup>23,25,32</sup>

At present, simultaneous enhancement of both activity and stability of RuIr OER electrocatalysts under acidic conditions is still unavailable, the OER performance generally being limited by the monometallic oxides.<sup>10</sup> This could be due to the fact that so far the studies are focused on the composition-dependent performance of OER catalysts, whereas the optimization of bimetallic oxide nanostructures and modification of their electronic properties are rarely investigated.<sup>21,22</sup> It is noteworthy that in the well-developed field of oxygen reduction reaction, a considerable effort has been devoted to the exploration of the structural effects on the catalytic behavior of Pt-based bimetallic nanocatalysts.<sup>33–35</sup> Many strategies have been developed to design Pt nanostructures with increased activity and stability such as alloying Pt with secondary metals,<sup>36</sup> forming a Pt skin or skeleton on the surface of nanocatalysts;<sup>37</sup> and constructing core-shell nanostructures with Pt-rich shells.<sup>1</sup> Such nanostructure engineering of Pt-based catalysts can modify electronic structures of Pt and thus increase its catalytic properties,<sup>34</sup> which may also shed the light on the design of RuIr bimetallic oxides for OER electrocatalysis. Thus, the remaining major challenge is to find a way to promote Ru and Ir components to work cooperatively toward surpassing their individual limits.

Herein, we propose a strategy to enhance simultaneously the activity and stability of RuIr bimetallic oxide electrocatalysts by taking advantage of the synergistic effect achieved by tuning their electronic properties and nanostructure. Namely, the charge redistribution across the metal-metal oxide heterojunction is generated via a rational design of a core-shell RuIr nanostructure (Ru@IrO<sub>x</sub>) with a highly strained and disordered Ru core and a partially oxidized Ir shell. Because of the favorable valence state of active sites, the as-prepared Ru@IrO<sub>x</sub> nanostructure can offer an overpotential of only 282 mV to deliver an anodic current density of 10 mA cm<sup>-2</sup> together with an activity retention of 90% over a 24-hr test in acidic environments.

## RESULTS AND DISCUSSION

### Synthesis and Structure Characterization of Nanocrystals

The Ru@IrO<sub>x</sub> core-shell nanocrystals were synthesized via a sequential polyol method,<sup>38</sup> whereby Ru nanocrystals were first obtained by reduction of ruthenium(III) acetylacetonate (Ru(acac)<sub>3</sub>·xH<sub>2</sub>O) in ethylene glycol (EG) with poly-(vinylpyrrolidone) (PVP) as a stabilizer under refluxing conditions. Next, the coating of IrO<sub>x</sub> shells on Ru cores was

<sup>1</sup>School of Chemical Engineering, University of Adelaide, Adelaide, SA 5005, Australia

<sup>2</sup>Department of Chemical Engineering and State Key Laboratory Breeding Base of Green Chemistry Synthesis Technology, Zhejiang University of Technology, Hangzhou 310014, China

<sup>3</sup>National Synchrotron Radiation Laboratory, University of Science and Technology of China, Hefei 230029, China

<sup>4</sup>Department of Chemistry and Biochemistry, Kent State University, Kent, OH 44242, USA

<sup>5</sup>These authors contributed equally

<sup>6</sup>Lead Contact

\*Correspondence:  
yao.zheng01@adelaide.edu.au (Y.Z.),  
s.qiao@adelaide.edu.au (S.-Z.Q.)

<https://doi.org/10.1016/j.chempr.2018.11.010>

achieved by adding iridium(III) chloride hydrate ( $\text{IrCl}_3 \cdot x\text{H}_2\text{O}$ ) into the Ru colloidal nanocrystals and heating the system under refluxing conditions. To study the structural effect of  $\text{Ru@IrO}_x$  core-shell nanocrystals, we also synthesized RuIr oxide alloy as a control sample by a co-reduction process (see [Experimental Procedures](#) for details). The resultant  $\text{Ru@IrO}_x$  and RuIr oxide alloy ( $\text{RuIrO}_x$ ) nanocrystals both display narrow size distribution with ultra-small diameters. The  $\text{Ru@IrO}_x$  sample is monodispersed, whereas the  $\text{RuIrO}_x$  sample has a certain degree of aggregation ([Figure S1](#)).

As shown in the X-ray diffraction (XRD) patterns ([Figure 1A](#)), the broad reflections indicate the ultrafine crystalline sizes of Ru and Ir oxide nanocrystals.<sup>18,39</sup> Both  $\text{Ru@IrO}_x$  core-shell and  $\text{RuIrO}_x$  nanocrystals exhibit diffraction peaks dominated by Ir (JCPDS #06-0598), together with an extra shoulder reflection at around  $44^\circ$  that arises from Ru (JCPDS #06-0663). In addition, the high-angle annular dark-field scanning transmission electron microscopy (HAADF-STEM) image ([Figures 1B and S2](#)) together with the histogram of particle diameters in [Figure S3](#) verified that the  $\text{Ru@IrO}_x$  nanocrystals exhibit an ultra-small particle size of  $4.35 \pm 0.34$  nm with a narrow distribution. The corresponding energy-dispersive spectroscopy (EDX) elemental maps and linear profiles clearly reveal that the Ru and Ir species are segregated from each other and form a RuIr core-shell heterostructure ([Figures 1C–1F](#)). By inspecting the EDX spectra collected at the core and shell regions ([Figure S4](#)), a sharp increase in the K-edge signal of oxygen was observed in the later region, implying that the Ir shell was partially oxidized in the  $\text{Ru@IrO}_x$  heterostructure.

In the HAADF-STEM image of a randomly chosen  $\text{Ru@IrO}_x$  nanocrystal ([Figure 2A](#)), an Ir-containing shell with brighter contrast and a Ru core with darker contrast can be clearly identified. This is totally different from the uniform contrast of a  $\text{RuIrO}_x$  as shown in [Figure S5](#). On the basis of the similar experimental and simulated atomic-resolution HAADF-STEM image and corresponding fast Fourier transforms (FFTs), the  $\text{Ru@IrO}_x$  nanocrystal closely resembles an *f.c.c.* structured  $\text{Ru}_{147}\text{@Ir}_{414}$  multiply twinned icosahedral model heterostructure projected along the  $[112]$  direction ([Figures 2B and 2C](#)).<sup>40</sup> Notably, a considerable difference between the Ru cores in the  $\text{Ru@IrO}_x$  sample and in the  $\text{Ru}_{147}\text{@Ir}_{414}$  model structure is observed, whereby the former exhibits a highly strained and distorted lattice. This can be further verified by the disappearance of  $(2\bar{2}0)$  reflections marked by green dashed circles in the FFT of the whole icosahedral nanocrystal ([Figures 2A and 2B](#), insets), which originates from the reduced ordering of the  $[112]$  projected crystalline Ru core and is indicative of a strong interaction between the Ru core and the Ir-containing shell ([Figure 2D](#)).

In addition, it is also very interesting to observe from an enlarged view of the HAADF-STEM image that the  $[110]$  oriented subgrains near the shell region of the  $\text{Ru@IrO}_x$  icosahedral nanocrystal are highly strained ([Figure 2E](#)). The corresponding lattice contrast is distorted anisotropically and exhibits an interplanar spacing as large as  $2.53 \text{ \AA}$ . Given that the oxygen contrast can hardly be observed by HAADF-STEM and the tetragonal  $\text{IrO}_2$  structure exhibits very similar structural projection along  $[100]$  with that of Ir along  $[110]$  except for a larger interplanar spacing ( $2.58$  versus  $2.22 \text{ \AA}$ , as shown in [Figures 2E and 2F](#)), it is most likely that the Ir-containing shells are not purely metallic but partially oxidized, which matches well with the previous observations by EDX. The Ir-containing shell can thus be properly denoted as  $\text{IrO}_x$  and accounts for the observed large strain in the Ru core through core-shell interaction.

### Surface Chemical States Analysis

It has been widely reported that an optimal electronic structure (e.g., modified-valence sites) of nanostructured electrocatalysts are essential for improved OER electrocatalytic

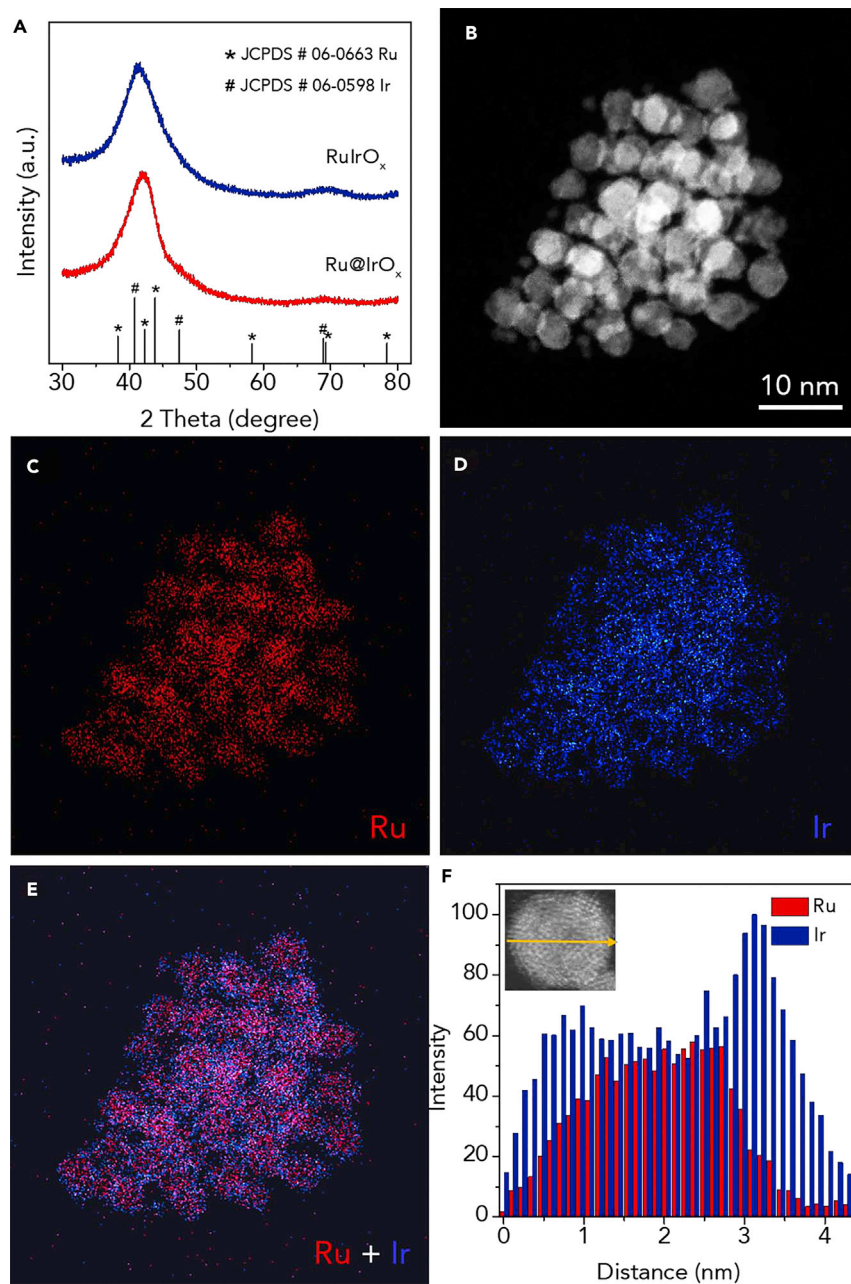


**Figure 1. Structure Characterization of Ru@IrO<sub>x</sub> Nanocrystals**

(A) XRD patterns of Ru@IrO<sub>x</sub> and RuIrO<sub>x</sub> nanoparticles.

(B–E) HAADF-STEM image (B) and the corresponding EDX elemental maps (C–E) of Ru@IrO<sub>x</sub> nanocrystals, in which red refers to Ru and blue refers to Ir, and the overlap image (E) of the Ru and Ir elements indicates the well-defined core-shell structure. Scale bar: 10 nm.

(F) EDX line profile across an individual Ru@IrO<sub>x</sub> nanocrystal with a diameter of around 4.5 nm.

See also Figure S1.

performance.<sup>41–43</sup> First, a series of *ex situ* X-ray photoelectron spectra (XPS) and synchrotron-based X-ray absorption near-edge spectroscopy (XANES) measurements were performed on the as-prepared nanocrystals to study the structural effect on their valence states. As shown in Figure 3A, the Ru 3d XPS spectra of Ru@IrO<sub>x</sub> can be fitted with two sets of doublets; the lower-energy couples at 280.5 and 284.7 eV can be

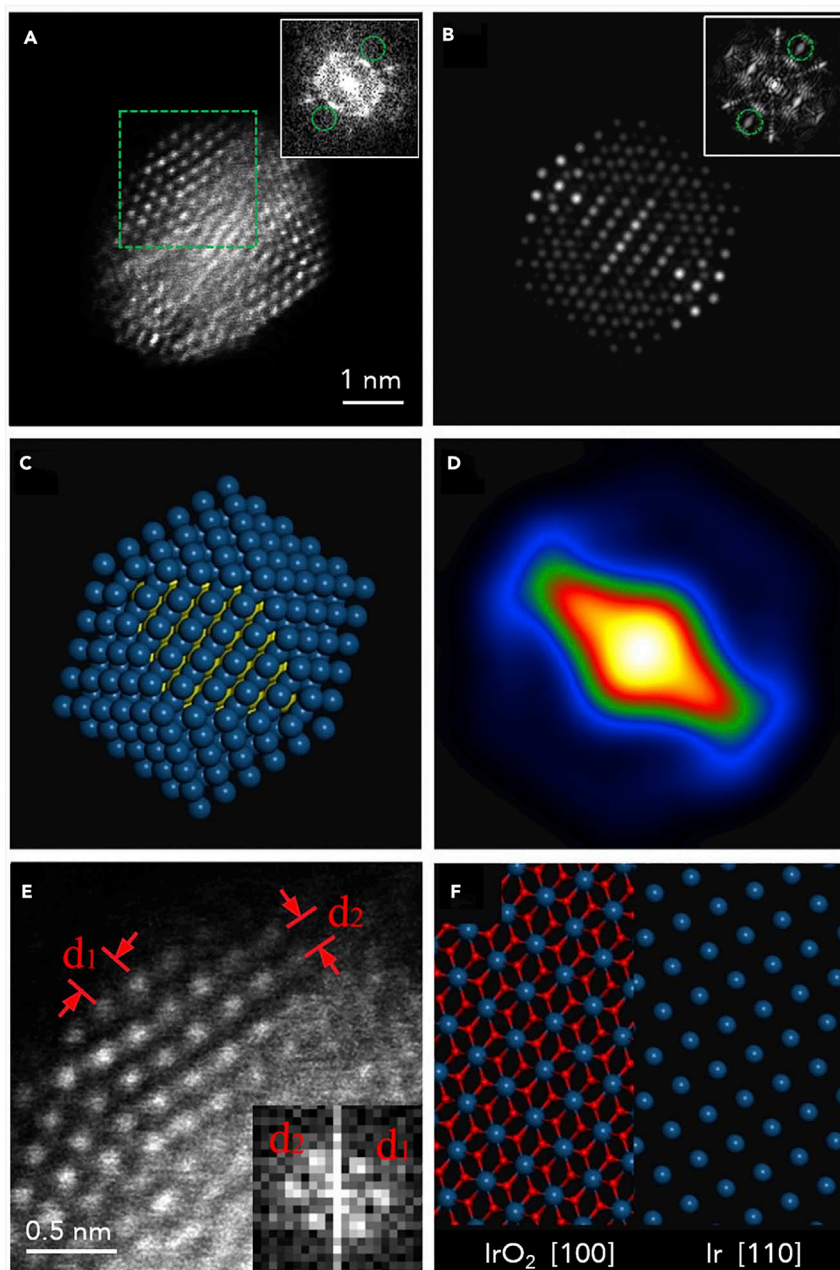


**Figure 2. HAADF-STEM Analysis of Ru@IrO<sub>x</sub> Nanocrystals**

(A) HAADF-STEM image of a randomly chosen Ru@IrO<sub>x</sub> core-shell icosahedral nanocrystal along the [112] axis. Scale bar: 1 nm.

(B and C) Simulated HRSTEM image (B) and structural projection (C) of a Ru<sub>147</sub>@Ir<sub>414</sub> icosahedral model structure along its [112] axis (model adopted and modified from Wang et al.<sup>40</sup>).

(D) Inverse FFT image (Sobel filtered and Gaussian blurred) of the masked reflections in FFT of simulated HRSTEM image in (B).

(E) An enlarged view of the rectangular region in (A) where  $d_1 = 2.53 \text{ \AA}$  and  $d_2 = 2.20 \text{ \AA}$ . Scale bar: 0.5 nm.

(F) Projected structural models of tetragonal IrO<sub>2</sub> and f.c.c. Ir along their [100] and [110] axes, respectively.

Insets in (A), (B), and (E) refer to the corresponding FFT results. See also Figures S2–S5.

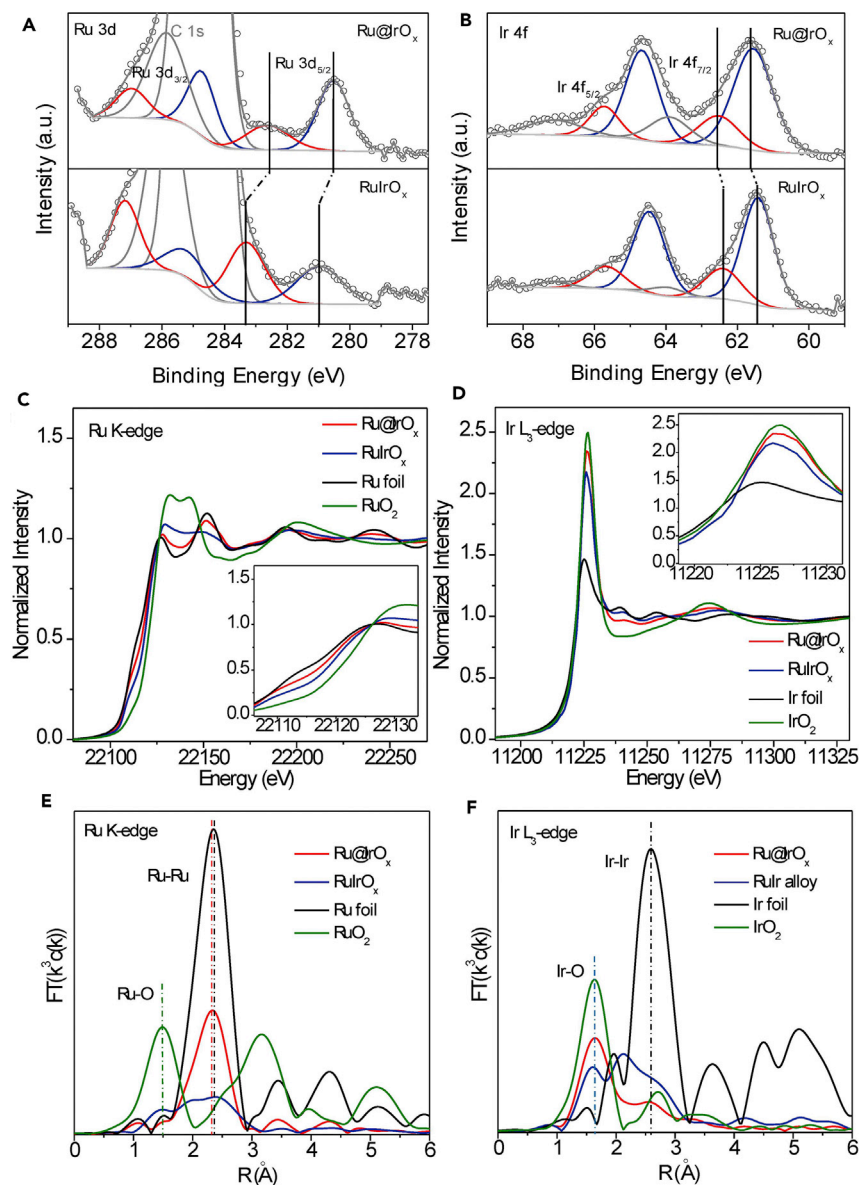


**Figure 3. XPS and XAS Characterization of Ru@IrO<sub>x</sub> and RuIrO<sub>x</sub>**

(A and B) Ru 3d (A) and Ir 4f XPS (B) spectra of Ru@IrO<sub>x</sub> and RuIrO<sub>x</sub>.

(C and D) Ru K-edge (C) and Ir L<sub>3</sub>-edge (D) synchrotron-based XANES data of Ru@IrO<sub>x</sub> and RuIrO<sub>x</sub> electrocatalysts and the references.

(E and F) Fourier-transformed EXAFS spectra at the Ru K-edge (E) and Ir L<sub>3</sub>-edge (F) collected for Ru@IrO<sub>x</sub> and RuIrO<sub>x</sub> electrocatalysts and the references.

See also [Figures S6–S8](#) and [Tables S1](#) and [S2](#).

assigned to metallic Ru and Ru oxides,<sup>44</sup> respectively. The existence of a thin Ru oxide shell covering the metallic Ru core can greatly facilitate the coating of IrO<sub>x</sub> shell and prevent the formation of single metal nanocrystals mixture.<sup>38</sup> Likewise, the RuIrO<sub>x</sub> nanocrystals also show metallic Ru and Ru oxide signals, with both doublets centered at higher binding energies than those observed for Ru@IrO<sub>x</sub>. The positive shift of the binding energies and the different proportions of Ru species demonstrate that Ru core in Ru@IrO<sub>x</sub> exhibits a lower valence state than its counterpart in RuIrO<sub>x</sub>. Interestingly, an opposite trend is visible on the Ir 4f profiles (Figure 3B). The profile of Ru@IrO<sub>x</sub> can

be fitted with three pairs of peaks centered at 61.6 and 64.7 eV, 62.6 and 65.7 eV, and 63.8 and 67.0 eV, which can be attributed to Ir<sup>0</sup>, Ir<sup>3+</sup>, and Ir<sup>4+</sup>, respectively.<sup>45,46</sup> Correspondingly, the RuIrO<sub>x</sub> shows three sets of doublets with lower binding energies, which indicates that Ru@IrO<sub>x</sub> has higher Ir valence state than RuIrO<sub>x</sub>. Hence, compared with RuIrO<sub>x</sub> nanocrystals, Ru@IrO<sub>x</sub> nanocrystals show an obvious lower valence state of Ru core, which results in the relatively higher valence state of IrO<sub>x</sub> shell. This converse shift of Ru and Ir valence states within the Ru@IrO<sub>x</sub> core-shell nanocrystals could be attributed to charge redistribution across the metal core-oxide shell heterojunction caused by the difference in the work functions between the Ru metal (4.7 eV) and IrO<sub>2</sub> (4.2 eV).<sup>47–52</sup>

The electron transition behaviors of these two nanocrystals were further characterized by the white line of XANES, the intensity analysis of which offers a clear view of valence states.<sup>53,54</sup> As is shown in the enlarged white-line region of Ru K-edge (Figure 3C, inset), the white-line adsorption energy decreases in the order RuO<sub>2</sub> > RuIrO<sub>x</sub> > Ru@IrO<sub>x</sub> > Ru foil, indicating the same order for Ru valence state. In addition, the Ir valence state can be more easily observed by characterizing white-line intensity of Ir L<sub>3</sub>-edge spectra, which is magnified in Figure 3D (inset) and demonstrates an order of IrO<sub>2</sub> > Ru@IrO<sub>x</sub> > RuIrO<sub>x</sub> > Ir foil. In addition, we quantitatively measured the Ru and Ir valence state by the adsorption energy (E<sub>0</sub>) of the catalysts, which are analyzed and summarized in Figure S6 and Table S1. Besides, the Fourier transforms of the extended X-ray absorption fine structure (EXAFS) spectra (Figures 3E and 3F) and the corresponding k<sup>3</sup>-weighted EXAFS spectra (Figures S7 and S8) at the Ru K-edge and Ir L<sub>3</sub>-edge were conducted to reveal the structure of the catalysts, including coordination numbers and interatomic distances. The k range of Ru K-edge EXAFS fitting is 2.7–12.7 Å<sup>-1</sup>, whereas that of Ir L<sub>3</sub>-edge EXAFS fitting is 2.7–13 Å<sup>-1</sup>. It can be observed in Table S2 that the Ru@IrO<sub>x</sub> exhibits a decreased Ru-Ru interatomic distance in comparison with that of Ru foil due to the strain effect of Ru core, supporting the high-resolution STEM (HRSTEM) observations. On the Ir L<sub>3</sub>-edge (Figure 3F), the Ru@IrO<sub>x</sub> displays peaks arising from the electronic backscatters from Ir to neighboring O (Ir–O bonds) and Ir (Ir–Ir bonds) atoms, respectively, which is in good agreement with EDX analysis and previous reports.<sup>46</sup>

### OER Electrocatalytic Activity

To set up the correlation between the unusual surface valence state and electrocatalytic activity, we evaluated the performance of Ru@IrO<sub>x</sub> in comparison with RuIrO<sub>x</sub> as well as the state-of-the-art commercial RuO<sub>2</sub> nanoparticles (RuO<sub>2</sub> NPs) and IrO<sub>2</sub> nanoparticles (IrO<sub>2</sub> NPs) electrocatalysts in 0.05 M H<sub>2</sub>SO<sub>4</sub> electrolytes. Apparently, the linear sweep voltammetry (LSV) curves normalized with regard to the geometrical area of electrode disk of all electrocatalysts manifest an activity order of Ru@IrO<sub>x</sub> > RuIrO<sub>x</sub> > RuO<sub>2</sub> NPs > IrO<sub>2</sub> NPs (Figure 4A). As can be seen from the profile, the Ru@IrO<sub>x</sub> core-shell nanocrystals exhibit an outstanding activity with a small overpotential (η) of 282 mV at 10 mA cm<sup>-2</sup><sub>geo</sub>, significantly exceeding the performance of the other samples. Besides, the smallest Tafel slope for Ru@IrO<sub>x</sub> (69.1 mV dec<sup>-1</sup>) indicates the fastest kinetics in comparison with all control samples (Figure 4B).

The specific activity of nanostructured samples was normalized according to the surface roughness factor (R<sub>f</sub>), which was estimated from the electrochemical double-layer capacitance (C<sub>dl</sub>)<sup>55</sup> (Figures S9 and S10). As summarized in Table S3, in line with C<sub>dl</sub>, the surface area and R<sub>f</sub> exhibit the same trends among the samples. The increased roughness of Ru@IrO<sub>x</sub> and RuIrO<sub>x</sub> electrocatalysts could originate from the well-constructed nanostructures compared with commercial samples. Furthermore, the RuIrO<sub>x</sub> shows larger surface area than Ru@IrO<sub>x</sub> because of its smaller

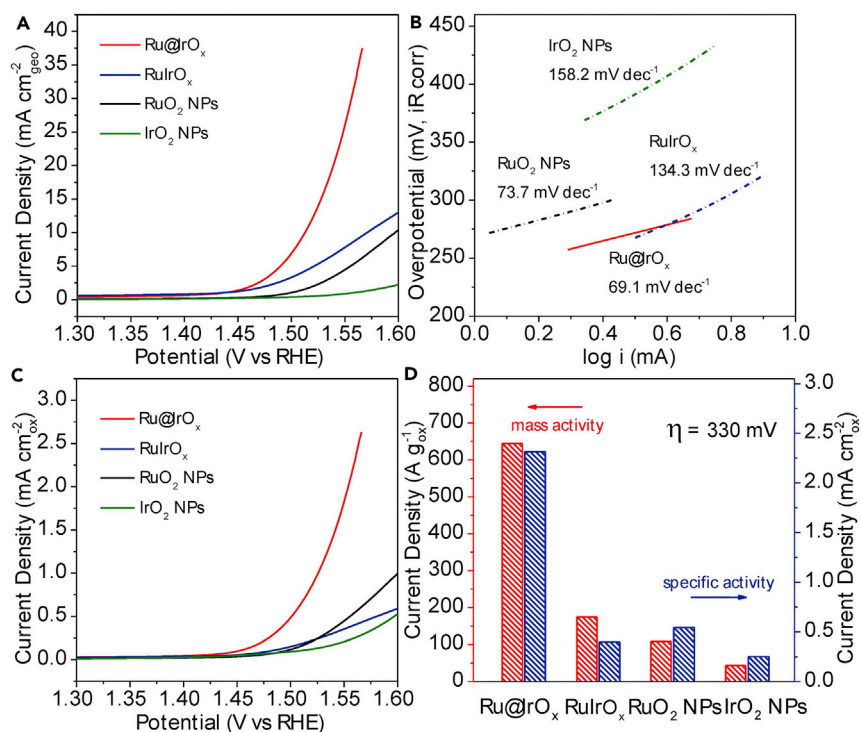


**Figure 4. OER Electrocatalytic Activity Analysis in 0.05 M H<sub>2</sub>SO<sub>4</sub> Solutions**

(A and B) LSV curves (A) normalized by using geometrical surface area and corresponding Tafel plots (B) of various electrocatalysts in N<sub>2</sub>-saturated 0.05 M H<sub>2</sub>SO<sub>4</sub> solutions.

(C) LSV curves normalized by using electrochemical active surface areas determined by C<sub>dil</sub> of various electrocatalysts.

(D) Comparison of the mass activity and specific activity at an overpotential of 330 mV for various electrocatalysts. “O<sub>x</sub>” refers to the surface areas of the oxide electrocatalysts studied.

See also Figures S9 and S10 and Table S3.

particle size with increased exposure of active sites. Afterward, the LSV profiles indicate the following trend in the specific activity: Ru@IrO<sub>x</sub> > RuO<sub>2</sub> NPs > RuIrO<sub>x</sub> > IrO<sub>2</sub> NPs (Figures 4C and 4D). In terms of the catalyst’s mass-normalized activity (Figure 4D), the Ru@IrO<sub>x</sub> shows the highest current density of 644.8 A g<sup>-1</sup> (under an overpotential of 330 mV), which is approximately 3.7, 5.9, and 14.8 times higher than that of RuIrO<sub>x</sub>, RuO<sub>2</sub> NPs, and IrO<sub>2</sub> NPs, respectively. It should be noted that the RuIrO<sub>x</sub> shows specific activity superior to IrO<sub>2</sub> NPs yet poorer than RuO<sub>2</sub> NPs, which agrees well with data previously reported for RuIr solid solutions;<sup>23,28</sup> however, the superior mass activity of RuIrO<sub>x</sub> to RuO<sub>2</sub> NPs and IrO<sub>2</sub> NPs can be attributed to its large surface area derived from ultra-small nanoparticle size.

The enhancement in the OER activity (in terms of all geometrical area normalized activity, mass activity, and specific activity) of Ru@IrO<sub>x</sub> in comparison with RuIrO<sub>x</sub> can be attributed to the favorable surface valence state achieved by charge redistribution at the core-shell interface, which may lead to the optimized adsorption of oxygen intermediates.<sup>43,56</sup> In addition, the Ru@IrO<sub>x</sub> sample shows obvious superiority to the long-regarded state-of-the-art commercial OER electrocatalysts RuO<sub>2</sub> NPs and IrO<sub>2</sub> NPs, which can be ascribed to the adjusted electronic structure of Ru cores.<sup>57</sup> More importantly, Ru@IrO<sub>x</sub> is also one of the most active electrocatalysts among recently reported Ru- and Ir-based OER electrocatalysts in acidic electrolytes (Figure 5A and Table S4).



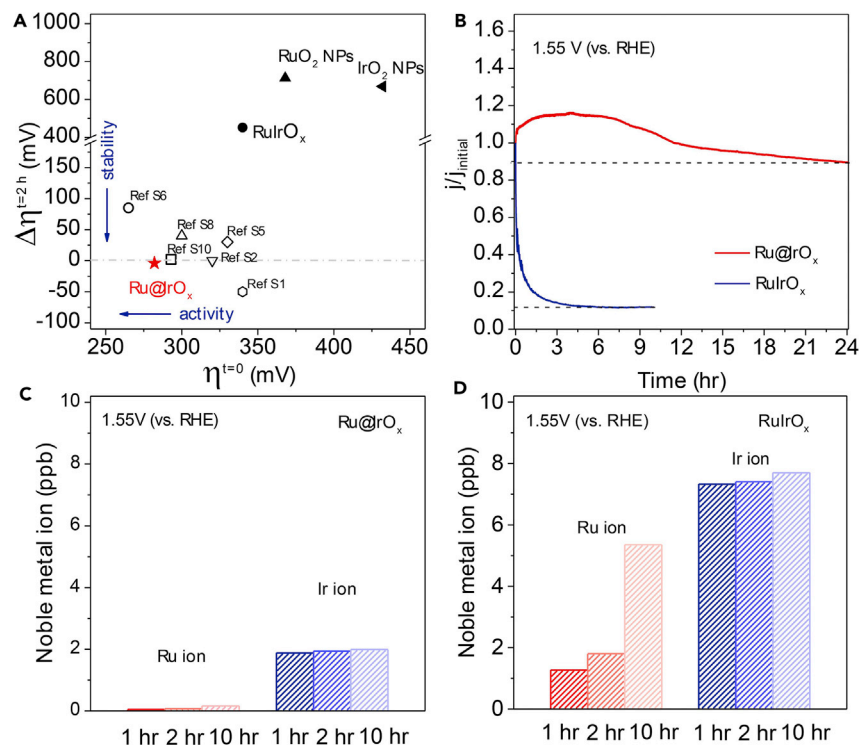


**Figure 5. OER Electrochemical Stability Analysis in 0.05 M H<sub>2</sub>SO<sub>4</sub> Solutions**

(A) Stability-activity plot for various OER electrocatalysts. The x axis is the overpotential required to achieve a current density of 10 mA cm<sup>-2</sup> at  $t = 0$ , and the y axis is the difference between overpotential required to reach 10 mA cm<sup>-2</sup> after 2-hr chronopotentiometric hold and the initial one. The dashed line across  $y = 0$  signifies the ideal stable electrocatalyst with no change in the activity. "Ref S1," etc., refer to the cited references in the [Supplemental Information](#).

(B) Current-time chronoamperometric response of Ru@IrO<sub>x</sub> and RuIrO<sub>x</sub> electrocatalysts at 1.55 V. (C and D) ICP-MS analysis data for Ru@IrO<sub>x</sub> (C) and RuIrO<sub>x</sub> (D) after different reaction times; the red and blue bars represent the Ru and Ir ion concentrations in the electrolyte, respectively. See also [Tables S4](#) and [S5](#).

### OER Electrochemical Stability

The stability issue is particularly critical for acidic OER electrocatalysts due to the highly corrosive electrolytes and oxidative operating conditions. The stability of various electrocatalysts was further evaluated by three different approaches. First, a term of  $\Delta\eta = \eta_{\text{final}} - \eta_{\text{initial}}$ , the difference between initial overpotential and overpotential after the 2-hr chronopotentiometric hold at the current density of 10 mA cm<sup>-2</sup><sub>geo</sub>, was introduced.<sup>16,19,55</sup> As plotted in [Figure 5A](#), the horizontal dashed line across  $y = 0$  represents an ideal stability performance with no change in the activity after the chronopotentiometric experiment. Obviously, the Ru@IrO<sub>x</sub> lies quite close to the x axis origin and even slightly below the dashed line, which demonstrates its outstanding catalytic activity and activity retention in comparison with the control samples and the other reported OER electrocatalysts.

Second, a current-time chronoamperometric experiment was performed under a potential of 1.55 V versus reversible hydrogen electrode (RHE) ([Figure 5B](#)). The Ru@IrO<sub>x</sub> electrocatalyst shows continuous activity improvement during the first 4 hr of the test, after which the  $j/j_{\text{initial}}$  value declines slowly to nearly 0.9 at the end of the 24-hr test. The initial enhancement in the activity could be attributed to the increase of the catalyst surface area caused by slight dissolution of surface sites. In contrast,

the RuIrO<sub>x</sub> lost nearly 80% of its activity within less than 1 hr; after 10-hr test, only ~12% of activity remained. The dramatic contrast between Ru@IrO<sub>x</sub> and RuIrO<sub>x</sub> in the OER stability can be ascribed to a few factors: (1) the relatively high-valence state of Ir in Ru@IrO<sub>x</sub> makes it less prone to be further oxidized into soluble species,<sup>58</sup> thus impeding the loss of active sites; (2) an increased exposure of active sites was achieved after some loosely bonded surface Ir sites were dissolved; (3) the highly active but sensitive Ru core can be effectively protected by the IrO<sub>x</sub> shell and in return helps to maintain the stability of the IrO<sub>x</sub> shell.<sup>59</sup>

Third, inductively coupled plasma mass spectrometry (ICP-MS) analysis was further conducted to detect the amounts of dissolved Ru and Ir ions in electrolytes at different times during the stability test (Table S5). For the Ru@IrO<sub>x</sub> sample, the extremely low Ru ion concentration in the electrolyte manifests the effective protection of IrO<sub>x</sub> shell by the Ru core (Figure 5C). The Ir ion concentration is a little higher than that of Ru ion, which could be caused by the dissolution of some loosely bonded surface Ir sites. Nevertheless, it is still at a very low level (less than 2.0 ppb), and changes slightly with the prolongation of time. By contrast, the electrolyte's Ru ion concentration on RuIrO<sub>x</sub> is approximately 30-fold higher than that observed in the case of Ru@IrO<sub>x</sub>, and the amount of dissolved Ir ions is also much higher (Figure 5D). In the homogeneous RuIrO<sub>x</sub>, the exposed Ru sites can be easily dissolved and result in exposure of more Ir sites, which will greatly accelerate the dissolution of Ir sites and even lead to structure degradation.

### Origin of the Enhanced OER Stability

The changes in the surface chemical states of Ru and Ir species during the OER processes were further studied by XPS (Figures 6A and 6B). For polarization processes at the OER operating potentials, both Ru and Ir in the Ru@IrO<sub>x</sub> sample show higher chemical states compared with those of the as-prepared sample, indicating that Ru and Ir species are oxidized during OER. A similar phenomenon also applies to RuIr oxide alloy samples (Figure S11). Interestingly, after increasing the potential from 1.0 V to 1.7 V, the chemical states do not change dramatically for Ru and Ir species in Ru@IrO<sub>x</sub>; however, the changes observed for RuIrO<sub>x</sub> are much more significant. More specifically, the Ru<sup>>4+</sup>/Ru<sup><4+</sup> and Ir<sup>4+</sup>/Ir<sup>3+</sup> ratio plots are shown in Figures 6C and 6D. Clearly the chemical states of Ru in Ru@IrO<sub>x</sub> are always lower than those in RuIrO<sub>x</sub> and the fluctuation of the Ru@IrO<sub>x</sub> line is less pronounced. On the other hand, compared with RuIrO<sub>x</sub>, Ru@IrO<sub>x</sub> offers a larger initial value of Ir<sup>4+</sup>/Ir<sup>3+</sup> ratio but its change under different applied anodic potentials is much smaller. Such a trend is also observed during *in situ* electrochemical cyclic voltammetry (CV) measurements (Figure S12). As the upper potential limit increases from 0.5 to 1.3 V, no obvious redox peaks are observed on the CV profiles of the Ru@IrO<sub>x</sub>. Comparatively, an obvious Ir oxidation peak shows up on the RuIrO<sub>x</sub> curves when the potential limits increase to over 0.9 V, suggesting that the RuIrO<sub>x</sub> was oxidized to a higher degree than Ru@IrO<sub>x</sub> under the same potential. The nanostructure integrity of Ru@IrO<sub>x</sub> electrocatalysts was also confirmed by morphology characterization. As shown in Figure 6E, the core-shell structure of Ru@IrO<sub>x</sub> nanocrystal basically remained after a 24-hr stability test. Furthermore, the corresponding maps (Figures 6F–6H) display the uniform distribution of Ru and Ir elements, with a larger area of Ir shell overlapping a smaller area of Ru core. Therefore, both the stable chemical states and core-shell nanostructure play significant roles in facilitating the catalytic stability of Ru@IrO<sub>x</sub> electrocatalysts: the former factors help to prevent the formation of dissolvable high-valence intermediate species during the OER process and the latter provides effective protection over active Ru sites from loss in electrolyte.

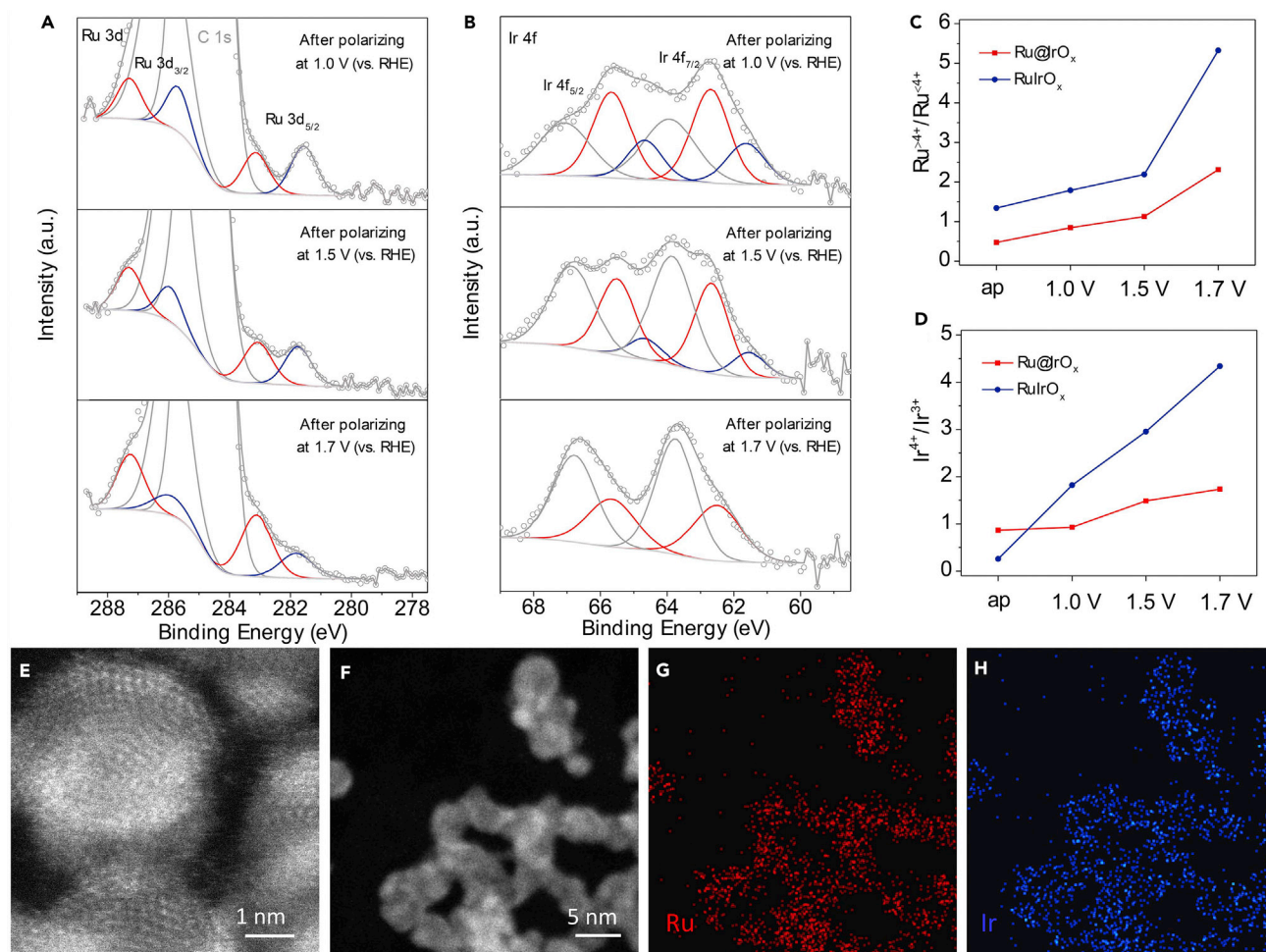


**Figure 6. Surface Chemical States and Structure Analysis on Ru@IrO<sub>x</sub> Electro catalysts after OER Processes**

(A and B) The XPS Ru 3d (A) and Ir 4f (B) spectra of as-prepared Ru@IrO<sub>x</sub> electro catalyst and the samples after polarizing at 1.0, 1.5, and 1.7 V for 30 min. (C and D) Ru<sup>4+</sup>/Ru<sup>3+</sup> ratio curve (C) and Ir<sup>4+</sup>/Ir<sup>3+</sup> ratio curve (D) obtained for Ru@IrO<sub>x</sub> and RuIrO<sub>x</sub> electro catalysts before OER (the as-prepared samples, which are denoted as “ap”) and after polarizing at different potentials.

(E–H) HAADF-STEM image (E) and the corresponding EDX elemental maps (F–H) of Ru@IrO<sub>x</sub> electro catalysts after 24-hr stability test. Ru is given in red and Ir is given in blue. Scale bars: 1 nm (E) and 5 nm (F).

See also Figures S11 and S12.

In conclusion, this work presents a rational design to achieve both high activity and good stability of OER electro catalysts in acidic environments by modifying electronic properties and nanostructures. On one hand, the superior electrocatalytic performance of the Ru@IrO<sub>x</sub> core-shell nanocrystals compared with homogeneous RuIr oxide alloy can be attributed to the favorable surface valence states in the former due to the charge redistribution at the metal core-oxide shell heterojunction. On the other hand, the core-shell nanostructure with much better structural stability as well as more effective protection for inner sites results in significantly reduced metal cation dissolution rates and excellent activity retention. Considering the capability of exceeding the properties of monometallic oxide electro catalysts, our investigation opens a new horizon for developing efficient electro catalysts by rational promotion of charge redistribution within heterostructures to achieve enhancement of both activity and stability simultaneously.

## EXPERIMENTAL PROCEDURES

### Synthesis of Nanocrystals

The synthesis of Ru@IrO<sub>x</sub> core-shell nanocrystals was achieved by a sequential polyol method as reported previously.<sup>38</sup> In a typical procedure, 80.0 mg of Ru(acac)<sub>3</sub> and 55.0 mg of PVP were mixed in 40 mL of EG to get a transparent solution. A rapid heating process was then applied to the system. After refluxing the glycol solution under vigorous stirring at 198°C for 3 hr, Ru colloids (cores) were formed. In the second step, 59.7 mg of IrCl<sub>3</sub>·xH<sub>2</sub>O was added into the as-obtained colloidal Ru suspension under vigorous stirring. Next, the system was heated rapidly to 130°C and then slowly to 198°C with a speed of 1°C–2°C/min. After 1.5 hr of refluxing, the reaction was quenched by ice. The resultant suspension was diluted with acetone and centrifuged. Next, washing with ethanol, sonication, and centrifugation was repeated five times. The formed Ru@IrO<sub>x</sub> core-shell nanocrystals were obtained after drying the precipitate at 60°C overnight in a vacuum oven.

RuIr oxide alloy nanocrystals were synthesized by a co-reduction process in EG. In short, 41.4 mg of ruthenium(III) chloride hydrate (RuCl<sub>3</sub>·xH<sub>2</sub>O), 59.7 mg of IrCl<sub>3</sub>·xH<sub>2</sub>O, and 55.0 mg of PVP were mixed in 40 mL of EG to get a transparent solution, which was then heated rapidly to 198°C under vigorous stirring and kept under reflux for 3 hr. After centrifugation, washing, and drying processes as above, the RuIr oxide alloy nanocrystals were collected.

### Characterization

Low-resolution transmission electron microscopy was conducted on an FEI Tecnai-G2 instrument at an acceleration voltage of 120 kV. HAADF-STEM images were recorded by an FEI Titan G2 80-300 microscope at 300 kV equipped with a probe corrector. HRSTEM simulations were carried out by using the qSTEM program with the following simulation conditions: 300 kV; Cs = 10 μm; Δf = -5.4 nm; α = 17 mrad; inner/outer detector angle = 70/200 mrad; a pixel array of 300 × 300 with 0.01 nm point sampling. EDX imaging was conducted with an FEI Titan Themis 80-200 microscope equipped with a SuperX detector. The synchrotron-based XAFS measurements were performed at beamline 14W1 in the Shanghai Synchrotron Radiation Facility. XPS characterization was carried out on a PHI Quantera X-ray photoelectron spectrometer with an Al cathode as the X-ray source. XRD data were collected on a Rigaku MiniFlex 600 X-Ray Diffractometer. ICP-MS analysis was conducted by an Agilent 7500cx instrument with attached laser ablation systems.

### Electrochemical Measurements

Electrocatalyst inks were prepared by dispersing the freshly synthesized catalyst powders (2 mg) in a solution containing distilled water (Milli-Q, 965 μL) and 5 wt % Nafion solution (35 μL), followed by ultrasonication for 2 hr. Catalyst ink (5 μL) was then deposited onto a polished gold (Au) electrode (diameter 5 mm, area 0.196 cm<sup>2</sup>; Pine Research Instrumentation). All electrochemical experiments were carried out in a three-electrode glass cell with an Au wire as the counter electrode and Ag/AgCl as the reference electrode (Pine Research Instrumentation). The electrolyte, 0.05 M H<sub>2</sub>SO<sub>4</sub> solution, was prepared by diluting 98% H<sub>2</sub>SO<sub>4</sub> with Milli-Q water. The reference electrode was calibrated in H<sub>2</sub>-saturated 0.05 M H<sub>2</sub>SO<sub>4</sub> solution before the experiments. All potentials were converted to the RHE and corrected with iR compensation.

OER measurements were conducted in a N<sub>2</sub>-saturated 0.05 M H<sub>2</sub>SO<sub>4</sub> electrolyte with a CHI potentiostat (CHI 760D) at a rotating disk electrode at a rotating speed of 1,600 rpm. First, CV analysis was performed with a scan rate of 50 mV s<sup>-1</sup>, starting

from a lower potential limit of  $-0.05$  V; the upper potential limits were adopted to be 0.5, 0.7, 0.9, 1.2, and 1.3 V. The polarization curves were then recorded before and after the chronopotentiometric experiment in the range of 1.2 and 1.7 V with a sweeping rate of  $5 \text{ mV s}^{-1}$ .

The  $C_{dl}$  of the electrocatalysts was measured by CV in a non-faradic potential window, which was taken here as 0.873–0.973 V. The current densities measured from CVs at a series of different scan rates (2, 4, 6, 8, and  $10 \text{ mV s}^{-1}$ ) were recorded at 0.923 V and then plotted with scan rates, the slope of the appropriate linear relation equaling the  $C_{dl}$ .  $R_f$  was calculated by dividing the obtained  $C_{dl}$  by the specific capacitance of metal oxide with smooth planar surface, which is generally taken as  $0.06 \text{ mF cm}^{-2}$ . Surface areas of electrocatalysts were then measured by multiplying the electrode geometrical area by  $R_f$  and then normalizing with the mass loading of electrocatalysts.

For the stability study, the electrocatalysts were polarized at different potentials (e.g., 1.0, 1.5, 1.7 V) for 30 min. The electrocatalyst paste was then scraped off the electrodes and washed with ethanol several times to remove the Nafion species, and after centrifugation and drying, the obtained powder was stuck onto silicon wafer to run the XPS tests. In addition, ICP-MS measurements were carried out to detect the amounts of dissolved Ru and Ir ions in electrolytes after 1, 2, and 10 hr of the chronoamperometric experiments at a certain overpotential polarization.

## SUPPLEMENTAL INFORMATION

Supplemental Information includes 12 figures and 5 tables and can be found with this article online at <https://doi.org/10.1016/j.chempr.2018.11.010>.

## ACKNOWLEDGMENTS

This work was financially supported by the Australian Research Council through the Discovery Project programs (FL170100154, DP160104866, and DP170104464) and the Discovery Early Career Researcher Award (DE160101163 and DE160101293). J.S. was supported by the Chinese CSC Scholarship Program. Y. Zhu acknowledges financial support from the Thousand Talents Program for Distinguished Young Scholars, the National Natural Science Foundation of China (51701181), and the Zhejiang Provincial Natural Science Foundation of China (LR18B030003). The authors thank Dr. Ashley D. Slattery, Chao Ye, and Ke Zhang for their help in material characterization. Dr. Bo You provided valuable comments on the manuscript.

## AUTHOR CONTRIBUTIONS

J.S. performed the material synthesis and electrocatalytic experiments. Y. Zheng and S.-Z.Q. designed the experiments. Y. Zhu conducted the HAADF-STEM analysis. S.C. and L.S. conducted the XAS characterization. J.S., C.G., Y. Zhu, M.J., Y. Zheng, and S.-Z.Q. contributed to writing the paper.

## DECLARATION OF INTERESTS

The authors declare no competing interests.

Received: August 8, 2018

Revised: September 4, 2018

Accepted: November 14, 2018

Published: December 20, 2018

## REFERENCES AND NOTES

1. Strasser, P., Koh, S., Anniyev, T., Greeley, J., More, K., Yu, C., Liu, Z., Kaya, S., Nordlund, D., Ogasawara, H., et al. (2010). Lattice-strain control of the activity in dealloyed core-shell fuel cell catalysts. *Nat. Chem.* **2**, 454–460.
2. Kim, Y.T., Lopes, P.P., Park, S.A., Lee, A.Y., Lim, J., Lee, H., Back, S., Jung, Y., Danilovic, N., Stamenkovic, V., et al. (2017). Balancing activity, stability and conductivity of nanoporous core-shell iridium/iridium oxide oxygen evolution catalysts. *Nat. Commun.* **8**, 1449.
3. Mahmood, J., Li, F., Jung, S.M., Okyay, M.S., Ahmad, I., Kim, S.J., Park, N., Jeong, H.Y., and Baek, J.B. (2017). An efficient and pH-universal ruthenium-based catalyst for the hydrogen evolution reaction. *Nat. Nanotechnol.* **12**, 441–446.
4. Greeley, J., Stephens, I.E., Bondarenko, A.S., Johansson, T.P., Hansen, H.A., Jaramillo, T.F., Rossmeisl, J., Chorkendorff, I., and Nørskov, J.K. (2009). Alloys of platinum and early transition metals as oxygen reduction electrocatalysts. *Nat. Chem.* **1**, 552–556.
5. Zheng, Y., Jiao, Y., Zhu, Y., Li, L.H., Han, Y., Chen, Y., Jaroniec, M., and Qiao, S.Z. (2016). High electrocatalytic hydrogen evolution activity of an anomalous ruthenium catalyst. *J. Am. Chem. Soc.* **138**, 16174–16181.
6. Staszak-Jirkovsky, J., Malliakas, C.D., Lopes, P.P., Danilovic, N., Kota, S.S., Chang, K.C., Genorio, B., Strmcnik, D., Stamenkovic, V.R., Kanatzidis, M.G., et al. (2016). Design of active and stable Co-Mo-Sx chalcogenides as pH-universal catalysts for the hydrogen evolution reaction. *Nat. Mater.* **15**, 197–203.
7. Danilovic, N., Subbaraman, R., Chang, K.C., Chang, S.H., Kang, Y.J., Snyder, J., Paulikas, A.P., Strmcnik, D., Kim, Y.T., Myers, D., et al. (2014). Activity-stability trends for the oxygen evolution reaction on monometallic oxides in acidic environments. *J. Phys. Chem. Lett.* **5**, 2474–2478.
8. Wang, X., Liu, D., Song, S., and Zhang, H. (2012). Synthesis of highly active Pt-CeO<sub>2</sub> hybrids with tunable secondary nanostructures for the catalytic hydrolysis of ammonia borane. *Chem. Commun.* **48**, 10207–10209.
9. Li, Y., and El-Sayed, M. (2001). The effect of stabilizers on the catalytic activity and stability of Pd colloidal nanoparticles in the Suzuki reactions in aqueous solution. *J. Phys. Chem. B* **105**, 8938–8943.
10. Reier, T., Nong, H.N., Teschner, D., Schlögl, R., and Strasser, P. (2017). Electrocatalytic oxygen evolution reaction in acidic environments—reaction mechanisms and catalysts. *Adv. Energy Mater.* **7**, 1601275.
11. Jiao, Y., Zheng, Y., Jaroniec, M., and Qiao, S.Z. (2015). Design of electrocatalysts for oxygen- and hydrogen-involving energy conversion reactions. *Chem. Soc. Rev.* **44**, 2060–2086.
12. Feng, J., Lv, F., Zhang, W., Li, P., Wang, K., Yang, C., Wang, B., Yang, Y., Zhou, J., Lin, F., et al. (2017). Iridium-based multimetallic porous hollow nanocrystals for efficient overall-water-splitting catalysis. *Adv. Mater.* **29**, 1703798.
13. Huynh, M., Bediako, D.K., and Nocera, D.G. (2014). A functionally stable manganese oxide oxygen evolution catalyst in acid. *J. Am. Chem. Soc.* **136**, 6002–6010.
14. Fabbri, E., Haberer, A., Waltar, K., Kötzt, R., and Schmidt, T.J. (2014). Developments and perspectives of oxide-based catalysts for the oxygen evolution reaction. *Catal. Sci. Technol.* **4**, 3800–3821.
15. Lebedev, D., Povia, M., Waltar, K., Abdala, P.M., Castelli, I.E., Fabbri, E., Blanco, M.V., Fedorov, A., Copéret, C., Marzari, N., et al. (2017). Highly active and stable iridium pyrochlores for oxygen evolution reaction. *Chem. Mater.* **29**, 5182–5191.
16. Spori, C., Kwan, J.T.H., Bonakdarpour, A., Wilkinson, D.P., and Strasser, P. (2017). The stability challenges of oxygen evolving catalysts: towards a common fundamental understanding and mitigation of catalyst degradation. *Angew. Chem. Int. Ed.* **56**, 5994–6021.
17. Cherevko, S., Geiger, S., Kasian, O., Kulyk, N., Grote, J.-P., Savan, A., Shrestha, B.R., Merzlikin, S., Breitbach, B., Ludwig, A., et al. (2016). Oxygen and hydrogen evolution reactions on Ru, RuO<sub>2</sub>, Ir, and IrO<sub>2</sub> thin film electrodes in acidic and alkaline electrolytes: a comparative study on activity and stability. *Catal. Today* **262**, 170–180.
18. Reier, T., Oezaslan, M., and Strasser, P. (2012). Electrocatalytic oxygen evolution reaction (OER) on Ru, Ir, and Pt catalysts: a comparative study of nanoparticles and bulk materials. *ACS Catal.* **2**, 1765–1772.
19. McCrory, C.C., Jung, S., Ferrer, I.M., Chatman, S.M., Peters, J.C., and Jaramillo, T.F. (2015). Benchmarking hydrogen evolving reaction and oxygen evolving reaction electrocatalysts for solar water splitting devices. *J. Am. Chem. Soc.* **137**, 4347–4357.
20. Lee, Y., Suntivich, J., May, K.J., Perry, E.E., and Shao-Horn, Y. (2012). Synthesis and activities of rutile IrO<sub>2</sub> and RuO<sub>2</sub> nanoparticles for oxygen evolution in acid and alkaline solutions. *J. Phys. Chem. Lett.* **3**, 399–404.
21. Pedersen, A.F., Escudero-Escribano, M., Sebok, B., Bodin, A., Paoli, E., Frydendal, R., Friebel, D., Stephens, I.E.L., Rossmeisl, J., Chorkendorff, I., et al. (2018). Operando XAS study of the surface oxidation state on a monolayer IrO<sub>x</sub> on RuO<sub>x</sub> and Ru oxide based nanoparticles for oxygen evolution in acidic media. *J. Phys. Chem. B* **122**, 878–887.
22. Escudero-Escribano, M., Pedersen, A.F., Paoli, E.A., Frydendal, R., Friebel, D., Malacrida, P., Rossmeisl, J., Stephens, I.E.L., and Chorkendorff, I. (2018). Importance of surface IrO<sub>x</sub> in stabilizing RuO<sub>2</sub> for oxygen evolution. *J. Phys. Chem. B* **122**, 947–955.
23. Cheng, J., Zhang, H., Chen, G., and Zhang, Y. (2009). Study of Ir<sub>x</sub>Ru<sub>1-x</sub>O<sub>2</sub> oxides as anodic electrocatalysts for solid polymer electrolyte water electrolysis. *Electrochim. Acta* **54**, 6250–6256.
24. Sardar, K., Petrucco, E., Hiley, C.I., Sharman, J.D., Wells, P.P., Russell, A.E., Kashtiban, R.J., Sloan, J., and Walton, R.I. (2014). Water-splitting electrocatalysis in acid conditions using ruthenate-iridate pyrochlores. *Angew. Chem. Int. Ed.* **53**, 10960–10964.
25. Kötzt, R., and Stucki, S. (1986). Stabilization of RuO<sub>2</sub> by IrO<sub>2</sub> for anodic oxygen evolution in acid media. *Electrochim. Acta* **31**, 1311–1316.
26. Kötzt, R., Stucki, S., Scherson, D., and Kolb, D.M. (1984). In-situ identification of RuO<sub>4</sub> as the corrosion product during oxygen evolution on ruthenium in acid media. *J. Electroanal. Chem.* **172**, 211–219.
27. Wohlfahrt-Mehrens, M., and Heitbaum, J. (1987). Oxygen evolution on Ru and RuO<sub>2</sub> electrodes studied using isotope labelling and on-line mass spectrometry. *J. Electroanal. Chem.* **237**, 251–260.
28. Mamaca, N., Mayousse, E., Arrii-Clacens, S., Napporn, T.W., Servat, K., Guillet, N., and Kokoh, K.B. (2012). Electrochemical activity of ruthenium and iridium based catalysts for oxygen evolution reaction. *Appl. Catal. B Environ.* **111–112**, 376–380.
29. Owe, L.-E., Tsympkin, M., Wallwork, K.S., Haverkamp, R.G., and Sunde, S. (2012). Iridium-ruthenium single phase mixed oxides for oxygen evolution: composition dependence of electrocatalytic activity. *Electrochim. Acta* **70**, 158–164.
30. Wang, L., Saveleva, V.A., Zafeirotas, S., Savinova, E.R., Lettenmeier, P., Gazdzicki, P., Gago, A.S., and Friedrich, K.A. (2017). Highly active anode electrocatalysts derived from electrochemical leaching of Ru from metallic Ir<sub>0.7</sub>Ru<sub>0.3</sub> for proton exchange membrane electrolyzers. *Nano Energy* **34**, 385–391.
31. Kasian, O., Geiger, S., Stock, P., Polymeros, G., Breitbach, B., Savan, A., Ludwig, A., Cherevko, S., and Mayrhofer, K.J.J. (2016). On the origin of the improved ruthenium stability in RuO<sub>2</sub>-IrO<sub>2</sub> mixed oxides. *J. Electrochem. Soc.* **163**, F3099–F3104.
32. Danilovic, N., Subbaraman, R., Chang, K.C., Chang, S.H., Kang, Y., Snyder, J., Paulikas, A.P., Strmcnik, D., Kim, Y.T., Myers, D., et al. (2014). Using surface segregation to design stable Ru-Ir oxides for the oxygen evolution reaction in acidic environments. *Angew. Chem. Int. Ed.* **53**, 14016–14021.
33. Luo, M., and Guo, S. (2017). Strain-controlled electrocatalysis on multimetallic nanomaterials. *Nat. Rev. Mater.* **2**, <https://doi.org/10.1038/natrevmats.2017.59>.
34. Liu, X., Wang, D., and Li, Y. (2012). Synthesis and catalytic properties of bimetallic nanomaterials with various architectures. *Nano Today* **7**, 448–466.
35. Bing, Y., Liu, H., Zhang, L., Ghosh, D., and Zhang, J. (2010). Nanostructured Pt-alloy electrocatalysts for PEM fuel cell oxygen reduction reaction. *Chem. Soc. Rev.* **39**, 2184–2202.
36. Antolini, E. (2007). Platinum-based ternary catalysts for low temperature fuel cells. *Appl. Catal. B Environ.* **74**, 324–336.
37. Stamenkovic, V., Mun, B., Mayrhofer, K., Ross, P., and Markovic, N. (2006). Effect of surface composition on electronic structure, stability,

- and electrocatalytic properties of Pt-transition metal alloys: Pt-skin versus Pt-skeleton surfaces. *J. Am. Chem. Soc.* **128**, 8813–8819.
38. Alayoglu, S., Nilekar, A.U., Mavrikakis, M., and Eichhorn, B. (2008). Ru-Pt core-shell nanoparticles for preferential oxidation of carbon monoxide in hydrogen. *Nat. Mater.* **7**, 333–338.
39. Nong, H.N., Gan, L., Willinger, E., Teschner, D., and Strasser, P. (2014). IrO<sub>x</sub> core-shell nanocatalysts for cost- and energy-efficient electrochemical water splitting. *Chem. Sci.* **5**, 2955–2963.
40. Wang, X., Zhu, Y., Vasileff, A., Jiao, Y., Chen, S., Song, L., Zheng, B., Zheng, Y., and Qiao, S.Z. (2018). Strain effect in bimetallic electrocatalysts in the hydrogen evolution reaction. *ACS Energy Lett.* **3**, 1198–1204.
41. Matsumoto, Y., and Sato, E. (1986). Electrocatalytic properties of transition metal oxides for oxygen evolution. *Mater. Chem. Phys.* **14**, 397–426.
42. Strasser, P. (2016). Free electrons to molecular bonds and back: closing the energetic oxygen reduction (ORR)-oxygen evolution (OER) cycle using core-shell nanoelectrocatalysts. *Acc. Chem. Res.* **49**, 2658–2668.
43. Zheng, X., Zhang, B., De Luna, P., Liang, Y., Comin, R., Voznyy, O., Han, L., Garcia de Arquer, F.P., Liu, M., Dinh, C.T., et al. (2018). Theory-driven design of high-valence metal sites for water oxidation confirmed using in situ soft X-ray absorption. *Nat. Chem.* **10**, 149–154.
44. Kim, K.S., and Winograd, N. (1974). X-ray photoelectron spectroscopic studies of ruthenium-oxygen surfaces. *J. Catal.* **35**, 66–72.
45. Kim, S.J., Park, H.-Y., Ahn, S.H., Lee, B.-s., Kim, H.-J., Cho, E., Henkensmeier, D., Nam, S.W., Kim, S.H., Yoo, S.J., et al. (2014). Highly active and CO<sub>2</sub> tolerant Ir nanocatalysts for H<sub>2</sub>/CO<sub>2</sub> separation in electrochemical hydrogen pumps. *Appl. Catal. B Environ.* **158–159**, 348–354.
46. Oh, H.S., Nong, H.N., Reier, T., Bergmann, A., Glied, M., Ferreira de Araujo, J., Willinger, E., Schlögl, R., Teschner, D., and Strasser, P. (2016). Electrochemical catalyst-support effects and their stabilizing role for IrO<sub>x</sub> nanoparticle catalysts during the oxygen evolution reaction. *J. Am. Chem. Soc.* **138**, 12552–12563.
47. Tang, W., and Henkelman, G. (2009). Charge redistribution in core-shell nanoparticles to promote oxygen reduction. *J. Chem. Phys.* **130**, 194504.
48. Chalamala, B.R., Wei, Y., Reuss, R.H., Aggarwal, S., Gnade, B.E., Ramesh, R., Bernhard, J.M., Sosa, E.D., and Golden, D.E. (1999). Effect of growth conditions on surface morphology and photoelectric work function characteristics of iridium oxide thin films. *Appl. Phys. Lett.* **74**, 1394–1396.
49. Sigalas, M., Papaconstantopoulos, D.A., and Bacalis, N.C. (1992). Total energy and band structure of the 3d, 4d, and 5d metals. *Phys. Rev. B* **45**, 5777–5783.
50. Kim, S.-M., Jo, Y.-G., Lee, M.-H., Saito, N., Kim, J.-W., and Lee, S.-Y. (2017). The plasma-assisted formation of Ag@Co<sub>3</sub>O<sub>4</sub> core-shell hybrid nanocrystals for oxygen reduction reaction. *Electrochim. Acta* **233**, 123–133.
51. Ye, C., Zhang, L., Guo, C., Li, D., Vasileff, A., Wang, H., and Qiao, S.Z. (2017). A 3D hybrid of chemically coupled nickel sulfide and hollow carbon spheres for high performance lithium-sulfur batteries. *Adv. Funct. Mater.* **27**, 1702524.
52. Ye, C., Jiao, Y., Jin, H., Slattery, A.D., Davey, K., Wang, H., and Qiao, S.Z. (2018). 2D Mon-VN heterostructure as a model sulfur host to regulate polysulfides for highly efficient lithium-sulfur batteries. *Angew. Chem. Int. Ed.* <https://doi.org/10.1002/anie.201810579>.
53. Stolojan, V., Walsh, C., Yuan, J., Brown, L., and Kiely, C. (1999). Calibration of the relationship between white-line intensity and valence states for the first transition series. In *Institute of Physics Conference Series, 161 Section 5* Institute of Physics Conference Series (IOP Publishing), pp. 235–238.
54. Guo, C., Zheng, Y., Ran, J., Xie, F., Jaroniec, M., and Qiao, S.Z. (2017). Engineering high-energy interfacial structures for high-performance oxygen-involving electrocatalysis. *Angew. Chem. Int. Ed.* **56**, 8539–8543.
55. McCrory, C.C., Jung, S., Peters, J.C., and Jaramillo, T.F. (2013). Benchmarking heterogeneous electrocatalysts for the oxygen evolution reaction. *J. Am. Chem. Soc.* **135**, 16977–16987.
56. Zhang, B., Zheng, X., Voznyy, O., Comin, R., Bajdich, M., Melchor, M., Han, L., Xu, J., Liu, M., Zheng, L., et al. (2016). Homogeneously dispersed multimetal oxygen-evolving catalysts. *Science* **352**, 333–337.
57. Zheng, Y., Jiao, Y., Jaroniec, M., and Qiao, S.Z. (2015). Advancing the electrochemistry of the hydrogen-evolution reaction through combining experiment and theory. *Angew. Chem. Int. Ed.* **54**, 52–65.
58. Kasian, O., Grote, J.P., Geiger, S., Cherevko, S., and Mayrhofer, K.J.J. (2018). The common intermediates of oxygen evolution and dissolution reactions during water electrolysis on iridium. *Angew. Chem. Int. Ed.* **57**, 2488–2491.
59. Zhu, H., Gu, L., Yu, D., Sun, Y., Wan, M., Zhang, M., Wang, L., Wang, L., Wu, W., Yao, J., et al. (2017). The marriage and integration of nanostructures with different dimensions for synergistic electrocatalysis. *Energy Environ. Sci.* **10**, 321–330.

Chem, Volume 5

## Supplemental Information

### Charge-Redistribution-Enhanced Nanocrystalline Ru@IrO<sub>x</sub> Electrocatalysts for Oxygen Evolution in Acidic Media

Jieqiong Shan, Chunxian Guo, Yihan Zhu, Shuangming Chen, Li Song, Mietek Jaroniec, Yao Zheng, and Shi-Zhang Qiao



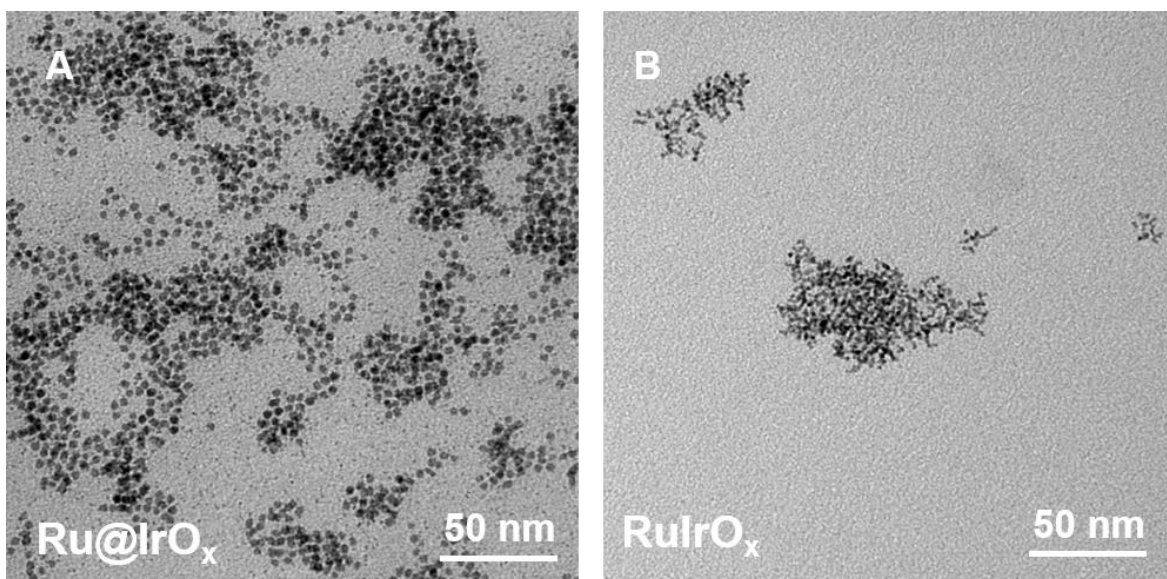


**Figure S1** Low-resolution TEM images of (A) Ru@IrO<sub>x</sub> and (B) RuIrO<sub>x</sub> nanoparticles. Scale bar: 50 nm. Related to Figure 1.

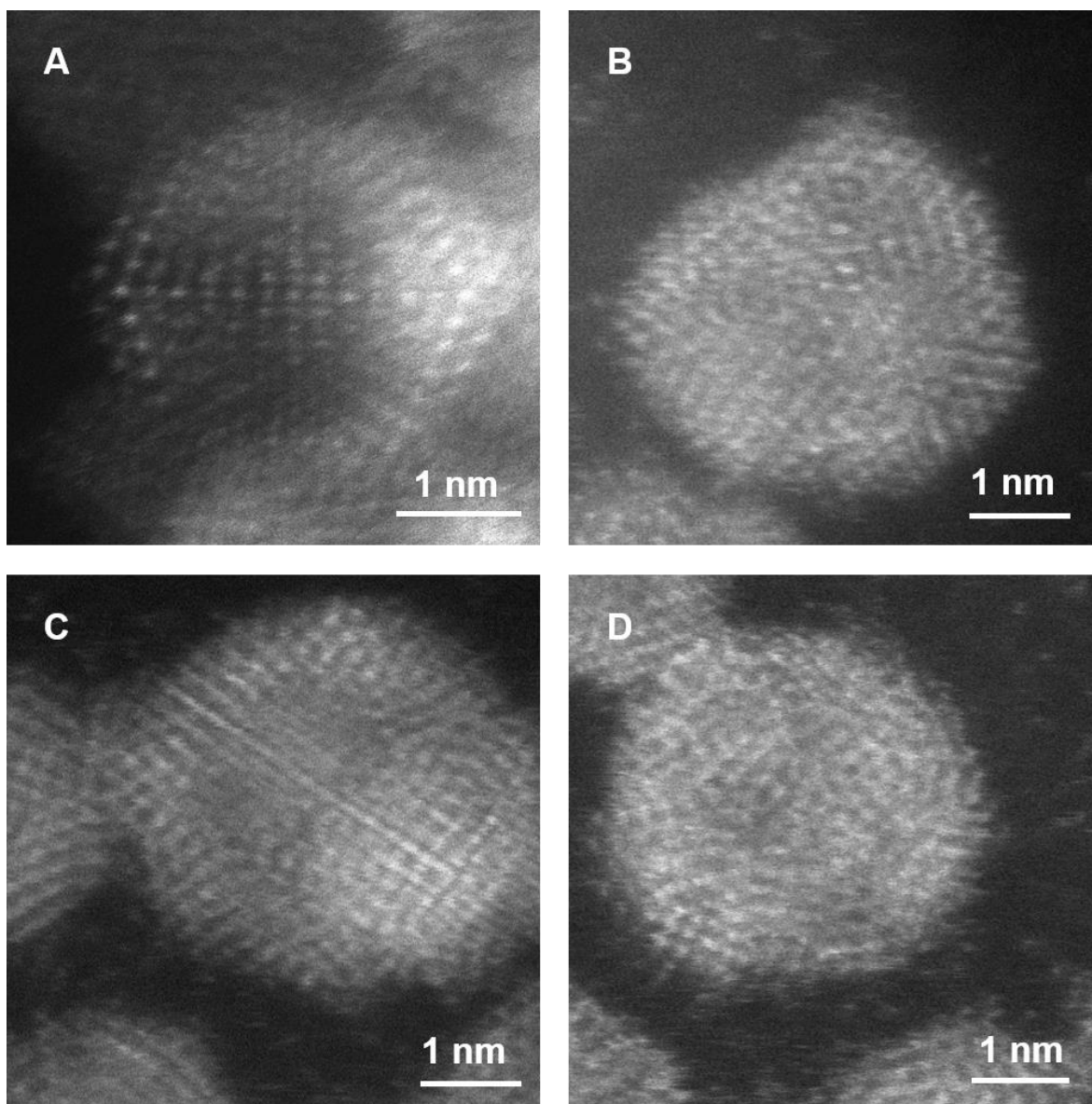


**Figure S2** HAADF-STEM images of different single Ru@IrO<sub>x</sub> nanoparticles. Scale bar: 1 nm. Related to Figure 2.

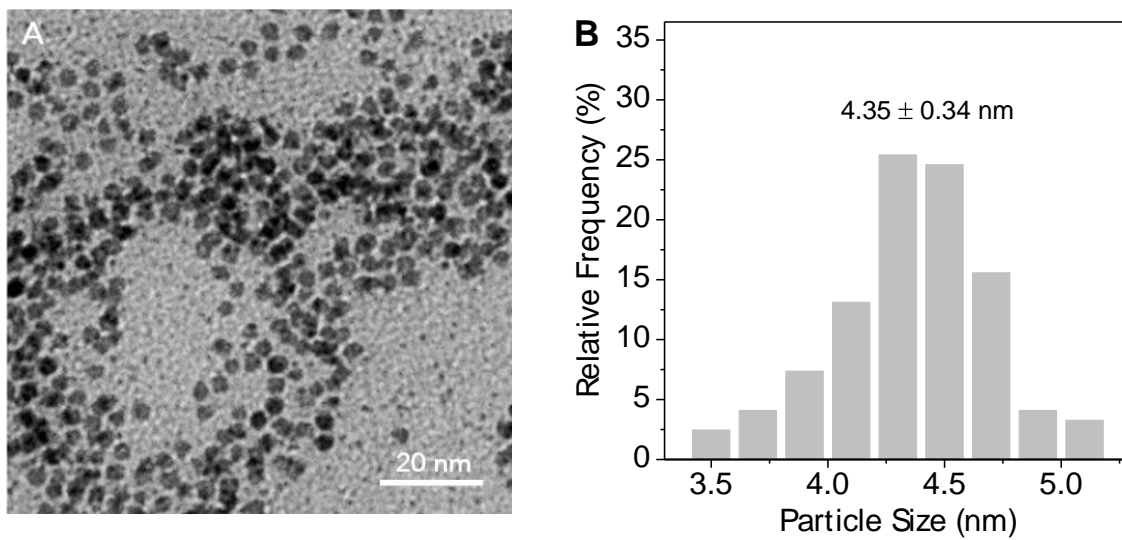


**Figure S3.** (A) TEM images of Ru@IrO<sub>x</sub> and corresponding (B) histogram of particle sizes. Scale bar: 20 nm. Related to Figure 2.

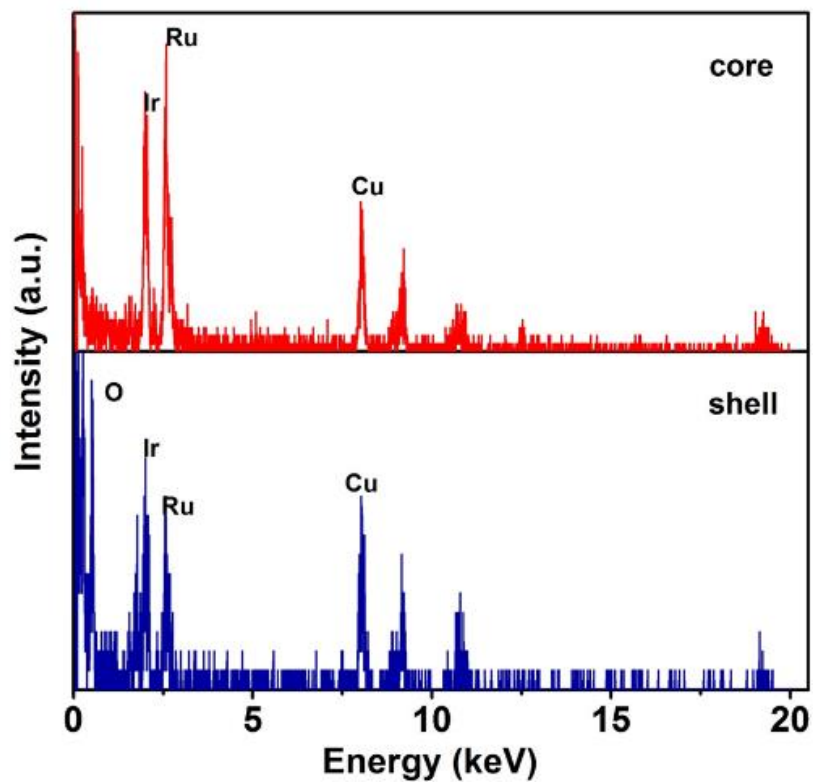


**Figure S4** EDX spectra of core and shell regions of a Ru@IrO<sub>x</sub> nanocrystal. Related to Figure 2.

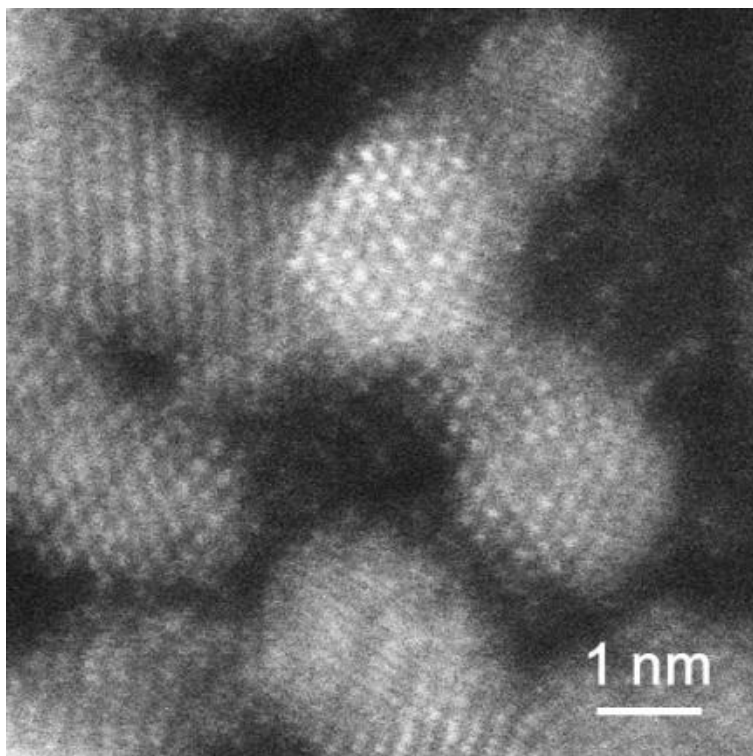


**Figure S5** HAADF-STEM images of RuIrO<sub>x</sub> nanoparticles. Scale bar: 1 nm. Related to Figure 2.

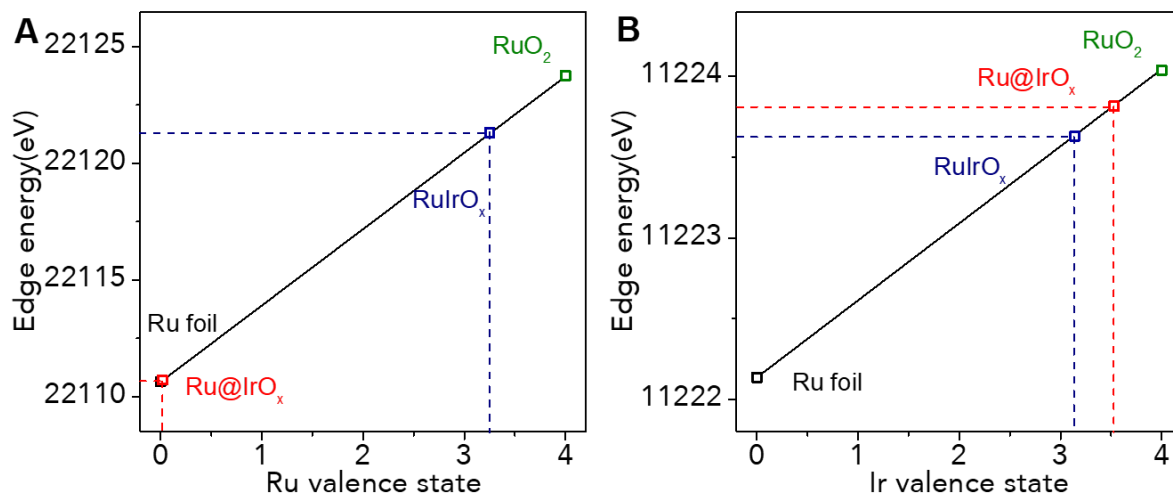


**Figure S6.** Relationship between Ru K-edge (A) and Ir L<sub>3</sub>-edge (B) adsorption energy ( $E_o$ ) and valence states for Ru@IrO<sub>x</sub>, RuIrO<sub>x</sub> electrocatalysts and the references. Related to Figure 3.

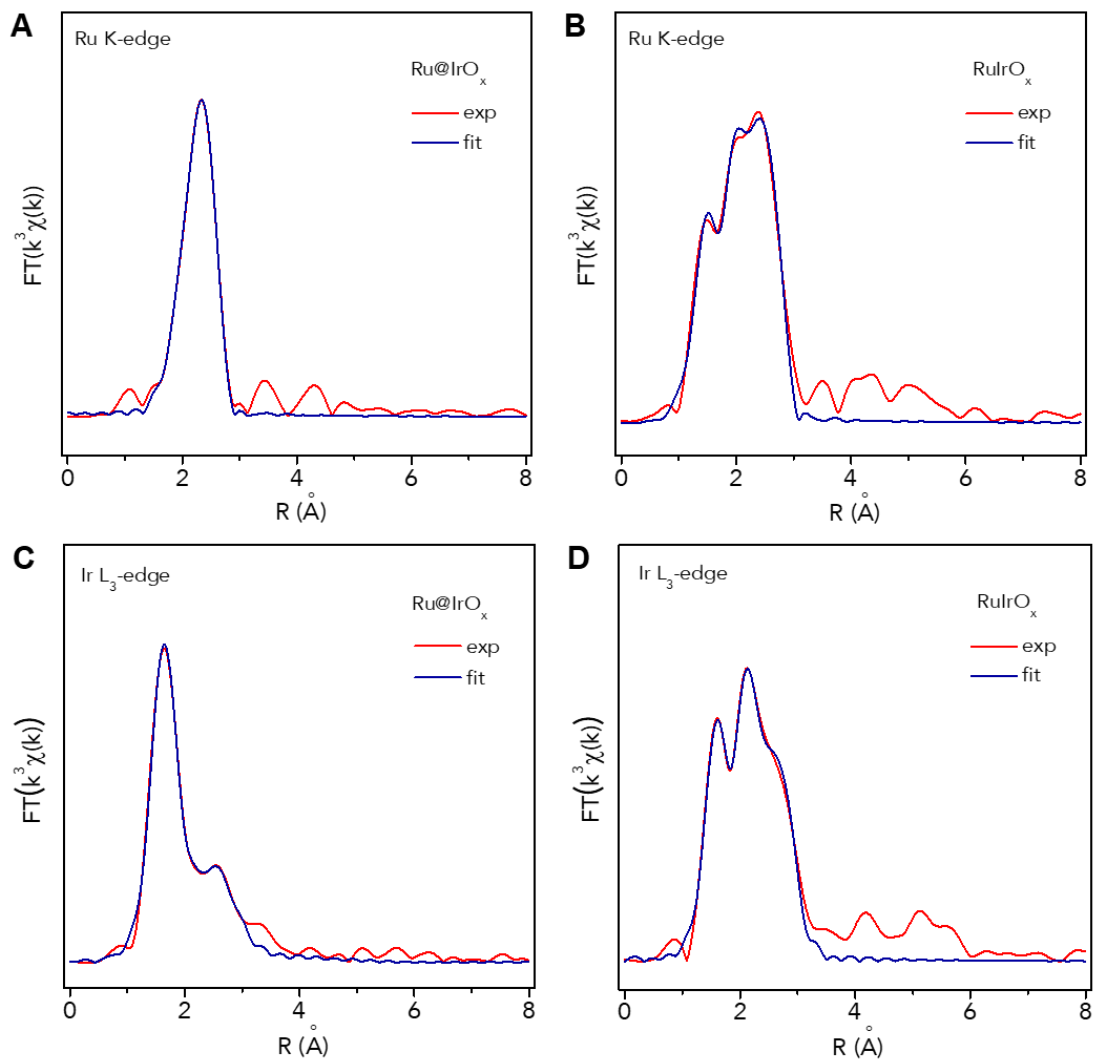


**Figure S7.** Fourier transform magnitude of the Ru K-edge experimental data (denoted as exp) and fit of  $Ru@IrO_x$  (A),  $RuIrO_x$  (B) and Ir  $L_3$ -edge experimental data (denoted as exp) and fit of  $Ru@IrO_x$  (C),  $RuIrO_x$  (D). Related to Figure 3.

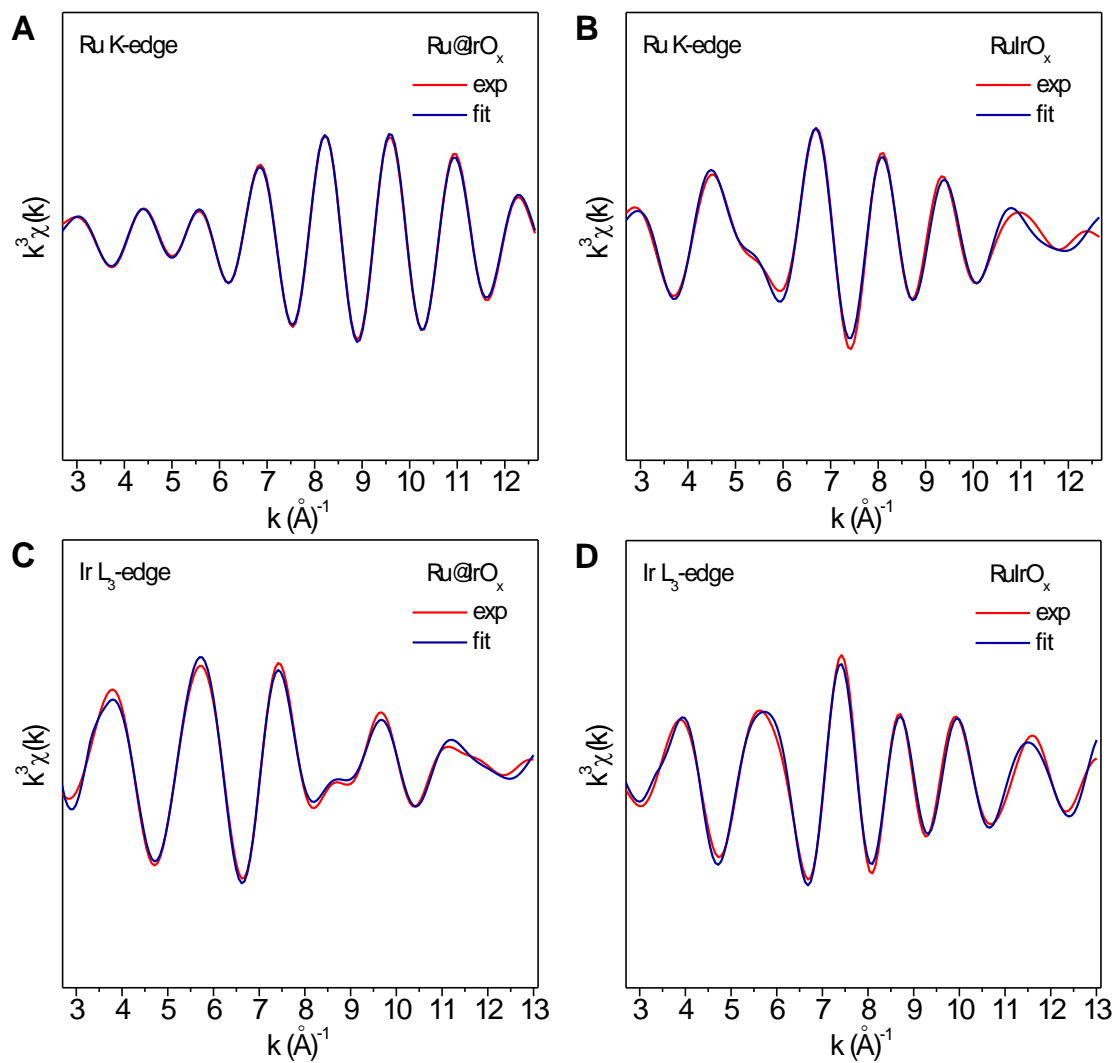


**Figure S8.**  $k_3$ -weighted EXAFS spectra at the Ru K-edge collected for  $\text{Ru@IrO}_x$  (A) and  $\text{RuIrO}_x$  samples (B) and at the Ir  $L_3$ -edge collected for  $\text{Ru@IrO}_x$  (C) and  $\text{RuIrO}_x$  samples (D). Related to Figure 3.

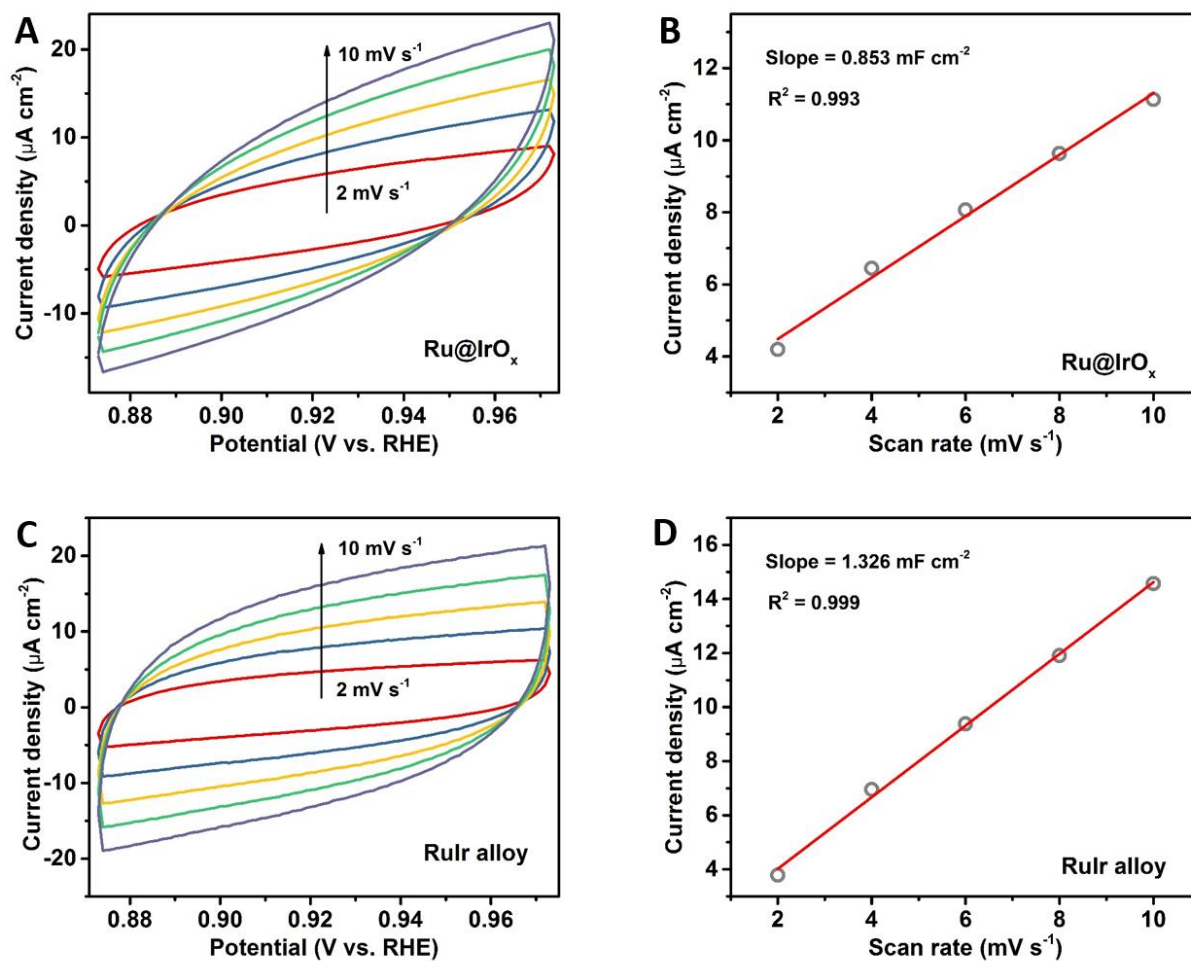


**Figure S9** CVs measured for (A) Ru@IrO<sub>x</sub> and (C) RuIrO<sub>x</sub> nanoparticles in 0.05 M H<sub>2</sub>SO<sub>4</sub>. (B), (D) Corresponding plots of the current density at 0.923 V vs. the scan rate. Related to Figure 4.

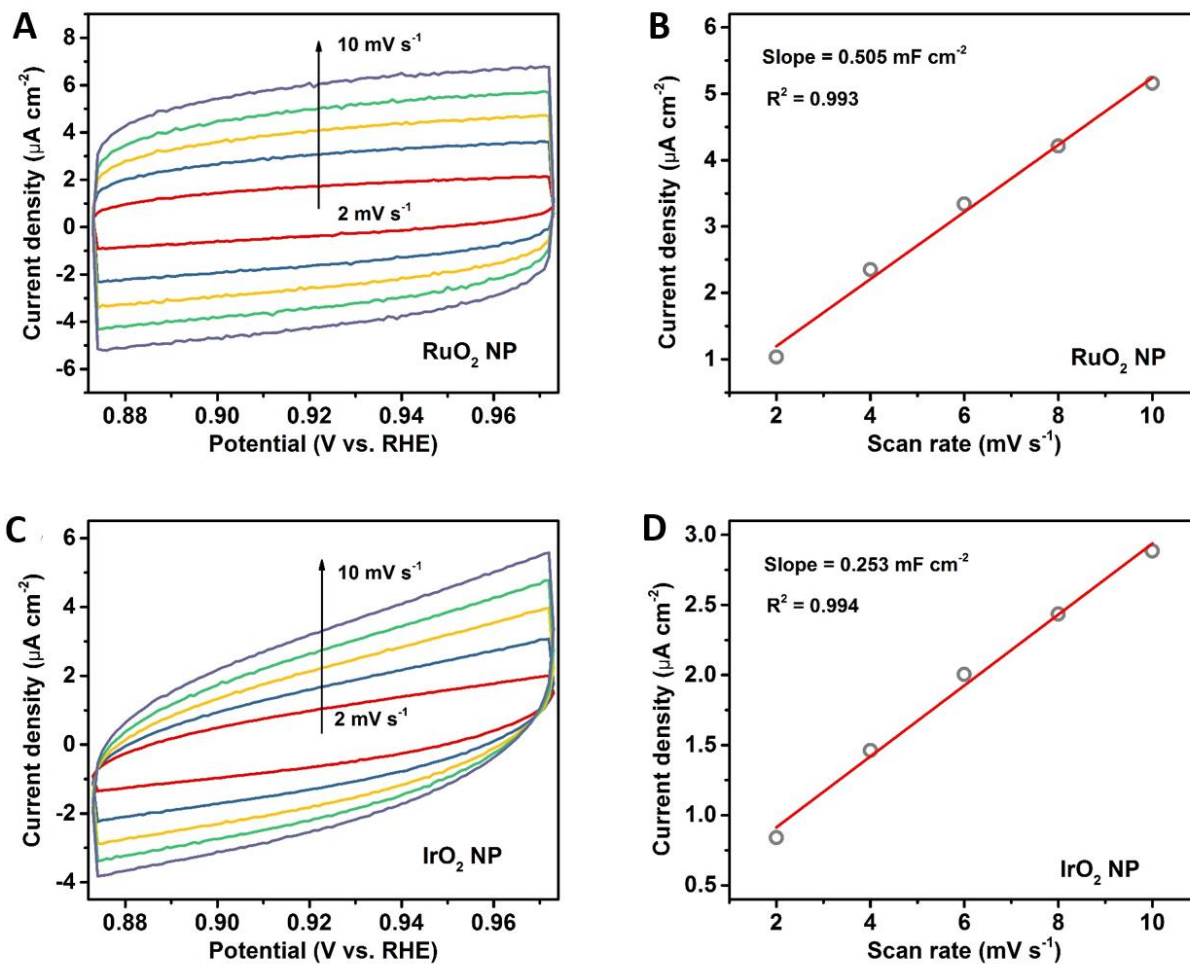


**Figure S10** CVs measured for (A)  $\text{RuO}_2$  and (C)  $\text{IrO}_2$  NPs in  $0.05 \text{ M H}_2\text{SO}_4$ . (B), (D) Corresponding plots of the current density at  $0.923 \text{ V}$  vs. the scan rate. Related to Figure 4.



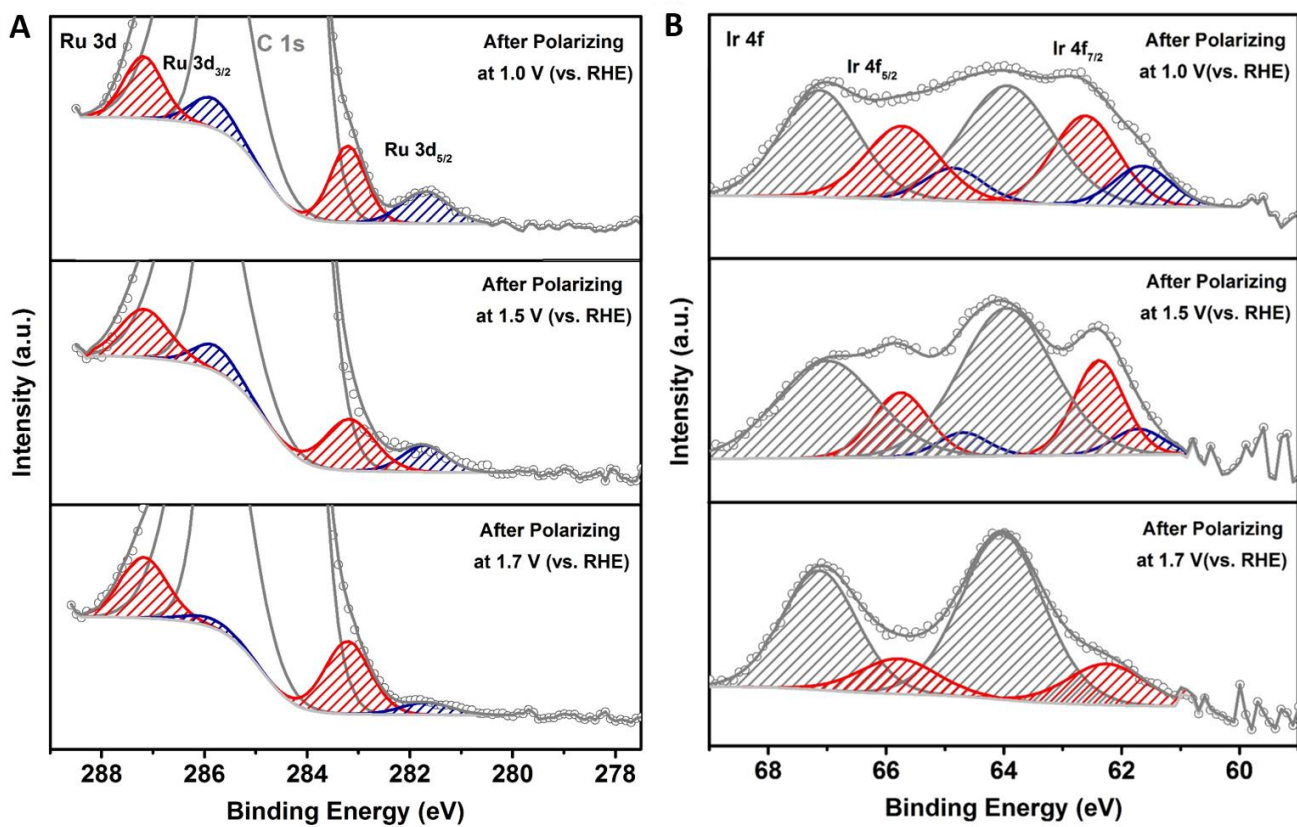


**Figure S11** (A) Ru 3d XPS spectra of the as-prepared RuIrO<sub>x</sub> electrocatalyst and the samples after polarizing at 1.0, 1.5, 1.7 V for 30 min. (B) Ir 4f XPS spectra of the as-prepared RuIrO<sub>x</sub> electrocatalyst and the samples after polarizing at 1.0, 1.5, 1.7 V for 30 min. Related to Figure 6.

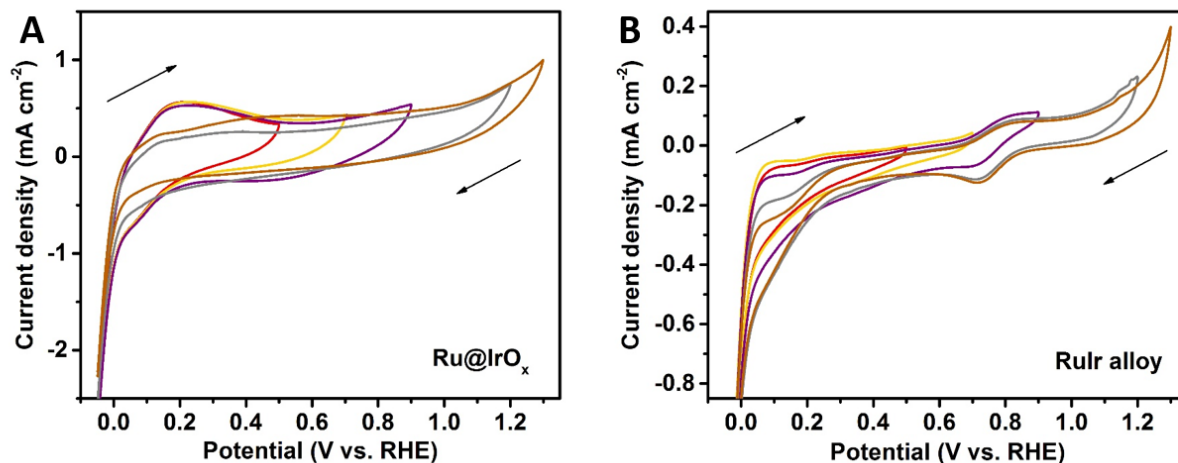


**Figure S12** CV curves measured for (A) Ru@IrO<sub>x</sub> and (B) RuIrO<sub>x</sub> electrocatalysts with starting potential of -0.05 V, the upper potential limits increase from 0.5 V to 0.7, 0.9, 1.2 and 1.3 V. Related to Figure 6.

**Table S1.** Summary of Ru K-edge and Ir L<sub>3</sub>-edge adsorption energy ( $E_0$ ) and valence states for Ru@IrO<sub>x</sub>, RuIrO<sub>x</sub> electrocatalysts and the references. Related to Figure 3.

	<i>Ru Edge Energy (eV)</i>	<i>Ru Valence State</i>	<i>Ir Edge Energy (eV)</i>	<i>Ir Valence State</i>
<i>Ru@IrO<sub>x</sub></i>	22110.72	+0.02	11223.81	+3.53
<i>RuIrO<sub>x</sub></i>	22121.31	+3.25	11223.63	+3.14
<i>RuO<sub>2</sub></i>	22123.76	+4	N/A	N/A
<i>Ru foil</i>	22110.65	0	N/A	N/A
<i>IrO<sub>2</sub></i>	N/A	N/A	11224.04	+4
<i>Ir foil</i>	N/A	N/A	11222.14	0

**Table S2.** EXAFS fit parameters for Ru@IrO<sub>x</sub>, RuIrO<sub>x</sub> and the references. Related to Figure 3.

		<i>N</i>	<i>Interatomic distance (Å)</i>	$\sigma^2(10^{-3} \text{ \AA}^2)$
<i>Ru@IrO<sub>x</sub></i>	Ru-Ru	6.5	2.67	6.0
	Ru-Ir	1.0	2.65	3.2
	Ir-O	3.6	2.01	6.1
	Ir-Ru	0.2	2.65	3.2
	Ir-Ir	4.2	2.67	11.0
<i>RuIrO<sub>x</sub></i>	Ru-O	2.0	1.99	7.1
	Ru-Ru	2.7	2.68	6.5
	Ru-Ir	4.5	2.68	7.5
	Ir-O	2.1	1.97	5.8
	Ir-Ru	3.1	2.68	7.5
	Ir-Ir	5.7	2.68	9.2
<i>Ru foil</i>	Ru-Ru	12*	2.68	4.4
<i>RuO<sub>2</sub></i>	Ru-O	4*	1.90	2.9
	Ru-O	2*	2.02	2.9
<i>Ir foil</i>	Ir-Ir	12*	2.71	3.0
<i>IrO<sub>2</sub></i>	Ir-O	6*	2.00	6.0

*N*, coordination number; *R*, interatomic distance;  $\sigma^2$ , Debye-Waller factor; Error bounds (accuracies) were estimated as *N*,  $\pm 10\%$ ; *R*,  $\pm 1\%$ ;  $\sigma^2$ ,  $\pm 10\%$ . \* is fixed coordination number according to the standard crystal structure. For comparison, the expected interatomic distances of reference systems based on their standard crystal structures are presented here: Ir foil: Ir-Ir, 2.76 Å; IrO<sub>2</sub>: Ir-O, 1.96 Å, 2.00 Å; Ru foil: Ru-Ru, 2.71 Å; RuO<sub>2</sub>: Ru-O, 1.94 Å, 1.99 Å.

**Table S3** Comparison of the surface parameters, mass activity and specific activity for electrocatalysts investigated in 0.05 M H<sub>2</sub>SO<sub>4</sub>. Related to Figure 4.

<i>Samples</i>	$C_{dl}$ (mF cm <sup>-2</sup> )	$R_f^a$	<i>Surface area</i> <sup>b</sup> (m <sup>2</sup> g <sup>-1</sup> )	<i>Mass activity</i> <sup>c</sup> (A g <sub>ox</sub> <sup>-1</sup> )	<i>Specific activity</i> <sup>c</sup> (mA cm <sub>ox</sub> <sup>-2</sup> )
<i>Ru@IrO<sub>x</sub></i>	0.853	14.22	27.87	644.8	2.315
<i>RuIrO<sub>x</sub></i>	1.326	22.10	43.32	174.6	0.400
<i>RuO<sub>2</sub> NPs</i>	0.505	8.42	16.50	108.5	0.542
<i>IrO<sub>2</sub> NPs</i>	0.253	4.22	8.27	43.5	0.252

<sup>a</sup>: the  $R_f$  was calculated by dividing  $C_{dl}$  by the capacitance of ideal planar metal oxides with smooth surface, which was taken as 0.06 mF cm<sup>-2</sup>; <sup>b</sup>: the surface area was calculated by multiplying the electrode geometrical area by  $R_f$  and then normalized by taking into account the loading mass of electrocatalysts; <sup>c</sup>: the mass and specific activity were obtained from the current density values at an overpotential of 330 mV.

**Table S4** Comparison of the recently reported Ru/Ir-based electrocatalysts in acidic media. Related to Figure 5.

Catalyst	Structure	Electrolyte	Current density	$\eta$ /mV	Stability	Reference
$Ru@IrO_x$	Core-shell nanoparticle	0.05 M $H_2SO_4$	10 mA $cm^{-2}$ ; 5 mA $cm^{-2}$	282; 258	$\eta_{10mAcm^{-2}}^{2h} = 282$ mV	This work
$IrO_x/SrIrO_3$	Perovskite	0.5 M $H_2SO_4$	10 mA $cm^{-2}$	$\eta_{10mAcm^{-2}}^{initial} = 340$ ; $\eta_{10mAcm^{-2}}^{10min} = 320$	$\eta_{10mAcm^{-2}}^{2h} = 270$ $\sim 290$ mV	Science, 2016, 353, 1011 <sup>1</sup>
$Ba_2YIrO_6$	Ir-based double perovskites	0.1 M $HClO_4$	10 mA $cm^{-2}$	$\sim 330$	$\eta_{10mAcm^{-2}}^{1h} \approx 360$ mV	Nat. Comm., 2016, 7, 12363 <sup>2</sup>
$Ir-Ni$ oxide	Mixed oxide thin film	0.05 M $H_2SO_4$	5 mA $cm^{-2}$	$\sim 290$		J. Am. Chem. Soc., 2015, 137, 13031 <sup>3</sup>
$Ir$	Commercial	1 M $H_2SO_4$	10 mA $cm^{-2}$	$340 \pm 10$	$\eta_{10mAcm^{-2}}^{2h} = 360 \pm 20$	J. Am. Chem. Soc., 2015, 137, 4347 <sup>4</sup>
$Ru$	Commercial	1 M $H_2SO_4$	10 mA $cm^{-2}$	$280 \pm 30$	$\eta_{10mAcm^{-2}}^{2h} = 340 \pm 50$	
$Y_2Ru_2O_{7-6}$	Pyrochlore	0.1 M $HClO_4$	5 mA $cm^{-2}$	$\sim 320$	$\eta_{5mAcm^{-2}}^{10k cycles} \approx 320$ mV	J. Am. Chem. Soc., 2017, 139, 12076 <sup>5</sup>
$IrCoNi$ PHNC	Porous hollow nanocrystals	0.1 M $HClO_4$	10 mA $cm^{-2}$	303	$\eta_{5mAcm^{-2}}^{t=0} \approx 265$ mV; $\eta_{5mAcm^{-2}}^{t=200min} \approx 350$ mV	Adv. Mater., 2017, 29, 1703798 <sup>6</sup>
Annealed $Ru_{0.5}Ir_{0.5}$ oxide	Nano-segregated bimetallic alloy	0.1 M $HClO_4$	5 mA $cm^{-2}$	320		Angew. Chem., 2014, 126, 14240 <sup>7</sup>
$IrNiO_x/ATO$	Oxide-supported Ir-based core-shell particles	0.05 M $H_2SO_4$	10 mA $cm^{-2}$	$\sim 330$	$\eta_{1mAcm^{-2}}^{t=0} \approx 300$ mV; $\eta_{1mAcm^{-2}}^{t=20h} \approx 340$ mV	Angew. Chem. Int. Ed., 2015, 54, 2975 <sup>8</sup>
$IrO_x-Ir$	Oxidized Ir catalysts with metallic core	0.5 M $H_2SO_4$	10 mA $cm^{-2}$	$\sim 290$		Angew. Chem. Int. Ed., 2016, 55, 742 <sup>9</sup>
$Co-IrCu$ ONC	Hollow multimetallic nanostructure	0.1 M $HClO_4$	10 mA $cm^{-2}$	293	$\eta_{10mAcm^{-2}}^{2k cycles} \approx 295$ mV	Adv. Funct. Mater., 2017, 27, 1604688 <sup>10</sup>

**Table S5** Concentrations of Ru and Ir ions in electrolyte. Related to Figure 5.

<i>Samples</i>	<i>Ru ion concentration (ppb)</i>			<i>Ir ion concentration (ppb)</i>		
	<i>1 h</i>	<i>2 h</i>	<i>10 h</i>	<i>1 h</i>	<i>2 h</i>	<i>10 h</i>
<i>Ru@IrO<sub>x</sub></i>	0.05	0.07	0.16	1.88	1.94	1.99
<i>RuIrO<sub>x</sub></i>	1.27	1.80	5.36	7.33	7.40	7.70

## Supplemental References

1. Seitz, L. C.; Dickens, C. F.; Nishio, K.; Hikita, Y.; Montoya, J.; Doyle, A.; Kirk, C.; Vojvodic, A.; Hwang, H. Y.; Norskov, J. K.; Jaramillo, T. F., *Science* **2016**, *353*, 1011-1014.
2. Diaz-Morales, O.; Raaijman, S.; Kortlever, R.; Kooyman, P. J.; Wezendonk, T.; Gascon, J.; Fu, W. T.; Koper, M. T., *Nat. Commun.* **2016**, *7*, 12363.
3. Reier, T.; Pawolek, Z.; Cherevko, S.; Bruns, M.; Jones, T.; Teschner, D.; Selve, S.; Bergmann, A.; Nong, H. N.; Schlogl, R.; Mayrhofer, K. J.; Strasser, P., *J. Am. Chem. Soc.* **2015**, *137*, 13031-13040.
4. McCrory, C. C.; Jung, S.; Ferrer, I. M.; Chatman, S. M.; Peters, J. C.; Jaramillo, T. F., *J. Am. Chem. Soc.* **2015**, *137*, 4347-4357.
5. Kim, J.; Shih, P. C.; Tsao, K. C.; Pan, Y. T.; Yin, X.; Sun, C. J.; Yang, H., *J. Am. Chem. Soc.* **2017**, *139*, 12076-12083.
6. Feng, J.; Lv, F.; Zhang, W.; Li, P.; Wang, K.; Yang, C.; Wang, B.; Yang, Y.; Zhou, J.; Lin, F.; Wang, G. C.; Guo, S., *Adv. Mater.* **2017**, *29*, 1703798.
7. Danilovic, N.; Subbaraman, R.; Chang, K. C.; Chang, S. H.; Kang, Y.; Snyder, J.; Paulikas, A. P.; Strmcnik, D.; Kim, Y. T.; Myers, D.; Stamenkovic, V. R.; Markovic, N. M., *Angew. Chem. Int. Ed.* **2014**, *53*, 14016-14021.
8. Nong, H. N.; Oh, H. S.; Reier, T.; Willinger, E.; Willinger, M. G.; Petkov, V.; Teschner, D.; Strasser, P., *Angew. Chem. Int. Ed.* **2015**, *54*, 2975-2979.
9. Lettenmeier, P.; Wang, L.; Golla-Schindler, U.; Gazdzicki, P.; Canas, N. A.; Handl, M.; Hiesgen, R.; Hosseiny, S. S.; Gago, A. S.; Friedrich, K. A., *Angew. Chem. Int. Ed.* **2016**, *55*, 742-746.
10. Kwon, T.; Hwang, H.; Sa, Y. J.; Park, J.; Baik, H.; Joo, S. H.; Lee, K., *Adv. Funct. Mater.* **2017**, *27*, 1604688.

## **Chapter 4 Transition-Metal-Doped RuIr Bifunctional Nanocrystals for Overall Water**

### **Splitting in Acidic Environments**

#### **4.1. Introduction and Significance**

For clean hydrogen fuel generation, overall water splitting in acidic environments is the key to PEM-based water electrolyzers. At present however, OER and HER bifunctional electrocatalysts - with high activity and long-term stability in acidic solution - are lacking. Moreover, rational catalyst design principles for bifunctionality are not clearly elucidated. This chapter reports transition metal-doped RuIr alloy nanocrystals (M-RuIr, M=Co, Ni, Fe) with controllably modified electronic properties for OER/HER bifunctionality in harsh acidic media. A dual effect of dopants is proposed: dopant leaching results in increased concentration of surface  $O^{\cdot-}$  to boost OER kinetics; simultaneously the charge transfer induced by dopants gives rise to modified surface valence states, which optimizes hydrogen adsorption and significantly enhances HER. Among the catalysts, the Co-RuIr exhibits small overpotentials of 235 mV for OER and 14 mV for HER (@ 10 mA cm<sup>-2</sup> current density) in 0.1 M HClO<sub>4</sub> media. This performance is amongst the best ones for water splitting catalysts in acidic environments. More importantly, using the M-RuIr model we establish electrocatalytic activity trends which are dependent on concentration of reactive oxygen species for OER, and valence states of surface sites for HER. This novel composition-activity relationship provides rational design principles for bifunctional catalysts.



#### **4.2. Transition-Metal-Doped RuIr Bifunctional Nanocrystals for Overall Water Splitting in Acidic Environments**

This section is included as a journal paper by Jieqiong Shan, Tao Ling, Kenneth Davey, Yao Zheng and Shi-Zhang Qiao, Transition-Metal-Doped RuIr Bifunctional Nanocrystals for Overall Water Splitting in Acidic Environments, *Adv. Mater.* 2019, 31, 1900510.

# Statement of Authorship

Title of Paper	Transition-Metal-Doped RuIr Bifunctional Nanocrystals for Overall Water Splitting in Acidic Environments
Publication Status	<input checked="" type="checkbox"/> Published <input type="checkbox"/> Accepted for Publication <input type="checkbox"/> Submitted for Publication <input type="checkbox"/> Unpublished and Unsubmitted work written in manuscript style
Publication Details	Shan, J., Ling, T., Davey, K., Zheng, Y. and Qiao, S. Z. (2019). Transition-metal-doped RuIr bifunctional nanocrystals for overall water splitting in acidic environments. <i>Advanced Materials</i> , 31(17), 1900510.

## Principal Author

Name of Principal Author (Candidate)	Jieqiong Shan		
Contribution to the Paper	Jieqiong Shan synthesized the materials, conducted physical characterizations and electrocatalytic experiments and wrote the paper.		
Overall percentage (%)	70%		
Certification:	This paper reports on original research I conducted during the period of my Higher Degree by Research candidature and is not subject to any obligations or contractual agreements with a third party that would constrain its inclusion in this thesis. I am the primary author of this paper.		
Signature		Date	20 Jan 2021

## Co-Author Contributions

By signing the Statement of Authorship, each author certifies that:

- i. the candidate's stated contribution to the publication is accurate (as detailed above);
- ii. permission is granted for the candidate to include the publication in the thesis; and
- iii. the sum of all co-author contributions is equal to 100% less the candidate's stated contribution.

Name of Co-Author	Tao Ling		
Contribution to the Paper	Prof. Tao Ling contributed to analysing the HAADF-STEM result and writing the paper.		
Signature		Date	20 Jan 2021

Name of Co-Author	Kenneth Davey		
Contribution to the Paper	Dr. Kenneth Davey contributed to this work in an advisory capacity and revised the paper.		
Signature		Date	25 Jan 2021

Name of Co-Author	Yao Zheng		
Contribution to the Paper	Dr. Yao Zheng designed the experiments and contributed to writing the paper.		
Signature		Date	20 Jan 2021

Name of Co-Author	Shi-Zhang Qiao		
Contribution to the Paper	Prof. Shi-Zhang Qiao designed the experiments and contributed to writing the paper.		
Signature		Date	21 Jan 2021

# Transition-Metal-Doped RuIr Bifunctional Nanocrystals for Overall Water Splitting in Acidic Environments

Jieqiong Shan, Tao Ling, Kenneth Davey, Yao Zheng,\* and Shi-Zhang Qiao\*

The establishment of electrocatalysts with bifunctionality for efficient oxygen evolution reaction (OER) and hydrogen evolution reaction (HER) in acidic environments is necessary for the development of proton exchange membrane (PEM) water electrolyzers for the production of clean hydrogen fuel. RuIr alloy is considered to be a promising electrocatalyst because of its favorable OER performance and potential for HER. Here, the design of a bifunctional electrocatalyst with greatly boosted water-splitting performance from doping RuIr alloy nanocrystals with transition metals that modify electronic structure and binding strength of reaction intermediates is reported. Significantly, Co-RuIr results in small overpotentials of 235 mV for OER and 14 mV for HER (@ 10 mA cm<sup>-2</sup> current density) in 0.1 M HClO<sub>4</sub> media. Therefore a cell voltage of just 1.52 V is needed for overall water splitting to produce hydrogen and oxygen. More importantly, for a series of M-RuIr (M = Co, Ni, Fe), the catalytic activity dependence at fundamental level on the chemical/valence states is used to establish a novel composition-activity relationship. This permits new design principles for bifunctional electrocatalysts.

Hydrogen is widely regarded as a practical alternative energy to environmentally polluting fossil fuels.<sup>[1,2]</sup> An attractive and simple means to produce hydrogen from abundant renewable sources is via water electrolysis. This involves two related electrochemical reactions in an electrolyzer, namely, an anodic oxygen evolution reaction (OER) and a cathodic hydrogen evolution reaction (HER).<sup>[1,3]</sup> In contrast to alkaline electrolyzers, proton exchange membrane (PEM) water electrolyzers offer significant benefits. These include greater voltage efficiency and gas purity, together with a more compact design.<sup>[4]</sup> To implement overall water electrolysis in an integrated PEM electrolyzer, it is desirable to couple OER and HER electrocatalysts in an acidic environment.<sup>[5-7]</sup> Despite significant progress in developing bifunctional water splitting electrocatalysts for alkaline electrolytes, no similar

progress has been reported for acidic environments. This remains a challenge. Although many transition metal derivatives can be highly efficient for OER and HER in alkaline environments, a serious drawback is their degradation in harsh acidic environments.<sup>[8,9]</sup> It is known that typical HER catalysts with good performance in acidic solutions, including Pt and MoS<sub>2</sub>, undergo oxidation and exhibit poor activity in OER.<sup>[3,10]</sup> Overall therefore, it was reckoned that design for acidic water splitting electrocatalysts should be based on binary ruthenium and iridium alloy (RuIr) electrocatalysts because of favorable OER performance and potential for HER.<sup>[11,12]</sup> However, electrocatalysts with comparable bifunctional catalytic activity with state-of-the-art RuO<sub>2</sub> (for OER) and Pt (for HER) in acidic environments have not been reported. A consequence is the present lack of understanding of the composition-activity relationship for RuIr alloy.<sup>[13-15]</sup>

There are, in general terms, two strategies to boost activity of catalysts. These are to: 1) significantly increase the number of active sites or 2) improve the intrinsic activity of each single site.<sup>[16-18]</sup> Importantly, the alloying or doping of electrocatalysts with transition metals has been shown to be an effective means to tune electrochemical properties at the atomic level.<sup>[19-21]</sup> Specifically, the incorporation of transition metals can: 1) modify the local electronic environment (e.g., *d*-band center)<sup>[22]</sup>; 2) increase the concentration of highly active surface species (e.g., surface hydroxyl groups)<sup>[23]</sup>; and 3) optimize geometrical factors of active sites (e.g., interatomic distances, coordination numbers).<sup>[24]</sup> These impacts are facilitated by ligand and strain effects of foreign metals and result in regulated chemisorption behavior of intermediate species.<sup>[25,26]</sup> So far substantial research has been undertaken using theoretical models to predict catalytic activity of metal alloyed/doped catalysts based on adsorption energy of intermediates.<sup>[27,28]</sup> However these predictions can readily lead to inaccurate results when significant differences between real-catalysts and theoretical-models exist. Taking into account, therefore, the physiochemical factors of real-catalysts provides a better strategy to determine catalytic activity trends.<sup>[16,29]</sup> For example, coordination numbers of Pt sites have been reported to be a predictive descriptor and provide a connection between geometry, adsorption energy and ORR activity.<sup>[30]</sup> With this as a strategy it is practical to establish a composition-activity relationship for overall water splitting.

J. Shan, Dr. K. Davey, Dr. Y. Zheng, Prof. S.-Z. Qiao  
School of Chemical Engineering  
The University of Adelaide  
Adelaide, SA 5005, Australia  
E-mail: yao.zheng01@adelaide.edu.au; s.qiao@adelaide.edu.au  
Prof. T. Ling, Prof. S.-Z. Qiao  
School of Materials Science and Engineering  
Tianjin University  
Tianjin 300072, China

 The ORCID identification number(s) for the author(s) of this article can be found under <https://doi.org/10.1002/adma.201900510>.

DOI: 10.1002/adma.201900510

Here, we report transition metal-doped RuIr alloy electrocatalysts (M-RuIr, M = Co, Ni, Fe) designed to boost bifunctionality through modification of electronic structure and resulting physiochemical properties. We show that with optimal chemical/valence states, Co-RuIr nanocrystals exhibit excellent OER and HER catalytic activity with long-term stability, which are amongst the best reported for overall water splitting in acidic environments. Moreover, we establish electrocatalytic activity trends on reactive oxygen species concentration for OER, and surface sites valence state for HER. We demonstrate a linear activity dependence on reaction intermediates binding strength and highlight that chemical/valence states of catalysts provide a good indication of activity at the fundamental level.

To synthesize Co-RuIr and RuIr nanocrystals, a co-reduction polyol method was adopted to reduce metal salts by refluxing ethylene glycol (EG) with poly-(vinylpyrrolidone) (PVP) as a stabilizer (see the Experimental Section for details). To study the effect of different transition metal dopants, Ni-RuIr and Fe-RuIr nanocrystals were prepared using a similar procedure. The as-obtained Co-RuIr nanocrystals were characterized by high-angle annular dark-field scanning transmission-electron microscopy (HAADF-STEM). The images indicated an ultra-small diameter of Co-RuIr ( $2.1 \pm 0.1$  nm) with a narrow distribution (Figure 1a, Figures S1 and S2, Supporting Information). The lattice distances of Co-RuIr were measured at 0.22 nm and 0.19 nm (Figure 1b), corresponding, respectively, to the {111} and {200} planes of RuIr alloy nanocrystals. This was confirmed by X-ray diffraction (XRD) patterns (JCPDS # 65-5546), Figure S3

(Supporting Information). RuIr nanocrystals showed similar particle size and crystalline structure (Figure S4, Supporting Information). This finding highlights that the Co dopants do not change the intrinsic morphology of RuIr nanocrystals.

Energy-dispersive spectroscopy (EDX) elemental maps (Figure 1c) revealed that Ru and Ir atoms exhibited signals of comparable density and were distributed in the same area, whereas Co atoms were randomly distributed with low concentration. This observation confirmed formation of a Co-doped homogeneous RuIr alloy. This is attributed to simultaneous reduction of Ru, Ir, and Co precursors. Synchrotron-based X-ray photoelectron spectra (XPS) survey and Co  $L_{3,2}$  edge X-ray absorption near-edge spectra (XANES) further confirmed the existence of the Co dopants in Co-RuIr nanocrystals with low concentration (Figures S5 and S6, Supporting Information). Additionally, the synthesis procedure was applicable to prepare various transition metal doped nanocrystals, e.g., Ni-RuIr and Fe-RuIr, which can serve as control samples (Figures S3, S5, and S6, Supporting Information).

Synchrotron-based XANES and high-resolution XPS were carried out to investigate the surface chemical and valence states of the catalysts. Importantly, these parameters are widely reported to play a key role in determining electrocatalytic properties.<sup>[31,32]</sup> For OER, optimal activity depends on appropriate binding energies of oxygen intermediates.<sup>[3]</sup> Different oxygen species on the surface of an oxide catalyst exhibit different binding behavior. For example, lattice oxygen species show much stronger intermediates binding than surface OH groups.

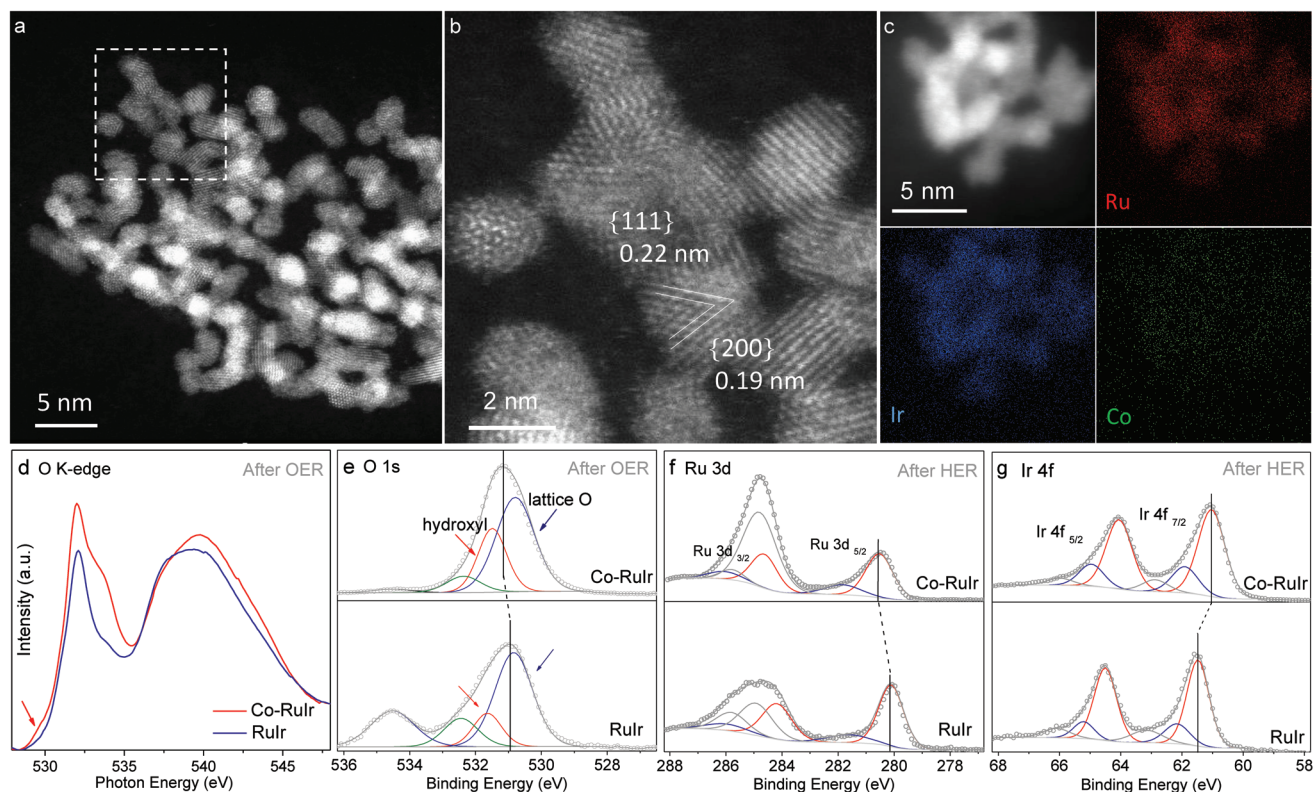


**Figure 1.** a) HAADF-STEM image of Co-RuIr nanocrystal. b) An enlarged view of the rectangular region in (a). c) STEM-EDX mappings of Co-RuIr nanocrystals. d) O K-edge XANES and e) O 1s XPS spectra of Co-RuIr and RuIr electrocatalysts after OER tests. f) Ru 3d and g) Ir 4f XPS spectra for Co-RuIr and RuIr electrocatalysts after HER tests.

Therefore because intermediates are expected to be bound too strongly on lattice oxygen species, they do not have a direct role in OER.<sup>[23]</sup> From reported studies<sup>[28]</sup> both RuO<sub>2</sub> and IrO<sub>2</sub> were expected to bind oxygen intermediates too strongly, and thereby impeded an ideal balanced binding energy. Because of (inevitable) Co leaching in Co-RuIr during OER testing in acidic solutions, some lattice oxygen atoms lose binding partners and consequently become low-coordinated oxygen species.<sup>[23]</sup> From the O K-edge XANES spectra of post-OER Co-RuIr and RuIr catalysts, Figure 1d, the shoulder peak around 529 eV of the Co-RuIr curve demonstrates existence of O<sup>1-</sup> species. These O<sup>1-</sup> species are reported as electrophilic and susceptible to nucleophilic attack from water, therefore promote catalytic activity in OER.<sup>[33,34]</sup> In the O1s XPS spectra, Figure 1e, the peaks at around 530.7 and 531.5 eV are identified as, respectively, lattice oxygen and hydroxyl groups.<sup>[35]</sup> The Co-RuIr displays a greater proportion of hydroxyl group compared with that for RuIr – confirming the XANES evidence.

At the same time, fundamental studies about HER electrocatalysts in acidic environments suggested that the Ru bound hydrogen too strongly, while Ir exhibited slightly weak binding strength, both of which were unfavorable for hydrogen evolution and led to the relatively poor HER performances.<sup>[3]</sup> As can be seen in the Ru 3d spectra, Figure 1f, Co-RuIr exhibits a meaningful positive-shift of Ru 3d<sub>5/2</sub> and Ru 3d<sub>3/2</sub>

peaks (280.6 and 284.7 eV) in comparison with those for RuIr (280.1 and 284.2 eV). This underscores the higher Ru valence state of Co-RuIr. This increase in valence state makes Ru sites less prone to bind hydrogen intermediates with positive charge. The general result is an optimized hydrogen binding behavior. The Ir 4f spectrum of Co-RuIr exhibits a slight negative shift when compared with that for RuIr, i.e., lower-valence Ir sites. This indicates the slightly enhanced hydrogen binding ability of Ir sites, Figure 1g. These altered valence states are attributed to charge transfer amongst components induced by differences in work function (Ru: 4.71, Ir: 5.27, Co: 5.0). These findings overall, therefore readily demonstrate that Co doping modifies the valence states of Ru and Ir sites and leads to optimization of hydrogen intermediate binding energy in HER.

To correlate the composition-induced modified surface chemical/valence states of the catalyst with OER/HER performance, electrochemical testing was conducted on Co-RuIr and RuIr, together with commercial samples. OER performance was tested in O<sub>2</sub>-saturated 0.1 M HClO<sub>4</sub> solution. As can be seen in the linear sweep voltammetry (LSV) curves, Figure 2a, Co-RuIr exhibited significantly greater activity when compared with RuIr and state-of-the-art (commercial) RuO<sub>2</sub> and IrO<sub>2</sub>. To deliver a current density of 10 mA cm<sup>-2</sup>, the Co-RuIr required a small overpotential of 235 mV with the lowest Tafel slope of 66.9 mV dec<sup>-1</sup>, whilst RuIr required 344 mV and

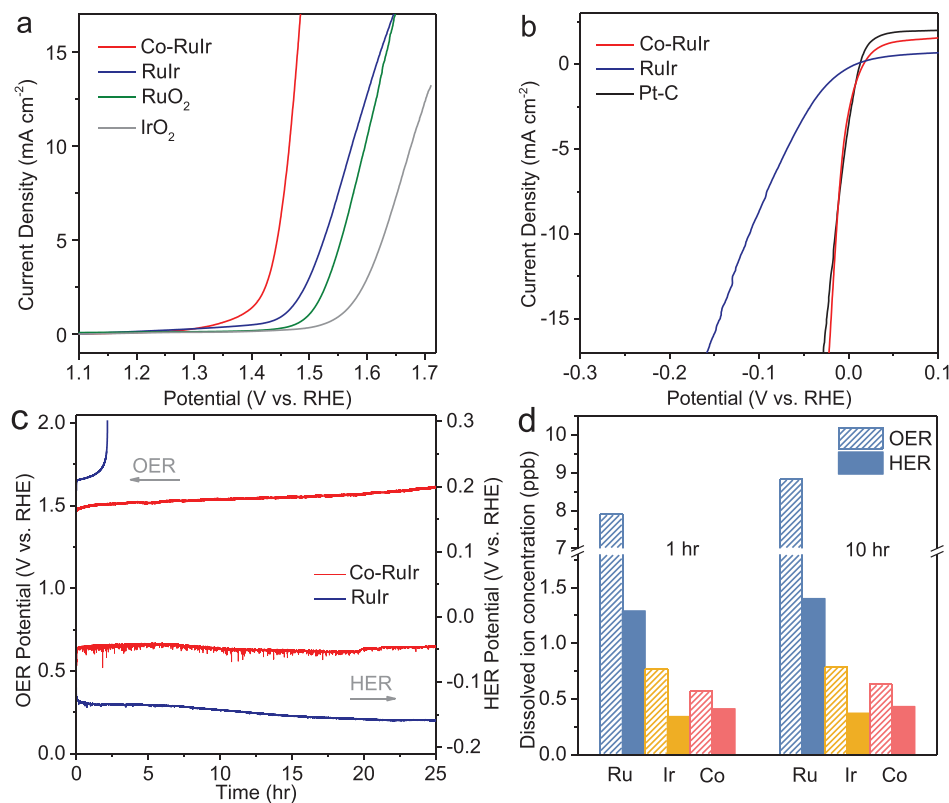


**Figure 2.** a) LSV curves for Co-RuIr, RuIr, RuO<sub>2</sub>, and IrO<sub>2</sub> electrocatalysts for OER in O<sub>2</sub>-saturated 0.1 M HClO<sub>4</sub> solutions. b) LSV curves of Co-RuIr, RuIr and Pt-C electrocatalysts for HER in H<sub>2</sub>-saturated 0.1 M HClO<sub>4</sub> solution. c) Constant current chronopotentiometric stability measurements at anodic (left y-axis) or cathodic (right y-axis) current density of 10 mA cm<sup>-2</sup> for Co-RuIr and RuIr. d) ICP-MS analysis data for Co-RuIr after various reaction times under OER (pattern filled) and HER (color filled) stability testing. Blue, yellow, and red bars represent, respectively, Ru, Ir, and Co ion concentrations in electrolyte.

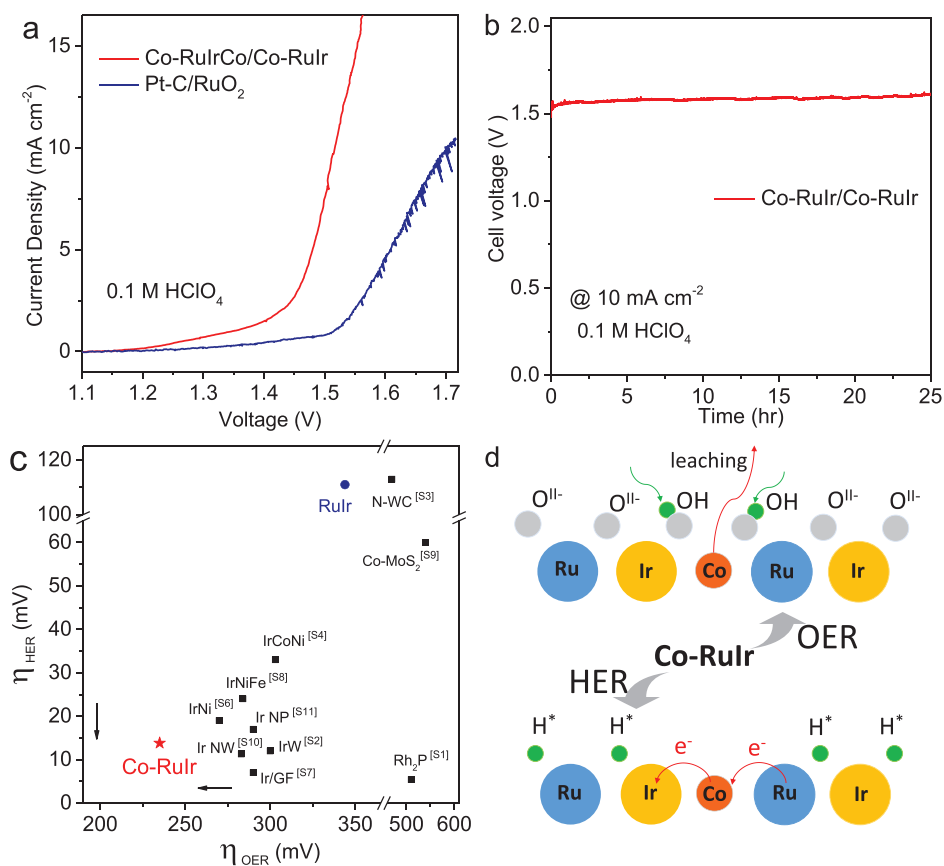


**Figure 3.** a) Overall water splitting performance of Co-RuIr/Co-RuIr and Pt-C/ $\text{RuO}_2$  in  $\text{N}_2$ -saturated 0.1 M  $\text{HClO}_4$  solution with a two-electrode configuration. b) Constant current chronopotentiometric stability tests for Co-RuIr/Co-RuIr and Pt-C/ $\text{RuO}_2$  for overall water splitting at current density of  $10 \text{ mA cm}^{-2}$ . c) Bifunctional water splitting performance for various OER electrocatalysts. The x-axis is overpotential required to achieve a current density of  $10 \text{ mA cm}^{-2}$  (unless otherwise specified in Table S1, Supporting Information) for OER, while the y-axis is the overpotential required to achieve a current density of  $10 \text{ mA cm}^{-2}$  (unless otherwise specified in Table S1, Supporting Information) for HER. The '[S1]' refer to cited references in Supporting Information. d) Schematic of OER and HER mechanism on Co-RuIr electrocatalyst in acidic media.

$111.5 \text{ mV dec}^{-1}$ . This indicates the fast kinetics of Co-RuIr catalysts (Figure S7, Supporting Information). HER performance was tested in  $\text{H}_2$ -saturated 0.1 M  $\text{HClO}_4$  solution. RuIr exhibited low catalytic activity with a large overpotential of 110 mV to deliver a current density of  $10 \text{ mA cm}^{-2}$  (Figure 2b). Following Co doping of RuIr alloy, the HER of the Co-RuIr exhibited a significant improvement with an overpotential of just 14 mV with a low Tafel slope of  $31.1 \text{ mV dec}^{-1}$  ( $@ 10 \text{ mA cm}^{-2}$ ). Significantly, this demonstrated that the electrocatalytic performance of Co-RuIr is directly comparable with that of the state-of-the-art Pt/C.

The stability of the Co-RuIr electrocatalyst was evaluated using constant chronopotentiometric measurement (Figure 2c). Throughout a 25 h testing period the electrode potential of the Co-RuIr electrocatalysts remained constant for both OER and HER. In contrast, the RuIr electrode exhibited a continuously increasing electrode potential to ultimate activity degradation in the OER test. Importantly, the morphology of the Co-RuIr nanocrystals following the long-term OER stability test was unchanged from that of the fresh, as-prepared catalyst (Figure S8, Supporting Information). As is shown in the inductively coupled plasma mass spectrometry (ICP-MS), Figure 2d, the dissolved concentration of Ru, Ir and Co ions is low, and

changed little for both OER and HER over the stability tests. The initial dissolution of metal ions is attributed to unstable surface sites. This little change however suggests exceptional stability of the Co-RuIr catalyst for both OER and HER.

An overall water splitting experiment was carried with Co-RuIr as both cathodic and anodic electrocatalysts (electrolysis cell noted as Co-RuIr/Co-RuIr) in  $\text{N}_2$ -saturated 0.1 M  $\text{HClO}_4$  solution. The results in Figure 3a show the Co-RuIr/Co-RuIr gave excellent activity with a low cell voltage of 1.52 V ( $@ 10 \text{ mA cm}^{-2}$ ). By contrast, the present best commercial electrocatalyst (Pt-C/ $\text{RuO}_2$ ) required a significantly higher cell voltage of 1.70 V to deliver this same current density. Furthermore, the Co-RuIr/Co-RuIr remained stable over 25 h of continuous overall water electrolysis (Figure 3b). Moreover, as is summarized in Figure 3c and Table S1 (Supporting Information), Co-RuIr outperformed a representative range of reported water splitting catalysts. Significantly, this performance therefore positions Co-RuIr amongst the most active overall water splitting catalysts in acidic environments.

This favorable bifunctional catalytic performance of Co-RuIr can be explained by a dual effect of Co dopants. This effect is shown schematically as Figure 3d. Under OER, inevitable Co leaching results in increased concentration of  $\text{O}^{1-}$  species

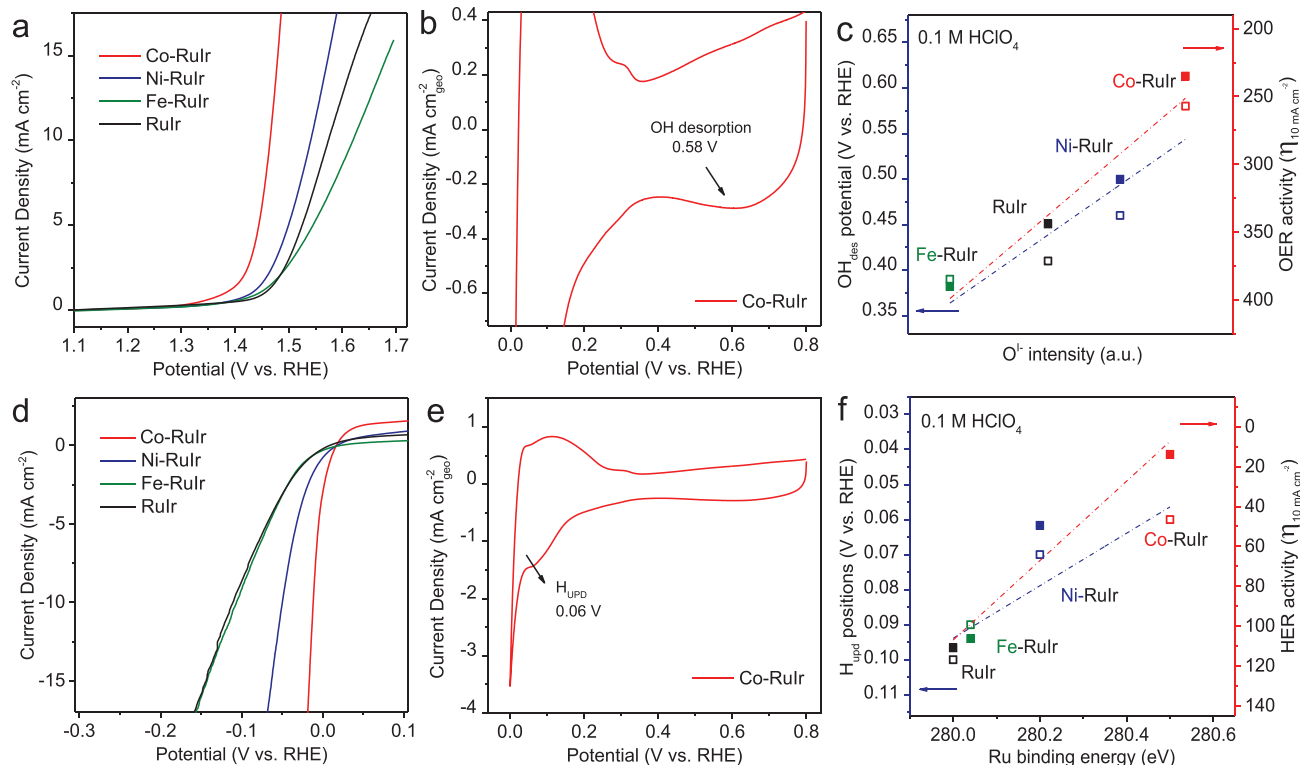


**Figure 4.** a) LSV curves of M-RuIr (M = Co, Ni, Fe) and RuIr electrocatalysts for OER in  $O_2$ -saturated 0.1 M  $HClO_4$  solution. b) CV curve for Co-RuIr at a scan rate of  $50\text{ mV s}^{-1}$  with arrow indicating OH desorption potential. c) Relationships between  $O^{1-}$  species concentration and OH desorption ( $OH_{des}$ ) potential (left y-axis, hollow points), and that for OER activity (represented by overpotential at current density of  $10\text{ mA cm}^{-2}$ , right y-axis, solid points) on M-RuIr and RuIr electrocatalysts. d) LSV curves of M-RuIr (M = Co, Ni, Fe) and RuIr electrocatalysts for HER in  $H_2$ -saturated 0.1 M  $HClO_4$  solution. e) CV curve of Co-RuIr at a scan rate of  $50\text{ mV s}^{-1}$  with the arrow indicating  $H_{UPD}$  potential. f) Relationships between Ru binding energy and  $H_{UPD}$  potential (left y-axis, hollow points), and that for HER activity (represented by overpotential at current density of  $10\text{ mA cm}^{-2}$ , right y-axis, solid points) on M-RuIr and RuIr electrocatalysts.

which significantly promote OER catalytic activity. With HER the charge transfer induced by Co dopants gives rise to modified surface valence states that optimize hydrogen adsorption and consequently boost catalytic activity.

To establish a composition-activity relationship, Ni-RuIr and Fe-RuIr electrocatalysts were also measured using the same methods (Figures S9 and S10, Supporting Information). The LSV profiles in OER (Figure 4a and Figure S11, Supporting Information) showed that catalytic activity decreased as ordered  $Co-RuIr > Ni-RuIr > RuIr > Fe-RuIr$ . Significantly, an approximate linear correlation was observed between OER activity (recorded by the overpotentials at  $10\text{ mA cm}^{-2}$ ) and the intensity of  $O^{1-}$  species (Figure S12, Supporting Information).

To extend this composition-activity relationship to a fundamental level, we also performed cyclic voltammetry (CV) experiments on M-RuIr in  $N_2$ -saturated 0.1 M  $HClO_4$  solution with scan rates of  $50\text{ mV s}^{-1}$ . Figure 4b and Figure S13 (Supporting Information) depict the  $OH^-$  desorption peak positions and show a decreasing trend such that  $Co-RuIr > Ni-RuIr > RuIr > Fe-RuIr$ . This finding indicates that by doping with different transition metals, the intermediate adsorption/desorption is actually regulated. Doping with Co and Ni weakens the oxygen intermediates adsorption/desorption, and thereby boosts OER performance. Figure 4c shows that linear relationships result

for both  $OH^-$  desorption peak (left y-axis) positions and OER activity (right y-axis) with intensity of  $O^{1-}$  species (x-axis). The double-linear relationship suggests that the concentration of oxygen species reflects the general oxygen adsorption strength of M-RuIr. The former therefore provides a reasonable indication for the trend in OER electrocatalytic activity.

The electrocatalysts were studied under similar procedures to assess catalytic behavior and performance of M-RuIr toward HER (Figure 4d and Figure S14, Supporting Information). HER activity of the catalysts was found to be ordered as  $Co-RuIr > Ni-RuIr > Fe-RuIr \approx RuIr$ . Additionally, a linear correlation between Ru binding energies and HER activity (recorded by overpotentials at  $10\text{ mA cm}^{-2}$ ) was achieved (Figure S15 and S16, Supporting Information). To determine the hydrogen intermediate adsorption strength, underpotential deposition (UPD) hydrogen adsorption ( $H_{UPD}$ ) voltammetry was measured (Figure 4e and Figure S17, Supporting Information).<sup>[3]</sup> The lowest  $H_{UPD}$  potential was for Co-RuIr. This suggested a weakened hydrogen adsorption that is clearly beneficial for HER activity—a finding confirmed in the XPS results. A linear dependence was similarly observed for both  $H_{UPD}$  positions (left y-axis) and HER activity (right y-axis) with Ru valence states (x-axis) (Figure 4f). This is evidence that the cause of boosted HER activity of M-RuIr is the modified



hydrogen binding energy that was realized by modifying the Ru valence states. It is concluded overall therefore that for this system the  $O^{1-}$  intensity and Ru binding energy, respectively correlate well with predicted OER and HER activity.

In summary, through introducing transition metal doping in RuIr alloy nanocrystals, we have demonstrated the design of a series of bifunctional electrocatalysts toward OER and HER in acidic environments. Overall best catalytic performance, together with excellent long-term stability, was most evident for Co-RuIr. Significantly, this positions it amongst the most active and stable overall water splitting catalyst reported in acidic environments. The boost in OER and HER activity of Co-RuIr is attributed to a dual effect that modifies concentration of O-based species and Ru sites valence states. This dual modification applies also to other transition metal dopants. At a fundamental level the catalytic activity dependence on chemical/valence states was demonstrated for a series of M-RuIr (M = Co, Ni, Fe). This was used to establish a novel composition-activity relationship that will permit new design principles for bifunctional electrocatalysts.

## Experimental Section

**Synthesis of Nanocrystals:** The synthesis of Co-RuIr nanocrystals was achieved by a coreduction polyol method reported previously.<sup>[36]</sup> In a typical procedure, 41.4 mg of Ruthenium (III) chloride hydrate ( $RuCl_3 \cdot xH_2O$ ), 59.7 mg of Iridium (III) chloride hydrate ( $IrCl_3 \cdot xH_2O$ ), 11.9 mg Cobalt (II) chloride hexahydrate ( $CoCl_2 \cdot 6H_2O$ ) and 55.0 mg of PVP were mixed in 40 mL of EG to a transparent solution. This was heated rapidly to 198 °C under vigorous stirring and refluxed for 3 h. The reaction was quenched by ice cooling and the resultant suspension was washed three times with ethanol. The Co-RuIr nanocrystals were obtained after drying the precipitate at 60 °C overnight in a vacuum-oven. The RuIr, Ni-RuIr, and Fe-RuIr nanocrystals were synthesized by similar procedure but without addition of cobalt salt, or, with addition of 11.9 mg Nickel (II) chloride hexahydrate ( $NiCl_2 \cdot 6H_2O$ ) and 10.0 mg Iron (II) chloride tetrahydrate ( $FeCl_2 \cdot 4H_2O$ ).

**Characterization:** HAADF-STEM images were recorded using an FEI Titan G2 80–300 microscope at 300 kV equipped with a probe corrector. EDX imaging was conducted with an FEI Titan Themis 80–200 microscope equipped with a SuperX detector. The synchrotron-based XPS and XANES characterization were performed on the soft X-ray spectroscopy beamline in the Australian Synchrotron Radiation Facility, Melbourne. For the ex situ XPS tests, the electrocatalysts were polarized at anodic, or cathodic potentials, for 30 min, then the electrocatalyst paste was scraped off the electrodes and washed several times with ethanol to remove the Nafion species. After centrifugation and drying, the obtained powder was tested as electrocatalysts after OER and HER. Additionally, ICP-MS measurements were carried out to detect the amounts of dissolved Ru, Ir, and Co ions in electrolytes after 1 and 10 h of chronoamperometric experiment under anodic or cathodic current density of 10 mA  $cm^{-2}$ . XRD data were collected on a Rigaku MiniFlex 600 X-Ray Diffractometer. ICP-MS analysis was conducted using an Agilent 7500cx instrument with attached laser ablation systems.

**Electrochemical Measurements:** Electrocatalyst ink was prepared by dispersing freshly synthesized catalyst powder (2 mg) in a solution containing distilled water (Milli-Q, 965  $\mu L$ ) and 5 wt% Nafion solution (35  $\mu L$ ) followed by ultrasonication for 2 h. 5  $\mu L$  of catalyst ink was then deposited onto a polished Au-electrode (diameter = 5 mm, area = 0.196  $cm^2$ , Pine Research Instrumentation). All electrochemical experiments were carried out in a three-electrode glass cell with an Au-wire as the counter electrode and an Ag/AgCl as the reference electrode (Pine Research Instrumentation). The 0.1 M  $HClO_4$  electrolyte solution was prepared by diluting 70%  $HClO_4$  with

Milli-Q water. The reference electrode was calibrated in  $H_2$ -saturated 0.1 M  $HClO_4$  solution. All potentials were converted to the reversible hydrogen electrode (RHE) and corrected with iR-compensation. OER measurements were conducted in  $O_2$ -saturated 0.1 M  $HClO_4$  electrolyte with a CHI potentiostat (CHI 760D) at a rotating speed of 1600 rpm. CV analysis was performed with a scan rate of 50  $mV s^{-1}$  and the polarization curves was recorded with a sweeping rate of 5  $mV s^{-1}$ . HER measurements were conducted in  $H_2$ -saturated 0.1 M  $HClO_4$  electrolyte using a similar procedure. For overall water splitting, Co-RuIr was used as both the anode and cathode electrocatalyst in a two-electrode configuration with commercial Pt-C/ $RuO_2$  as control.

## Supporting Information

Supporting Information is available from the Wiley Online Library or from the author.

## Acknowledgements

This work was financially supported by the Australian Research Council through the Discovery Project programs (FL170100154, DP160104866, and DP170104464), the Discovery Early Career Researcher Award (DE160101163), and Natural Science Foundation of China (21576202 and 51722103). J.Q.S. was supported by the Chinese CSC Scholarship Program.

## Conflict of Interest

The authors declare no conflict of interest.

## Keywords

acidic environment, bifunctional electrocatalysis, composition-activity relationship, overall water splitting, transition metal doping

Received: January 22, 2019

Revised: January 30, 2019

Published online: February 27, 2019

- [1] M. Momirlan, T. Veziroglu, *Int. J. Hydrogen Energy* **2005**, *30*, 795.
- [2] Z. W. Seh, J. Kibsgaard, C. F. Dickens, I. Chorkendorff, J. K. Nørskov, T. F. Jaramillo, *Science* **2017**, *355*, eaad4998.
- [3] Y. Jiao, Y. Zheng, M. Jaroniec, S. Z. Qiao, *Chem. Soc. Rev.* **2015**, *44*, 2060.
- [4] T. Reier, H. N. Nong, D. Teschner, R. Schlögl, P. Strasser, *Adv. Energy Mater.* **2017**, *7*, 1601275.
- [5] B. You, N. Jiang, M. Sheng, M. W. Bhushan, Y. Sun, *ACS Catal.* **2016**, *6*, 714.
- [6] B. You, N. Jiang, M. Sheng, S. Gul, J. Yano, Y. Sun, *Chem. Mater.* **2015**, *27*, 7636.
- [7] N. Jiang, B. You, M. Sheng, Y. Sun, *Angew. Chem., Int. Ed.* **2015**, *54*, 6251.
- [8] J. Li, Y. Wang, T. Zhou, H. Zhang, X. Sun, J. Tang, L. Zhang, A. M. Al-Enizi, Z. Yang, G. Zheng, *J. Am. Chem. Soc.* **2015**, *137*, 14305.
- [9] J. Lai, S. Li, F. Wu, M. Saqib, R. Luque, G. Xu, *Energy Environ. Sci.* **2016**, *9*, 1210.
- [10] M. R. Gao, J. X. Liang, Y. R. Zheng, Y. F. Xu, J. Jiang, Q. Gao, J. Li, S. H. Yu, *Nat. Commun.* **2015**, *6*, 5982.

- [11] J. Cheng, H. Zhang, G. Chen, Y. Zhang, *Electrochim. Acta* **2009**, *54*, 6250.
- [12] K. Sardar, E. Petrucco, C. I. Hiley, J. D. Sharman, P. P. Wells, A. E. Russell, R. J. Kashtiban, J. Sloan, R. I. Walton, *Angew. Chem., Int. Ed.* **2014**, *53*, 10960.
- [13] T.-C. Wen, C.-C. Hu, *J. Electrochem. Soc.* **1992**, *139*, 2158.
- [14] S. Cherevko, S. Geiger, O. Kasian, N. Kulyk, J.-P. Grote, A. Savan, B. R. Shrestha, S. Merzlikin, B. Breitbach, A. Ludwig, K. J. J. Mayrhofer, *Catal. Today* **2016**, *262*, 170.
- [15] T. Reier, M. Oezaslan, P. Strasser, *ACS Catal.* **2012**, *2*, 1765.
- [16] J. S. Kim, B. Kim, H. Kim, K. Kang, *Adv. Energy Mater.* **2018**, *8*, 1702774.
- [17] N. B. Halck, V. Petrykin, P. Krtil, J. Rossmeisl, *Phys. Chem. Chem. Phys.* **2014**, *16*, 13682.
- [18] J. Shan, C. Guo, Y. Zhu, S. Chen, L. Song, M. Jaroniec, Y. Zheng, S.-Z. Qiao, *Chem* **2019**, *5*, 445.
- [19] F. Lv, J. Feng, K. Wang, Z. Dou, W. Zhang, J. Zhou, C. Yang, M. Luo, Y. Yang, Y. Li, P. Gao, S. Guo, *ACS Cent. Sci.* **2018**, *4*, 1244.
- [20] Q. Zhao, J. Yang, M. Liu, R. Wang, G. Zhang, H. Wang, H. Tang, C. Liu, Z. Mei, H. Chen, F. Pan, *ACS Catal.* **2018**, *8*, 5621.
- [21] B. Bayatsarmadi, Y. Zheng, Y. Tang, M. Jaroniec, S. Z. Qiao, *Small* **2016**, *12*, 3703.
- [22] V. R. Stamenkovic, B. S. Mun, M. Arenz, K. J. Mayrhofer, C. A. Lucas, G. Wang, P. N. Ross, N. M. Markovic, *Nat. Mater.* **2007**, *6*, 241.
- [23] T. Reier, Z. Pawolek, S. Cherevko, M. Bruns, T. Jones, D. Teschner, S. Selve, A. Bergmann, H. N. Nong, R. Schlogl, K. J. Mayrhofer, P. Strasser, *J. Am. Chem. Soc.* **2015**, *137*, 13031.
- [24] M. Luo, S. Guo, *Nat. Rev. Mater.* **2017**, *2*, 17059.
- [25] I. E. Stephens, A. S. Bondarenko, F. J. Perez-Alonso, F. Calle-Vallejo, L. Bech, T. P. Johansson, A. K. Jepsen, R. Frydendal, B. P. Knudsen, J. Rossmeisl, I. Chorkendorff, *J. Am. Chem. Soc.* **2011**, *133*, 5485.
- [26] F. Calle-Vallejo, M. T. Koper, A. S. Bandarenka, *Chem. Soc. Rev.* **2013**, *42*, 5210.
- [27] H. Zhu, L. Gu, D. Yu, Y. Sun, M. Wan, M. Zhang, L. Wang, L. Wang, W. Wu, J. Yao, M. Du, S. Guo, *Energy Environ. Sci.* **2017**, *10*, 321.
- [28] J. Feng, F. Lv, W. Zhang, P. Li, K. Wang, C. Yang, B. Wang, Y. Yang, J. Zhou, F. Lin, G. C. Wang, S. Guo, *Adv. Mater.* **2017**, *29*, 1703798.
- [29] V. Fung, F. F. Tao, D. E. Jiang, *J. Phys. Chem. Lett.* **2017**, *8*, 2206.
- [30] F. Calle-Vallejo, M. D. Pohl, D. Reinisch, D. Loffreda, P. Sautet, A. S. Bandarenka, *Chem. Sci.* **2017**, *8*, 2283.
- [31] T. Ling, D. Y. Yan, H. Wang, Y. Jiao, Z. Hu, Y. Zheng, L. Zheng, J. Mao, H. Liu, X. W. Du, M. Jaroniec, S. Z. Qiao, *Nat. Commun.* **2017**, *8*, 1509.
- [32] Y. Jiao, Y. Zheng, P. Chen, M. Jaroniec, S. Z. Qiao, *J. Am. Chem. Soc.* **2017**, *139*, 18093.
- [33] C. Massue, V. Pfeifer, M. van Gastel, J. Noack, G. Algara-Siller, S. Cap, R. Schlogl, *ChemSusChem* **2017**, *10*, 4786.
- [34] V. Pfeifer, T. E. Jones, J. J. Velasco Velez, C. Massue, M. T. Greiner, R. Arrigo, D. Teschner, F. Girgsdies, M. Scherzer, J. Allan, M. Hashagen, G. Weinberg, S. Piccinin, M. Havecker, A. Knop-Gericke, R. Schlogl, *Phys. Chem. Chem. Phys.* **2016**, *18*, 2292.
- [35] N. Roy, Y. Sohn, K. T. Leung, D. Pradhan, *J. Phys. Chem. C* **2014**, *118*, 29499.
- [36] S. Alayoglu, A. U. Nilekar, M. Mavrikakis, B. Eichhorn, *Nat. Mater.* **2008**, *7*, 333.

# ADVANCED MATERIALS

## Supporting Information

for *Adv. Mater.*, DOI: 10.1002/adma.201900510

Transition-Metal-Doped RuIr Bifunctional Nanocrystals for  
Overall Water Splitting in Acidic Environments

*Jieqiong Shan, Tao Ling, Kenneth Davey, Yao Zheng,\* and  
Shi-Zhang Qiao\**

## Supporting Information

### Transition Metal Doped RuIr Bifunctional Nanocrystals for Overall Water Splitting in Acidic Environments

Jieqiong Shan, Tao Ling, Kenneth Davey, Yao Zheng,\* and Shi-Zhang Qiao\*

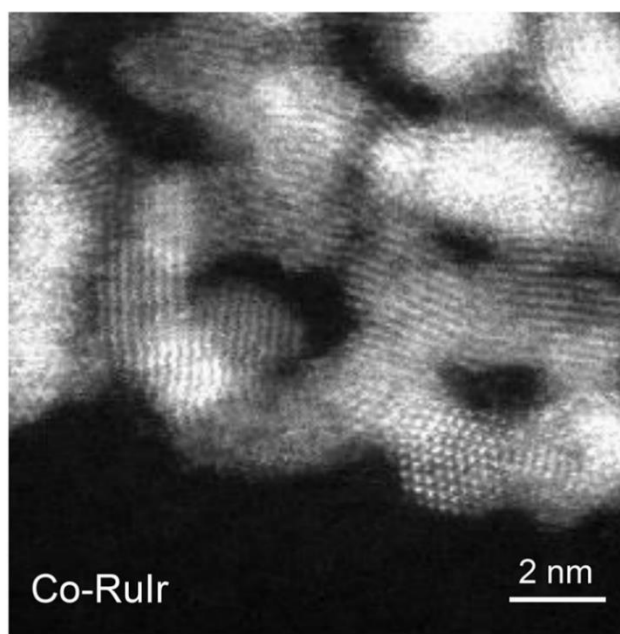


**Figure S1.** HAADF-STEM image of Co-RuIr nanocrystals.

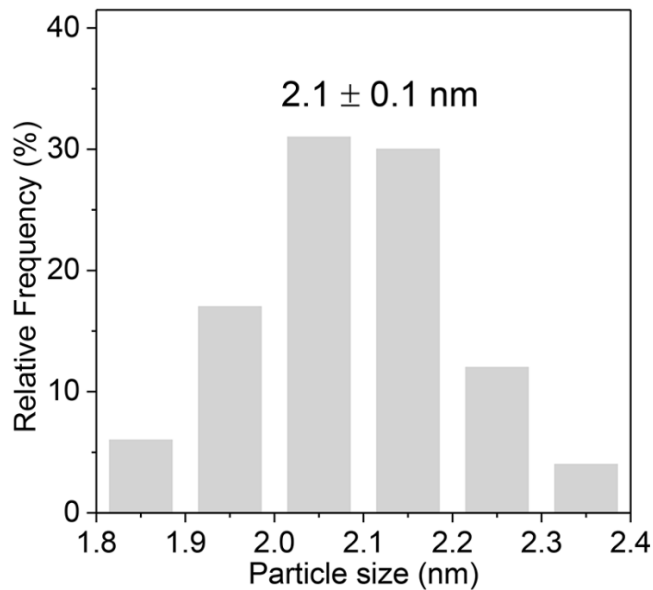


**Figure S2.** Particle size histogram for Co-RuIr nanocrystals (analyzed from Figure 1a).

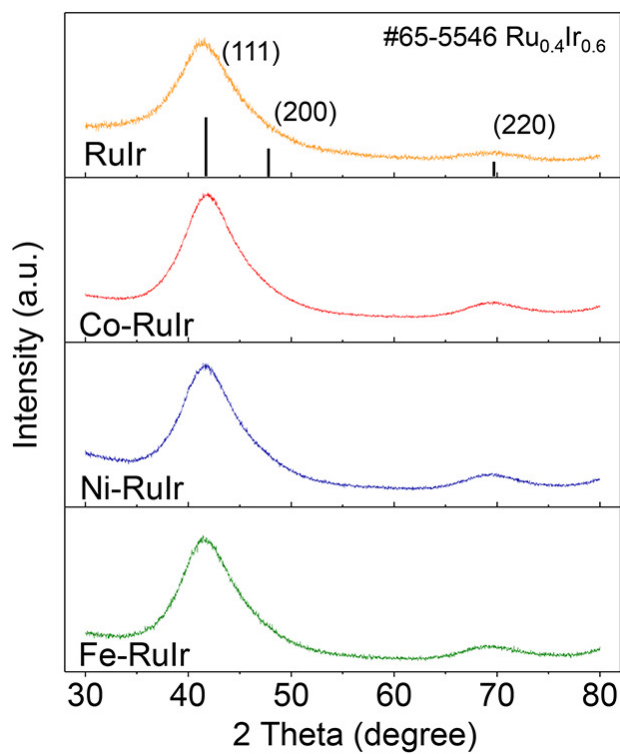


**Figure S3.** XRD patterns for RuIr, Co-RuIr, Ni-RuIr and Fe-RuIr nanocrystals, all of which resemble the diffraction peaks of Ru<sub>0.4</sub>Ir<sub>0.6</sub> (JCPDS #65-5546).

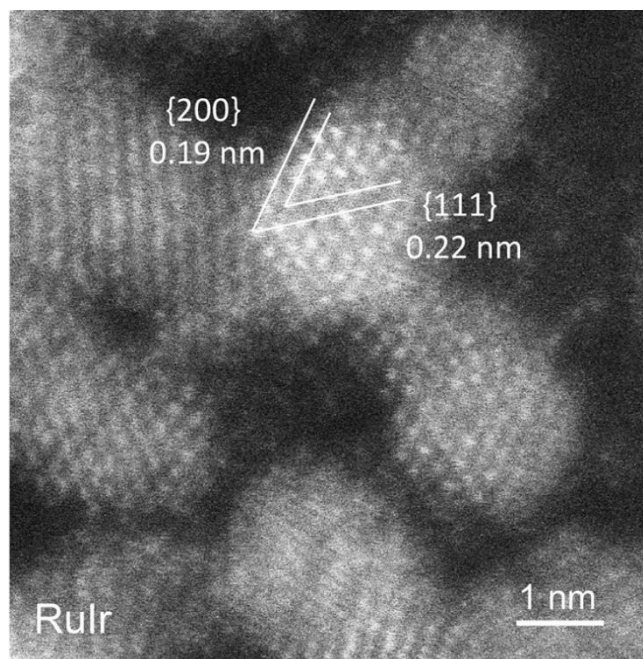


**Figure S4.** HAADF-STEM image of RuIr nanocrystals.

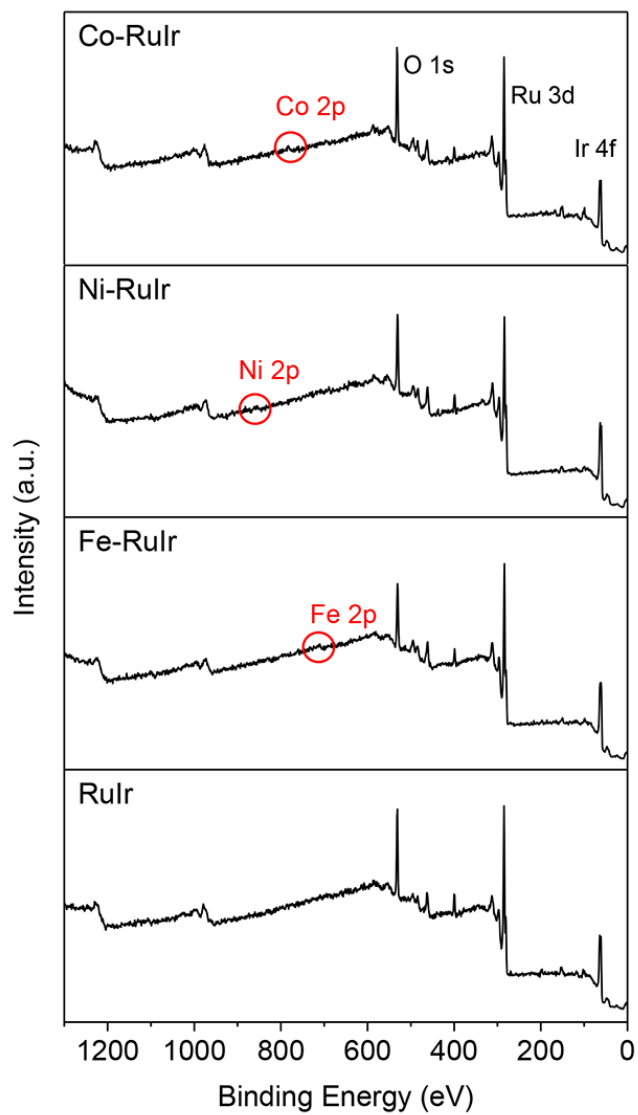


**Figure S5.** XPS survey spectra for Co-RuIr, Ni-RuIr, Fe-RuIr and RuIr nanocrystals.

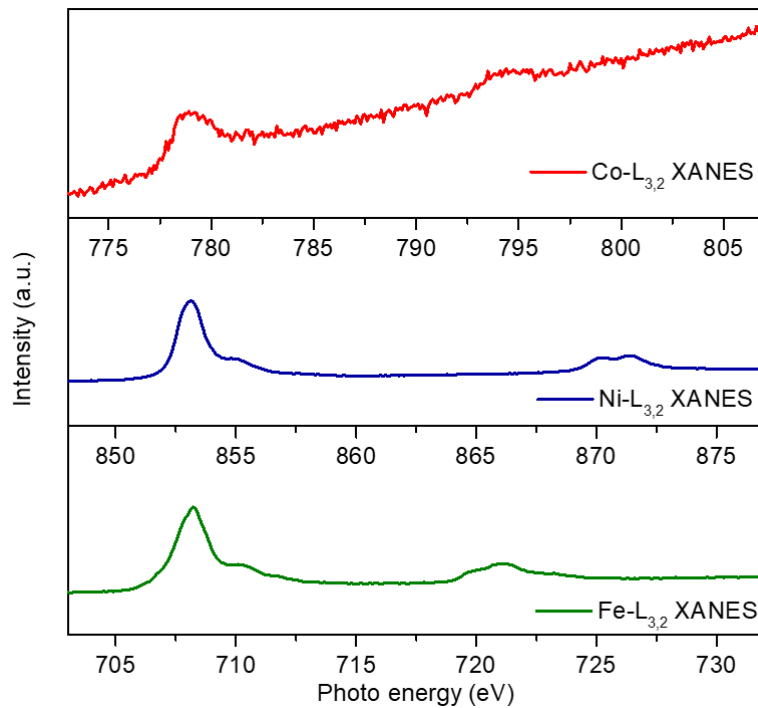


**Figure S6.**  $L_{3,2}$ -edge XANES for Co, Ni and Fe in Co-RuIr, Ni-RuIr and Fe-RuIr nanocrystals.

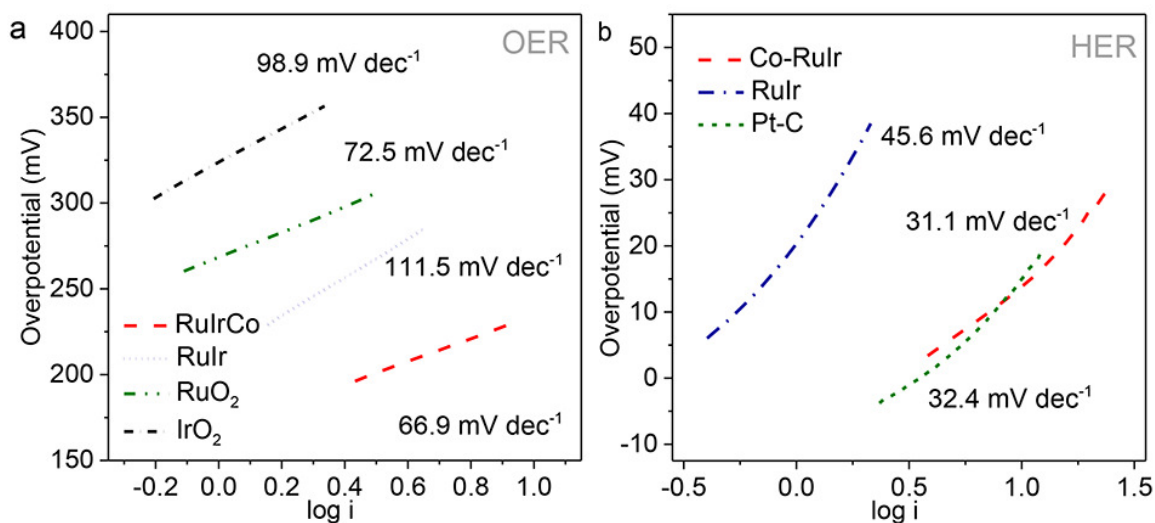


**Figure S7.** Tafel plots for Co-RuIr, RuIr and commercial catalysts under (a) OER and (b) HER processes.



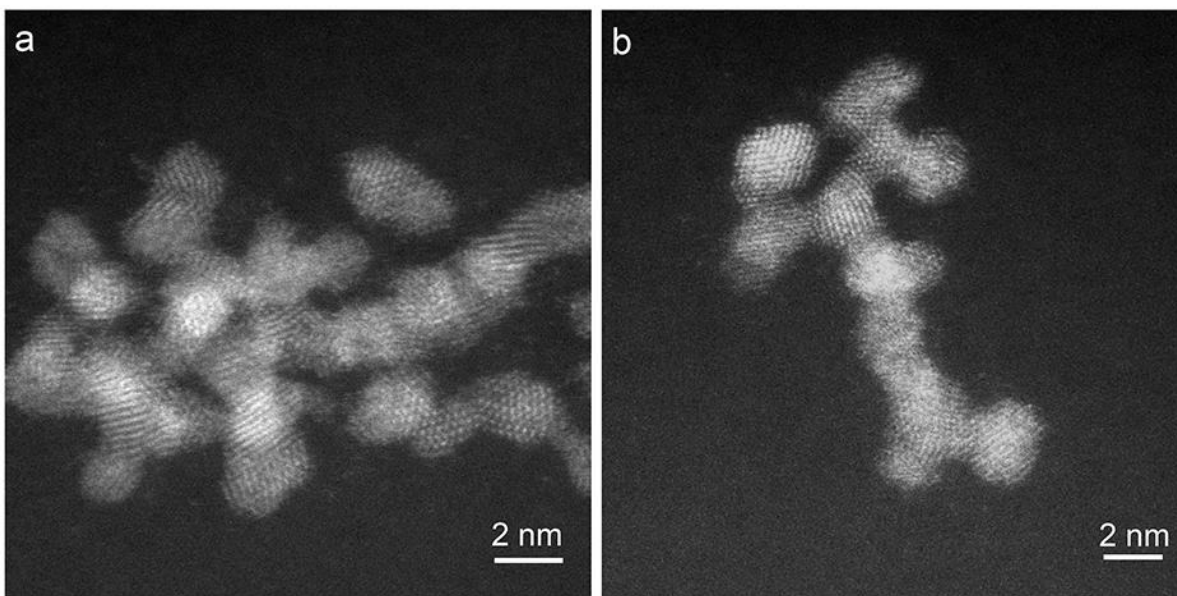


**Figure S8.** HAADF-STEM images of Co-RuIr nanocrystals after OER tests.

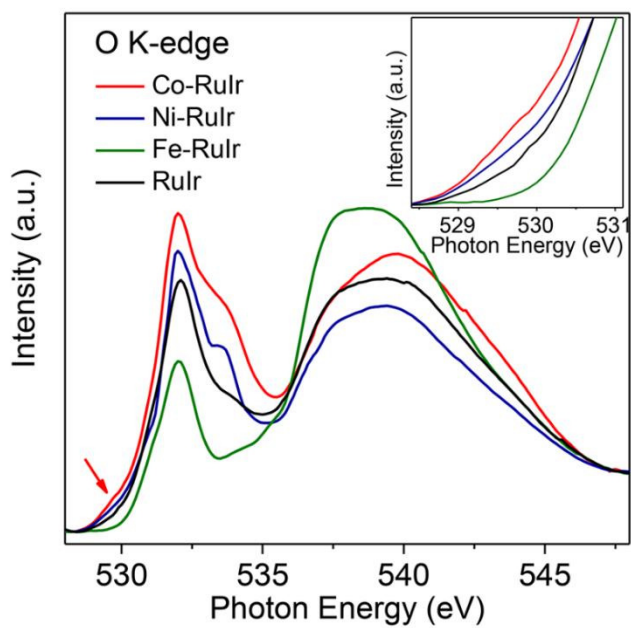


**Figure S9.** O K-edge XANES spectra for Co-RuIr, Ni-RuIr, Fe-RuIr and RuIr catalysts after OER. Inset shows enlarged spectra with photon energy from 528.4 to 531.1 eV.

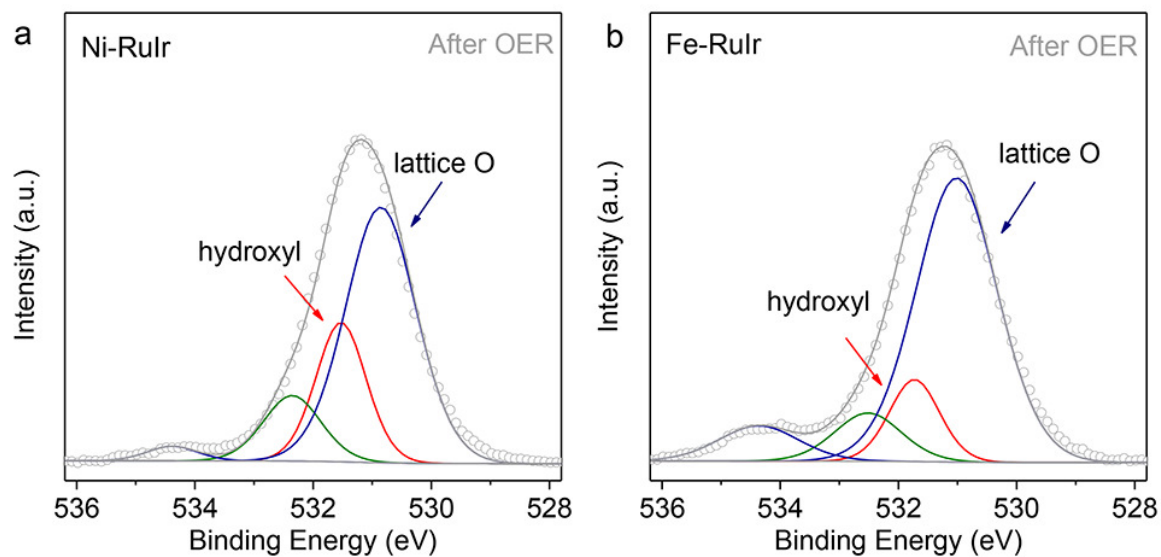


**Figure S10.** O 1s XPS spectra for (a) Ni-RuIr and (b) Fe-RuIr electrocatalysts after OER tests.

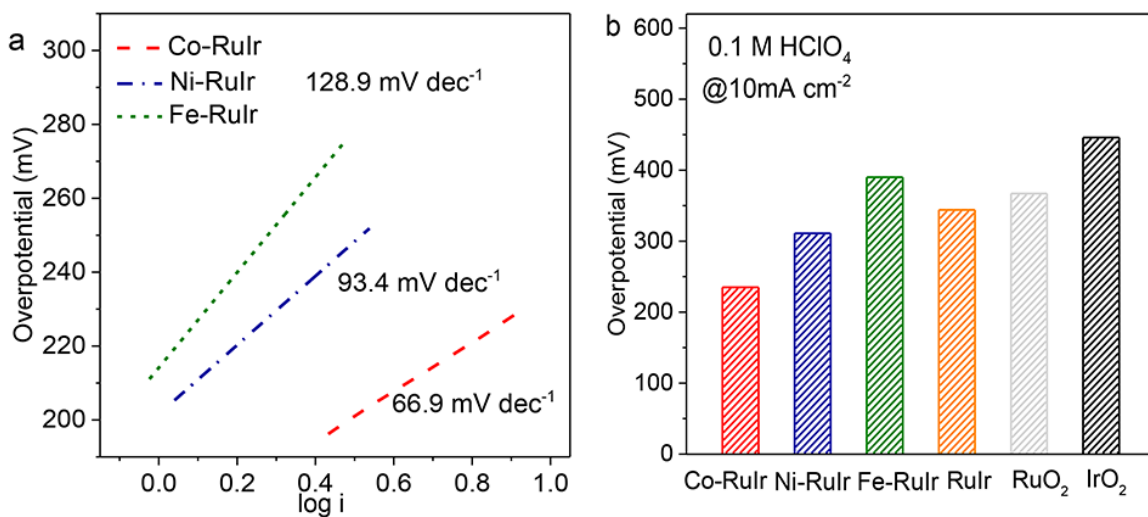


**Figure S11.** (a) Tafel plots of M-RuIr (M=Co, Ni, Fe) catalysts in OER; (b) Overpotentials for M-RuIr (M=Co, Ni, Fe), RuIr and RuO<sub>2</sub> catalysts to reach a current density of 10 mA cm<sup>-2</sup> in OER.

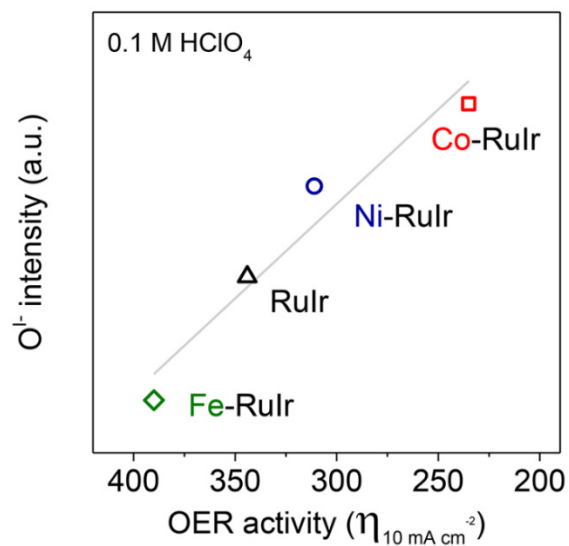


**Figure S12.** Relationship between O<sup>-</sup> species intensity and OER activity (represented by overpotential at current density of 10 mA cm<sup>-2</sup>) for M-RuIr and RuIr catalysts.

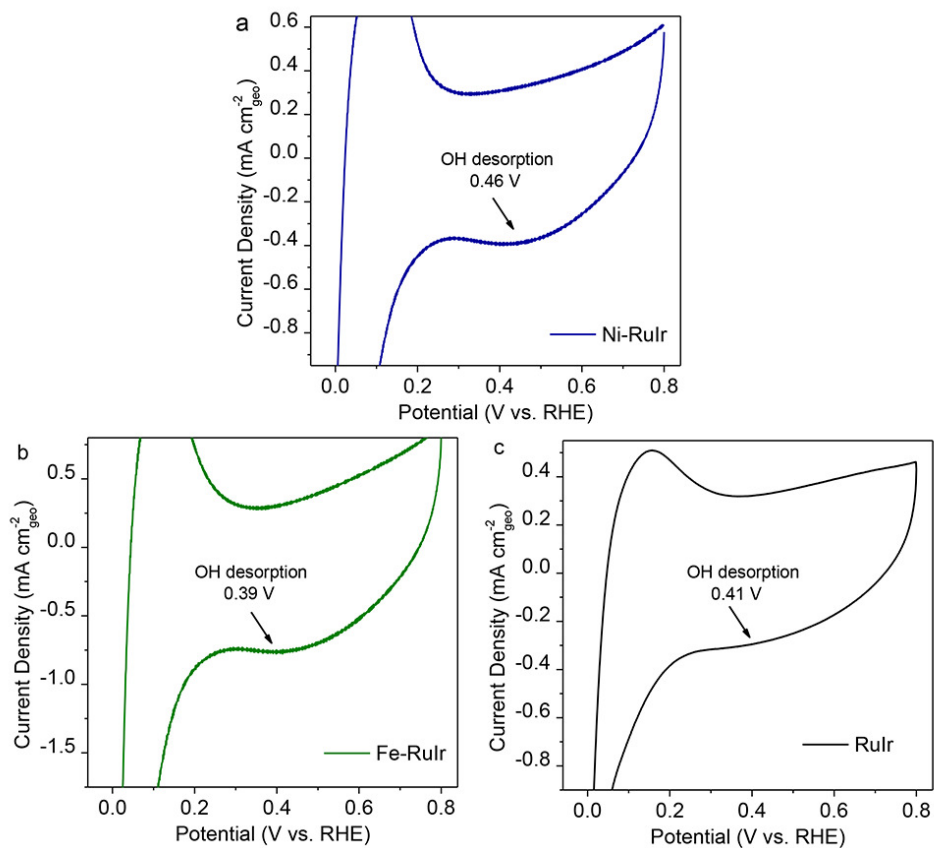


**Figure S13.** OH<sup>-</sup> desorption behavior of (a) Ni-RuIr, (b) Fe-RuIr and (c) RuIr catalysts with scan rates of 50 mV s<sup>-1</sup>.

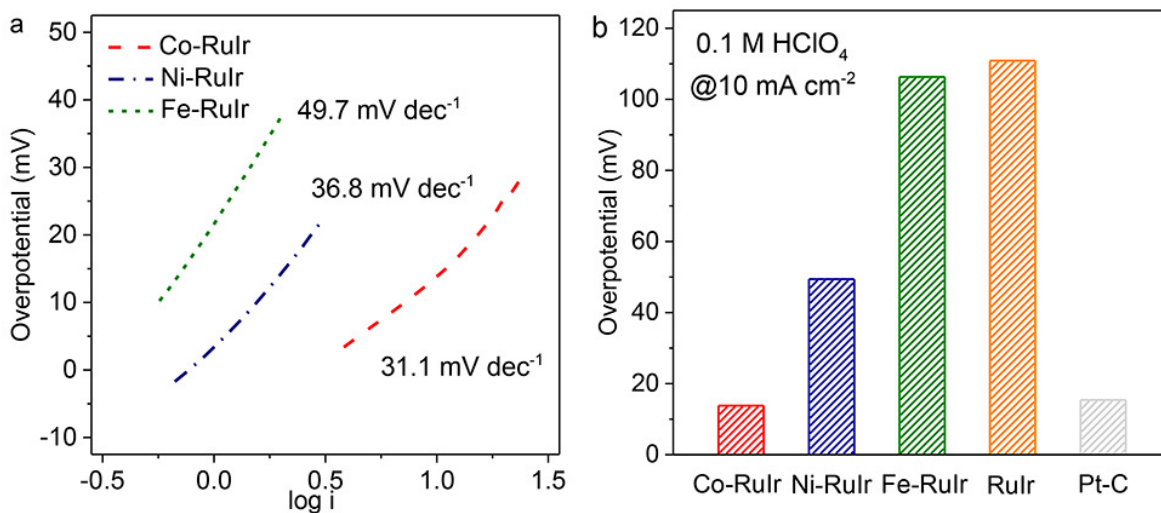


**Figure S14.** (a) XPS spectra of Ru 3d for Ni-RuIr and Fe-RuIr catalysts before and after HER; (b) XPS spectra of Ir 4f for Ni-RuIr and Fe-RuIr catalysts before and after HER.

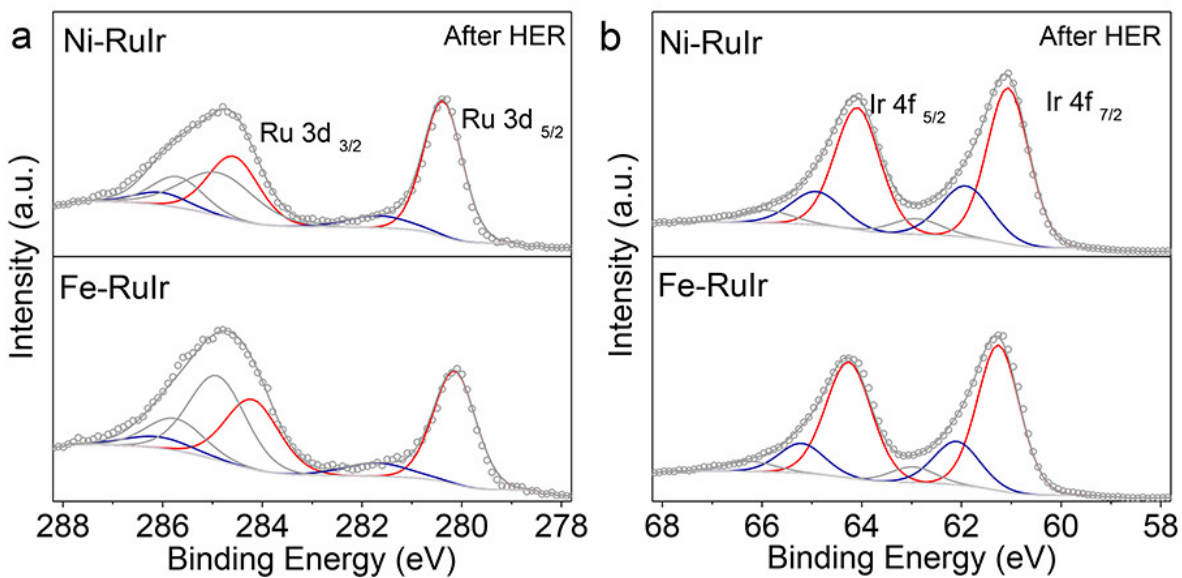


**Figure S15.** (a) Ru 3d and (b) Ir 4f XPS spectra for Ni-RuIr and Fe-RuIr electrocatalysts after HER tests.

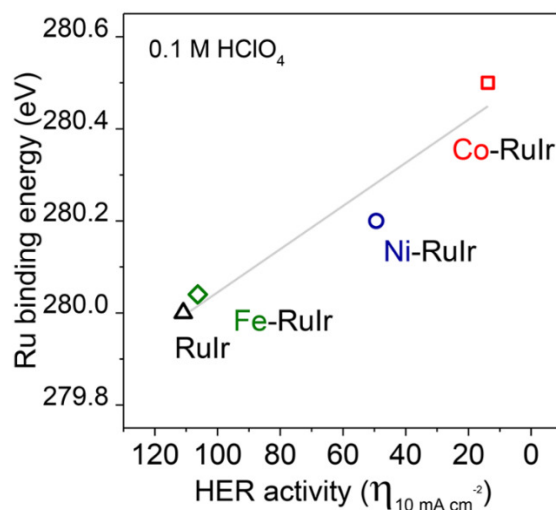


**Figure S16.** Relationship between Ru binding energy and HER activity (represented by overpotential at current density of 10 mA cm<sup>-2</sup>) for M-RuIr and RuIr catalysts.

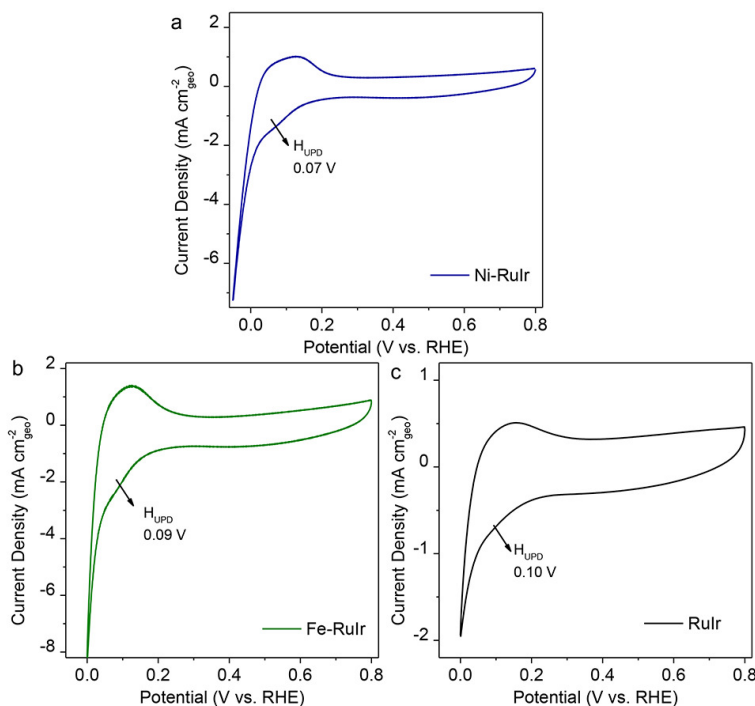


**Figure S17.** H<sub>UPD</sub> behavior of (a) Ni-RuIr, (b) Fe-RuIr and (c) RuIr catalysts with scan rate of 50 mV s<sup>-1</sup>.

**Table S1.** Comparison of performance of bifunctional electrocatalysts for overall water splitting in acidic environments

Samples	Electrolytes	HER $\eta^a$ (mV)	HER work life	OER $\eta^b$ (mV)	OER work life	Overall water splitting cell voltage <sup>c</sup> (V)	Overall water splitting work life	Ref
<b>Co- RuIr</b>	0.1 M HClO <sub>4</sub>	13.8	25 hr	235	25 hr	1.52	25 hr	This work
<b>Rh<sub>2</sub>P</b>	0.5 M H <sub>2</sub> SO <sub>4</sub>	$\eta_5 =$ 5.4	2000 s	510	1000 s	N.A.	N.A.	[1]
<b>IrW</b>	0.1 M HClO <sub>4</sub>	12	N.A.	$\eta_{8.1} =$ 300	N.A.	$E_{10\ 0.5M\ H_2SO_4, on}$ CFP = 1.48	8 hr	[2]
<b>N-WC</b>	0.5 M H <sub>2</sub> SO <sub>4</sub>	113	20 hr	$\eta_{60} =$ 470	60 min	$E_{onset} = 1.4$	N.A.	[3]
<b>IrCoNi</b>	0.1 M HClO <sub>4</sub>	33	N.A.	303	200 min	$E_{10\ 0.5M\ H_2SO_4} =$ 1.65	1000 cycles	[4]
<b>N, P-C</b>	0.5 M H <sub>2</sub> SO <sub>4</sub>	N.A.	N.A.	470	10 hr	N.A.	N.A.	[5]
<b>IrNi</b>	0.1 M HClO <sub>4</sub>	$\eta_{20} =$ 19	60 min	$\eta_{9.1} =$ 270	120 min	1.58	600 min	[6]
<b>Ir/GF</b>	0.5 M H <sub>2</sub> SO <sub>4</sub>	7	10 hr	290	10 hr	1.55	10 hr	[7]
<b>IrNiFe</b>	0.5 M HClO <sub>4</sub>	24	20 000 s	284	20 000 s	1.64	20 000 s	[8]
<b>Co- MoS<sub>2</sub></b>	0.5 M H <sub>2</sub> SO <sub>4</sub>	60	40 000 s	540	40 000 s	1.9	N.A.	[9]

<b>Ir NW</b>	0.1 M HClO <sub>4</sub>	11.3	25 000 s	283	25 000 s	1.62	40 000 s	[10]
<b>Ir NP</b>	0.5 M HClO <sub>4</sub>	17	20 000 s	290	20 000 s	1.59	20 000 s	[11]

a: Unless otherwise specified,  $\eta$  refers to overpotentials required to reach current density of 10 mA cm<sup>-2</sup> in HER; b: Unless otherwise specified,  $\eta$  refers to overpotentials required to reach current density of 10 mA cm<sup>-2</sup> in OER; c: Unless otherwise specified, E refers to cell voltages required to reach current density of 10 mA cm<sup>-2</sup> in overall water splitting.

### Supplemental References:

- [1] H. Duan, D. Li, Y. Tang, Y. He, S. Ji, R. Wang, H. Lv, P. P. Lopes, A. P. Paulikas, H. Li, S. X. Mao, C. Wang, N. M. Markovic, J. Li, V. R. Stamenkovic, Y. Li, *J. Am. Chem. Soc.* **2017**, 139, 5494.
- [2] F. Lv, J. Feng, K. Wang, Z. Dou, W. Zhang, J. Zhou, C. Yang, M. Luo, Y. Yang, Y. Li, P. Gao, S. Guo, *ACS Central Sci.* **2018**, 4, 1244.
- [3] N. Han, K. R. Yang, Z. Lu, Y. Li, W. Xu, T. Gao, Z. Cai, Y. Zhang, V. S. Batista, W. Liu, X. Sun, *Nat. Commun.* **2018**, 9, 924.
- [4] J. Feng, F. Lv, W. Zhang, P. Li, K. Wang, C. Yang, B. Wang, Y. Yang, J. Zhou, F. Lin, G. C. Wang, S. Guo, *Adv. Mater.* **2017**, 29, 1703798.
- [5] J. Lai, S. Li, F. Wu, M. Saqib, R. Luque, G. Xu, *Energy Environ. Sci.* **2016**, 9, 1210.
- [6] Y. Pi, Q. Shao, P. Wang, J. Guo, X. Huang, *Adv. Funct. Mater.* **2017**, 27, 1700886.
- [7] J. Zhang, G. Wang, Z. Liao, P. Zhang, F. Wang, X. Zhuang, E. Zschech, X. Feng, *Nano Energy* **2017**, 40, 27.
- [8] L. Fu, G. Cheng, W. Luo, *J. Mater. Chem. A* **2017**, 5, 24836.
- [9] Q. Xiong, X. Zhang, H. Wang, G. Liu, G. Wang, H. Zhang, H. Zhao, *Chem. Commun.* **2018**, 54, 3859.
- [10] L. Fu, F. Yang, G. Cheng, W. Luo, *Nanoscale* **2018**, 10, 1892.
- [11] L. Fu, X. Zeng, C. Huang, P. Cai, G. Cheng, W. Luo, *Inorg. Chem. Front.* **2018**, 5, 1121.

## Chapter 5 Short-Range Ordered Iridium Single Atoms Integrated into Cobalt Oxide

### Spinel Structure for Highly Efficient Electrocatalytic Water Oxidation

#### 5.1. Introduction and Significance

Noble metals, with unique electronic structures and irreplaceable catalytic activities for a wide range of applications, are restricted by the limited choices of packing variants and geometric structures spanning single atoms, clusters, nanoparticles and bulk crystals. Here, we propose a simple and general strategy to overcome this limitation by allocating noble metal atoms within the lattice of transition metal oxides. Various kinds of noble metal atoms (e.g. Ir, Pt, Pd, Au, Ru) have been atomically accommodated into the cationic sites of oxides (e.g.  $\text{Co}_3\text{O}_4$ ,  $\text{Mn}_5\text{O}_8$ , NiO) with an identical spatial correlation with the host lattice. The correlated substitution creates noble metal analogues with artificial topologies and bridges the gap between single atoms with no spatial correlation and close-packed structures with inherently restricted interatomic distances.

Taking Ir-substituted  $\text{Co}_3\text{O}_4$  ( $\text{Ir}_{0.06}\text{Co}_{2.94}\text{O}_4$ ) as an example, the parent transition metal oxide can be catalytically activated and stabilized upon correlated substitution of Ir atoms, towards challenging OER electrocatalysis in acidic environments. This chapter shows that the as-synthesized  $\text{Ir}_{0.06}\text{Co}_{2.94}\text{O}_4$  exhibits a noble-metal-like catalytic performance towards acidic OER. The activity is not only unprecedented for transition metal oxides but among the best noble-metal-based catalysts (e.g. outperforms that of commercial  $\text{IrO}_2$  catalyst by over two orders of magnitude).



By successfully extending the strategy to diverse transition metal oxide systems, our work holds a great promise for the diversification of noble metal analogues and for the activation/stabilization of transition metal oxides for extensive applications.

## **5.2. Short-Range Ordered Iridium Single Atoms Integrated into Cobalt Oxide Spinel Structure for Highly Efficient Electrocatalytic Water Oxidation**

This section is included as a journal paper by Jieqiong Shan, Chao Ye, Shuangming Chen, Tulai Sun, Yan Jiao, Lingmei Liu, Chongzhi Zhu, Li Song, Yu Han, Mietek Jaroniec, Yihan Zhu, Yao Zheng and Shi-Zhang Qiao, Short-Range Ordered Iridium Single Atoms Integrated into Cobalt Oxide Spinel Structure for Highly Efficient Electrocatalytic Water Oxidation. *J. Am. Chem. Soc.*, 143, DOI: 10.1021/jacs.1c01525.

# Statement of Authorship

Title of Paper	Short-Range Ordered Iridium Single Atoms Integrated into Cobalt Oxide Spinel Structure for Highly Efficient Electrocatalytic Water Oxidation
Publication Status	<input checked="" type="checkbox"/> Published <input type="checkbox"/> Accepted for Publication <input type="checkbox"/> Submitted for Publication <input type="checkbox"/> Unpublished and Unsubmitted work written in manuscript style
Publication Details	Shan, J., Ye, C., Chen, S., Sun, T., Jiao, Y., Liu, L., Zhu, C., Song, L., Han, Y., Jaroniec, M., Zhu, Y., Zheng, Y., Qiao, S.Z. (2021). Short-Range Ordered Iridium Single Atoms Integrated into Cobalt Oxide Spinel Structure for Highly Efficient Electrocatalytic Water Oxidation. <i>Journal of the American Chemical Society</i> , 143, DOI: 10.1021/jacs.1c01525.

## Principal Author

Name of Principal Author (Candidate)	Jieqiong Shan			
Contribution to the Paper	Jieqiong Shan synthesized the materials, conducted physical characterizations and electrocatalytic experiments and wrote the paper.			
Overall percentage (%)	60%			
Certification:	This paper reports on original research I conducted during the period of my Higher Degree by Research candidature and is not subject to any obligations or contractual agreements with a third party that would constrain its inclusion in this thesis. I am the primary author of this paper.			
Signature	<table border="1" style="width: 100%;"> <tr> <td style="width: 60%;"></td> <td style="width: 20%;">Date</td> <td style="width: 20%;">20 Jan 2021</td> </tr> </table>		Date	20 Jan 2021
	Date	20 Jan 2021		

## Co-Author Contributions

By signing the Statement of Authorship, each author certifies that:

- i. the candidate's stated contribution to the publication is accurate (as detailed above);
- ii. permission is granted for the candidate to include the publication in the thesis; and
- iii. the sum of all co-author contributions is equal to 100% less the candidate's stated contribution.

Name of Co-Author	Chao Ye			
Contribution to the Paper	Dr. Chao Ye conducted the theoretical calculations and contributed to writing the paper.			
Signature	<table border="1" style="width: 100%;"> <tr> <td style="width: 60%;"></td> <td style="width: 20%;">Date</td> <td style="width: 20%;">20 Jan 2021</td> </tr> </table>		Date	20 Jan 2021
	Date	20 Jan 2021		

Name of Co-Author	Shuangming Chen			
Contribution to the Paper	Prof. Shuangming Chen conducted the XAS characterization.			
Signature	<table border="1" style="width: 100%;"> <tr> <td style="width: 60%;"></td> <td style="width: 20%;">Date</td> <td style="width: 20%;">20 Jan 2021</td> </tr> </table>		Date	20 Jan 2021
	Date	20 Jan 2021		

Name of Co-Author	Tulai Sun		
Contribution to the Paper	Dr. Tulai Sun conducted the HRSTEM imaging.		
Signature		Date	20 Jan 2021

Name of Co-Author	Yan Jiao		
Contribution to the Paper	Dr. Yan Jiao conducted the theoretical calculations and revised the paper.		
Signature		Date	21 Jan 2021

Name of Co-Author	Lingmei Liu		
Contribution to the Paper	Dr. Lingmei Liu conducted the HRSTEM imaging.		
Signature		Date	20 Jan 2021

Name of Co-Author	Chongzhi Zhu		
Contribution to the Paper	Chongzhi Zhu analyzed the HRSTEM data.		
Signature		Date	20 Jan 2021

Name of Co-Author	Li Song		
Contribution to the Paper	Prof. Li Song conducted the XAS characterization.		
Signature		Date	21 Jan 2021

Name of Co-Author	Yu Han		
-------------------	--------	--	--

Contribution to the Paper	Prof. Yu Han conducted the HRSTEM imaging.		
Signature		Date	21 Jan 2021

Name of Co-Author	Mietek Jaroniec		
Contribution to the Paper	Prof. Mietek Jaroniec contributed to this work in an advisory capacity and revised the paper.		
Signature		Date	20 Jan 2021

Name of Co-Author	Yihan Zhu		
Contribution to the Paper	Prof. Yihan Zhu conducted the HAADF-STEM analysis, conceived the concept and contributed to writing the paper.		
Signature		Date	20 Jan 2021

Name of Co-Author	Yao Zheng		
Contribution to the Paper	Dr. Yao Zheng conceived the concept and contributed to writing the paper.		
Signature		Date	20 Jan 2021

Name of Co-Author	Shi-Zhang Qiao		
Contribution to the Paper	Prof. Shi-Zhang Qiao conceived the concept and revised the paper.		
Signature		Date	21 Jan 2021

# Short-Range Ordered Iridium Single Atoms Integrated into Cobalt Oxide Spinel Structure for Highly Efficient Electrocatalytic Water Oxidation

Jieqiong Shan, Chao Ye, Shuangming Chen, Tulai Sun, Yan Jiao, Lingmei Liu, Chongzhi Zhu, Li Song, Yu Han, Mietek Jaroniec, Yihan Zhu,\* Yao Zheng,\* and Shi-Zhang Qiao\*

Cite This: <https://doi.org/10.1021/jacs.1c01525>

Read Online

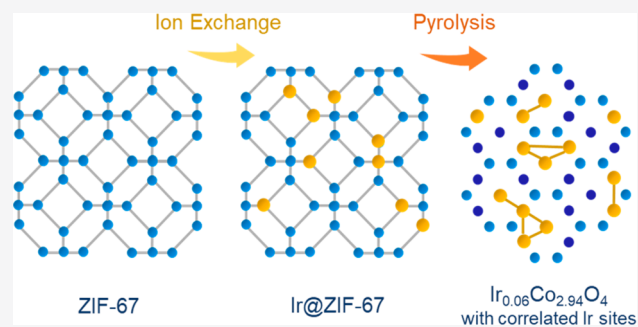
ACCESS |

Metrics & More

Article Recommendations

Supporting Information

**ABSTRACT:** Noble metals manifest themselves with unique electronic structures and irreplaceable activity toward a wide range of catalytic applications but are unfortunately restricted by limited choice of geometric structures spanning single atoms, clusters, nanoparticles, and bulk crystals. Herein, we propose how to overcome this limitation by integrating noble metal atoms into the lattice of transition metal oxides to create a new type of hybrid structure. This study shows that iridium single atoms can be accommodated into the cationic sites of cobalt spinel oxide with short-range order and an identical spatial correlation as the host lattice. The resultant  $\text{Ir}_{0.06}\text{Co}_{2.94}\text{O}_4$  catalyst exhibits much higher electrocatalytic activity than the parent oxide by 2 orders of magnitude toward the challenging oxygen evolution reaction under acidic conditions. Because of the strong interaction between iridium and cobalt oxide support, the  $\text{Ir}_{0.06}\text{Co}_{2.94}\text{O}_4$  catalyst shows significantly improved corrosion resistance under acidic conditions and oxidative potentials. This work eliminates the “close-packing” limitation of noble metals and offers promising opportunity to create analogues with desired topologies for various catalytic applications.



## INTRODUCTION

Noble metals, elements with extremely low abundance in the earth and unique catalytic properties toward many processes,<sup>1,2</sup> are located at a lower corner of the periodic table. The “nobleness” and “reactivity” of these elements are essentially determined by their electronic structure, namely, an appropriate level of orbital hybridization essential for molecular adsorption and the degree of antibonding filling.<sup>3</sup> As a consequence, the center of gravity ( $\epsilon_d$ ) for d-bands of the metal catalysts has been widely used to qualitatively evaluate the adsorption energy, activation energy, and desorption energy of reactive intermediate(s) in many reactions.<sup>4,5</sup> Clearly, the  $\epsilon_d$  value is straightforwardly determined by arrangement of atoms in noble metals, namely, by their geometric structure including size and packing.<sup>6</sup> For example, bulk Au is generally inert while the nanometer-sized Au becomes catalytically active.<sup>7</sup> This effect is even more pronounced for the Au cluster with a “magic number” of 55, which exhibits an extraordinary activity for selective oxidation.<sup>8</sup> Similarly, a cubic close-packed Ru nanostructure outperforms a hexagonal one in the electrocatalytic hydrogen evolution reaction because of its proper value of  $\epsilon_d$  and, consequently, favorable adsorption energies of the key reaction intermediates.<sup>9</sup> However, almost all currently available physical forms of noble metals in clusters, nanoparticles and bulk crystals are

inherently restricted by their interatomic distances due to the strong chemical bonding.<sup>10,11</sup> Accordingly, the modulation of their atomic spatial correlation and coordination chemistry, i.e., arrangement of the nearest and second-nearest neighbors in a controllable manner, is significantly restricted. Single atoms do not show such restriction that inherently exists in nanoparticles and bulk crystals, but they suffer from random and uncontrollable spatial distribution as well as the lack of collective effects among active sites. Therefore, a full engineering of atomic spatial correlation including both interatomic distance and coordination geometry for noble metals would largely diversify their topologies beneficial for a wider range of applications.

Diversification of noble metal structures is essential for the design of renewable energy systems able to convert electricity into chemical energy.<sup>12</sup> Taking the acidic oxygen evolution reaction (OER) as an example, which is the key component of proton exchange membrane electrolyzers, noble Ir, Ru, and

Received: February 8, 2021

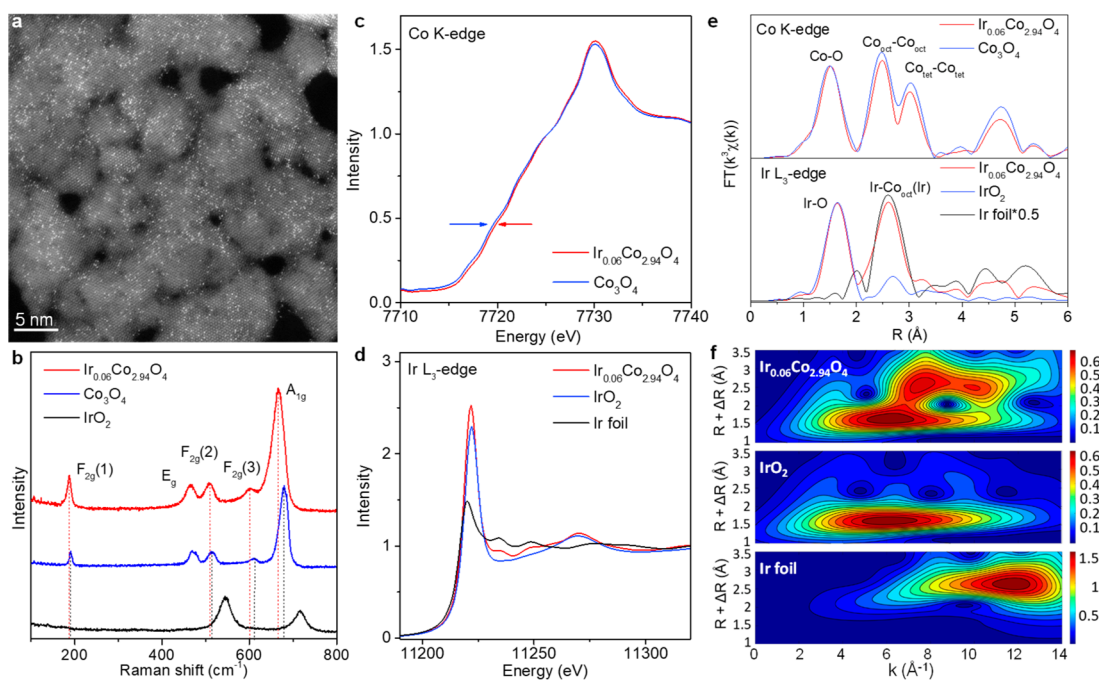


**Figure 1.** Local geometric structure determination of fresh  $\text{Ir}_{0.06}\text{Co}_{2.94}\text{O}_4$  catalyst. (a) HAADF-HRSTEM image of  $\text{Ir}_{0.06}\text{Co}_{2.94}\text{O}_4$  collected on randomly chosen domain. (b) Raman spectra of  $\text{Ir}_{0.06}\text{Co}_{2.94}\text{O}_4$  and  $\text{Co}_3\text{O}_4$ . The  $A_{1g}$  and  $F_{2g}(1)$  Raman bands of  $\text{Co}_3\text{O}_4$  at  $\sim 680$  and  $\sim 190$   $\text{cm}^{-1}$  can be assigned to Co–O stretching vibrations in octahedral units ( $\text{CoO}_6$ ) and tetrahedral units ( $\text{CoO}_4$ ), respectively. (c) Co K-edge XANES spectra of  $\text{Ir}_{0.06}\text{Co}_{2.94}\text{O}_4$  and  $\text{Co}_3\text{O}_4$ . (d) Ir  $L_{3}$ -edge XANES spectra of  $\text{Ir}_{0.06}\text{Co}_{2.94}\text{O}_4$ ,  $\text{IrO}_2$  and Ir foil. (e) FT-EXAFS spectra at the Co K-edge and Ir  $L_{3}$ -edge of  $\text{Ir}_{0.06}\text{Co}_{2.94}\text{O}_4$  and reference samples. (f) Ir  $L_{3}$ -edge WT-EXAFS of  $\text{Ir}_{0.06}\text{Co}_{2.94}\text{O}_4$  and reference samples.

their derivatives are still the best candidates because of their appropriate electronic structures and high resistance against the oxidative potentials.<sup>13,14</sup> Benefiting from the flexible composition and tunable filling of d-orbitals, the earth-abundant transition metal oxides (TMOs) like rutile, perovskite, and spinel structures are well suited to replace noble metal OER electrocatalysts under alkaline conditions.<sup>15–17</sup> In acidic electrolytes, some pioneering works have reported the surface reconstruction and formation of iridium oxides on perovskite-based hybrid catalysts due to the partial leaching of metal species.<sup>18,19</sup> However, the major challenge of enhancing the activity and long-term stability of TMO catalyst systems still exists.<sup>20,21</sup> A promising strategy toward the rational design of ideal acidic OER electrocatalysts is the correlated substitution at transition metal sites by noble metal atoms with desired coordination geometry, which simultaneously maximizes their utilization and enables a full tunability of the atomic spatial correlation. Nevertheless, because of the large lattice discrepancy between noble metals and the TMO host, it is a great challenge to directly substitute noble metal atoms into the TMO frameworks instead of being physically deposited onto the surfaces.<sup>22,23</sup>

Herein, we report the successful allocation of Ir into cationic sublattice of TMO structures (e.g., spinel cobalt oxide) via an ion exchange–pyrolysis procedure mediated by metal–organic frameworks. An identical spatial correlation between noble metal substitution sites and TMO host lattice is unambiguously observed, and these noble metal single atoms show a short-range order. The resultant Ir-substituted  $\text{Ir}_{0.06}\text{Co}_{2.94}\text{O}_4$  electrocatalyst exhibits distinct properties from the conventional surface supported single-atom catalysts or bulk metals. It shows an extremely high mass activity together with a significantly improved corrosion resistance for acidic OER and even outperforms most noble metal catalysts.<sup>24</sup> The

essential catalytic effects of correlated Ir substitutions are twofold: a downshifted d-band center of Co sites together with a band gap Ir-5d state is responsible for the boosted activity, while a deepened valence band maximum accounts for the enhanced oxidation resistance, resulting in better durability of the catalyst.

## RESULTS AND DISCUSSION

**Local Geometric Structure.** The properly controlled ion exchange–pyrolysis of the Co-based zeolitic imidazolate framework (ZIF-67) with incorporated Ir ions into the structure ensures an identical spatial correlation between the dopant and the cationic sublattice of the host.<sup>25,26</sup> The doping amount of Ir in a  $\text{Co}_3\text{O}_4$  host, determined by an inductively coupled plasma mass spectrometry (ICP-MS), was 4.93 wt % (equaling to 0.916 atom %), and thus the chemical formula of the resultant hybrid is  $\text{Ir}_{0.06}\text{Co}_{2.94}\text{O}_4$ . The high-angle annular dark-field high-resolution scanning transmission electron microscopy (HAADF-HRSTEM) image of  $\text{Ir}_{0.06}\text{Co}_{2.94}\text{O}_4$  shows a typical single-atom catalyst by revealing the atomically distributed Ir atoms with brighter contrast clearly identified from the crystal lattice of  $\text{Co}_3\text{O}_4$  (Figure 1a). The Raman spectrum of  $\text{Ir}_{0.06}\text{Co}_{2.94}\text{O}_4$  evidences the Ir substitution-induced lattice expansion by the red-shift of Raman bands in comparison with those of pure  $\text{Co}_3\text{O}_4$  and  $\text{IrO}_2$  (Figure 1b). Notably, the  $A_{1g}$  band of  $\text{Ir}_{0.06}\text{Co}_{2.94}\text{O}_4$  exhibits the most pronounced red-shift, while the wavenumber of its  $F_{2g}(1)$  band only decreases slightly. Given the  $A_{1g}$  band shows a strong dependence upon the exchange of octahedral cations and the  $F_{2g}(1)$  band depends on tetrahedral cations,<sup>27</sup> it is indicated that the Ir dopants are located at the position of Co(III) sites in octahedral units ( $\text{Co}_{\text{oct}}$ ) rather than the tetrahedral Co(II) sites ( $\text{Co}_{\text{tet}}$ ). This can be attributed to the preference of cations

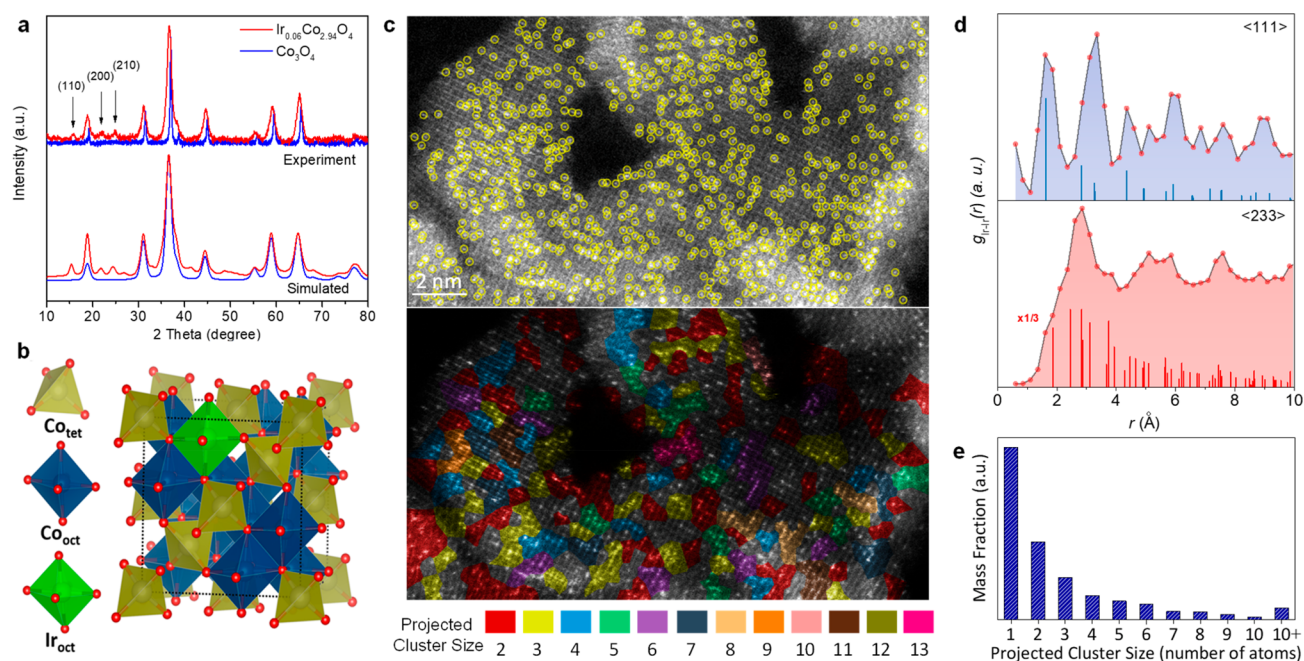


**Figure 2.** Structural elucidations of  $\text{Ir}_{0.06}\text{Co}_{2.94}\text{O}_4$ . (a) Experimental and simulated XRD patterns of fresh  $\text{Ir}_{0.06}\text{Co}_{2.94}\text{O}_4$  and  $\text{Co}_3\text{O}_4$ . An anisotropic coherent length (i.e., 8 nm along the  $\langle 011 \rangle$  direction for correlated Ir substitution at  $\text{Co}_{\text{oct}}$  sites) is used for Ir substituted  $\text{Co}_3\text{O}_4$ , while an isotropic one is used for pure  $\text{Co}_3\text{O}_4$ . (b) Structural model of Ir-substituted cobalt spinel oxide in a polyhedral representation. (c) Upper: HAADF-HRSTEM image of a typical  $\text{Ir}_{0.06}\text{Co}_{2.94}\text{O}_4$  nanocrystal after OER test projected along the  $\langle 233 \rangle$  direction with Ir sites searched and labeled by yellow circles; Lower: cluster distribution graph for correlated Ir sites (see the Methods section). (d) Calculated projection-specific pPDF profiles for  $\text{Ir}_{0.06}\text{Co}_{2.94}\text{O}_4$  after OER test based on a statistical analysis of 4650 Ir sites labeled in multiple HAADF-HRSTEM images (upper:  $\langle 111 \rangle$  projection; lower:  $\langle 233 \rangle$  projection). The navy and red bars refer to calculated pPDF histograms for the projected  $\text{Co}_{\text{oct}}$  cationic lattice of the  $\text{Co}_3\text{O}_4$  framework along  $\langle 111 \rangle$  and  $\langle 233 \rangle$  directions, respectively. A minimum Ir–Ir distance cutoff of 1.5 Å for pPDF calculation is used, and the first calculated correlation bar of  $\langle 233 \rangle$  projection is squeezed to 1/3 of the original height. (e) Mass fraction histogram of the identified projected clusters with different numbers of correlated Ir dopant sites.

with larger radii for locating at the octahedral sites and the tendency of smaller cations to occupy the tetrahedral sites.<sup>28</sup>

Compared to that of pure  $\text{Co}_3\text{O}_4$ , the Co K-edge X-ray absorption near-edge structure (XANES) of  $\text{Ir}_{0.06}\text{Co}_{2.94}\text{O}_4$  shows an increased valence state of Co cations induced by Ir substitution (Figure 1c). Ir  $L_3$ -edge XANES shows that  $\text{Ir}_{0.06}\text{Co}_{2.94}\text{O}_4$  exhibits a high Ir valence state of approximately 4+ (Figure 1d), distinct from those in nanoparticles or supported single atoms.<sup>29</sup> The Co K-edge Fourier transform (FT)-extended X-ray absorption fine structure (EXAFS) reveals three distinct interatomic distances characteristic of Co–O, octahedral  $\text{Co}_{\text{oct}}\text{--Co}_{\text{oct}}$  and tetrahedral  $\text{Co}_{\text{tet}}\text{--Co}_{\text{tet}}$  pairs in the  $\text{Ir}_{0.06}\text{Co}_{2.94}\text{O}_4$  phase (Figure 1e, upper panel). The Ir  $L_3$ -edge FT-EXAFS of  $\text{Ir}_{0.06}\text{Co}_{2.94}\text{O}_4$  shows two interatomic distances assigned to Ir–O and Ir– $\text{Co}_{\text{oct}}$  which agree well with the Ir–O scattering of  $\text{IrO}_2$  and the Ir–Ir scattering of Ir foil, respectively (Figure 1e, lower panel). No Ir–N coordination is observed. The wavelet transform (WT)-EXAFS analysis of the  $\text{Ir}_{0.06}\text{Co}_{2.94}\text{O}_4$  spectrum reveals two characteristic regions: a first-shell domain for Ir–O scattering with a local maximum at  $R = 1.7 \text{ \AA}$  and  $k = 6.2 \text{ \AA}^{-1}$  and a second-shell domain at  $R = 2.6 \text{ \AA}$  scattering with dual local maxima centered at  $k = 7.6$  and  $9.9 \text{ \AA}^{-1}$ , implying the coexistence of both Ir–Co and Ir–Ir second-shell scattering (Figure 1f). The fitting results of the Ir  $L_3$ -edge FT-EXAFS spectrum of  $\text{Ir}_{0.06}\text{Co}_{2.94}\text{O}_4$  provide the first-shell Ir–O coordination number (CN) of 5.7, which is very close to the theoretical value of  $\text{Co}_{\text{oct}}\text{--O}$  (CN = 6.0) in  $\text{Co}_3\text{O}_4$  (Figure S1 and Table S1). In addition, the CN value of the second shell obtained by summation of the values for Ir–Ir and Ir– $\text{Co}_{\text{oct}}$  species reaches 6.7, which is also close to that of  $\text{Co}_{\text{oct}}\text{--}$

$\text{Co}_{\text{oct}}$  (CN = 6.0) but very different from that of  $\text{Co}_{\text{tet}}\text{--Co}_{\text{tet}}$  (CN = 12.0) in  $\text{Co}_3\text{O}_4$ . It is also found that the interatomic distance of Ir– $\text{Co}_{\text{oct}}$  in  $\text{Ir}_{0.06}\text{Co}_{2.94}\text{O}_4$  (2.91 Å) is very close to that of  $\text{Co}_{\text{oct}}\text{--Co}_{\text{oct}}$  (2.90 Å) in  $\text{Co}_3\text{O}_4$  but different from that of  $\text{Co}_{\text{tet}}\text{--Co}_{\text{tet}}$  (3.50 Å). These results clearly support the conclusions of Raman spectra that the majority of Ir ions in  $\text{Ir}_{0.06}\text{Co}_{2.94}\text{O}_4$  occupy the position of  $\text{Co}_{\text{oct}}$  sites and coordinate with the lattice oxygen of  $\text{Co}_3\text{O}_4$ .

**Structure Elucidation.** A careful inspection of the X-ray diffraction (XRD) patterns permits an unambiguous identification of multiple weak and broad diffuse scattering peaks on the pattern of  $\text{Ir}_{0.06}\text{Co}_{2.94}\text{O}_4$ , which are totally absent on the spectrum of  $\text{Co}_3\text{O}_4$  that adopts an  $Fd\bar{3}m$  symmetry (Figure 2a). Three representative peaks at  $2\theta$  of  $\sim 16^\circ$ ,  $\sim 22^\circ$ , and  $\sim 24^\circ$  can be assigned to the (110), (200), and (210) reflections of a cubic structure. They originate from the simultaneous breakage of F centering and diamond glide plane symmetry of the  $\text{Co}_3\text{O}_4$  lattice because of the Ir substitution. Similar phenomena are observed in a defective MOF system.<sup>30</sup> In addition, a careful examination of the XRD patterns excludes the possibility that these reflections may originate from other impurity phases (Figure S2). Importantly, the appearance of these diffuse scattering peaks is a strong indication that the Ir substitution is the short range correlated to coherent lengths characterized by respective peak widths. Accordingly, we simulated an XRD pattern based on the model of  $\text{Ir}_{0.06}\text{Co}_{2.94}\text{O}_4$ , where Ir ions occupy the octahedral sites in the spinel structure with a short-range order (Figure 2b and Table S2). This coincides with the observed Ir–Ir pair by WT-EXAFS analysis.

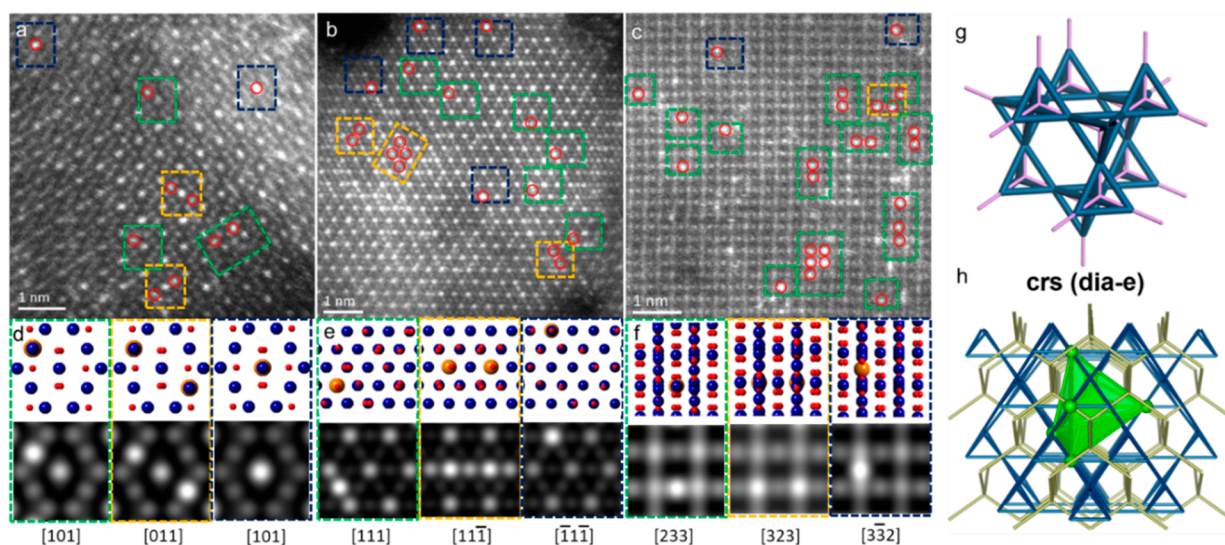


**Figure 3.** Atomic-resolution HAADF-HRSTEM images of  $\text{Ir}_{0.06}\text{Co}_{2.94}\text{O}_4$  after OER test from diverse projections. (a–c) Experimental HRSTEM images with Ir sites labeled by red circles, (d–f) (upper) structural projections and (lower) simulated projected  $Z^2$ -maps (a point spread function width of 1 Å is used) along different symmetry-related  $\langle 011 \rangle$ ,  $\langle 111 \rangle$ , and  $\langle 233 \rangle$  directions of an identical doping configuration. These structural projections can be well discriminated in the HRSTEM image, which are labeled by the dashed rectangles with different colors. Ir sites are represented as large orange spheres. Topology illustration of (g) the octahedral cationic sites as a crs net (dia-e) (blue): an edge net of dia topology (purple) and (h) interpenetrating crs net (blue) and dia net (yellow) representing the octahedral and tetrahedral cationic sites, respectively, in the cobalt spinel oxide structure. The green polyhedron schematically illustrates the correlated substitution of Ir sites at the octahedral cationic sites.

A careful inspection of Z-contrast HAADF-HRSTEM image of the  $\text{Ir}_{0.06}\text{Co}_{2.94}\text{O}_4$  hybrid after OER test suggests that the Ir sites feature much brighter contrast compared with the  $\text{Co}_3\text{O}_4$  framework (Figure 2c, upper). It is indicated that the majority of Ir atoms are fully accommodated at the projected lattice sites in the spinel phase while only a very small fraction is distributed randomly on the surface. We analyzed a large number of Ir sites along different projections, where the coordinates of individual Ir sites and projected distance for the correlated Ir sites can be accurately predicted and measured. By labeling individual 4650 Ir sites in multiple-projection images (Figures S3 and S4), the partial projected pair distribution function (pPDF) of these sites can be directly calculated. As shown in the projection-specific pPDF profiles for  $\langle 111 \rangle$  and  $\langle 233 \rangle$  axes (Figure 2d), multiple sharp correlation peaks unambiguously confirm that majority Ir sites show a short-range correlation. A comparison with the calculated pPDF histograms of the projected  $\text{Co}_{\text{Oct}}$  cationic sublattice of  $\text{Co}_3\text{O}_4$  along these projections confirms that these Ir sites adopt an identical spatial correlation with the  $\text{Co}_3\text{O}_4$  host lattice. Any deviation of Ir–Ir pair probability distribution from that of the host cationic sublattice, especially at short Ir–Ir separations, may arise from the additional energy modulation on the correlated Ir substitution. Notwithstanding this, the presence of several correlation peaks below 4 Å for projected Ir–Ir pairs also indicates a high probability of local clustering of Ir sites within the spinel framework. Although the accurate 3D positioning of individual Ir sites is difficult from the projected STEM images, identifying “projected Ir clusters” over ultrathin regions with a few nanometers thickness offers a sensible evaluation of the 3D clustering probability of Ir sites, combined with the minimized channeling effect by using a low-symmetry projection or slightly off-axis condition. The location and size of such “projected clusters” defined by short-range correlated Ir sites can be well determined based on the projected nearest-neighbor distances between  $\text{Co}_{\text{Oct}}$  sites. After

proper labeling and classification of these Ir sites with short-range order over the ultrathin edge regions of interconnected and nanometer-sized  $\text{Ir}_{0.06}\text{Co}_{2.94}\text{O}_4$  hybrid particles, a demonstrative distribution graph of projected Ir clusters along the low-symmetry  $\langle 233 \rangle$  projection can be produced as shown in Figure 2c (lower). It indicates that the distribution of nanodomains with correlated Ir substitution is inhomogeneous, and these nanodomains tend to aggregate within the  $\text{Co}_3\text{O}_4$  spinel framework. Furthermore, the relative population of projected clusters with a certain size can be statistically analyzed and evaluated in terms of the mass fraction (Figure 2e). Generally, it is found that the majority of Ir sites adopt short-range order rather than exist as isolated sites within the cationic lattice of  $\text{Co}_3\text{O}_4$ , and moreover the mass fraction of clusters decreases as cluster size increases.

**Atomic Structure Identification.** From the magnified atomic-resolution STEM images of the catalyst after OER test, it is also possible to directly identify individual Ir sites with brighter contrast in the spinel structure based on  $\langle 011 \rangle$ ,  $\langle 111 \rangle$ , and  $\langle 233 \rangle$  projections (Figure 3). The explicit identification of the Ir substitution sites can be achieved according to a comprehensive simulation of the structural projections for both Ir sites and diverse substitution configurations (Figures S5–S7). Specifically, the seemingly distinct Ir sites can actually be assigned to the structural projections from diverse symmetry-equivalent  $\langle 011 \rangle$  directions of the cubic spinel lattice with an identical doping configuration, which is clearly visualized by three representative structural projections of a geometry with correlated Ir substitution at  $\text{Co}_{\text{Oct}}$  sites along the  $\langle 011 \rangle$  direction and the corresponding simulated  $Z^2$  maps (Figure 3d). On the basis of the above observations, it is confirmed that Ir preferentially substitutes the cationic  $\text{Co}_{\text{Oct}}$  sites in the  $\text{Co}_3\text{O}_4$  structure. Similar comparison can be made for HRSTEM images taken along the other two directions (i.e.,  $\langle 111 \rangle$  and  $\langle 233 \rangle$  projections in Figure 3e,f). A schematic illustration of the short-range correlated substitution of Ir sites



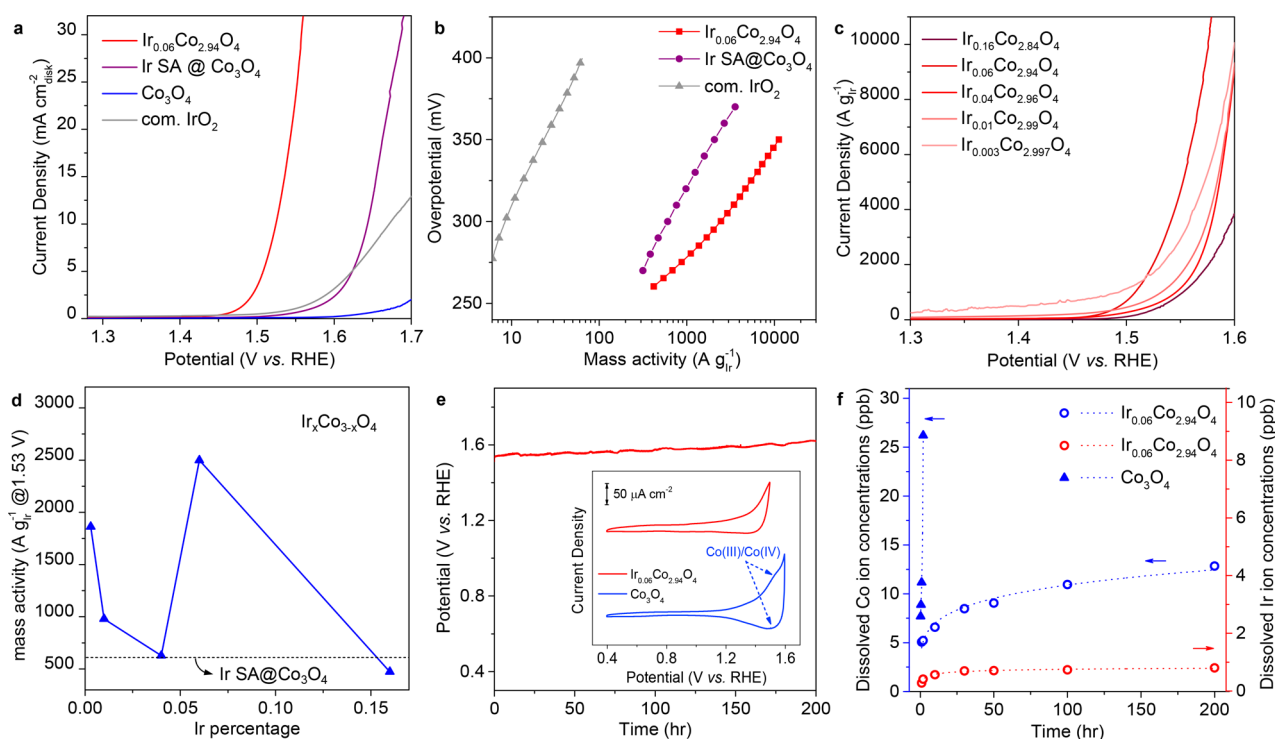


**Figure 4.** OER performance evaluation of various electrocatalysts. (a) Polarization curves normalized to the surface area of disk electrodes made from  $\text{Ir}_{0.06}\text{Co}_{2.94}\text{O}_4$ , Ir SA@ $\text{Co}_3\text{O}_4$ ,  $\text{Co}_3\text{O}_4$ , and commercial  $\text{IrO}_2$  catalysts in  $\text{O}_2$ -saturated 0.1 M  $\text{HClO}_4$ . (b) Comparison of the mass activity of various catalysts as a function of overpotential. (c) LSV curves of  $\text{Ir}_x\text{Co}_{3-x}\text{O}_4$  catalysts normalized to the mass of Ir. (d) Comparison of the mass activity of  $\text{Ir}_x\text{Co}_{3-x}\text{O}_4$  and Ir SA@ $\text{Co}_3\text{O}_4$  catalysts at 1.53 V vs RHE. (e) Constant current chronopotentiometric stability measurements at an anodic current density of  $10 \text{ mA cm}^{-2}$  for  $\text{Ir}_{0.06}\text{Co}_{2.94}\text{O}_4$ . Inset is CV curves of  $\text{Ir}_{0.06}\text{Co}_{2.94}\text{O}_4$  and  $\text{Co}_3\text{O}_4$ . (f) The dissolved Co (left-y axis) and Ir (right-y axis) ion concentrations measured for  $\text{Ir}_{0.06}\text{Co}_{2.94}\text{O}_4$  (hollow points) and  $\text{Co}_3\text{O}_4$  (solid points) in electrolyte by ICP-MS.

in the  $\text{Co}_{\text{OCT}}$  sublattice is shown in Figure 3g,h, which adopts a crs topology with a 3D network composed of corner-shared tetrahedra in a staggered fashion. This arrangement eliminates the close-packing limitation in most metallic Ir phases that usually adopt an fcc or hcp topology through the oxygen-bridged noble metal arrangements.

**Catalytic OER Performance.** Electrocatalytic OER performance of the synthesized and commercial catalysts was evaluated in  $\text{O}_2$ -saturated 0.1 M  $\text{HClO}_4$  electrolytes (Figure 4a). The onset potential of OER on  $\text{Ir}_{0.06}\text{Co}_{2.94}\text{O}_4$  catalyst was determined to be around 1.45 V vs reversible hydrogen electrode (RHE) by the rotating ring-disk electrode (RRDE) measurement (Figure S8). At an overpotential of 300 mV (1.53 V vs RHE),  $\text{Ir}_{0.06}\text{Co}_{2.94}\text{O}_4$  catalyst exhibits the best performance of an outstanding OER current density of  $5.99 \text{ mA cm}_{\text{ox}}^{-2}$  and a mass activity of  $2511 \text{ A g}_{\text{Ir}}^{-1}$  (Figure 4a,b, Figure S9 and Table S3). The mass activity of  $\text{Ir}_{0.06}\text{Co}_{2.94}\text{O}_4$  outperforms that of the commercial  $\text{IrO}_2$  catalyst by over 2 orders of magnitude and exceeds those of most noble-metal-based catalysts reported so far (Table S4 and Figure S10). It is also found that the activity of Ir-substituted  $\text{Ir}_{0.06}\text{Co}_{2.94}\text{O}_4$  catalyst greatly outperforms the conventional catalyst of surface adsorbed Ir single atom sites on  $\text{Co}_3\text{O}_4$  support without any spatial correlation (denoted as Ir SA@ $\text{Co}_3\text{O}_4$ , Figures S11 and S12).

We also prepared a series of Ir-substituted  $\text{Co}_3\text{O}_4$  ( $\text{Ir}_x\text{Co}_{3-x}\text{O}_4$ ) catalysts with different Ir ratios by adding different amounts of Ir precursor. ICP-MS results indicate the Ir ratios are  $x = 0.003, 0.01, 0.04, 0.06$ , and  $0.16$  (Table S5). It is found that the  $\text{Ir}_{0.06}\text{Co}_{2.94}\text{O}_4$  sample shows the best performance while the other samples exhibit poorer activity

(Figure 4c,d, Figures S13 and S14, Table S6). The poor performance of the samples with small Ir percentages may be due to the limited spatial ordering, while the sample with largest Ir percentage may suffer from reduced use of Ir sites. Importantly, it is also indicated that most of  $\text{Ir}_x\text{Co}_{3-x}\text{O}_4$  catalysts show enhanced activity in comparison with that of Ir SA@ $\text{Co}_3\text{O}_4$  catalyst (Figure 4a,d), suggesting that Ir sites alone are not the active sites for OER. Additionally, the greatly enhanced catalytic activity on  $\text{Ir}_{0.06}\text{Co}_{2.94}\text{O}_4$  catalyst in comparison with that of pure  $\text{Co}_3\text{O}_4$  demonstrates that Co sites alone are not the active sites for OER either. Therefore, we propose that in the  $\text{Ir}_{0.06}\text{Co}_{2.94}\text{O}_4$  catalyst the real active sites are nanodomains consisting of Ir octahedral sites with a short-range correlation and an enclosure of the Co sites, which contribute cooperatively to the enhanced OER activity. In addition, a Tafel slope of  $45 \text{ mV dec}^{-1}$  was obtained for the  $\text{Ir}_{0.06}\text{Co}_{2.94}\text{O}_4$  catalyst, which is different from the slopes for Ir SA@ $\text{Co}_3\text{O}_4$  and pure  $\text{Co}_3\text{O}_4$ , suggesting an electrochemical oxide path mechanism for this catalyst<sup>31</sup> (Figure S15).

**Corrosion Resistance in OER.** The long-term stability of  $\text{Ir}_{0.06}\text{Co}_{2.94}\text{O}_4$  catalyst under highly corrosive and oxidative conditions was investigated by a constant current chronopotentiometry at a current density of  $10 \text{ mA cm}^{-2}$  (Figure 4e). An ultralong continuous OER electrocatalysis for over 200 h can be offered by  $\text{Ir}_{0.06}\text{Co}_{2.94}\text{O}_4$ . In contrast, because of the weak interaction between Ir sites and a Co spinel oxide support, the Ir SA@ $\text{Co}_3\text{O}_4$  catalyst exhibits much worse stability in comparison to that of  $\text{Ir}_{0.06}\text{Co}_{2.94}\text{O}_4$  (Figure S16). As seen in the Figure 4e inset,  $\text{Co}_3\text{O}_4$  displays major redox peaks at  $\sim 1.53 \text{ V}$  vs RHE corresponding to the Co(III)/Co(IV) transition.<sup>32</sup> The oxidation of Co(III) can lead to the

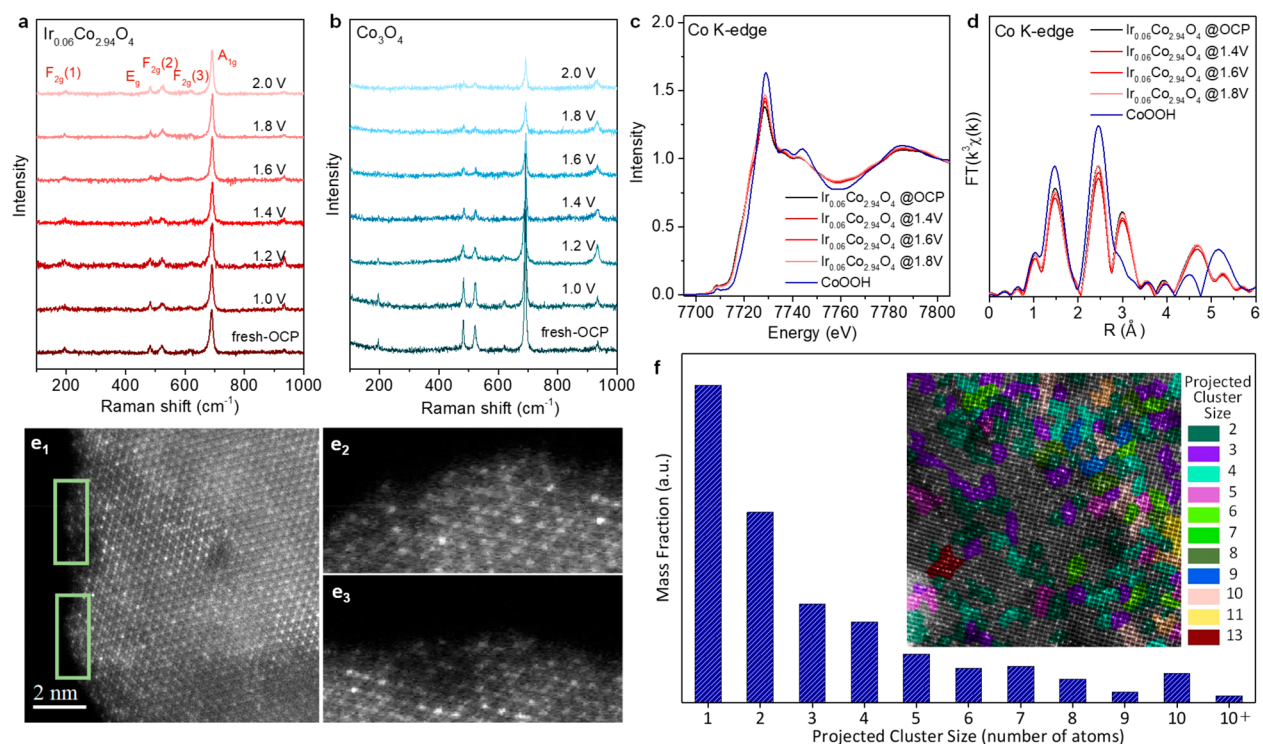


**Figure 5.** Corrosion resistance evaluation of  $\text{Ir}_{0.06}\text{Co}_{2.94}\text{O}_4$  (a, b) *In situ* Raman spectroscopy measurements for OER occurring on  $\text{Ir}_{0.06}\text{Co}_{2.94}\text{O}_4$  and pure  $\text{Co}_3\text{O}_4$  catalysts at various potentials vs Ag/AgCl. All the characteristic bands ( $A_{1g}$  at  $\sim 690\text{ cm}^{-1}$ ,  $F_{2g}(1-3)$  at  $\sim 197, 484,$  and  $523\text{ cm}^{-1}$ , and  $E_g$  at  $\sim 620\text{ cm}^{-1}$  originate from Co spinel oxide) of the  $\text{Ir}_{0.06}\text{Co}_{2.94}\text{O}_4$  catalyst are well maintained during OER experiments. The band at  $\sim 930\text{ cm}^{-1}$  comes from  $(\text{ClO}_4^-)$  in 0.1 M  $\text{HClO}_4$  electrolyte. (c) Co K-edge XANES spectra and (d) FT-EXAFS spectra of  $\text{Ir}_{0.06}\text{Co}_{2.94}\text{O}_4$  catalyst under open circuit potential (OCP) and various potentials (1.4, 1.6, and 1.8 V vs RHE) of the OER process. (e) Atomic resolution HRTEM images of the post-OER  $\text{Ir}_{0.06}\text{Co}_{2.94}\text{O}_4$  catalyst along with their enlarged edge regions ( $e_2$  and  $e_3$  correspond to the green boxes in  $e_1$ ). (f) Mass fraction histogram of identified projected clusters in the  $\text{Ir}_{0.06}\text{Co}_{2.94}\text{O}_4$  catalyst before OER with different numbers of correlated Ir dopant sites. The inset shows the distribution map for those correlated Ir sites on a typical HRSTEM image taken along the  $\langle 233 \rangle$  zone axis.

formation of high-valence sites such as  $\text{CoO}_x(\text{OH})_y$ ,<sup>33</sup> which dissolve during OER process and result in an irreversible loss of active sites (Figure S17). By contrast, the  $\text{Ir}_{0.06}\text{Co}_{2.94}\text{O}_4$  plot indicates no apparent redox peak before the onset potential of OER, suggesting such a transition was suspended due to Ir substitution. This is further supported by the ICP-MS measurements of the dissolved Co and/or Ir ion in electrolytes during the OER process exceeding 200 h (Figure 4f). For the  $\text{Ir}_{0.06}\text{Co}_{2.94}\text{O}_4$  catalyst, the dissolved Co and Ir ion concentrations slightly increased during the first few hours of aging period and are stabilized at a low level of 12.8 and 0.8 ppb afterward. Such a low concentration for Co ion is even lower than that obtained for pure  $\text{Co}_3\text{O}_4$  catalyst after a 2 h OER process. It is worth mentioning that the slight dissolution of surface Co sites in the  $\text{Ir}_{0.06}\text{Co}_{2.94}\text{O}_4$  catalyst during the first few hours of OER is to a certain extent consistent with the previous reports that transition metal species underwent surface leaching in acidic OER conditions.<sup>18,19</sup> After the initial period of aging, the newly derived catalyst exhibited an improved corrosion resistance in comparison with that of pure  $\text{Co}_3\text{O}_4$ , which is further supported by the fact that the ratio of Co and Ir species in  $\text{Ir}_{0.06}\text{Co}_{2.94}\text{O}_4$  after the OER stability test is almost identical with that of the fresh catalyst (Table S7).

A series of *in situ* and *ex situ* characterizations were conducted to elucidate the corrosion resistance of the  $\text{Ir}_{0.06}\text{Co}_{2.94}\text{O}_4$  catalyst regarding Co and Ir species, respectively. As shown in *in situ* Raman experiments conducted during OER process (Figure 5a,b and Figure S18), the  $\text{Ir}_{0.06}\text{Co}_{2.94}\text{O}_4$  catalyst shows no obvious surface phase evolution throughout

the whole process of OER, while the pure  $\text{Co}_3\text{O}_4$  catalyst undergoes evident loss of its original surface structure. Furthermore, we investigated the chemical nature of Co spinel oxide framework during OER process by recording Co K-edge XANES and FT-EXAFS spectra for  $\text{Ir}_{0.06}\text{Co}_{2.94}\text{O}_4$  under different oxidative potentials. As is shown in Figure 5c,d, no obvious increase in the Co oxidation state is observed. Additionally, the corresponding FT-EXAFS spectra probe the average coordination environment of Co sites, which remain nearly unaltered and confirm the negligible structural transformation, agreeing well with *in situ* Raman results. The above observations indicate that Co species in the  $\text{Ir}_{0.06}\text{Co}_{2.94}\text{O}_4$  catalyst adopt nearly identical structure before and after the OER experiments.

With regard to the possible *in situ* generation of surface Ir oxide phase as suggested by some other studies,<sup>34,35</sup> we present the selected area electron diffraction (SAED) patterns for post-OER  $\text{Ir}_{0.06}\text{Co}_{2.94}\text{O}_4$  catalyst, which only demonstrate the characteristic reflections of  $\text{Co}_3\text{O}_4$ , while those for Ir oxide phase are absent (Figure S19). This agrees with the results concluded from ICP-MS (Figure 4f). The atomic-resolution HRSTEM imaging and electron energy loss spectroscopy (EELS) analysis was also conducted to probe the possible evolution in the electronic structure of the post-OER  $\text{Ir}_{0.06}\text{Co}_{2.94}\text{O}_4$  catalyst. It is shown that the shapes and positions of the Co- $L_2/L_3$  energy loss peaks are identical among different regions throughout the post-OER  $\text{Ir}_{0.06}\text{Co}_{2.94}\text{O}_4$  nanoparticle (Figure S20), implying the consistent Co valence state and thus ruling out the surface evolution of the catalyst during

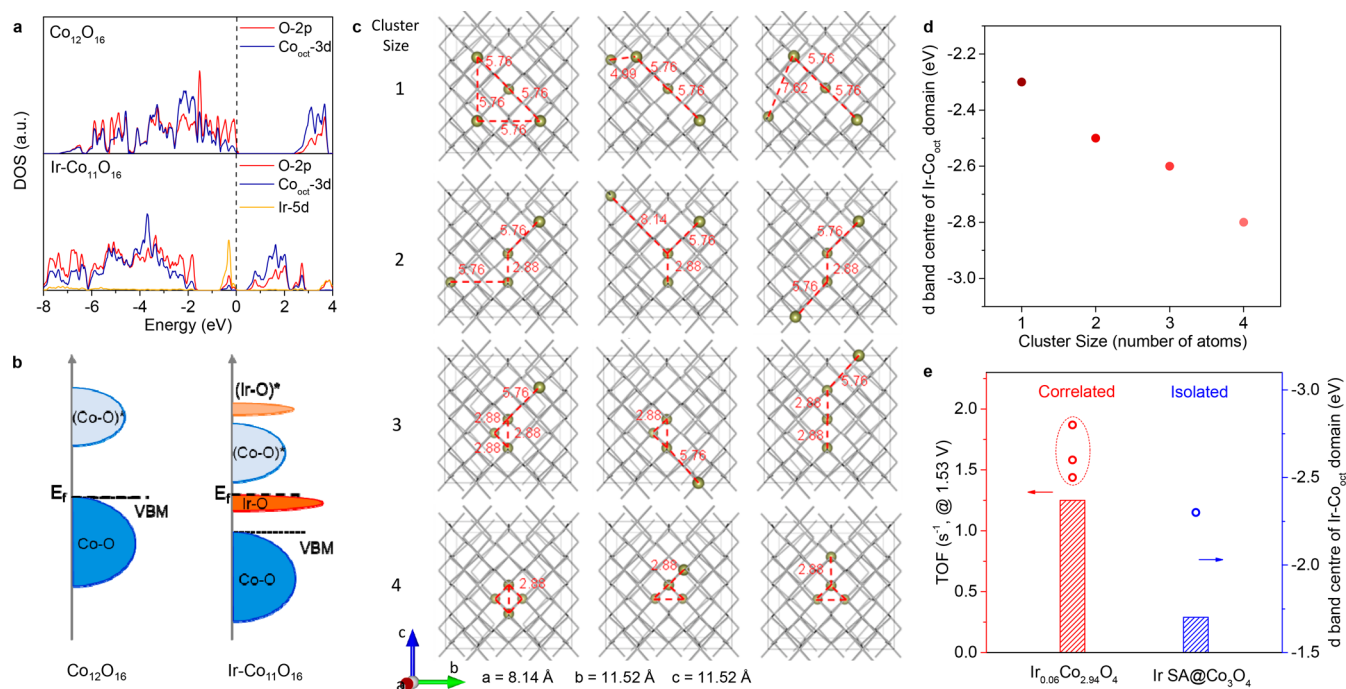


**Figure 6.** Electronic structure analysis. (a) Partial DOS of pure  $\text{Co}_{12}\text{O}_{16}$  (upper) and  $\text{Ir-Co}_{11}\text{O}_{16}$  (lower). (b) Schematic illustration of modification of DOS by Ir substitution, which exhibits the lowered VBM and the formation of localized Ir 5d–O 2p states (orange state) near the  $E_f$ . (c) Schematic illustrations of  $\text{Ir}_4\text{-Co}_{44}\text{O}_{64}$  models showing Ir (indicated by yellow spheres) clusters with various sizes (gray rods represent the  $\text{Co}_{\text{Oct}}\text{-O}$  bonds). The cluster size was determined by the interatomic distances among the Ir sites, which is indicated in figure (unit: Å). (d) The d-band center of the Ir- $\text{Co}_{\text{Oct}}$  domain consisting of Ir substitutions and the nearest-neighboring  $\text{Co}_{\text{Oct}}$  sites for configurations with different Ir cluster size. (e) Relationship between the OER activity for  $\text{Ir}_{0.06}\text{Co}_{2.94}\text{O}_4$  and Ir SA@ $\text{Co}_3\text{O}_4$  catalysts and d-band center of Ir- $\text{Co}_{\text{Oct}}$  domain for configurations with correlated and isolated Ir sites.

OER. In addition, for post-OER  $\text{Ir}_{0.06}\text{Co}_{2.94}\text{O}_4$  catalyst, the majority of Ir sites are confirmed to occupy the  $\text{Co}_{\text{Oct}}$  sites rather than the  $\text{Co}_{\text{Tet}}$  sites in the spinel structure by correlating the labeled Ir sites with indexed  $\text{Co}_{\text{Oct}}$  and  $\text{Co}_{\text{Tet}}$  sites in the  $\langle 110 \rangle$  projected spinel structures (Figure S21). To investigate the possible structure change of the catalyst during OER process, we also performed HAADF-HRSTEM characterization of fresh  $\text{Ir}_{0.06}\text{Co}_{2.94}\text{O}_4$  catalyst. Representative images of both fresh and post-OER catalysts confirm the correlated doping of Ir sites in the spinel framework rather than the presence of  $\text{IrO}_x$  nanoparticles (Figure 5e and Figure S22). Notwithstanding this, the spatial correlation of incorporated Ir sites in the spinel structure should be compared between catalysts before and after OER test. The pPDF profiles of both fresh and after-OER catalysts (total 7919 Ir atoms analysis) exhibit sharp correlation peaks for identified Ir atomic pairs, which confirms that the short-range correlation of Ir sites is also well-preserved after OER process (Figure 2d and Figure S23). Additionally, the statistical analysis of these Ir atomic columns permits the determination of spatial correlations of these Ir sites (Figures 2e and 5f, Figure S24). Therefore, by taking together the results from ICP-MS, *in situ* spectroscopy, and HAADF-HRSTEM imaging, it is demonstrated that despite the dissolution of minor amount of defective or weakly bonded surface species at the early stage, the majority of active sites—the nanodomains with correlated Ir substitutions and enclosed Co sites—are well-preserved after the OER process.

**Electronic Structure Analysis.** We performed the density functional theory (DFT) calculations to understand the noble-metal-like electrocatalytic properties of  $\text{Ir}_{0.06}\text{Co}_{2.94}\text{O}_4$  by constructing  $\text{Ir-Co}_{11}\text{O}_{16}$  and  $\text{Co}_{12}\text{O}_{16}$  models to represent

$\text{Ir}_{0.06}\text{Co}_{2.94}\text{O}_4$  and  $\text{Co}_3\text{O}_4$  catalysts, respectively (Figure S25). The valence band maximum edge (VBM, coincides with the highest energy level occupied by electron states) of the  $\text{Co}_{\text{Oct}}$  3d-band explains the electrochemical stability of  $\text{Ir-Co}_{11}\text{O}_{16}$  during the OER process.<sup>36</sup> As shown in the density of state (DOS) plots (Figure 6a,b), a downshifted VBM of  $\text{Co}_{\text{Oct}}$  3d-band in  $\text{Ir-Co}_{11}\text{O}_{16}$  refers to a lower tendency of the  $\text{Co}_{\text{Oct}}$  sites to lose valence electrons, namely, to be (electro)chemically oxidized.<sup>37,38</sup> This agrees well with the CV observations that show the absence of  $\text{Co(III)/Co(IV)}$  transition in  $\text{Ir}_{0.06}\text{Co}_{2.94}\text{O}_4$  during OER. In addition, the DOS and electron localization function (ELF) plots (Figure S26) indicate that compared to  $\text{Co}_{12}\text{O}_{16}$ , the data for  $\text{Ir-Co}_{11}\text{O}_{16}$  show the presence of a localized Ir 5d–O 2p state near the Fermi level ( $E_f$ ) within the band gap. This d-state suggests that the Ir substitutions contribute to the boosted OER catalytic activity because of the increased charge transfer rate between the reaction intermediates and the catalyst surface.<sup>39</sup>

Importantly, to investigate the difference of electronic structure between correlated Ir sites and isolated Ir sites, an  $\text{Ir}_4\text{-Co}_{44}\text{O}_{64}$  supercell model with Ir sites grouped into clusters with different size was built (Figure 6c). It is found that the relative energies of the corresponding configurations increase with increased Ir cluster size (Figure S27), which indicates a decreased population of larger clusters and agrees well with above statistical analysis based on HAADF-HRSTEM analysis (Figures 2e and 5f). We further investigated the electronic structure of the most stable configurations by calculating the d-band center of Ir- $\text{Co}_{\text{Oct}}$  nanodomains, which is also well correlated to the observed electrocatalytic activity. It is

demonstrated that in comparison to the configuration with isolated Ir sites those with correlated Ir sites exhibit a downshifted d-band center consisting of Ir substitutions and the nearest-neighbor Co<sub>oct</sub> sites (Figure 6d). These downshifted d-band center values can regulate the oxygen intermediates adsorption energy on the Ir<sub>0.06</sub>Co<sub>2.94</sub>O<sub>4</sub> catalyst and contribute to the greatly enhanced OER activity.<sup>20</sup> This agrees well with the experimental finding that Ir<sub>0.06</sub>Co<sub>2.94</sub>O<sub>4</sub> catalyst with correlated Ir sites has a much higher intrinsic activity in comparison to that of Ir SA@Co<sub>3</sub>O<sub>4</sub> catalyst with isolated Ir sites (Figure 6e). This observation also supports our conclusion that the active site in Ir<sub>0.06</sub>Co<sub>2.94</sub>O<sub>4</sub> catalyst is the correlated Ir substitution and an enclosure of Co sites.

## CONCLUSIONS

To summarize, we report a simple strategy to allocate noble metal atoms with identical atomic spatial correlations in TMO host structures, which greatly diversifies the noble metal analogues and offers promising geometric and electronic properties toward target electrocatalytic reactions. The extremely high mass activity and significantly improved corrosion resistance make Ir<sub>0.06</sub>Co<sub>2.94</sub>O<sub>4</sub> one of the best acidic OER electrocatalysts reported so far. The synergistic effects between Ir species and Co<sub>3</sub>O<sub>4</sub> host framework arise from correlated Ir sites dictated by the topology of the Co<sub>oct</sub> cationic sublattice and contribute to the attractive catalytic performance. Such a hybrid geometry secures a unique electronic structure distinct from either close-packed Ir nanoparticles or Ir single atoms adsorbed on the substrate. The origin of the improved catalytic activity and corrosion resistance of Ir<sub>0.06</sub>Co<sub>2.94</sub>O<sub>4</sub> in acidic medium is attributed to the modified electronic structure including the downshifted d-band center of Co together with a band gap Ir-5d band as well as a deepened valence band maximum. This work demonstrates how to eliminate the inherent geometric limitations of noble metals to create a large variety of analogues based on low-cost TMOs, which hold a great potential for a wide range of applications involving noble metals.

## METHODS

**Material Synthesis.** ZIF-67 nanocrystals were synthesized by a surfactant-mediated method reported previously.<sup>40</sup> In a typical procedure, 580 mg of cobalt(II) nitrate hexahydrate (Co(NO<sub>3</sub>)<sub>2</sub>·6H<sub>2</sub>O) was dissolved in 20 mL of deionized (DI) water containing 30 mg of hexadecyltrimethylammonium bromide (CTAB). Then, this solution was injected into 140 mL of aqueous solution with 9.08 g of 2-methylimidazole and stirred at room temperature for 60 min. The purple precipitate was collected by centrifugation and washed with ethanol five times. For the preparation of Ir<sub>0.06</sub>Co<sub>2.94</sub>O<sub>4</sub> catalyst, an ion exchange process was performed before pyrolysis. Typically, 100 mg of ZIF-67 nanocrystals was dispersed in 50 mL of DI water; then 9.5 mg (2 mmol L<sup>-1</sup>) of sodium hexachloroiridate(III) hydrate (Na<sub>3</sub>IrCl<sub>6</sub>·xH<sub>2</sub>O) were dissolved in 10 mL of DI water and added into the ZIF-67 solution slowly under stirring conditions. The reaction was quenched by centrifuging the suspension after 3 h; the precipitate was collected and washed twice with DI water and three times with ethanol. The Ir<sub>0.06</sub>Co<sub>2.94</sub>O<sub>4</sub> nanocrystals were obtained after drying the precipitate at 60 °C overnight in a vacuum oven and pyrolyzed at 300 °C in air for 4 h.

The synthesis of Ir<sub>x</sub>Co<sub>3-x</sub>O<sub>4</sub> was performed by the same ion exchange-pyrolysis procedure as that for Ir<sub>0.06</sub>Co<sub>2.94</sub>O<sub>4</sub> but with different concentrations of Na<sub>3</sub>IrCl<sub>6</sub>·xH<sub>2</sub>O (0.04, 0.2, 1, and 20 mmol L<sup>-1</sup>). The corresponding products of Ir<sub>x</sub>Co<sub>3-x</sub>O<sub>4</sub> with *x* = 0.003, 0.01, 0.04, and 0.16 were determined by ICP-MS. The synthesis of Ir SA@Co<sub>3</sub>O<sub>4</sub> was performed by immersing presynthesized Co<sub>3</sub>O<sub>4</sub> nano-

particles in the solution of Ir salt. Later, sodium borohydride was added to reduce Ir salt as well as immobilize Ir atoms to obtain the final product. The mass ratio of Ir in Ir SA@Co<sub>3</sub>O<sub>4</sub> determined by ICP-MS was to be about 0.7 wt %.

**Materials Characterization.** XRD data were collected on a Rigaku MiniFlex 600 X-ray diffractometer. Raman spectra were collected by using a HORIBA Scientific Raman spectroscopy instrument (laser excitation at 532 nm). ICP-MS analysis was conducted to detect the doping amounts of noble metals in catalysts by using an Agilent 7500cx instrument with attached laser ablation system. The synchrotron-based XPS characterization was performed on the soft X-ray spectroscopy beamline in the Australian Synchrotron Radiation Facility, Melbourne. The EXAFS measurements were performed at the beamline 14W1 in the Shanghai Synchrotron Radiation Facility. The raw absorption data were first background subtracted by fitting the pre-edge by using a least-squares method, and then all spectra were normalized to one at energies far from the edge.

**HRSTEM Imaging and Analysis.** HAADF-STEM images were recorded by using a FEI Titan G2 80-300 microscope at 300 kV equipped with a probe corrector. Projected Z<sup>2</sup>-map simulations were performed by using the qSTEM program.<sup>41</sup> After flat-field correction and background subtraction, the position searching, refining, and labeling of projected Ir sites with brighter contrast in the HRSTEM image were performed by using CalAtom software<sup>42</sup> with a multiple-ellipse-fitting (MEF) method.<sup>43</sup> The coordinates of refined positions for those projected Ir sites were manually checked to exclude mislabeled sites and then extracted for future analysis.

The pPDF (*g*<sub>Ir-Ir</sub>(*r*)) defined by using the probability of Ir-Ir pairs separated by a projected distance *r* according to the equation

$$g_{\text{Ir-Ir}}(r) = \frac{\rho(r)}{\rho} = \frac{\sum_{i=r}^{r+dr} N_i/N_{\text{ref}} 2\pi r dr}{\rho}$$

where  $\rho(r)$  and  $\rho$  refer to local (i.e., at a distance of *r*) and mean atomic densities. The former can be calculated by summing up the counted atoms (*N<sub>i</sub>*) separated by a distance between *r* and *r* + *dr* (*dr* refers an interval of 0.25 Å used here) from a reference atom, which is normalized by the number of reference atoms (*N<sub>ref</sub>*) and the projected area of 2π*r* *dr*.

The extracted coordinates of Ir sites are grouped into clusters once the measured distance between any two of these Ir sites are within the maximum projected nearest-neighbor distance between Co<sub>oct</sub> sites along a specific projection. The cluster distribution graph for correlated Ir sites is generated pixel by pixel. Each pixel is assigned into a specific cluster by evaluating the shortest distance from any Ir site as a member of this cluster.

**Electrochemical Measurements.** Electrocatalyst ink was prepared by dispersing a freshly synthesized catalyst powder (2 mg) in a solution containing distilled water (Milli-Q, 965 μL) and 5 wt % Nafion solution (35 μL) followed by ultrasonication for 2 h. Ten microliters of catalyst ink was then deposited onto a polished Au-electrode (diameter = 5 mm, area = 0.196 cm<sup>2</sup>, Pine Research Instrument). All electrochemical experiments were performed in a three-electrode glass cell with an Au wire as the counter electrode and an Ag/AgCl as the reference electrode (Pine Research Instrumentation). The 0.1 M HClO<sub>4</sub> electrolyte solution was prepared by diluting 70% HClO<sub>4</sub> with Milli-Q water. The reference electrode was calibrated in H<sub>2</sub>-saturated 0.1 M HClO<sub>4</sub> solution. All potentials were converted to the RHE and corrected for *iR* compensation. The OER measurements were conducted in O<sub>2</sub>-saturated 0.1 M HClO<sub>4</sub> electrolyte with a CHI potentiostat (CHI 760D) at a rotating speed of 1600 rpm. The LSV curves of the catalysts were obtained with a scan rate of 5 mV s<sup>-1</sup>.

**DFT Calculations.** DFT calculations were performed by using the Vienna ab initio Simulation Package (VASP).<sup>44,45</sup> The exchange-correlation interaction was described by generalized gradient approximation (GGA) with the Perdew–Burke–Ernzerhof (PBE) functional.<sup>46</sup> The projector augmented wave (PAW) pseudopotential scheme was used, and the force and energy convergence tolerance

values with respect to plane-wave cutoff and K-point density were set to be 0.01 eV Å<sup>-1</sup> and 10<sup>-5</sup> eV, respectively.<sup>47</sup> Free energies and formation energies of all the compounds were obtained by using the GGA-DFT plus Hubbard-*U* framework (GGA+*U*). Ferromagnetic spin-polarized calculations were employed for all magnetic materials. The GGA+*U* calculations were performed by using the model proposed based on the TEM images with the  $U_{\text{eff}}$  ( $U_{\text{eff}} = \text{Coulomb } U - \text{exchange } J$ ) values of 4.4, 6.7, and 0.7 eV for Co<sup>2+</sup>, Co<sup>3+</sup>, and Ir, respectively.<sup>48,49</sup> A Gaussian smearing of 0.1 eV was applied during the geometry optimization, while for the DOS computations, a tetrahedron method with Blöchl correction and a dense 8 × 8 × 8 Monkhorst–Pack K-points was employed.

## ■ ASSOCIATED CONTENT

### Supporting Information

The Supporting Information is available free of charge at <https://pubs.acs.org/doi/10.1021/jacs.1c01525>.

Detailed methods and additional XAS, XRD, HRSTEM, electrochemical and DFT data (PDF)

## ■ AUTHOR INFORMATION

### Corresponding Authors

**Yihan Zhu** – Center for Electron Microscopy, State Key Laboratory Breeding Base of Green Chemistry Synthesis Technology and College of Chemical Engineering, Zhejiang University of Technology, Hangzhou 310014, China; [orcid.org/0000-0003-0183-8350](https://orcid.org/0000-0003-0183-8350); Email: [yihanzhu@zjut.edu.cn](mailto:yihanzhu@zjut.edu.cn)

**Yao Zheng** – School of Chemical Engineering and Advanced Materials and Centre for Materials in Energy and Catalysis, The University of Adelaide, Adelaide SA5005, Australia; [orcid.org/0000-0002-2411-8041](https://orcid.org/0000-0002-2411-8041); Email: [yao.zheng01@adelaide.edu.au](mailto:yao.zheng01@adelaide.edu.au)

**Shi-Zhang Qiao** – School of Chemical Engineering and Advanced Materials and Centre for Materials in Energy and Catalysis, The University of Adelaide, Adelaide SA5005, Australia; [orcid.org/0000-0002-4568-8422](https://orcid.org/0000-0002-4568-8422); Email: [s.qiao@adelaide.edu.au](mailto:s.qiao@adelaide.edu.au)

### Authors

**Jieqiong Shan** – School of Chemical Engineering and Advanced Materials and Centre for Materials in Energy and Catalysis, The University of Adelaide, Adelaide SA5005, Australia; [orcid.org/0000-0003-4308-5027](https://orcid.org/0000-0003-4308-5027)

**Chao Ye** – School of Chemical Engineering and Advanced Materials and Centre for Materials in Energy and Catalysis, The University of Adelaide, Adelaide SA5005, Australia

**Shuangming Chen** – National Synchrotron Radiation Laboratory, University of Science and Technology of China, Hefei 230029, China; [orcid.org/0000-0001-7567-1552](https://orcid.org/0000-0001-7567-1552)

**Tulai Sun** – Center for Electron Microscopy, State Key Laboratory Breeding Base of Green Chemistry Synthesis Technology and College of Chemical Engineering, Zhejiang University of Technology, Hangzhou 310014, China

**Yan Jiao** – School of Chemical Engineering and Advanced Materials and Centre for Materials in Energy and Catalysis, The University of Adelaide, Adelaide SA5005, Australia; [orcid.org/0000-0003-1329-4290](https://orcid.org/0000-0003-1329-4290)

**Lingmei Liu** – Physical Sciences and Engineering Division, Advanced Membranes and Porous Materials Centre, King Abdullah University of Science and Technology, Thuwal, Saudi Arabia; [orcid.org/0000-0002-3273-9884](https://orcid.org/0000-0002-3273-9884)

**Chongzhi Zhu** – Center for Electron Microscopy, State Key Laboratory Breeding Base of Green Chemistry Synthesis

Technology and College of Chemical Engineering, Zhejiang University of Technology, Hangzhou 310014, China

**Li Song** – National Synchrotron Radiation Laboratory, University of Science and Technology of China, Hefei 230029, China; [orcid.org/0000-0003-0585-8519](https://orcid.org/0000-0003-0585-8519)

**Yu Han** – Physical Sciences and Engineering Division, Advanced Membranes and Porous Materials Centre, King Abdullah University of Science and Technology, Thuwal, Saudi Arabia; [orcid.org/0000-0003-1462-1118](https://orcid.org/0000-0003-1462-1118)

**Mietek Jaroniec** – Department of Chemistry and Biochemistry & Advanced Materials and Liquid Crystal Institute, Kent State University, Kent, Ohio 44242, United States; [orcid.org/0000-0002-1178-5611](https://orcid.org/0000-0002-1178-5611)

Complete contact information is available at: <https://pubs.acs.org/doi/10.1021/jacs.1c01525>

### Author Contributions

J.S., C.Y., S.C., and T.S. contributed equally to this work.

### Notes

The authors declare no competing financial interest.

## ■ ACKNOWLEDGMENTS

This work was financially supported by the Australian Research Council (FL170100154, DP160104866, and DP190103472). Y.H.Z. acknowledges financial support from Zhejiang Provincial Natural Science Foundation of China (LR18B030003), National Natural Science Foundation of China (51701181, 21771161), and the Thousand Talents Program for Distinguished Young Scholars. J.S. was supported by the Chinese CSC Scholarship Program. DFT computations were performed by using services offered from the National Computational Infrastructure (NCI) and Phoenix High Performance Computing, which are supported by the Australian Government and the University of Adelaide. XAS measurements were conducted at the Beijing Synchrotron Radiation Facility (1W1B, BSRF).

## ■ REFERENCES

- (1) Liu, L.; Corma, A. Metal Catalysts for Heterogeneous Catalysis: From Single Atoms to Nanoclusters and Nanoparticles. *Chem. Rev.* **2018**, *118*, 4981–5079.
- (2) Yu, N.-F.; Tian, N.; Zhou, Z.-Y.; Sheng, T.; Lin, W.-F.; Ye, J.-Y.; Liu, S.; Ma, H.-B.; Sun, S.-G. Pd Nanocrystals with Continuously Tunable High-Index Facets as a Model Nanocatalyst. *ACS Catal.* **2019**, *9*, 3144–3152.
- (3) Hammer, B.; Nørskov, J. K. Why gold is the noblest of all the metals. *Nature* **1995**, *376*, 238–240.
- (4) Christoffersen, E.; Liu, P.; Ruban, A.; Skriver, H. L.; Nørskov, J. K. Anode Materials for Low-Temperature Fuel Cells: A Density Functional Theory Study. *J. Catal.* **2001**, *199*, 123–131.
- (5) Hammer, B.; Morikawa, Y.; Nørskov, J. K. CO Chemisorption at Metal Surfaces and Overlayers. *Phys. Rev. Lett.* **1996**, *76*, 2141–2144.
- (6) Xin, H.; Linic, S. Communications: Exceptions to the d-band model of chemisorption on metal surfaces: The dominant role of repulsion between adsorbate states and metal d-states. *J. Chem. Phys.* **2010**, *132*, 221101.
- (7) Fujita, T.; Guan, P.; McKenna, K.; Lang, X.; Hirata, A.; Zhang, L.; Tokunaga, T.; Arai, S.; Yamamoto, Y.; Tanaka, N.; et al. Atomic origins of the high catalytic activity of nanoporous gold. *Nat. Mater.* **2012**, *11*, 775–780.
- (8) Turner, M.; Golovko, V. B.; Vaughan, O. P.; Abdulkin, P.; Berenguer-Murcia, A.; Tikhov, M. S.; Johnson, B. F.; Lambert, R. M. Selective oxidation with dioxygen by gold nanoparticle catalysts derived from 55-atom clusters. *Nature* **2008**, *454*, 981–983.

- (9) Zheng, Y.; Jiao, Y.; Zhu, Y.; Li, L. H.; Han, Y.; Chen, Y.; Jaroniec, M.; Qiao, S. Z. High Electrocatalytic Hydrogen Evolution Activity of an Anomalous Ruthenium Catalyst. *J. Am. Chem. Soc.* **2016**, *138*, 16174–16181.
- (10) Jalan, V.; Taylor, E. J. Importance of Interatomic Spacing in Catalytic Reduction of Oxygen in Phosphoric Acid. *J. Electrochem. Soc.* **1983**, *130*, 2299–2302.
- (11) Imaoka, T.; Akanuma, Y.; Haruta, N.; Tsuchiya, S.; Ishihara, K.; Okayasu, T.; Chun, W. J.; Takahashi, M.; Yamamoto, K. Platinum clusters with precise numbers of atoms for preparative-scale catalysis. *Nat. Commun.* **2017**, *8*, 688.
- (12) Kibsgaard, J.; Chorkendorff, I. Considerations for the scaling-up of water splitting catalysts. *Nat. Energy* **2019**, *4*, 430–433.
- (13) Shan, J.; Guo, C.; Zhu, Y.; Chen, S.; Song, L.; Jaroniec, M.; Zheng, Y.; Qiao, S.-Z. Charge-Redistribution-Enhanced Nanocrystalline Ru@IrOx Electrocatalysts for Oxygen Evolution in Acidic Media. *Chem.* **2019**, *5*, 445–459.
- (14) Shan, J.; Ling, T.; Davey, K.; Zheng, Y.; Qiao, S. Z. Transition-Metal-Doped RuIr Bifunctional Nanocrystals for Overall Water Splitting in Acidic Environments. *Adv. Mater.* **2019**, *31*, 1900510.
- (15) Huang, Z.-F.; Song, J.; Du, Y.; Xi, S.; Dou, S.; Nsanizimana, J. M. V.; Wang, C.; Xu, Z. J.; Wang, X. Chemical and structural origin of lattice oxygen oxidation in Co–Zn oxyhydroxide oxygen evolution electrocatalysts. *Nat. Energy* **2019**, *4*, 329–338.
- (16) Grimaud, A.; Diaz-Morales, O.; Han, B.; Hong, W. T.; Lee, Y. L.; Giordano, L.; Stoerzinger, K. A.; Koper, M. T. M.; Shao-Horn, Y. Activating Lattice Oxygen Redox Reactions in Metal Oxides to Catalyze Oxygen Evolution. *Nat. Chem.* **2017**, *9*, 457–465.
- (17) Wu, T.; Sun, S.; Song, J.; Xi, S.; Du, Y.; Chen, B.; Sasangka, W. A.; Liao, H.; Gan, C. L.; Scherer, G. G.; et al. Iron-facilitated dynamic active-site generation on spinel CoAl<sub>2</sub>O<sub>4</sub> with self-termination of surface reconstruction for water oxidation. *Nat. Catal.* **2019**, *2*, 763–772.
- (18) Seitz, L. C.; Dickens, C. F.; Nishio, K.; Hikita, Y.; Montoya, J.; Doyle, A.; Kirk, C.; Vojvodic, A.; Hwang, H. Y.; Nørskov, J. K.; et al. A Highly Active and Stable IrOx/SrIrO<sub>3</sub> Catalyst for the Oxygen Evolution Reaction. *Science* **2016**, *353*, 1011–1014.
- (19) Grimaud, A.; Demortière, A.; Saubanère, M.; Dachraoui, W.; Duchamp, M.; Doublet, M.-L.; Tarascon, J.-M. Activation of Surface Oxygen Sites on an Iridium-based Model Catalyst for the Oxygen Evolution Reaction. *Nat. Energy* **2017**, *2*, 16189.
- (20) Seh, Z. W.; Kibsgaard, J.; Dickens, C. F.; Chorkendorff, I.; Nørskov, J. K.; Jaramillo, T. F. Combining theory and experiment in electrocatalysis: Insights into materials design. *Science* **2017**, *355*, eaad4998.
- (21) Jiao, Y.; Zheng, Y.; Jaroniec, M.; Qiao, S. Z. Design of electrocatalysts for oxygen- and hydrogen-involving energy conversion reactions. *Chem. Soc. Rev.* **2015**, *44*, 2060–2086.
- (22) Lu, Y.; Wang, J.; Yu, L.; Kovarik, L.; Zhang, X.; Hoffman, A. S.; Gallo, A.; Bare, S. R.; Sokaras, D.; Kroll, T.; et al. Identification of the active complex for CO oxidation over single-atom Ir-on-MgAl<sub>2</sub>O<sub>4</sub> catalysts. *Nat. Catal.* **2019**, *2*, 149–156.
- (23) Li, J.; Guan, Q.; Wu, H.; Liu, W.; Lin, Y.; Sun, Z.; Ye, X.; Zheng, X.; Pan, H.; Zhu, J.; et al. Highly Active and Stable Metal Single-Atom Catalysts Achieved by Strong Electronic Metal-Support Interactions. *J. Am. Chem. Soc.* **2019**, *141*, 14515–14519.
- (24) Shan, J.; Zheng, Y.; Shi, B.; Davey, K.; Qiao, S.-Z. Regulating Electrocatalysts via Surface and Interface Engineering for Acidic Water Electrooxidation. *ACS Energy Lett.* **2019**, *4*, 2719–2730.
- (25) Wang, S.; Li, Q.; Kang, X.; Zhu, M. Customizing the Structure, Composition, and Properties of Alloy Nanoclusters by Metal Exchange. *Acc. Chem. Res.* **2018**, *51*, 2784–2792.
- (26) Lu, P.; Tan, X.; Zhao, H.; Xiang, Q.; Liu, K.; Zhao, X.; Yin, X.; Li, X.; Hai, X.; Xi, S.; et al. Atomically Dispersed Indium Sites for Selective CO<sub>2</sub> Electroreduction to Formic Acid. *ACS Nano* **2021**, DOI: 10.1021/acsnano.1c00858.
- (27) Preudhomme, J.; Tarte, P. Infrared studies of spinels—III: The normal II–III spinels. *Spectrochim. ActaA* **1971**, *27*, 1817–1835.
- (28) Zhao, Q.; Yan, Z.; Chen, C.; Chen, J. Spinels: Controlled Preparation, Oxygen Reduction/Evolution Reaction Application, and Beyond. *Chem. Rev.* **2017**, *117*, 10121–10211.
- (29) Xiao, M.; Zhu, J.; Li, G.; Li, N.; Li, S.; Cano, Z. P.; Ma, L.; Cui, P.; Xu, P.; Jiang, G.; et al. A Single-Atom Iridium Heterogeneous Catalyst in Oxygen Reduction Reaction. *Angew. Chem.* **2019**, *131*, 9742–9747.
- (30) Liu, L.; Chen, Z.; Wang, J.; Zhang, D.; Zhu, Y.; Ling, S.; Huang, K. W.; Belmabkhout, Y.; Adil, K.; Zhang, Y.; et al. Imaging defects and their evolution in a metal-organic framework at sub-unit-cell resolution. *Nat. Chem.* **2019**, *11*, 622–628.
- (31) Antolini, E. Iridium As Catalyst and Cocatalyst for Oxygen Evolution/Reduction in Acidic Polymer Electrolyte Membrane Electrolyzers and Fuel Cells. *ACS Catal.* **2014**, *4*, 1426–1440.
- (32) Bergmann, A.; Martinez-Moreno, E.; Teschner, D.; Chernev, P.; Glied, M.; de Araujo, J. F.; Reier, T.; Dau, H.; Strasser, P. Reversible amorphization and the catalytically active state of crystalline Co<sub>3</sub>O<sub>4</sub> during oxygen evolution. *Nat. Commun.* **2015**, *6*, 8625.
- (33) Bajdich, M.; Garcia-Mota, M.; Vojvodic, A.; Nørskov, J. K.; Bell, A. T. Theoretical investigation of the activity of cobalt oxides for the electrochemical oxidation of water. *J. Am. Chem. Soc.* **2013**, *135*, 13521–13530.
- (34) Nong, H. N.; Reier, T.; Oh, H.-S.; Glied, M.; Paciok, P.; Vu, T. H. T.; Teschner, D.; Heggen, M.; Petkov, V.; Schlögl, R.; et al. A Unique Oxygen Ligand Environment Facilitates Water Oxidation in Hole-doped IrNiOx Core-shell Electrocatalysts. *Nat. Catal.* **2018**, *1*, 841–851.
- (35) Zhang, R.; Dubouis, N.; Ben Osman, M.; Yin, W.; Sougrati, M. T.; Corte, D. A. D.; Giaume, D.; Grimaud, A. A Dissolution/Precipitation Equilibrium on the Surface of Iridium-Based Perovskites Controls Their Activity as Oxygen Evolution Reaction Catalysts in Acidic Media. *Angew. Chem.* **2019**, *131*, 4619–4623.
- (36) Jiao, Y.; Zheng, Y.; Davey, K.; Qiao, S.-Z. Activity origin and catalyst design principles for electrocatalytic hydrogen evolution on heteroatom-doped graphene. *Nat. Energy* **2016**, *1*, 16130.
- (37) Zhang, M.; Guo, X.; Li, Y. Synthesis and Characterization of a Copolymer Based on Thiazolothiazole and Dithienosilole for Polymer Solar Cells. *Adv. Energy Mater.* **2011**, *1*, 557–560.
- (38) Khetan, A.; Pitsch, H.; Viswanathan, V. Solvent Degradation in Nonaqueous Li-O<sub>2</sub> Batteries: Oxidative Stability versus H-Abstraction. *J. Phys. Chem. Lett.* **2014**, *5*, 2419–24.
- (39) Zheng, X.; Zhang, B.; De Luna, P.; Liang, Y.; Comin, R.; Voznyy, O.; Han, L.; Garcia de Arquer, F. P.; Liu, M.; Dinh, C. T.; et al. Theory-driven design of high-valence metal sites for water oxidation confirmed using in situ soft X-ray absorption. *Nat. Chem.* **2018**, *10*, 149–154.
- (40) Hu, H.; Guan, B. Y.; Lou, X. W. Construction of Complex CoS Hollow Structures with Enhanced Electrochemical Properties for Hybrid Supercapacitors. *Chem* **2016**, *1*, 102–113.
- (41) Koch, C. Determination of core structure periodicity and point defect density along dislocations, Arizona State University, 2002.
- (42) Zhang, Q.; Zhang, L. Y.; Jin, C. H.; Wang, Y. M.; Lin, F. CalAtom: A software for quantitatively analysing atomic columns in a transmission electron microscope image. *Ultramicroscopy* **2019**, *202*, 114–120.
- (43) Zhang, Q.; Jin, C. H.; Xu, H. T.; Zhang, L. Y.; Ren, X. B.; Ouyang, Y.; Wang, X. J.; Yue, X. J.; Lin, F. Multiple-ellipse fitting method to precisely measure the positions of atomic columns in a transmission electron microscope image. *Micron* **2018**, *113*, 99–104.
- (44) Kresse, G.; Furthmüller, J. Efficient iterative schemes for ab initio total-energy calculations using a plane-wave basis set. *Phys. Rev. B: Condens. Matter Mater. Phys.* **1996**, *54*, 11169–11186.
- (45) Kresse, G.; Furthmüller, J. Efficiency of ab-initio total energy calculations for metals and semiconductors using a plane-wave basis set. *Comput. Mater. Sci.* **1996**, *6*, 15–50.
- (46) Perdew, J. P.; Burke, K.; Ernzerhof, M. Generalized Gradient Approximation Made Simple. *Phys. Rev. Lett.* **1996**, *77*, 3865–3868.

- (47) Blöchl, P. E. Projector augmented-wave method. *Phys. Rev. B: Condens. Matter Mater. Phys.* **1994**, *50*, 17953–17979.
- (48) Chen, J.; Wu, X.; Selloni, A. Electronic structure and bonding properties of cobalt oxide in the spinel structure. *Phys. Rev. B: Condens. Matter Mater. Phys.* **2011**, *83*, 245204.
- (49) Lan, G.; Song, J.; Yang, Z. A linear response approach to determine Hubbard  $U$  and its application to evaluate properties of  $Y_2B_2O_7$ ,  $B =$  transition metals 3d, 4d and 5d. *J. Alloys Compd.* **2018**, *749*, 909–925.

# Supporting Information for

## **Short-range Ordered Iridium Single Atoms Integrated into Cobalt Oxide Spinel Structure for Highly Efficient Electrocatalytic Water Oxidation**

Jieqiong Shan<sup>1,2,†</sup>, Chao Ye<sup>1,2,†</sup>, Shuangming Chen<sup>4,†</sup>, Tulai Sun<sup>3,†</sup>, Yan Jiao<sup>1,2</sup>, Lingmei Liu<sup>5</sup>,  
Chongzhi Zhu<sup>3</sup>, Li Song<sup>4</sup>, Yu Han<sup>5</sup>, Mietek Jaroniec<sup>6</sup>, Yihan Zhu<sup>3\*</sup>, Yao Zheng<sup>1,2\*</sup> and Shi-Zhang  
Qiao<sup>1,2\*</sup>

\*Correspondence to: [yihanzhu@zjut.edu.cn](mailto:yihanzhu@zjut.edu.cn); [yao.zheng01@adelaide.edu.au](mailto:yao.zheng01@adelaide.edu.au);  
[s.qiao@adelaide.edu.au](mailto:s.qiao@adelaide.edu.au).

†These authors contributed equally.



## Determination of the mass activity and cost of catalysts

For simplification, we calculated the mass activity of  $\text{Ir}_{0.06}\text{Co}_{2.94}\text{O}_4$  based on the mass ratio of Ir because of the significantly higher price of Ir (\$52.6 per gram) in comparison with that of Co (\$33.0 per kilogram). Considering the aging process of  $\text{Ir}_{0.06}\text{Co}_{2.94}\text{O}_4$  catalyst under OER conditions, the mass activity of  $\text{Ir}_{0.06}\text{Co}_{2.94}\text{O}_4$  was achieved on the after-aging catalyst with Ir mass determined by ICP-MS. The cost of  $\text{Ir}_{0.06}\text{Co}_{2.94}\text{O}_4$  is approximately \$2.6 per gram (based on 4.93 wt% Ir), which is lower than that of the state-of-the-art OER catalyst  $\text{IrO}_2$  (~\$44.8 per gram) and  $\text{RuO}_2$  (~\$6.6 per gram, calculated using ruthenium price of \$8.7 per gram).

## Determination of surface area of catalysts

The double layer capacitance  $C_{dl}$  of the electrocatalysts was evaluated based on the CV data in a non-Faradaic potential window from 0.823 to 0.923 V. The current densities obtained from the CV curves at 0.873 V were measured at different scan rates (2, 4, 6, 8, 10, 20, 40, 60, 80 and 100  $\text{mV s}^{-1}$ ) and plotted as a function of the scan rate; the slope of the appropriate linear portion is equal to  $C_{dl}$ . The surface roughness factor ( $R_f$ ) was calculated by dividing the obtained  $C_{dl}$  by the specific capacitance of a given metal oxide with smooth planar surface<sup>1</sup>, which is generally assumed as 0.06  $\text{mF cm}^{-2}$ . The surface area of a given electrocatalyst was obtained by multiplication of the electrode geometrical area by  $R_f$  and then normalized to the mass of the loaded electrocatalyst.

## TOF calculation

The turnover frequency (TOF) values for  $\text{Ir}_x\text{Co}_{3-x}\text{O}_4$  were calculated by a similar method to that reported previously<sup>2</sup>:

$$\text{TOF} = \frac{\text{number of oxygen molecules}}{\text{number of active sites}}$$

where the number of oxygen molecules ( $N_{\text{O}}$ ) was obtained from the current density normalized to the surface area of the catalyst,  $j_{\text{catalyst}}$ , and the surface area of catalyst,  $A_{\text{catalyst}}$ , using the following equation:

$$N_{\text{O}} = j_{\text{catalyst}} \left( \frac{\text{mA}}{\text{cm}^2} \right) \times A_{\text{catalyst}} (\text{cm}^2) \times \left( \frac{1\text{C/s}}{1000 \text{ mA}} \right) \times \left( \frac{1 \text{ mol e}^-}{96485 \text{ C}} \right) \times \left( \frac{1 \text{ mol O}_2}{4 \text{ mol e}^-} \right) \times \left( \frac{6.02 \times 10^{23} \text{ O}_2}{1 \text{ mol O}_2} \right)$$

Taking  $\text{Ir}_{0.06}\text{Co}_{2.94}\text{O}_4$  as an example and considering activation of Co sites by Ir dopant (one Ir site and surrounding Co sites can be considered as one integral active site), the number of active sites ( $N_{\text{A}}$ ) for a given  $\text{Ir}_{0.06}\text{Co}_{2.94}\text{O}_4$  is estimated by the number of Ir atoms according to the following equation:

$$N_{\text{A}} = \text{loading mass of catalyst } (\mu\text{g}) \times \text{Ir mass percentage} \times \left( \frac{1 \text{ mol Ir}}{192 \text{ g}} \right) \times \left( \frac{6.02 \times 10^{23} \text{ Ir atoms}}{1 \text{ mol Ir}} \right)$$

For the purpose of comparison, the TOF values for  $\text{Co}_3\text{O}_4$  and  $\text{IrO}_2$  were also calculated, where the number of active sites was determined by calculating the number of all Co and Ir atoms in the respective OER electrocatalyst.

### **Determination of d-band centre**

The d-band centre ( $\varepsilon_d$ ) was determined as the weighted DOS centre of d-band as:

$$\varepsilon_d = \frac{\sum_i \varepsilon_i r_i}{\sum_i r_i}$$

where  $r_i$  is the DOS at energy  $\varepsilon_i$ .

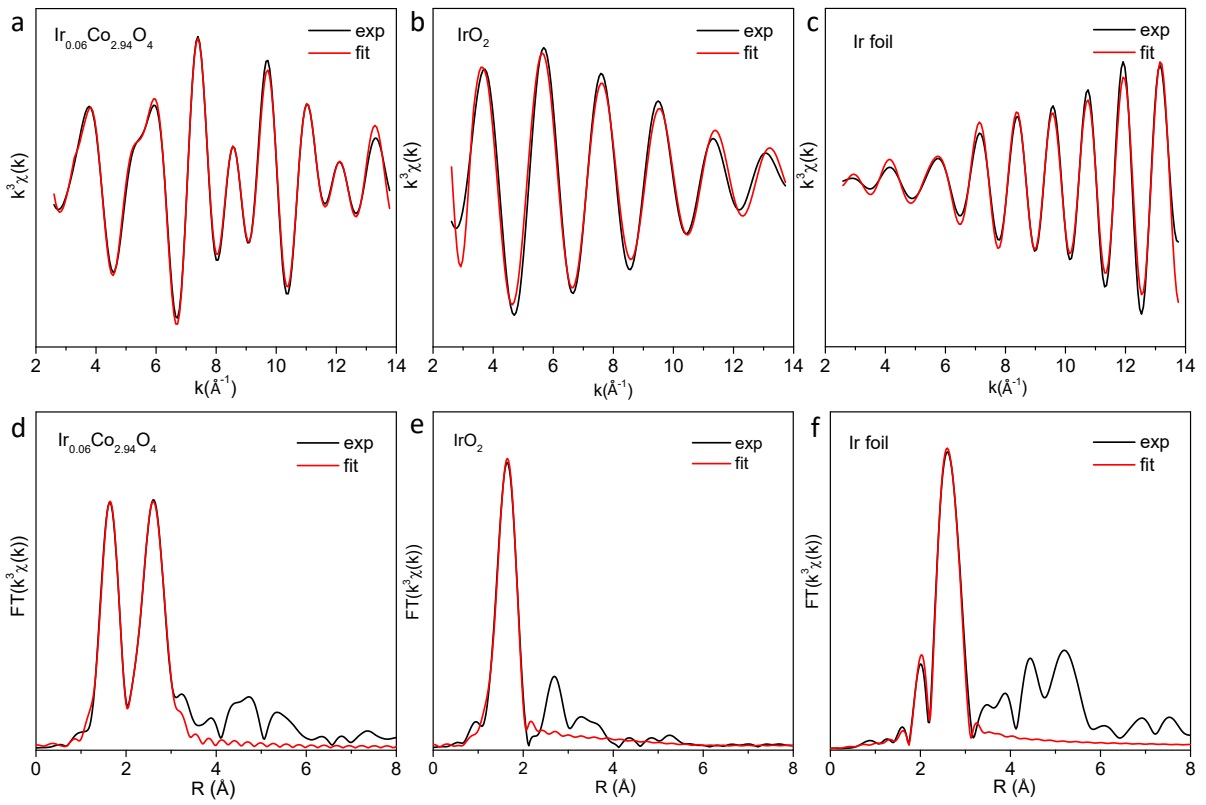


**Fig. S1.** (a-c)  $k^3$ -weighted  $k$ -space Ir  $L_3$ -edge experimental and fitting spectra of  $\text{Ir}_{0.06}\text{Co}_{2.94}\text{O}_4$  and references. (d-e) Corresponding  $k^3$ -weighted  $r$ -space Ir  $L_3$ -edge experimental and fitting spectra of  $\text{Ir}_{0.06}\text{Co}_{2.94}\text{O}_4$  and references.

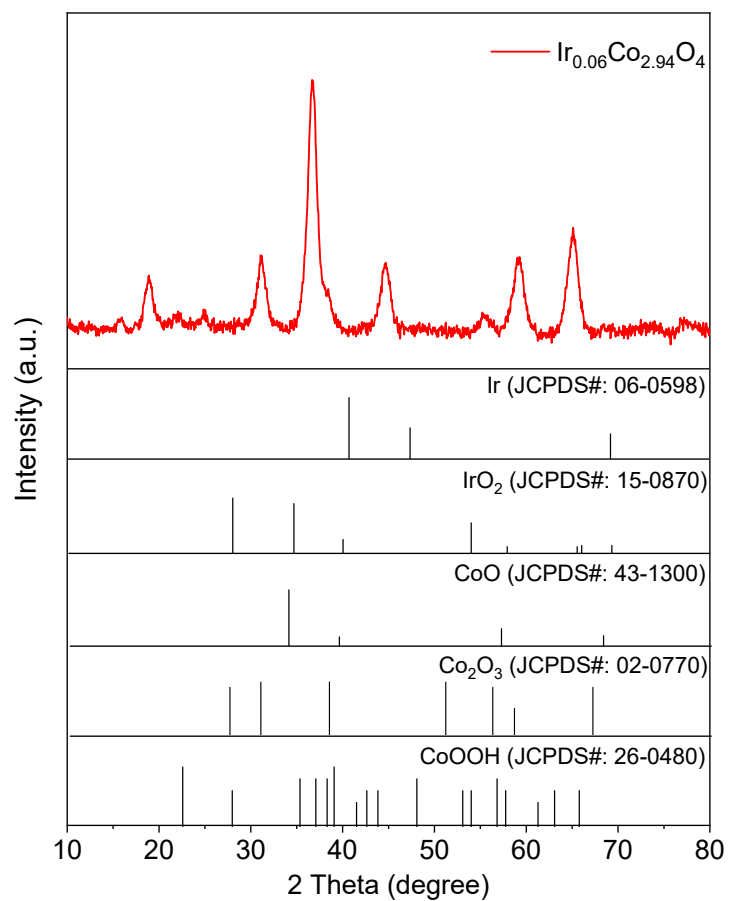


**Fig. S2.** XRD patterns of  $\text{Ir}_{0.06}\text{Co}_{2.94}\text{O}_4$  and the characteristic peaks of possible phases and impurities.

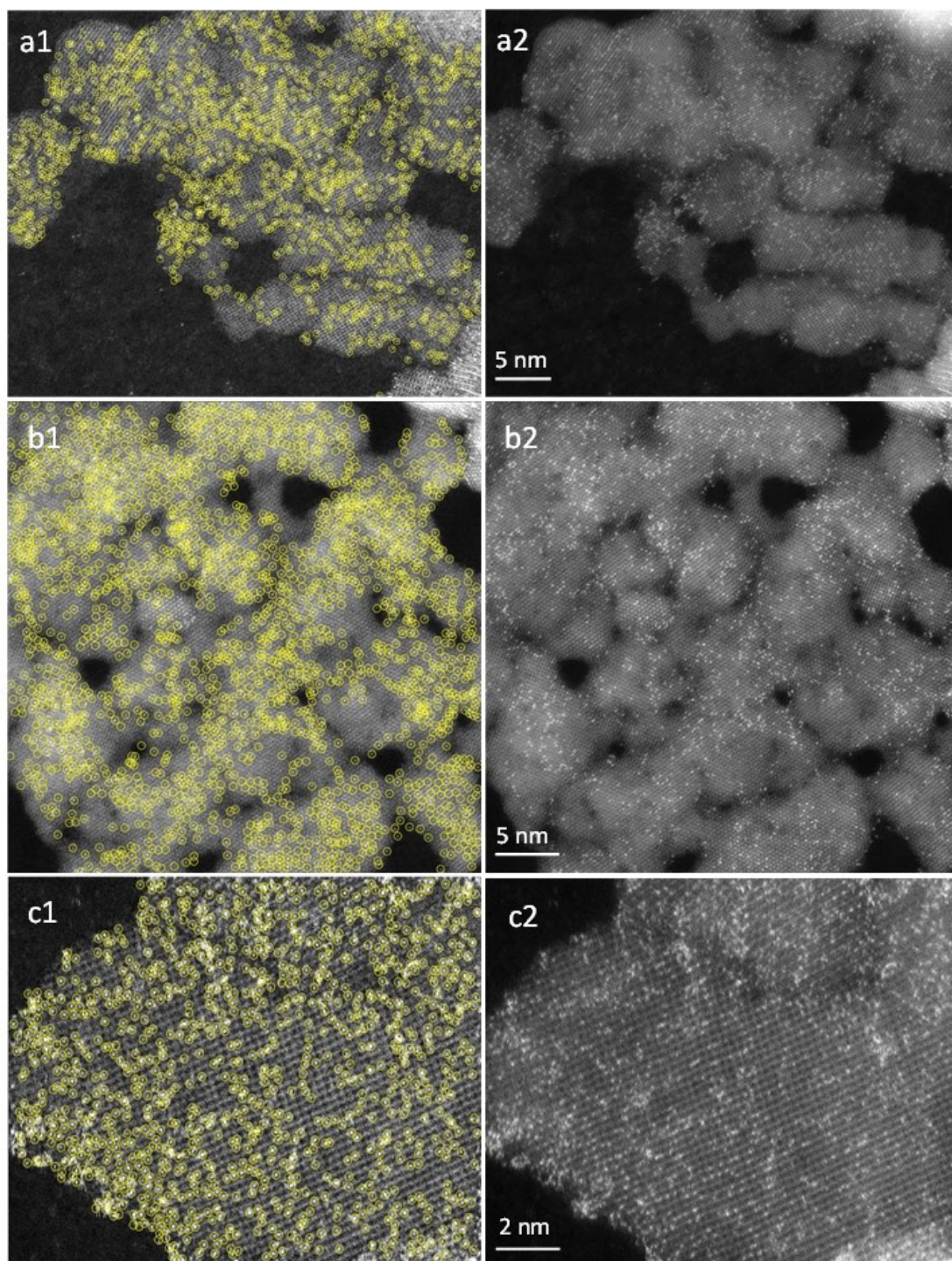


**Fig. S3.** STEM images of Ir<sub>0.06</sub>Co<sub>2.94</sub>O<sub>4</sub>. (a1) - (c1) with marked Ir doped species, while (a2) - (c2) are the corresponding raw images.

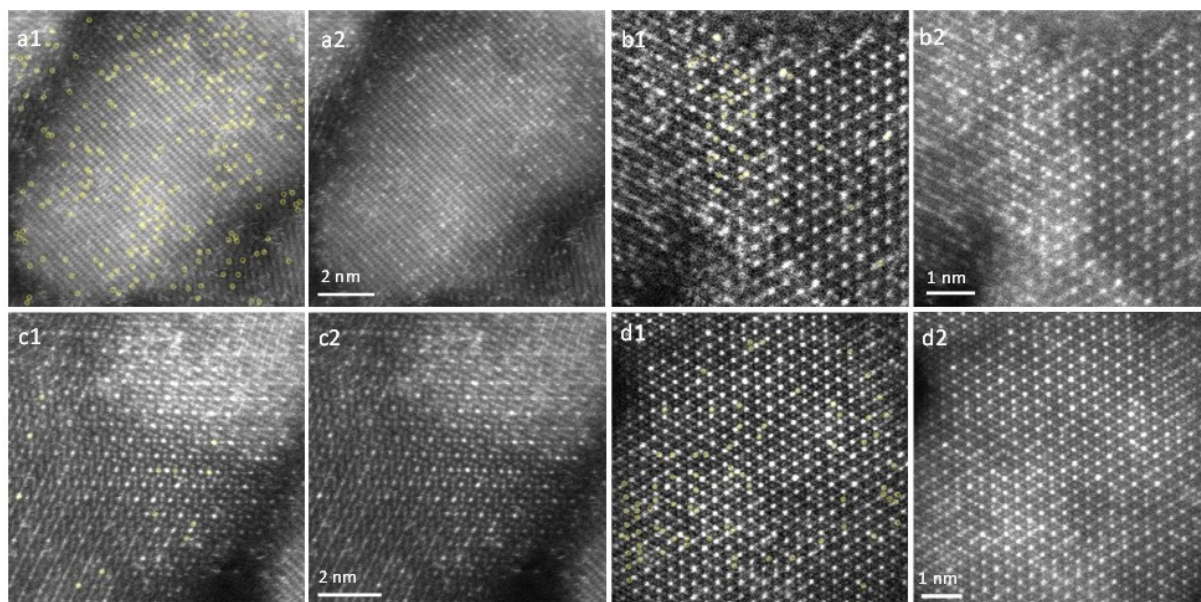


**Fig. S4.** HRSTEM images of  $\text{Ir}_{0.06}\text{Co}_{2.94}\text{O}_4$ . (a1) - (d1) with marked Ir doped species, while (a2) - (d2) are the corresponding raw images.

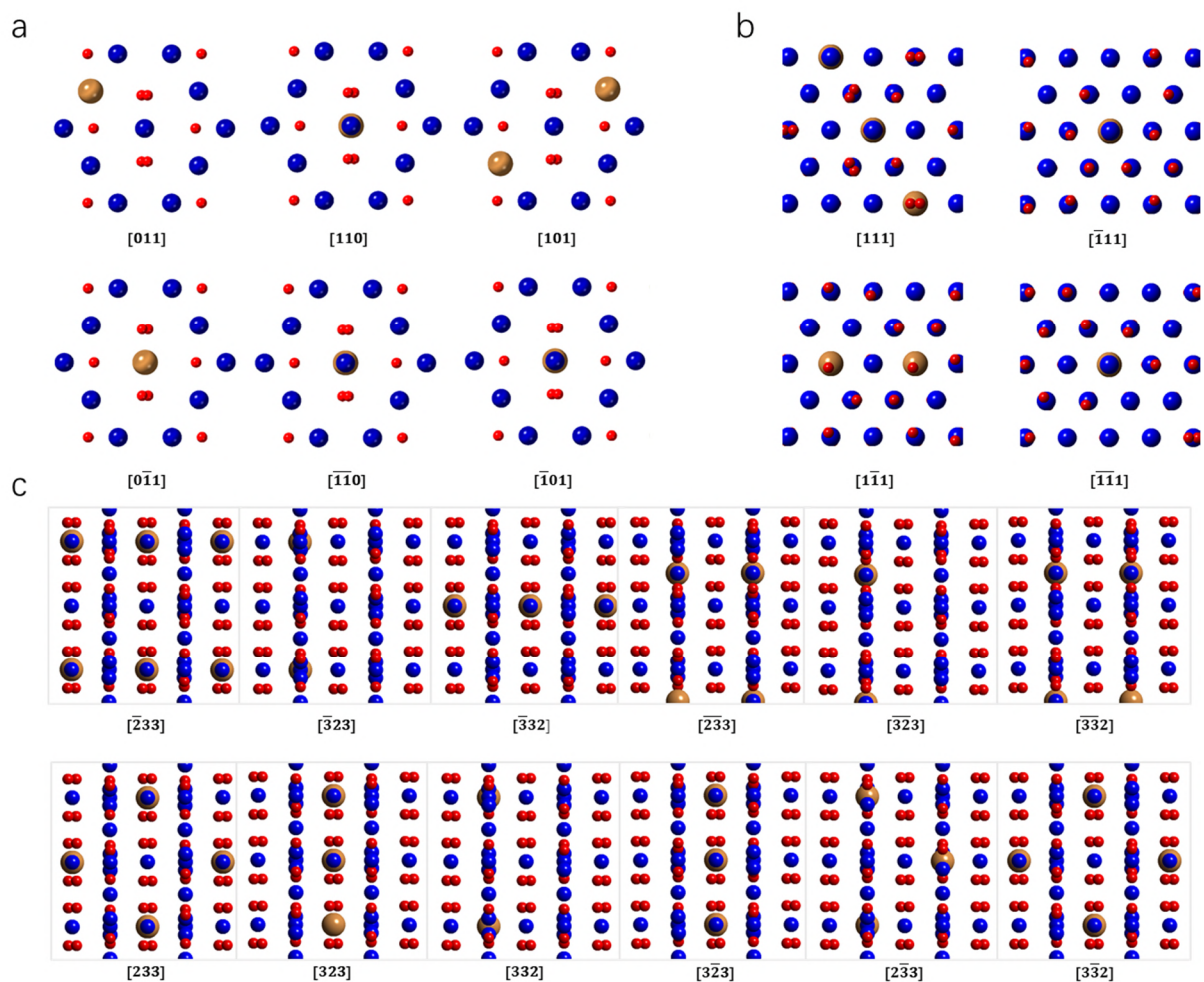


**Fig. S5.** Structural projections along all symmetry-equivalent  $\langle 011 \rangle$ ,  $\langle 111 \rangle$  and  $\langle 233 \rangle$  directions with a full column of octahedral sites substituted by Ir atoms. The blue, yellow and red spheres refer to cobalt, iridium and oxygen atoms, respectively.

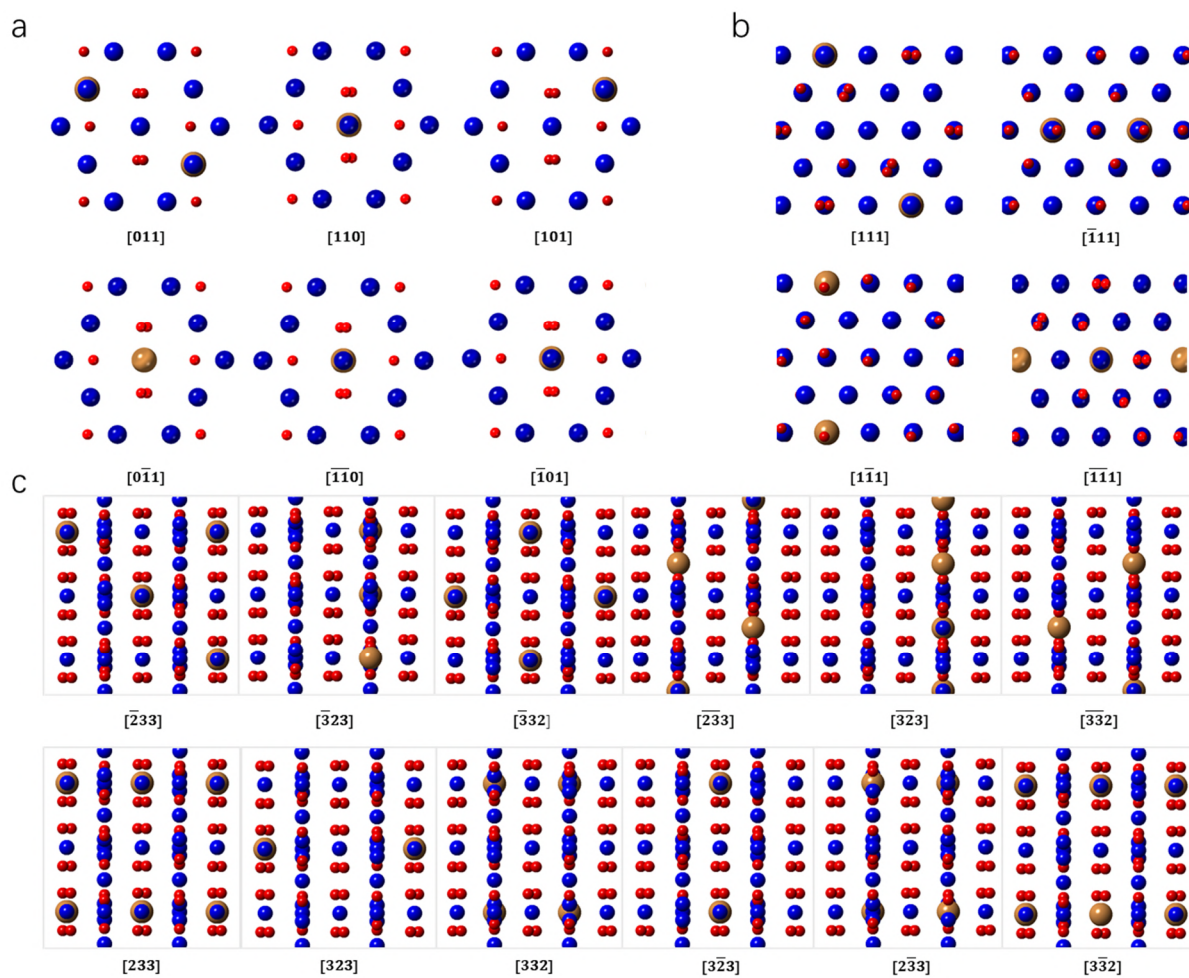


**Fig. S6.** Structural projections along all symmetry-equivalent  $\langle 011 \rangle$ ,  $\langle 111 \rangle$  and  $\langle 233 \rangle$  directions with a half column of octahedral sites substituted by Ir atoms. Colors are the same as in Fig. S5.



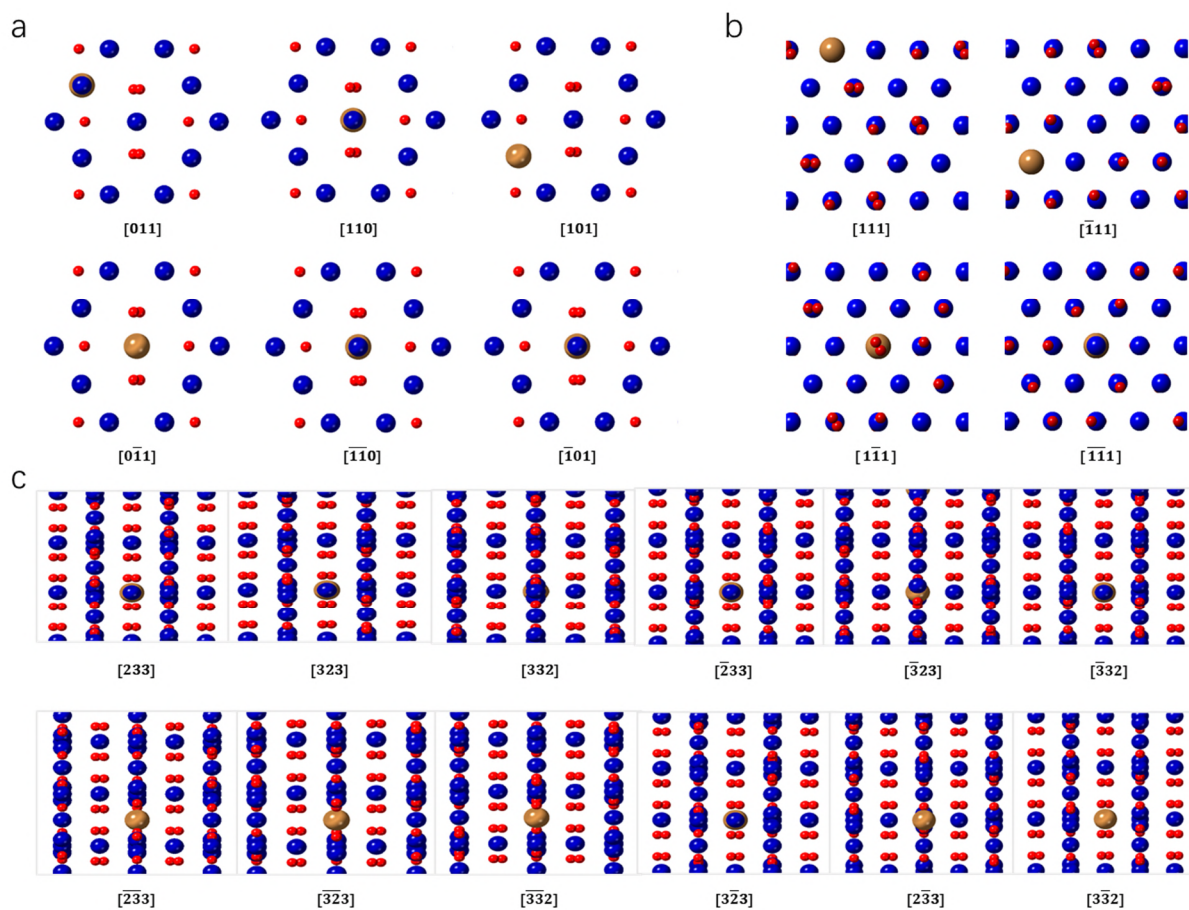


**Fig. S7.** Structural projections along all symmetry-equivalent  $\langle 011 \rangle$ ,  $\langle 111 \rangle$  and  $\langle 233 \rangle$  directions with a single octahedral site substituted by Ir atom. Colors are the same as in Fig. S5.

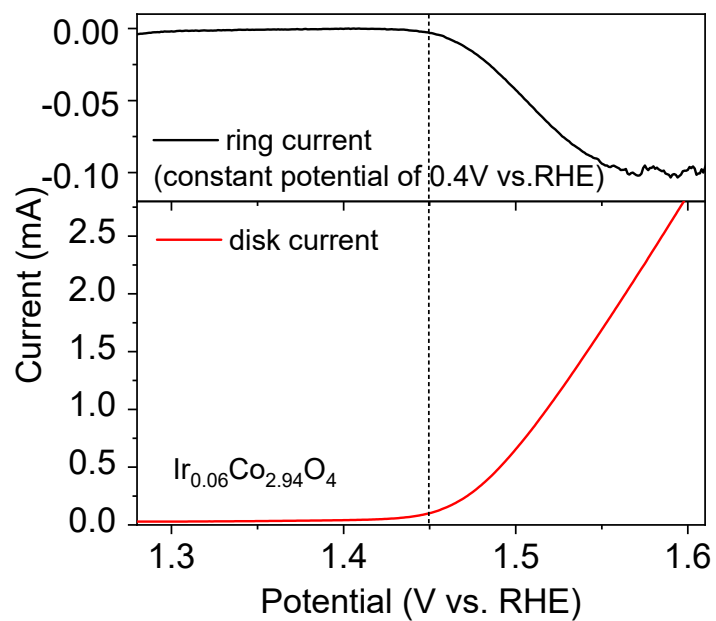


**Fig. S8.** Rotating ring disk electrode (RRDE) polarization curve recorded at the scan rate of  $5 \text{ mV s}^{-1}$  for  $\text{Ir}_{0.06}\text{Co}_{2.94}\text{O}_4$  with an electrode rotation speed of 1600 rpm. The ring potential was kept constant at 0.4 V vs. RHE, when the oxygen generated at the disk electrode was reduced to  $\text{OH}^-$ .

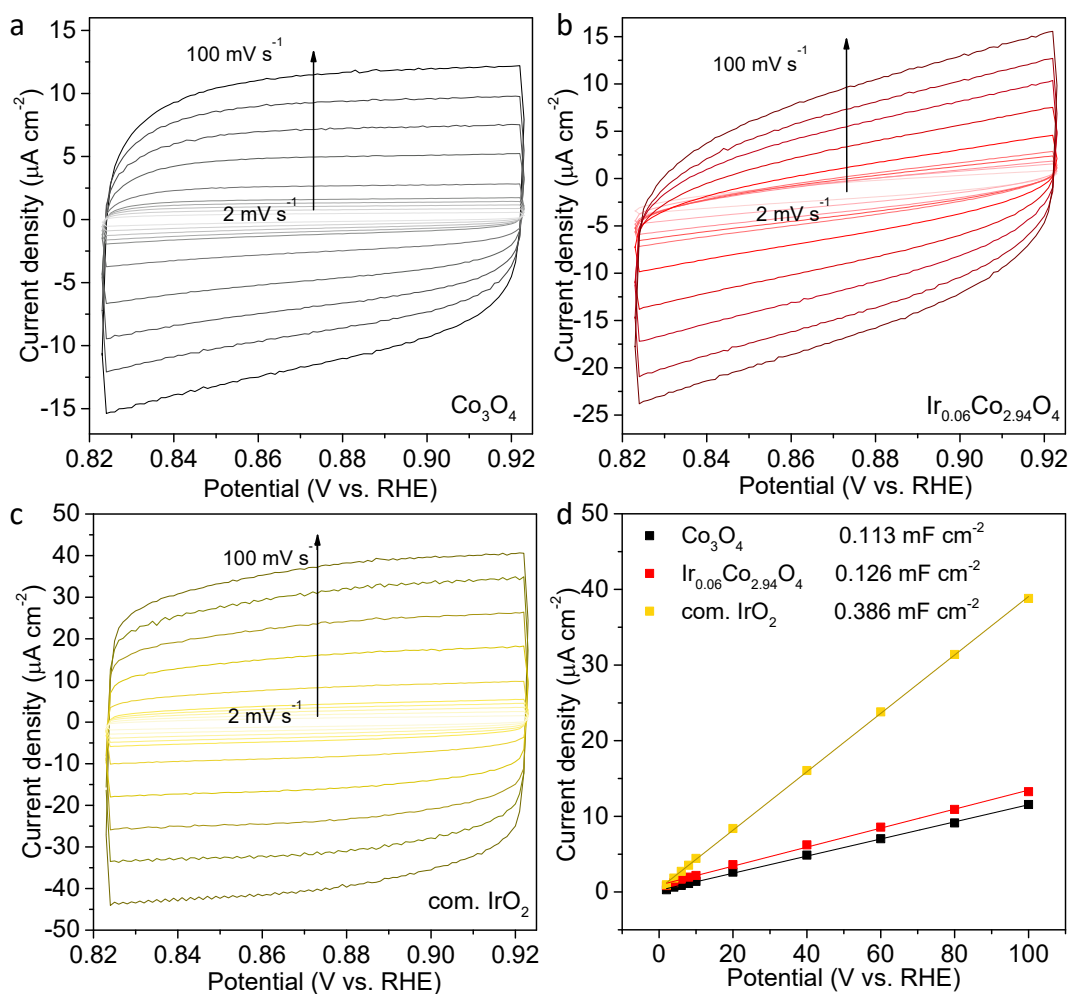


**Fig. S9.** CVs measured for (a)  $\text{Co}_3\text{O}_4$ , (b)  $\text{Ir}_{0.06}\text{Co}_{2.94}\text{O}_4$  and (c) commercial  $\text{IrO}_2$  in 0.1 M  $\text{HClO}_4$  at different scan rates of 2, 4, 6, 8, 10, 20, 40, 60, 80 and 100  $\text{mV s}^{-1}$ . (d) The corresponding plots of the current density at 0.873 V vs. the scan rate.

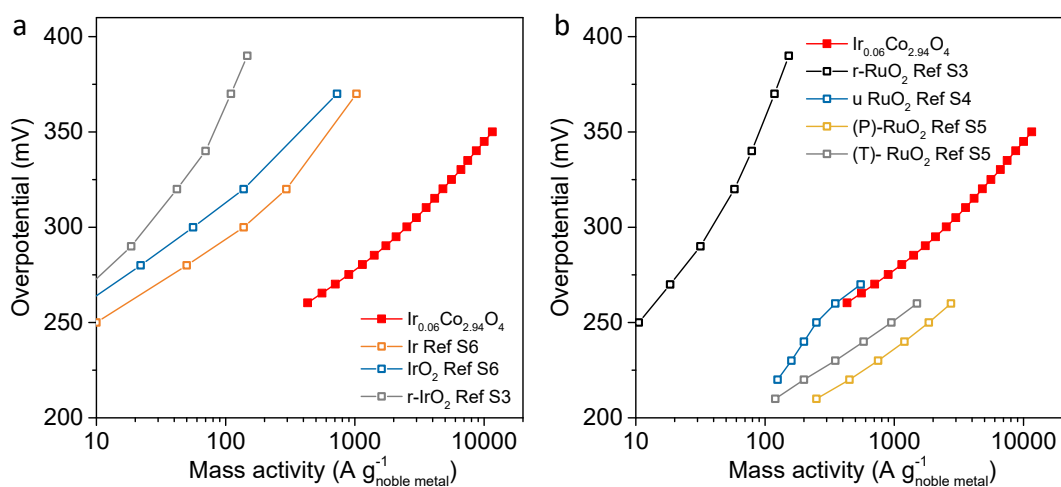


**Fig. S10.** Performance comparison for  $\text{Ir}_{0.06}\text{Co}_{2.94}\text{O}_4$  with the state-of-the-art (a) Ir and  $\text{IrO}_2$  catalysts and (b)  $\text{RuO}_2$  catalysts based on references 3, 4, 5 and 6

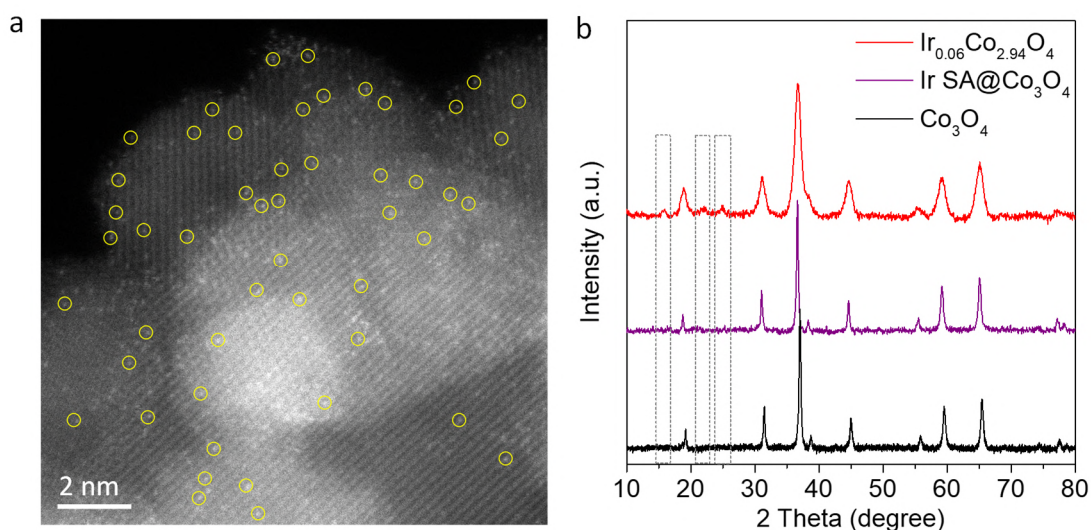


**Fig. S11.** (a) HRSTEM image of Ir SA@Co<sub>3</sub>O<sub>4</sub>, which clearly demonstrates Ir single atoms with yellow circles. (b) XRD patterns of Ir SA@Co<sub>3</sub>O<sub>4</sub> in comparison with those of Ir<sub>0.06</sub>Co<sub>2.94</sub>O<sub>4</sub> and pure Co<sub>3</sub>O<sub>4</sub>. Different from Ir<sub>0.06</sub>Co<sub>2.94</sub>O<sub>4</sub>, the Ir SA@Co<sub>3</sub>O<sub>4</sub> catalyst exhibits an identical XRD pattern of Co spinel oxide without any additional reflections.

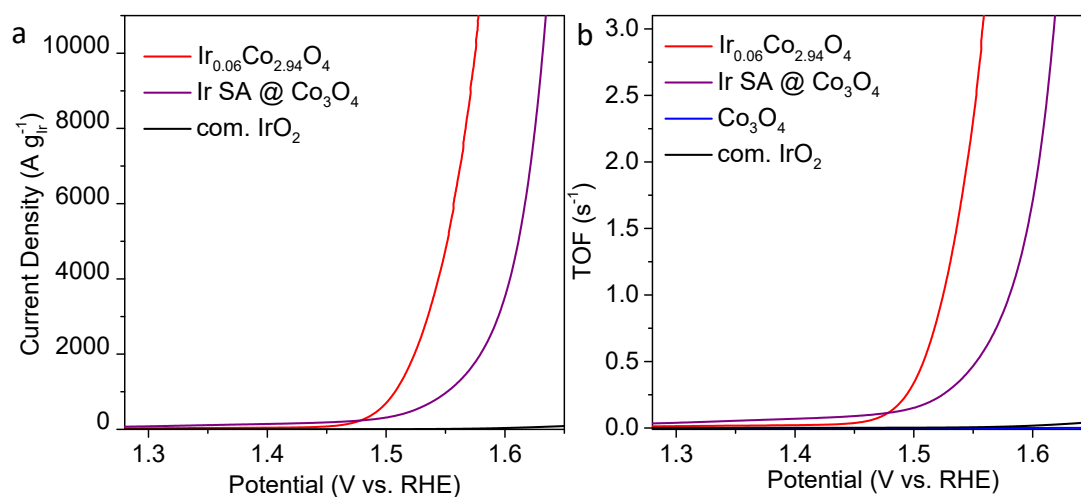


**Fig. S12.** Mass activity and TOF plotted as a function of the potential for various catalysts.

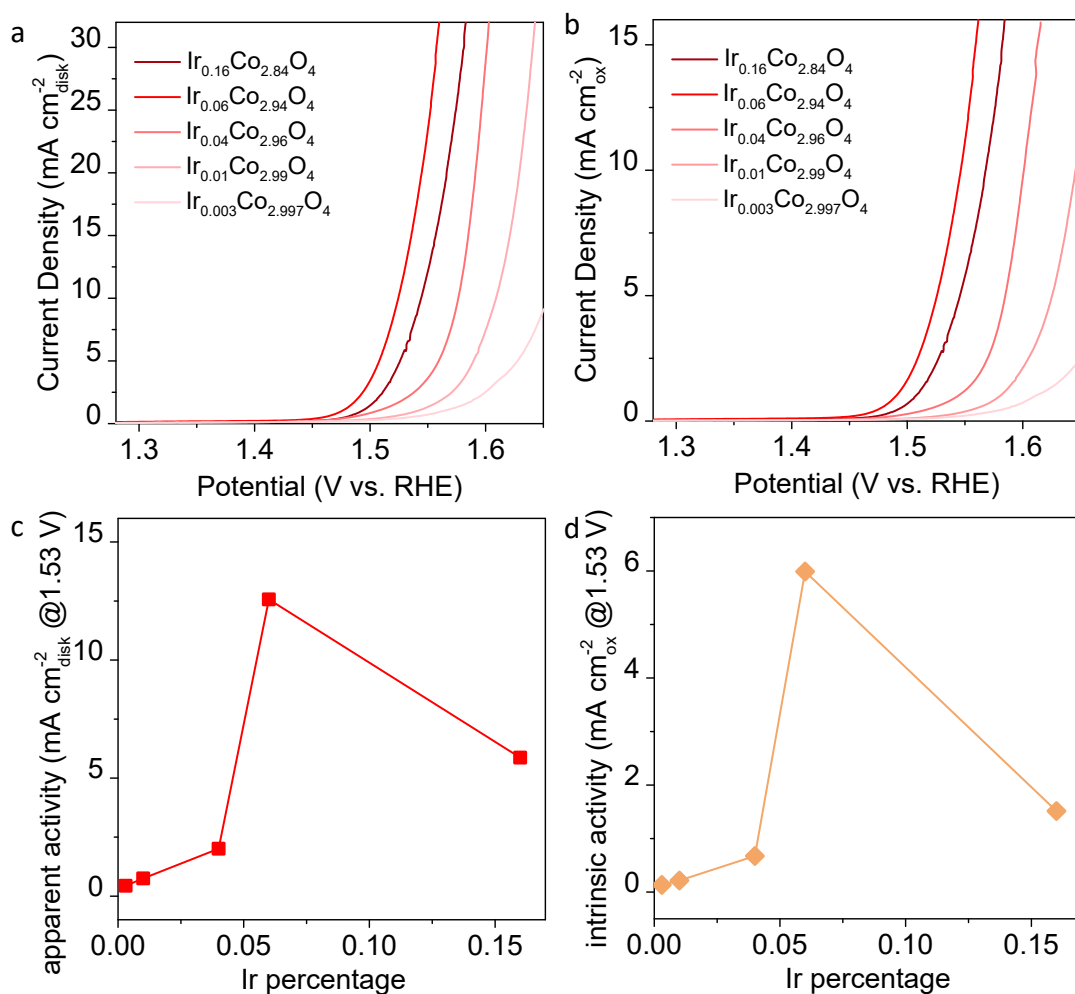


**Fig. S13.** LSV curves normalized to (a) the geometric area of the disk electrode and (b) the surface area of Ir<sub>x</sub>Co<sub>3-x</sub>O<sub>4</sub> catalysts. (c, d) The Ir percentage dependence of the apparent activity (based on the data in panel a) and intrinsic activity (based on the data in panel b) for different catalysts. Their apparent and intrinsic activities exhibit similar trends as Ir<sub>0.06</sub>Co<sub>2.94</sub>O<sub>4</sub> showing the best performance while the activity of other samples decreases with decreasing Ir ratio. We propose that the relatively poor performance of catalysts with lower ratios of Ir substitutions is due to the absence of ordering among Ir sites, while the catalyst with higher Ir substitution ratio can suffer from reduced use of Ir sites.

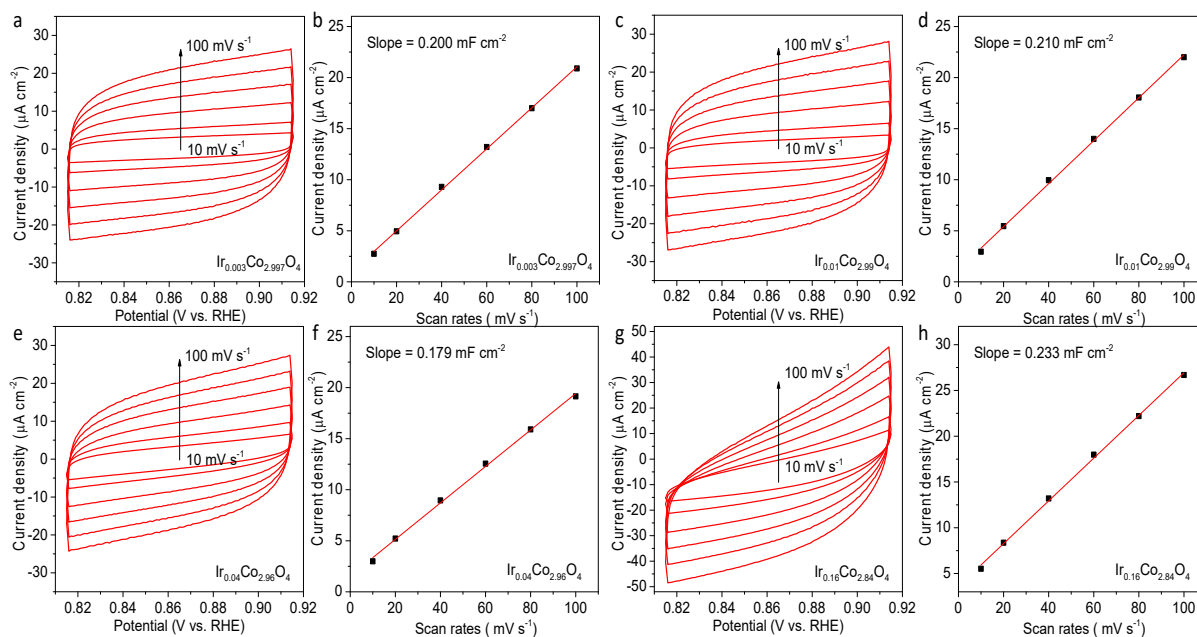


**Fig. S14.** CV curves and the corresponding plots of the current density at 0.873 V vs. the scan rate for various electrocatalysts.

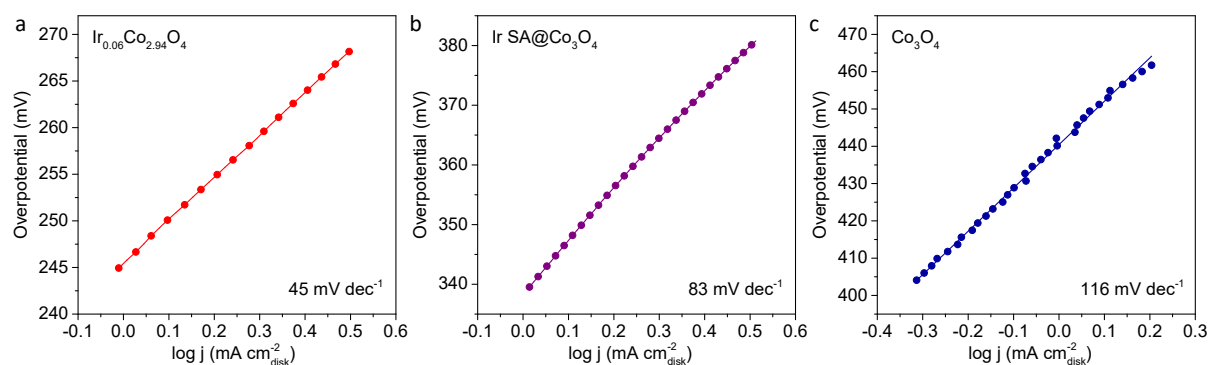


**Fig. S15.** Tafel plots of (a)  $\text{Ir}_{0.06}\text{Co}_{2.94}\text{O}_4$ , (b)  $\text{Ir SA@Co}_3\text{O}_4$  and (c) pure  $\text{Co}_3\text{O}_4$  catalysts.

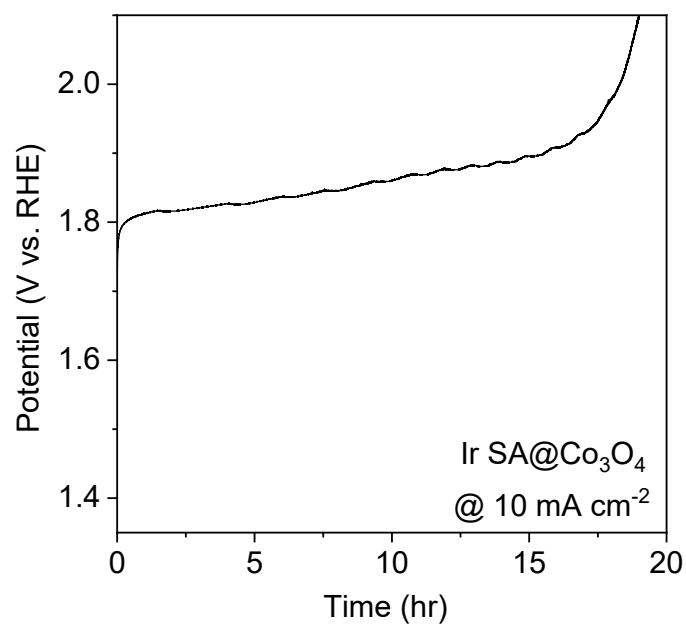


**Fig. S16.** Constant current chronopotentiometric stability measurement at an anodic current density of 10 mA cm<sup>-2</sup> for Ir SA@Co<sub>3</sub>O<sub>4</sub> in 0.1 M HClO<sub>4</sub>.

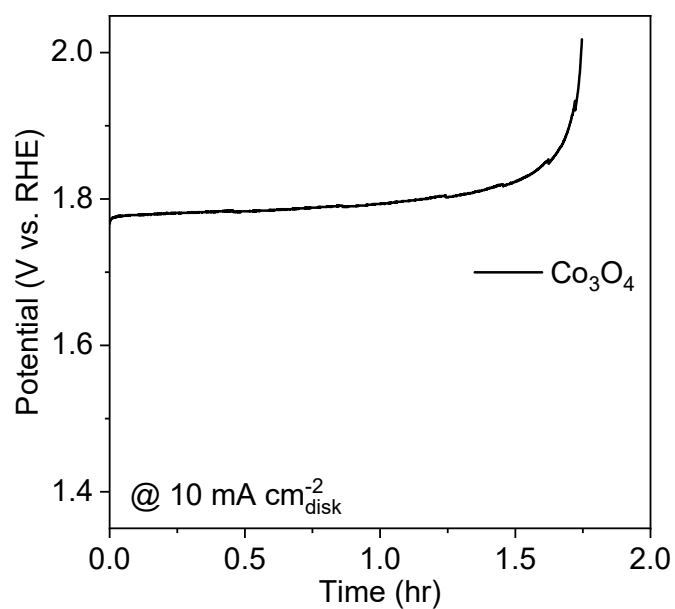


**Fig. S17.** Constant current chronopotentiometric stability measurements at anodic current density of 10 mA cm<sup>-2</sup> for Co<sub>3</sub>O<sub>4</sub> in 0.1 M HClO<sub>4</sub>.

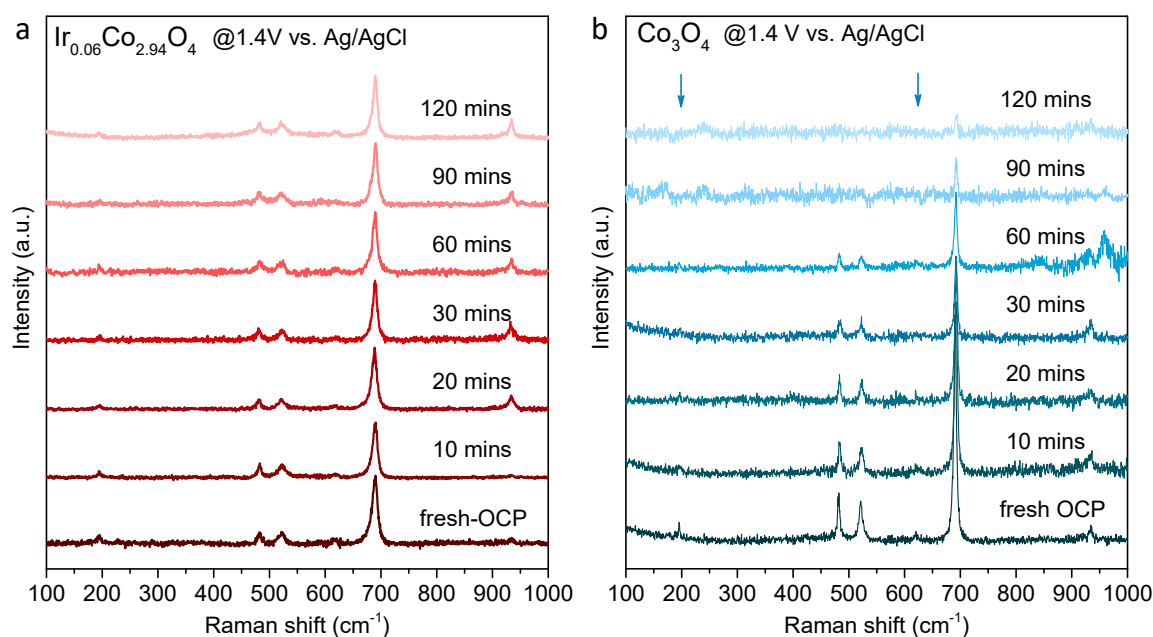


**Fig. S18.** *In-situ* Raman spectroscopy measurements for OER occurring on  $\text{Ir}_{0.06}\text{Co}_{2.94}\text{O}_4$  and  $\text{Co}_3\text{O}_4$  catalysts. The spectra were recorded at different time under a constant potential of 1.4 V vs. Ag/AgCl. All the characteristic bands ( $A_{1g}$  at  $\sim 690\text{ cm}^{-1}$ ,  $F_{2g}(1-3)$  at  $\sim 197, 484, 523\text{ cm}^{-1}$  and  $E_g$  at  $\sim 620\text{ cm}^{-1}$  originating from Co spinel oxide) of the  $\text{Ir}_{0.06}\text{Co}_{2.94}\text{O}_4$  catalyst are well maintained during continuous OER experiments under a constant potential of 1.4 V. By contrast, for the  $\text{Co}_3\text{O}_4$  catalyst, the Raman bands belonging to the  $\text{Co}_3\text{O}_4$  phase decrease significantly and almost no characteristic Raman bands belonging to cobalt spinel oxide can be observed after two-hour continuous OER process. The band at  $\sim 930\text{ cm}^{-1}$  comes from  $(\text{ClO}_4^-)$  in 0.1 M  $\text{HClO}_4$  electrolyte.



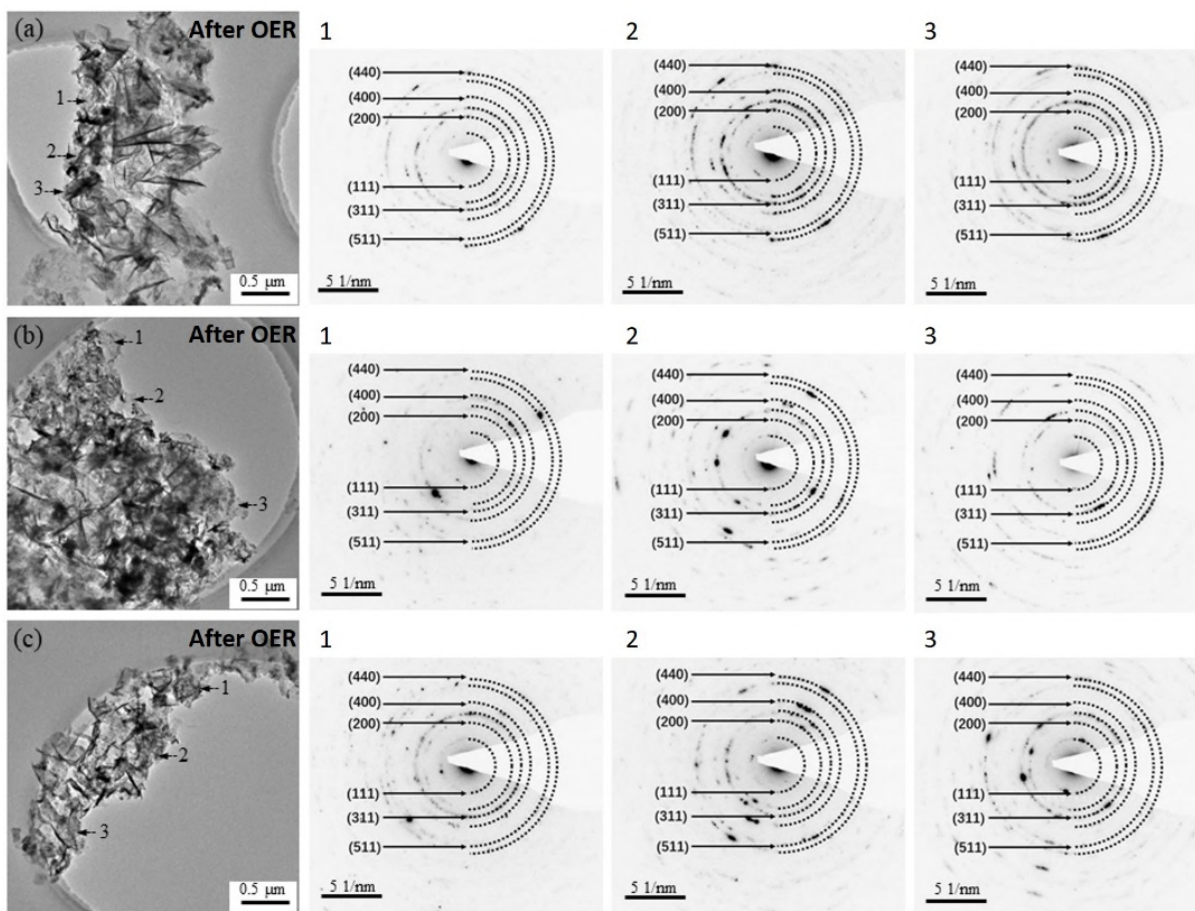


**Fig. S19.** (a-c) Randomly chosen spots in the  $\text{Ir}_{0.06}\text{Co}_{2.94}\text{O}_4$  catalyst after the OER testing for selected area electron diffraction (SAED) analysis. (a<sub>1-3</sub>, b<sub>1-3</sub>, c<sub>1-3</sub>) SAED patterns recorded for the marked 1, 2 and 3 regions in (a-c), respectively.

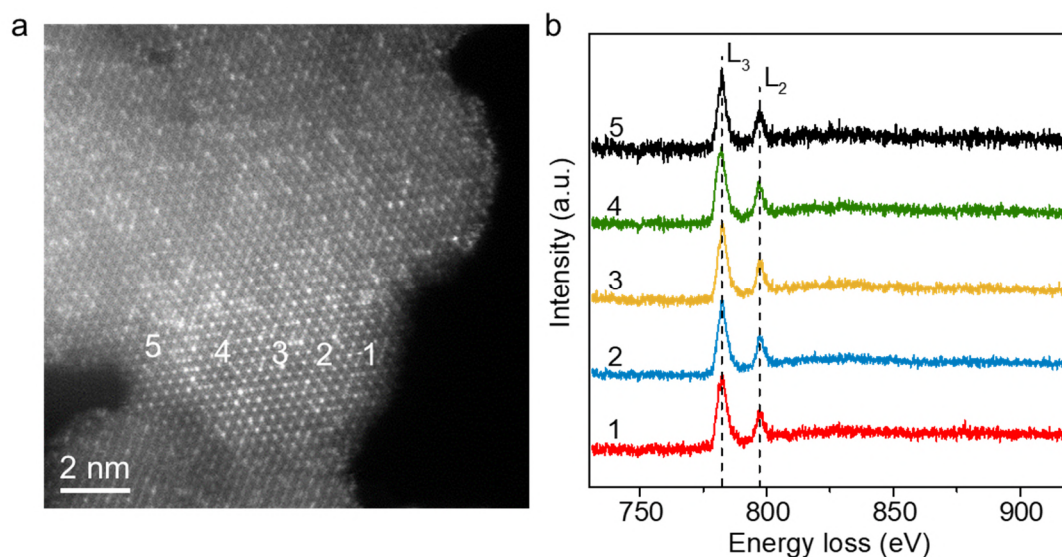


**Fig. S20.** (a) Atomic resolution HAADF image of a randomly chosen region in the post-OER  $\text{Ir}_{0.06}\text{Co}_{2.94}\text{O}_4$  catalyst for EELS. (b) EELS spectra corresponding to the collection points marked by numbers in (a).

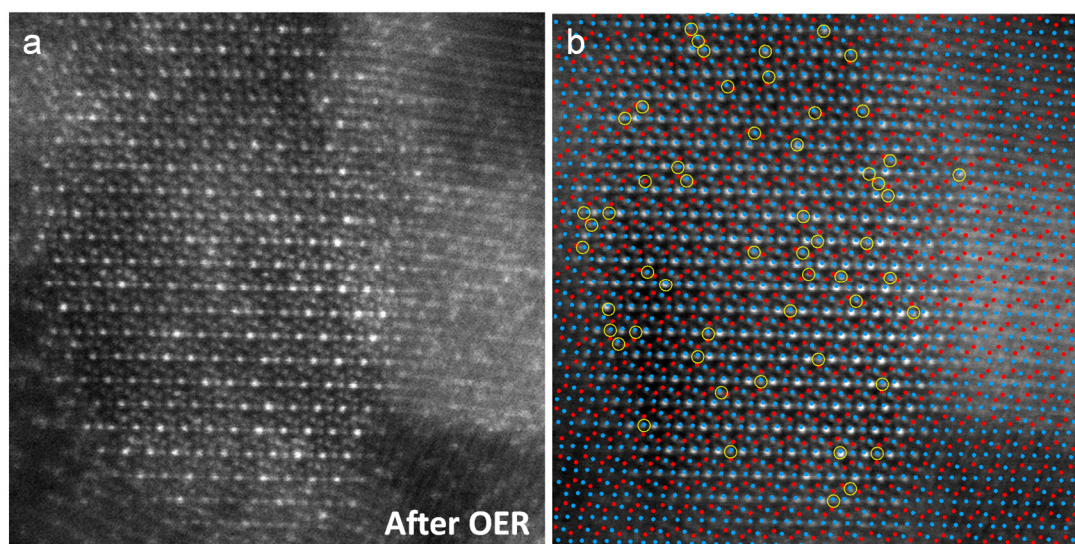


**Fig. S21.** (a) HRTEM image of the  $\text{Ir}_{0.06}\text{Co}_{2.94}\text{O}_4$  sample after the OER from zone  $\langle 110 \rangle$  with an unambiguous distribution of distinct sites, which are octahedral and tetrahedral. (b) The theoretical positions of different sites and Ir-substituting atom columns from experimental observation (a) are separated by marking them with blue (octahedral), red (tetrahedral) dots and yellow circles (Ir-substitution).

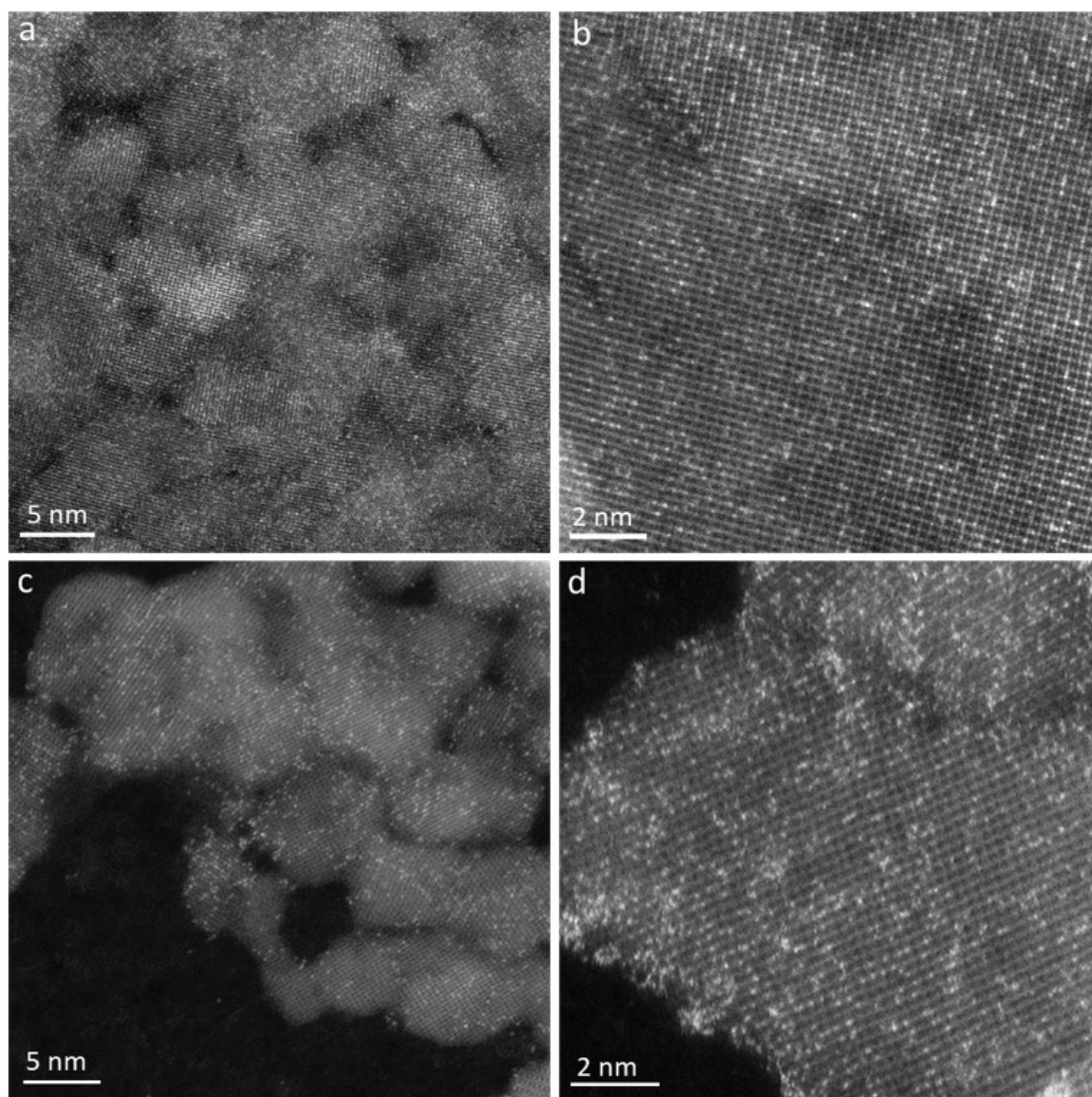


**Fig. S22.** HRSTEM images of (a, b) fresh and (c, d) post-OER  $\text{Ir}_{0.06}\text{Co}_{2.94}\text{O}_4$  catalysts.

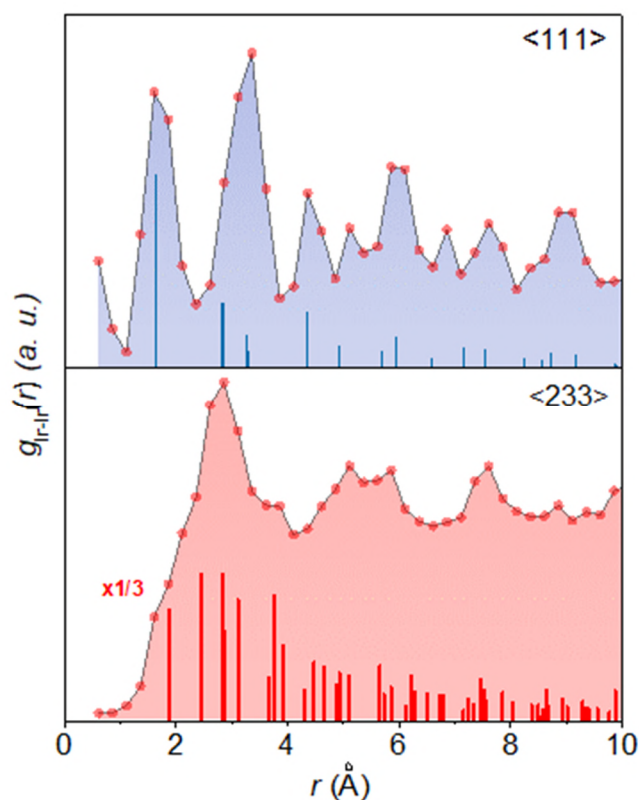


**Fig. S23.** The pPDF profiles for  $\langle 111 \rangle$  and  $\langle 233 \rangle$  projections for  $\text{Ir}_{0.06}\text{Co}_{2.94}\text{O}_4$  before OER test (achieved by labelling individual 3269 Ir sites in multiple-projection images). The navy and red bars refer to calculated pPDF histograms for the projected  $\text{Co}_{\text{oct}}$  cationic lattice of the  $\text{Co}_3\text{O}_4$  framework along  $\langle 111 \rangle$  and  $\langle 233 \rangle$  directions, respectively.

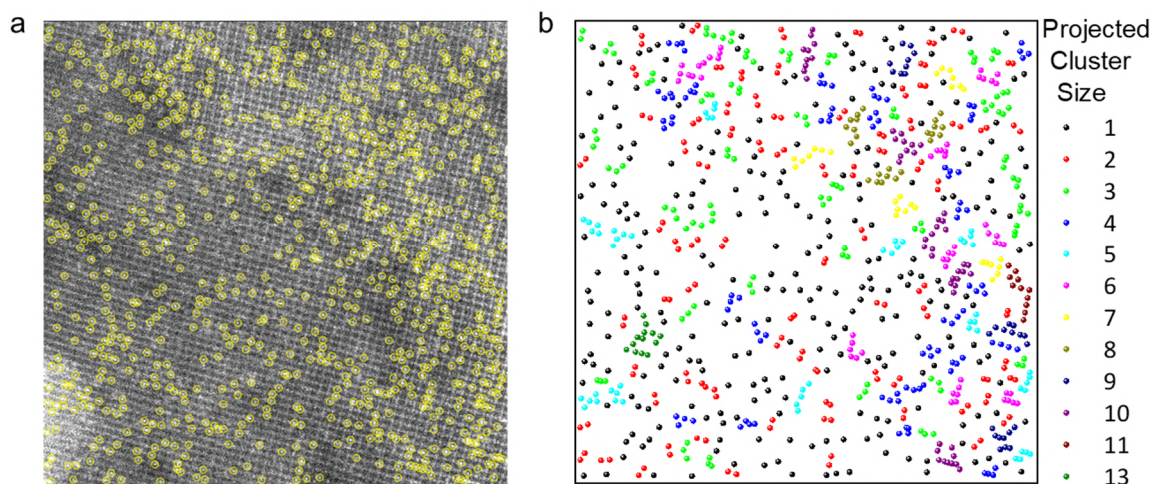


**Fig. S24.** (a) A typical HRSTEM image taken along  $\langle 233 \rangle$  zone axis of the  $\text{Ir}_{0.06}\text{Co}_{2.94}\text{O}_4$  catalyst before OER test, with Ir sites labelled by yellow circles. (b) Fitted, optimized and extracted coordinates for these Ir dopant sites.

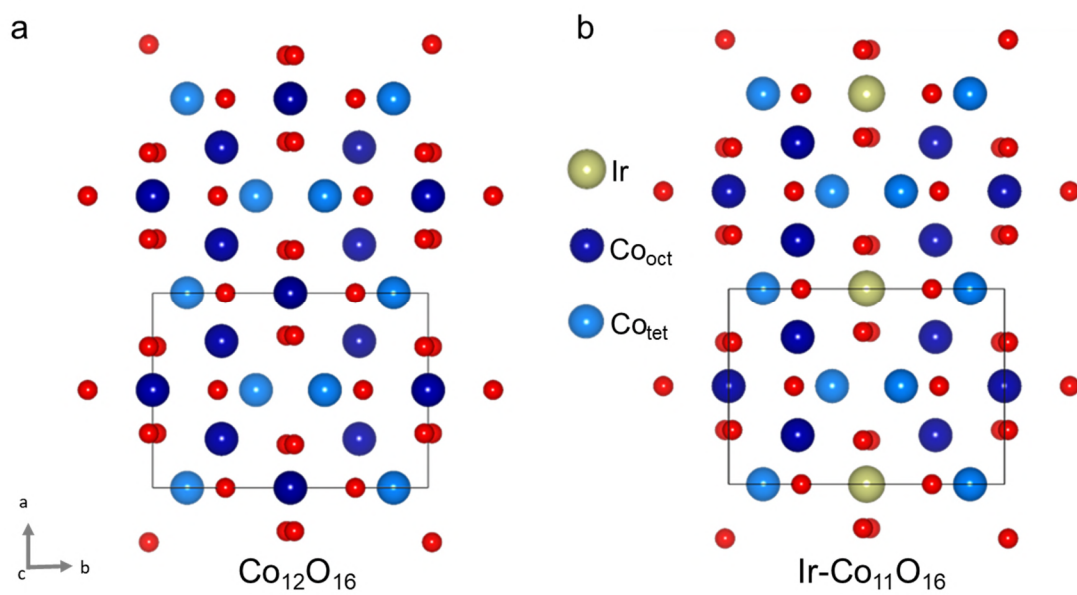


**Fig. S25.** Structure models of (a) pure  $\text{Co}_{12}\text{O}_{16}$  and (b)  $\text{Ir-Co}_{11}\text{O}_{16}$ .

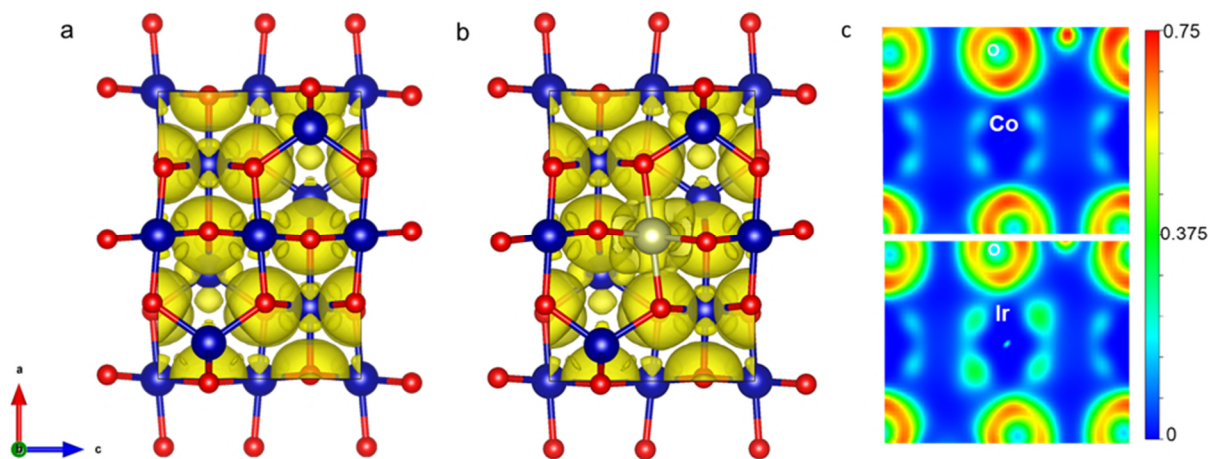


**Fig. S26.** ELF analysis of (a)  $\text{Co}_{12}\text{O}_{16}$  and (b)  $\text{Ir-Co}_{11}\text{O}_{16}$ . (c) ELF plots of  $\text{Co}_{12}\text{O}_{16}$  (upper) and  $\text{Ir-Co}_{11}\text{O}_{16}$  (lower) along the  $(0\ 1\ 0)$  plane with an isosurface value of  $0.2\ e\ \text{\AA}^{-3}$ .

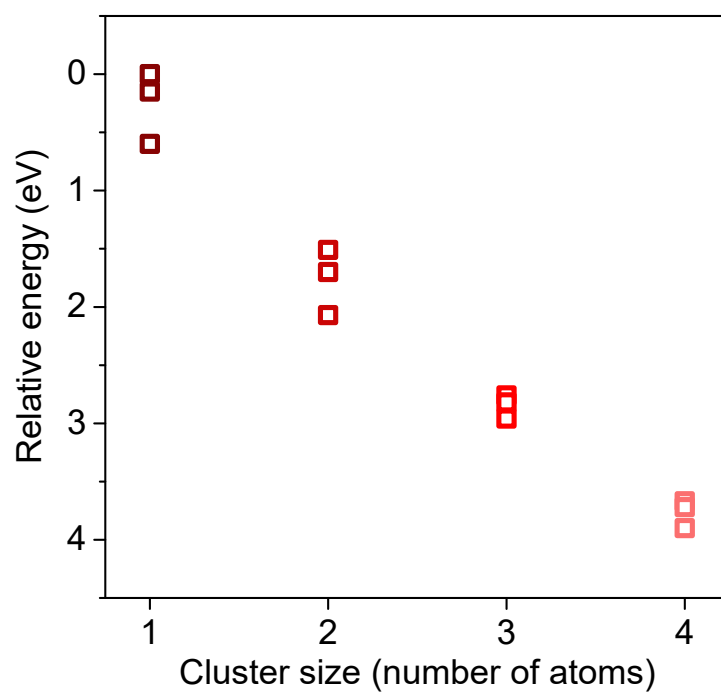


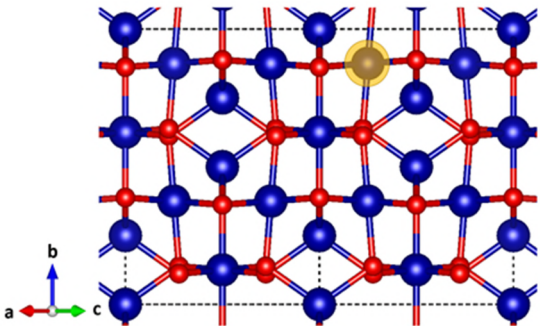
**Fig. S27.** Calculated relative energies of the Ir<sub>4</sub>-Co<sub>44</sub>O<sub>64</sub> models with different Ir cluster sizes. The configuration with the lowest free energy is defined as 0 eV and the relative energies of the other configurations were determined accordingly.

**Table S1.** Fitting parameters of Fourier transform Ir L<sub>3</sub>-edge XAFS data for Ir<sub>0.06</sub>Co<sub>2.94</sub>O<sub>4</sub>, IrO<sub>2</sub> and Ir foil.

Sample		CN	Bond length	$\sigma^2(10^{-3} \text{ \AA}^2)$
Ir <sub>0.06</sub> Co <sub>2.94</sub> O <sub>4</sub>	Ir-O	5.7	2.01	5.0
	Ir-Co	4.4	2.91	4.6
	Ir-Ir	2.3	2.75	5.5
IrO <sub>2</sub>	Ir-O	6*	2.01	5.4
Ir foil	Ir-Ir	12*	2.71	3.1

CN, coordination number;  $\sigma^2$ , Debye-Waller factor; Error limits (accuracies) were estimated as follows: CN,  $\pm 10\%$ ; bond length,  $\pm 1\%$ ;  $\sigma^2$ ,  $\pm 10\%$ . \* refers to the fixed coordination number according to the standard crystal structure.

**Table S2.** Simulation conditions of the XRD patterns.

Parameters	Value
Model	
Substitution sites	Co <sub>oct</sub>
Dopants	Ir
Diffractometer	Bragg-Brentano
Wavelength	1.54056 (I <sub>1</sub> )/1.54439 (I <sub>2</sub> ) Å, I <sub>2</sub> /I <sub>1</sub> = 0.5
Profile	Pseudo-Voigt
2θ range	5 ~ 90°
Coherent lengths	8 nm along <110>

**Table S3.** Comparison of the surface parameters, mass activity, intrinsic activity and TOF values for Ir<sub>0.06</sub>Co<sub>2.94</sub>O<sub>4</sub>, Co<sub>3</sub>O<sub>4</sub> and commercial IrO<sub>2</sub> electrocatalysts investigated in 0.1 M HClO<sub>4</sub>.

<b>Samples</b>	<b>C<sub>dl</sub></b> <b>(mF cm<sup>-2</sup>)</b>	<b>R<sub>f</sub></b>	<b>Surface</b> <b>area<sup>a</sup></b> <b>(m<sup>2</sup> g<sup>-1</sup>)</b>	<b>Mass</b> <b>activity<sup>b</sup> (A</b> <b>g<sup>-1</sup> noble</b> <b>metal)</b>	<b>Intrinsic</b> <b>activity<sup>b</sup></b> <b>(mA cm<sup>-2</sup></b> <b>catalyst)</b>	<b>TOF<sup>b</sup> (s<sup>-1</sup>)</b>
<b>Ir<sub>0.06</sub>Co<sub>2.94</sub>O<sub>4</sub></b>	0.126	2.10	2.1	2511	5.99	1.25
<b>Co<sub>3</sub>O<sub>4</sub></b>	0.113	1.88	1.8	-	0.059	0.00022
<b>IrO<sub>2</sub></b>	0.386	6.43	6.3	9	0.12	0.0042

<sup>a</sup>: the surface area was calculated by multiplying the electrode geometrical area by R<sub>f</sub> and then normalized by taking into account the loading mass of electrocatalysts; <sup>b</sup>: the mass activity, specific activity and TOF values were obtained from the current density values at an overpotential of 300 mV. The mass activity of Ir<sub>0.06</sub>Co<sub>2.94</sub>O<sub>4</sub> was achieved on the after-aging catalyst with Ir mass determined by ICP-MS.



**Table S4.** Comparison of the reported noble metal-based electrocatalysts in acidic media.

Catalyst	Electrolyte	Overpotential (mV)	Mass activity (A g <sup>-1</sup> )	Loading amount	Ref
<b>Ir<sub>0.06</sub>Co<sub>2.94</sub>O<sub>4</sub></b>	0.1 M HClO <sub>4</sub>	292@10 mA cm <sup>-2</sup>	2511 A g <sub>Ir</sub> <sup>-1</sup> @ 1.53 V	5 μg <sub>Ir</sub> cm <sup>-2</sup>	This work
<b>r-RuO<sub>2</sub></b>	0.1 M HClO <sub>4</sub>	450@10;250@10 μA cm <sub>ox</sub> <sup>-2</sup>	11 A g <sub>ox</sub> <sup>-1</sup> @ 1.48V	0.05 mg <sub>ox</sub> cm <sup>-2</sup>	3
<b>r-IrO<sub>2</sub></b>	0.1 M HClO <sub>4</sub>	435@10;250@4 μA cm <sub>ox</sub> <sup>-2</sup>	3 A g <sub>ox</sub> <sup>-1</sup> @ 1.48V	0.05 mg <sub>ox</sub> cm <sup>-2</sup>	3
<b>RuO<sub>2</sub></b>	0.1 M HClO <sub>4</sub>		~200 A g <sub>Ru</sub> <sup>-1</sup> @ 1.47V		4
<b>(P)-RuO<sub>2</sub></b>	0.05 M H <sub>2</sub> SO <sub>4</sub>		~1200 A g <sub>Ru</sub> <sup>-1</sup> @ 1.47V		5
<b>(T)-RuO<sub>2</sub></b>	0.5 M H <sub>2</sub> SO <sub>4</sub>		~580 A g <sub>Ru</sub> <sup>-1</sup> @ 1.47V		5
<b>IrNi nanowires</b>	0.1 M HClO <sub>4</sub>		1650 A g <sub>Ir</sub> <sup>-1</sup> @ 1.53V	27.7 μg <sub>Ir</sub> cm <sup>-2</sup>	6
<b>Cu doped RuO<sub>2</sub></b>	0.5 M H <sub>2</sub> SO <sub>4</sub>	188 @ 10 mA cm <sup>-2</sup>		~0.275 mg cm <sup>-2</sup> (0.251 mg <sub>Ru</sub> cm <sup>-2</sup> )	7
<b>IrW nanodendrites</b>	0.1 M HClO <sub>4</sub>	300 @ 8.1 mA cm <sup>-2</sup>		10.2 μg <sub>Ir</sub> cm <sup>-2</sup>	8
<b>Ru<sub>1</sub>-Pt<sub>3</sub>Cu</b>	0.1 M HClO <sub>4</sub>	220 @ 10	779 A g <sub>Pt+Ru</sub> <sup>-1</sup> 6615 A g <sub>Ru</sub> <sup>-1</sup> @ 1.51 V	0.0163 mg <sub>Pt+Ru</sub> cm <sup>-2</sup> 0.00192 mg <sub>Ru</sub> cm <sup>-2</sup>	9
<b>Ir-STO</b>	0.1 M HClO <sub>4</sub>	247 @ 10	820 A g <sub>Ir</sub> <sup>-1</sup> @ 1.525 V	0.21 mg cm <sup>-2</sup> , 0.0588 mg <sub>Ir</sub> cm <sup>-2</sup>	10
<b>Li-IrO<sub>x</sub></b>	0.5 M H <sub>2</sub> SO <sub>4</sub>	290 @ 10	100 A g <sub>Ir</sub> <sup>-1</sup> @ 1.52 V	50 μg cm <sup>-2</sup>	11
<b>SrCo<sub>0.9</sub>Ir<sub>0.1</sub>O<sub>3-δ</sub></b>	0.1 M HClO <sub>4</sub>	~300@10		255 μg cm <sup>-2</sup> ~23.5 μg <sub>Ir</sub> cm <sup>-2</sup>	12
<b>mesoporous Ir nanosheets</b>	0.5 M H <sub>2</sub> SO <sub>4</sub>	240@10	~260 A g <sub>Ir</sub> <sup>-1</sup> @ 1.5 V	136 μg <sub>Ir</sub> cm <sup>-2</sup>	13
<b>IrCoNi PHNC</b>	0.1 M HClO <sub>4</sub>	303@10		10.0 μg <sub>Ir</sub> cm <sup>-2</sup>	14
<b>IrO<sub>x</sub>/ATO</b>	0.05 M H <sub>2</sub> SO <sub>4</sub>			10.2 μg <sub>Ir</sub> cm <sup>-2</sup>	15
<b>Ba<sub>2</sub>YIrO<sub>6</sub></b>	0.1 M HClO <sub>4</sub>	~340@10		15 μg <sub>oxide</sub> cm <sub>disk</sub> <sup>-2</sup> 4.4 μg <sub>Ir</sub> cm <sup>-2</sup>	16
<b>IrNiO<sub>x</sub> /Meso-ATO</b>	0.05 M H <sub>2</sub> SO <sub>4</sub>	~320@10	~90 A g <sub>Ir</sub> <sup>-1</sup> @ 1.51 V	10.2 μg <sub>Ir</sub> cm <sup>-2</sup>	17
<b>Ir WNWs</b>	0.5 M HClO <sub>4</sub>	270@10		31 μg <sub>Ir</sub> cm <sup>-2</sup>	18
<b>NPC@RuO<sub>2</sub></b>	0.5 M H <sub>2</sub> SO <sub>4</sub>	220@10		0.357 mg cm <sup>-2</sup> 0.064 mg <sub>Ru</sub> cm <sup>-2</sup>	19

<b>IrNi</b>	0.1 M HClO <sub>4</sub>	270@9.1		12.5 μg <sub>Ir</sub> cm <sup>-2</sup>	20
<b>Ir/GF</b>	0.5 M H <sub>2</sub> SO <sub>4</sub>	290@10	200 A g <sub>Ir</sub> <sup>-1</sup> @ 390 mV	0.82 mg <sub>Ir</sub> cm <sup>-2</sup>	21
<b>IrNi<sub>0.57</sub>Fe<sub>0.82</sub></b>	0.5 M HClO <sub>4</sub>	284 @10		92 μg cm <sup>-2</sup>	22
<b>Pr<sub>2</sub>Ir<sub>2</sub>O<sub>7</sub></b>	0.1 M HClO <sub>4</sub>	290@10	424.5 A g <sub>Ir</sub> <sup>-1</sup> @ 300mV	0.057 mg cm <sup>-2</sup> , 0.028 mg <sub>Ir</sub> cm <sup>-2</sup>	23
<b>NaRuO<sub>2</sub></b>	0.1 M HClO <sub>4</sub>	255@10	42A g <sub>catalyst</sub> <sup>-1</sup> @ 250mV	0.2 mg cm <sup>-2</sup> , 0.13mg <sub>Ru</sub> cm <sup>-2</sup>	24
<b>Ru@IrO<sub>x</sub></b>	0.05 M H <sub>2</sub> SO <sub>4</sub>	282@10	645 A g <sub>catalyst</sub> <sup>-1</sup> @ 330mV	0.051 mg <sub>catalyst</sub> cm <sup>-2</sup>	25
<b>Co-RuIr</b>	0.1 M HClO <sub>4</sub>	235@10		0.051 mg <sub>catalyst</sub> cm <sup>-2</sup>	26
<b>6H-SrIrO<sub>3</sub></b>	0.5 M H <sub>2</sub> SO <sub>4</sub>	248@10	~76 A g <sub>Ir</sub> <sup>-1</sup> @ 1.525V	0.90 mg cm <sup>-2</sup> , 0.528 mg <sub>Ir</sub> cm <sup>-2</sup>	27
<b>P-IrCu<sub>1.4</sub></b>	0.05 M H <sub>2</sub> SO <sub>4</sub>	311@10	~220 A g <sub>Ir</sub> <sup>-1</sup> @ 1.55V	60 μg <sub>Ir</sub> cm <sup>-2</sup>	28
<b>Li-IrSe<sub>2</sub></b>	0.5 M H <sub>2</sub> SO <sub>4</sub>	220@10	66 A g <sub>Ir</sub> <sup>-1</sup> @ 1.45V	250 μg cm <sup>-2</sup> , ~150 μg <sub>Ir</sub> cm <sup>-2</sup>	29
<b>UfD-RuO<sub>2</sub>/CC</b>	0.5 M H <sub>2</sub> SO <sub>4</sub>	179@10		0.52 mg cm <sup>-2</sup> , 0.395 mg <sub>Ru</sub> cm <sup>-2</sup>	30
<b>ATO/IrO<sub>2</sub></b>	0.5 M H <sub>2</sub> SO <sub>4</sub>	210@1	63 A g <sub>Ir</sub> <sup>-1</sup> @ 1.53V	50 μg <sub>Ir</sub> cm <sup>-2</sup>	31
<b>a-RuTe<sub>2</sub> PNRs</b>	0.5 M H <sub>2</sub> SO <sub>4</sub>	245@10		204 μg cm <sup>-2</sup> , 40.8 μg <sub>Ru</sub> cm <sup>-2</sup>	32
<b>Ir<sub>0.6</sub>Cr<sub>0.4</sub>O<sub>x</sub>-350</b>	0.5 M H <sub>2</sub> SO <sub>4</sub>	250@10	55 A g <sub>IrO<sub>2</sub></sub> <sup>-1</sup> @ 1.51V (~64 A g <sub>Ir</sub> <sup>-1</sup> )	0.56 mg cm <sup>-2</sup>	33

**Table S5.** Dopant ratios obtained for Ir<sub>x</sub>Co<sub>3-x</sub>O<sub>4</sub> by ICP-MS analysis.

<b>Sample</b>	<b>Ir<sub>0.003</sub>Co<sub>2.997</sub> O<sub>4</sub></b>	<b>Ir<sub>0.01</sub>Co<sub>2.99</sub> O<sub>4</sub></b>	<b>Ir<sub>0.04</sub>Co<sub>2.96</sub> O<sub>4</sub></b>	<b>Ir<sub>0.06</sub>Co<sub>2.94</sub> O<sub>4</sub></b>	<b>Ir<sub>0.16</sub>Co<sub>2.84</sub> O<sub>4</sub></b>
Mass concentration of Ir in Ir <sub>x</sub> Co <sub>3-x</sub> O <sub>4</sub> (%wt)	0.2	0.8	3.1	4.9	11.7
Atomic concentration of Ir in Ir <sub>x</sub> Co <sub>3-x</sub> O <sub>4</sub> (%at)	0.04	0.14	0.57	0.92	2.29
Atomic ratio of Ir and Co	1: 1123.2	1: 294.1	1: 67.9	1: 45.8	1: 17.6

**Table S6.** Comparison of the surface parameters, mass activity, intrinsic activity and TOF values for  $\text{Ir}_x\text{Co}_{3-x}\text{O}_4$ , ( $x = 0.003, 0.01, 0.04, 0.16$ ) electrocatalysts investigated in 0.1 M  $\text{HClO}_4$ .

Samples	$C_{dl}$ ( $\text{mF cm}^{-2}$ )	$R_f$	Surface area <sup>a</sup> ( $\text{m}^2 \text{g}^{-1}$ )	Mass activity <sup>b</sup> (A $\text{g}^{-1}$ noble metal)	Intrinsic activity <sup>b</sup> ( $\text{mA cm}^{-2}$ catalyst)	TOF <sup>b</sup> ( $\text{s}^{-1}$ )
<b><math>\text{Ir}_{0.003}\text{Co}_{2.997}\text{O}_4</math></b>	0.200	3.33	3.3	1863	0.13	1.05
<b><math>\text{Ir}_{0.01}\text{Co}_{2.99}\text{O}_4</math></b>	0.210	3.50	3.4	980	0.21	0.48
<b><math>\text{Ir}_{0.04}\text{Co}_{2.96}\text{O}_4</math></b>	0.179	2.98	2.9	628	0.67	0.32
<b><math>\text{Ir}_{0.16}\text{Co}_{2.84}\text{O}_4</math></b>	0.233	3.88	3.8	473	1.51	0.23

<sup>a</sup>: the surface area was calculated by multiplying the electrode geometrical area by  $R_f$  and then normalized by taking into account the loading mass of electrocatalysts; <sup>b</sup>: the mass activity, specific activity and TOF values were obtained from the current density values at an overpotential of 300 mV.

**Table S7.** Dopant ratios obtained for  $\text{Ir}_{0.06}\text{Co}_{2.94}\text{O}_4$  before and after OER process by ICP-MS tests.

Sample	Post-OER	Fresh
Mass concentration of Ir in $\text{Ir}_x\text{Co}_{3-x}\text{O}_4$ (%wt)	4.8	4.9
Atomic concentration of Ir in $\text{Ir}_x\text{Co}_{3-x}\text{O}_4$ (%at)	0.93	0.92
Atomic ratio of Ir and Co	1: 45.3	1: 45.8

## References

- (1) McCrory, C. C.; Jung, S.; Peters, J. C.; Jaramillo, T. F., Benchmarking heterogeneous electrocatalysts for the oxygen evolution reaction. *J. Am. Chem. Soc.* **2013**, *135*, 16977-16987.
- (2) Kim, J.; Shih, P. C.; Tsao, K. C.; Pan, Y. T.; Yin, X.; Sun, C. J.; Yang, H., High-Performance Pyrochlore-Type Yttrium Ruthenate Electrocatalyst for Oxygen Evolution Reaction in Acidic Media. *J. Am. Chem. Soc.* **2017**, *139*, 12076-12083.
- (3) Lee, Y.; Suntivich, J.; May, K. J.; Perry, E. E.; Shao-Horn, Y., Synthesis and Activities of Rutile IrO<sub>2</sub> and RuO<sub>2</sub> Nanoparticles for Oxygen Evolution in Acid and Alkaline Solutions. *J. Phys. Chem. Lett.* **2012**, *3*, 399-404.
- (4) Paoli, E. A.; Masini, F.; Frydendal, R.; Deiana, D.; Schlaup, C.; Malizia, M.; Hansen, T. W.; Horch, S.; Stephens, I. E. L.; Chorkendorff, I., Oxygen evolution on well-characterized mass-selected Ru and RuO<sub>2</sub> nanoparticles. *Chem. Sci.* **2015**, *6*, 190-196.
- (5) Paoli, E. A.; Masini, F.; Frydendal, R.; Deiana, D.; Malacrida, P.; Hansen, T. W.; Chorkendorff, I.; Stephens, I. E. L., Fine-tuning the activity of oxygen evolution catalysts: The effect of oxidation pre-treatment on size-selected Ru nanoparticles. *Catal. Today* **2016**, *262*, 57-64.
- (6) Alia, S. M.; Shulda, S.; Ngo, C.; Pylypenko, S.; Pivovar, B. S., Iridium-Based Nanowires as Highly Active, Oxygen Evolution Reaction Electrocatalysts. *ACS Catal.* **2018**, *8*, 2111-2120.
- (7) Su, J.; Ge, R.; Jiang, K.; Dong, Y.; Hao, F.; Tian, Z.; Chen, G.; Chen, L., Assembling Ultrasmall Copper-Doped Ruthenium Oxide Nanocrystals into Hollow Porous Polyhedra: Highly Robust Electrocatalysts for Oxygen Evolution in Acidic Media. *Adv. Mater.* **2018**, *30*, 1801351.
- (8) Lv, F.; Feng, J.; Wang, K.; Dou, Z.; Zhang, W.; Zhou, J.; Yang, C.; Luo, M.; Yang, Y.; Li, Y., et al., Iridium-Tungsten Alloy Nanodendrites as pH-Universal Water-Splitting Electrocatalysts. *ACS Central Sci.* **2018**, *4*, 1244-1252.
- (9) Yao, Y.; Hu, S.; Chen, W.; Huang, Z.-Q.; Wei, W.; Yao, T.; Liu, R.; Zang, K.; Wang, X.; Wu, G., et al., Engineering the electronic structure of single atom Ru sites via compressive strain boosts acidic water oxidation electrocatalysis. *Nat. Catal.* **2019**, *2*, 304-313.
- (10) Liang, X.; Shi, L.; Liu, Y.; Chen, H.; Si, R.; Yan, W.; Zhang, Q.; Li, G. D.; Yang, L.; Zou, X., Activating Inert, Nonprecious Perovskites with Iridium Dopants for Efficient Oxygen Evolution Reaction under Acidic Conditions. *Angew. Chem. Int. Ed.* **2019**, *58*, 7631-7635.
- (11) Gao, J.; Xu, C. Q.; Hung, S. F.; Liu, W.; Cai, W.; Zeng, Z.; Jia, C.; Chen, H. M.; Xiao, H.; Li, J., et al., Breaking Long-Range Order in Iridium Oxide by Alkali Ion for Efficient Water Oxidation. *J. Am. Chem. Soc.* **2019**, *141*, 3014-3023.

- (12) Kim, B. J.; Fabbri, E.; Abbott, D. F.; Cheng, X.; Clark, A. H.; Nachtegaal, M.; Borlaf, M.; Castelli, I. E.; Graule, T.; Schmidt, T. J., Functional Role of Fe-doping in Co-based Perovskite Oxide Catalysts for Oxygen Evolution Reaction. *J Am Chem Soc* **2019**.
- (13) Jiang, B.; Guo, Y.; Kim, J.; Whitten, A. E.; Wood, K.; Kani, K.; Rowan, A. E.; Henzie, J.; Yamauchi, Y., Mesoporous Metallic Iridium Nanosheets. *J. Am. Chem. Soc.* **2018**, *140*, 12434-12441.
- (14) Feng, J.; Lv, F.; Zhang, W.; Li, P.; Wang, K.; Yang, C.; Wang, B.; Yang, Y.; Zhou, J.; Lin, F., et al., Iridium-Based Multimetallic Porous Hollow Nanocrystals for Efficient Overall-Water-Splitting Catalysis. *Adv. Mater.* **2017**, *29*, 1703798.
- (15) Oh, H. S.; Nong, H. N.; Reier, T.; Bergmann, A.; Gliech, M.; Ferreira de Araujo, J.; Willinger, E.; Schlogl, R.; Teschner, D.; Strasser, P., Electrochemical Catalyst-Support Effects and Their Stabilizing Role for IrO<sub>x</sub> Nanoparticle Catalysts during the Oxygen Evolution Reaction. *J. Am. Chem. Soc.* **2016**, *138*, 12552-12563.
- (16) Diaz-Morales, O.; Raaijman, S.; Kortlever, R.; Kooyman, P. J.; Wezendonk, T.; Gascon, J.; Fu, W. T.; Koper, M. T., Iridium-based double perovskites for efficient water oxidation in acid media. *Nat. Commun.* **2016**, *7*, 12363.
- (17) Nong, H. N.; Oh, H. S.; Reier, T.; Willinger, E.; Willinger, M. G.; Petkov, V.; Teschner, D.; Strasser, P., Oxide-supported IrNiO(x) core-shell particles as efficient, cost-effective, and stable catalysts for electrochemical water splitting. *Angew. Chem. Int. Ed.* **2015**, *54*, 2975-2979.
- (18) Fu, L.; Yang, F.; Cheng, G.; Luo, W., Ultrathin Ir nanowires as high-performance electrocatalysts for efficient water splitting in acidic media. *Nanoscale* **2018**, *10*, 1892-1897.
- (19) Yu, J.; Li, G.; Liu, H.; Zhao, L.; Wang, A.; Liu, Z.; Li, H.; Liu, H.; Hu, Y.; Zhou, W., Ru-Ru<sub>2</sub>P<sub>2</sub>O<sub>7</sub> NPC and NPC@RuO<sub>2</sub> Synthesized via Environment-Friendly and Solid-Phase Phosphating Process by Saccharomycetes as N/P Sources and Carbon Template for Overall Water Splitting in Acid Electrolyte. *Adv. Funct. Mater.* **2019**, *29*, 1901154.
- (20) Pi, Y.; Shao, Q.; Wang, P.; Guo, J.; Huang, X., General Formation of Monodisperse IrM (M = Ni, Co, Fe) Bimetallic Nanoclusters as Bifunctional Electrocatalysts for Acidic Overall Water Splitting. *Adv. Funct. Mater.* **2017**, *27*, 1700886.
- (21) Zhang, J.; Wang, G.; Liao, Z.; Zhang, P.; Wang, F.; Zhuang, X.; Zschech, E.; Feng, X., Iridium nanoparticles anchored on 3D graphite foam as a bifunctional electrocatalyst for excellent overall water splitting in acidic solution. *Nano Energy* **2017**, *40*, 27-33.
- (22) Fu, L.; Cheng, G.; Luo, W., Colloidal synthesis of monodisperse trimetallic IrNiFe nanoparticles as highly active bifunctional electrocatalysts for acidic overall water splitting. *J. Mater. Chem. A* **2017**, *5*, 24836-24841.

- (23) Shang, C.; Cao, C.; Yu, D.; Yan, Y.; Lin, Y.; Li, H.; Zheng, T.; Yan, X.; Yu, W.; Zhou, S., et al., Electron Correlations Engineer Catalytic Activity of Pyrochlore Iridates for Acidic Water Oxidation. *Adv. Mater.* **2019**, *31*, e1805104.
- (24) Laha, S.; Lee, Y.; Podjaski, F.; Weber, D.; Duppel, V.; Schoop, L. M.; Pielnhofer, F.; Scheurer, C.; Müller, K.; Starke, U., et al., Ruthenium Oxide Nanosheets for Enhanced Oxygen Evolution Catalysis in Acidic Medium. *Adv. Energy Mater.* **2019**, *9*, 1803795.
- (25) Shan, J.; Guo, C.; Zhu, Y.; Chen, S.; Song, L.; Jaroniec, M.; Zheng, Y.; Qiao, S.-Z., Charge-Redistribution-Enhanced Nanocrystalline Ru@IrO<sub>x</sub> Electrocatalysts for Oxygen Evolution in Acidic Media. *Chem* **2019**, *5*, 445-459.
- (26) Shan, J.; Ling, T.; Davey, K.; Zheng, Y.; Qiao, S. Z., Transition-Metal-Doped RuIr Bifunctional Nanocrystals for Overall Water Splitting in Acidic Environments. *Adv. Mater.* **2019**, *31*, 1900510.
- (27) Yang, L.; Yu, G.; Ai, X.; Yan, W.; Duan, H.; Chen, W.; Li, X.; Wang, T.; Zhang, C.; Huang, X., et al., Efficient oxygen evolution electrocatalysis in acid by a perovskite with face-sharing IrO<sub>6</sub> octahedral dimers. *Nat. Commun.* **2018**, *9*, 5236.
- (28) Pi, Y.; Guo, J.; Shao, Q.; Huang, X., Highly Efficient Acidic Oxygen Evolution Electrocatalysis Enabled by Porous Ir–Cu Nanocrystals with Three-Dimensional Electrocatalytic Surfaces. *Chem. Mater.* **2018**, *30*, 8571-8578.
- (29) Zheng, T.; Shang, C.; He, Z.; Wang, X.; Cao, C.; Li, H.; Si, R.; Pan, B.; Zhou, S.; Zeng, J., Intercalated Iridium Diselenide Electrocatalysts for Efficient pH-Universal Water Splitting. *Angew. Chem. Int. Ed.* **2019**, *58*, 14764-14769.
- (30) Ge, R.; Li, L.; Su, J.; Lin, Y.; Tian, Z.; Chen, L., Ultrafine Defective RuO<sub>2</sub> Electrocatalyst Integrated on Carbon Cloth for Robust Water Oxidation in Acidic Media. *Adv. Energy Mater.* **2019**, *9*, 1901313.
- (31) Böhm, D.; Beetz, M.; Schuster, M.; Peters, K.; Hufnagel, A. G.; Döblinger, M.; Böller, B.; Bein, T.; Fattakhova-Rohlfing, D., Efficient OER Catalyst with Low Ir Volume Density Obtained by Homogeneous Deposition of Iridium Oxide Nanoparticles on Macroporous Antimony-Doped Tin Oxide Support. *Adv. Funct. Mater.* **2019**, *29*, 1906670.
- (32) Wang, J.; Han, L.; Huang, B.; Shao, Q.; Xin, H. L.; Huang, X., Amorphization activated ruthenium-tellurium nanorods for efficient water splitting. *Nat. Commun.* **2019**, *10*, 5692.
- (33) Gou, W.; Zhang, M.; Zou, Y.; Zhou, X.; Qu, Y., Iridium-Chromium Oxide Nanowires as Highly Performed OER Catalysts in Acidic Media. *ChemCatChem* **2019**, *11*, 1-8.

## Chapter 6 Spatial Structure Tuning of Correlated Single-Atom Platinum Sites for Acidic

### Hydrogen Evolution and Oxidation Electrocatalysis

#### 6.1. Introduction and Significance

The design and fabrication of cost-effective catalysts is one of the major challenges in the development of heterogeneous catalysis. This is especially true for PEM fuel cells that are operated in harsh acidic environments and rely heavily on high-cost noble metal electrocatalysts. Up to date, the HER and HOR on platinum catalysts have attracted great research efforts yet the wide application is restricted by the scarcity of platinum. Reducing the usage and increasing the efficiency of platinum in catalysts is the vital target in this topic. Although much progress has been achieved in developing single-atom platinum catalysts towards HER/HOR, the effective tuning of their electronic structures towards substantial enhanced catalytic performance remains for further investigations. Here, we propose to regulate the spatial structure of the atomically dispersed platinum sites in the cobalt spinel oxide lattice to achieve significantly improved catalytic activity. The correlated platinum substitutions create unique spatial topologies and achieve modified hydrogen adsorption towards HER/HOR. The optimized  $\text{Pt}_{0.06}\text{Co}_{2.94}\text{O}_4$  catalyst exhibits a remarkable specific activity with an exchange current density of  $3.78 \text{ mA cm}_{\text{Pt}}^{-2}$ , more than one order of magnitude higher than that of state-of-the-art commercial Pt/C catalyst ( $0.38 \text{ mA cm}_{\text{Pt}}^{-2}$ ). This work provides a great promise for the design of noble metal analogues with tunable geometries towards extensive applications.

## **6.2. Spatial Structure Tuning of Correlated Single-Atom Platinum Sites for Acidic Hydrogen Evolution and Oxidation Electrocatalysis**

This section is included as a manuscript to be submitted by Jieqiong Shan, Chao Ye, Yihan Zhu, Yao Zheng and Shi-Zhang Qiao, Spatial Structure Tuning of Correlated Single-Atom Platinum Sites for Acidic Hydrogen Evolution and Oxidation Electrocatalysis.



# Statement of Authorship

Title of Paper	Spatial Structure Tuning of Correlated Single-Atom Platinum Sites for Acidic Hydrogen Evolution and Oxidation Electrocatalysis
Publication Status	<input type="checkbox"/> Published <input type="checkbox"/> Accepted for Publication <input type="checkbox"/> Submitted for Publication <input checked="" type="checkbox"/> Unpublished and Unsubmitted work written in manuscript style
Publication Details	To be submitted.

## Principal Author

Name of Principal Author (Candidate)	Jieqiong Shan		
Contribution to the Paper	Jieqiong Shan synthesized the materials, conducted physical characterizations and electrocatalytic experiments and wrote the paper.		
Overall percentage (%)	70%		
Certification:	This paper reports on original research I conducted during the period of my Higher Degree by Research candidature and is not subject to any obligations or contractual agreements with a third party that would constrain its inclusion in this thesis. I am the primary author of this paper.		
Signature		Date	20 Jan 2021

## Co-Author Contributions

By signing the Statement of Authorship, each author certifies that:

- i. the candidate's stated contribution to the publication is accurate (as detailed above);
- ii. permission is granted for the candidate to include the publication in the thesis; and
- iii. the sum of all co-author contributions is equal to 100% less the candidate's stated contribution.

Name of Co-Author	Chao Ye		
Contribution to the Paper	Dr. Chao Ye conducted the theoretical calculations and contributed to writing the paper.		
Signature		Date	20 Jan 2021

Name of Co-Author	Yihan Zhu		
Contribution to the Paper	Prof. Yihan Zhu conducted the HRSTEM analysis and contributed to writing the paper.		
Signature		Date	20 Jan 2021

Name of Co-Author	Yao Zheng		
Contribution to the Paper	Dr. Yao Zheng conceived the concept and contributed to writing the paper.		
Signature		Date	20 Jan 2021

Name of Co-Author	Shi-Zhang Qiao		
Contribution to the Paper	Prof. Shi-Zhang Qiao conceived the concept and revised the paper.		
Signature		Date	21 Jan 2021

# Spatial Structure Tuning of Correlated Single-Atom Platinum Sites for Acidic Hydrogen Evolution and Oxidation Electrocatalysis

Jieqiong Shan<sup>1,2,†</sup>, Chao Ye<sup>1,2,†</sup>, Yihan Zhu<sup>3\*</sup>, Yao Zheng<sup>1,2\*</sup> and Shi-Zhang Qiao<sup>1,2\*</sup>

<sup>1</sup> School of Chemical Engineering and Advanced Materials, The University of Adelaide, Adelaide, SA5005, Australia.

<sup>2</sup> Centre for Materials in Energy and Catalysis, The University of Adelaide, Adelaide, SA 5005, Australia.

<sup>3</sup> Center for Electron Microscopy, State Key Laboratory Breeding Base of Green Chemistry Synthesis Technology and College of Chemical Engineering, Zhejiang University of Technology, Hangzhou 310014, China.

\*Correspondence to: [yihanzhu@zjut.edu.cn](mailto:yihanzhu@zjut.edu.cn); [yao.zheng01@adelaide.edu.au](mailto:yao.zheng01@adelaide.edu.au); [s.qiao@adelaide.edu.au](mailto:s.qiao@adelaide.edu.au).

†These authors contributed equally.

**Abstract** As two fundamental reactions in electrochemical energy conversion systems, hydrogen evolution (HER) and oxidation reactions (HOR) in acidic environments generally rely on the large usage of Pt, which suffers from low abundance in earth and high cost. There are generally two types of interactions (metal-metal interaction and metal-support interaction) in noble metal catalysts but are difficult to be regulated simultaneously. To improve the atomic efficiency and intrinsic catalytic performance of Pt-based HER/HOR catalysts, a promising strategy is to regulate the Pt–Pt interaction on Pt single-atom catalyst. Here we report the design of atomically isolated Pt sites with adjustable spatial structure in the lattice of cobalt spinel oxide. With optimized spatial structure and favourable hydrogen adsorption strength of correlated Pt substitutions, the Pt<sub>0.06</sub>Co<sub>2.94</sub>O<sub>4</sub> catalyst exhibited more than one order of magnitude enhanced HER/HOR intrinsic catalytic performance in acidic environment in comparison with that of commercial 20 wt% Pt/C catalyst. This work provides promising solutions for

the effective spatial regulation of atomically dispersed noble metal sites towards enhanced catalytic activity.

Heterogenous catalysis, as a fundamental process in the generation and conversion of clean energy in response to the world-wide crisis of environment and energy, has attracted significant research interest yet relied heavily on the development of cost-effective catalysts<sup>1,2</sup>. Noble metals have been explored as highly efficient catalysts in many important and practical heterogenous catalytic applications because of their unique electronic structure and favourable adsorption energy towards reaction intermediates<sup>3</sup>. For example, platinum (Pt) has been regarded as the state-of-the-art catalysts in various electrocatalytic applications including hydrogen evolution reaction (HER) and hydrogen oxidation reaction (HOR) in acidic environment, which are key technologies in advanced proton-exchange membrane (PEM) based electrolyzers and fuel cells<sup>4</sup>. However, as the large-scale practical application of Pt-based HER/HOR catalysts is greatly inhibited by their elemental scarcity and high cost, the catalysts with high Pt atom usage and significantly improved catalytic performance in comparison of the commercial polycrystal Pt catalysts are particularly needed<sup>5</sup>.

There are generally two types of interactions in metal-based heterogeneous catalysts: the interaction between metal atoms and the interaction between metal atom and support material<sup>6,7</sup>. To realize substantially boosted catalytic performance, the regulation of metal–metal interaction and metal–support interaction is often adopted to optimize the electronic structure of noble metal catalysts. Specifically, the metal–metal interaction exists in various noble metal geometric structures including metal bulk crystals or nanoparticles and can be adjusted by strategies such as alloying<sup>8,9</sup>, size control<sup>10</sup>, morphology modification<sup>11</sup>, etc. However, the small surface-to-volume ratios of bulk and nanoparticle noble metals lead to relatively low metal atomic efficiency and restricted regulation of metal–support interaction<sup>12</sup>. By contrast, the metal–support interaction has been widely investigated in supported single-atom catalysts (SACs), which are promising in increasing the atomic efficiency of noble metals in heterogeneous

catalysts<sup>13,14</sup>. For instance, the tailoring of electronic structure of noble metal single atoms can be achieved by modifying metal–support interactions and results in improved adsorption of reaction intermediates<sup>15,16</sup>. Nevertheless, it remains a grand challenge to regulate the metal–metal interaction and spatial coordination of noble metal atoms in the supported SACs. In addition, the isolated single atoms dispersed on the supports can be unstable or aggregate during heterogeneous catalysis. Significantly, the emerging metal clusters have exhibited the high atomic efficiency of SACs and simultaneously provided opportunity to regulate metal-metal interaction because of the preserved crystal orientation from nanoparticles. So far, however, the design of metal clusters with desirable spatial structure and stable configuration remains to be investigated. This restricts the substantial improvement of intrinsic performance of noble metal catalysts<sup>17</sup>. Therefore, seeking for regulation of spatial structure among noble metal sites plays a key role in the establishment of size-dependent structure–performance relationship and subsequently, the optimization of catalytic performance on noble metal catalysts.

In this work, a facile ion exchange-pyrolysis strategy within metal-organic frameworks (MOFs) is presented to achieve site-specific integration of isolated Pt atoms with different spatial structure in the lattice of Co spinel oxide ( $\text{Co}_3\text{O}_4$ ). Based on atomic resolution scanning transmission-electron microscopy imaging and analysis, the different spatial correlations of Pt substitutions were determined on a series of hybrid materials of Pt substituted  $\text{Co}_3\text{O}_4$  ( $\text{Pt}_n\text{Co}_{3-n}\text{O}_4$ ). The optimized  $\text{Pt}_{0.06}\text{Co}_{2.94}\text{O}_4$  catalyst exhibited more than one order of magnitude enhanced HER/HOR specific catalytic activity in acidic environment in comparison with that of commercial 20 wt% Pt/C catalyst. Theoretical investigations attribute the exceptional performance to the modified electronic structure and favourable hydrogen adsorption energy of  $\text{Pt}_n\text{Co}_{3-n}\text{O}_4$  catalysts induced by spatial correlated Pt substitutions. This study not only illustrates a promising strategy of developing cost-efficient noble metal catalysts but greatly extends the current understanding of regulating the spatial structure of isolated noble metal atoms to bridge the conventional bulk crystals, nanoparticles and SACs.

## Results and discussion

**Structure prediction.** Recently we reported the integration of Ir substitutions with short-range order into the cobalt spinel oxide framework<sup>18</sup>. To explore the correlated substitution in the  $\text{Co}_3\text{O}_4$  host by more types of noble metals, we performed the density function theory (DFT) calculations to predict the thermodynamic stability of the noble metal-substituted Co spinel oxide catalyst. First, we investigated the thermodynamic stability of Ir- $\text{Co}_{11}\text{O}_{16}$  among different competing phases (e.g.,  $\text{IrO}_2$ ,  $\text{Co}_3\text{O}_4$ , Ir- $\text{Co}_{11}\text{O}_{16\_tet}$  with Ir substituting  $\text{Co}_{tet}$  sites, etc.) by constructing a ternary phase diagram (Fig. S1, see Methods for calculation details). The existence of blue region in the diagram indicates the thermodynamically stable Ir- $\text{Co}_{11}\text{O}_{16}$  structure with Ir atoms substituting the  $\text{Co}_{oct}$  sites (**Fig. 1a1**). Similarly, the constructed ternary phase diagrams for a series of noble metals substituted Co spinel oxides (M- $\text{Co}_{11}\text{O}_{16}$ , M = Pt, Ru and Pd) demonstrate that the M ions can substitute the  $\text{Co}_{oct}$  sites, forming stable M- $\text{Co}_{11}\text{O}_{16}$  compounds (**Fig. 1b1-d1** and Fig. S1). For Au-incorporated  $\text{Co}_3\text{O}_4$  system, a compound of Au- $\text{Co}_{11}\text{O}_{16}$  cannot exist against the competing phases but Au- $\text{Co}_{47}\text{O}_{64}$  with lower Au concentration in the  $\text{Co}_{oct}$  site is stable (**Fig. 1e1** and Fig. S2).

As a proof-of-concept, the fabrication of M-substituted cobalt spinel oxide was conducted *via* an ion exchange-pyrolysis strategy with ZIF-67 as a host (Fig. S3)<sup>18,19</sup>. The molecular formulae of  $\text{M}_x\text{Co}_{3-x}\text{O}_4$  were determined by ICP-MS as  $\text{Pt}_{0.06}\text{Co}_{2.93}\text{O}_4$ ,  $\text{Ru}_{0.06}\text{Co}_{2.94}\text{O}_4$  and  $\text{Pd}_{0.08}\text{Co}_{2.92}\text{O}_4$ . The Z-contrast high-angle annular dark-field high-resolution scanning transmission electron microscopy (HAADF-HRSTEM) investigations on these samples demonstrate that almost all alien ions are incorporated into the spinel oxide lattice (**Fig. 1a2-d2**). However, in the Au integrated  $\text{Co}_3\text{O}_4$  spinel oxides, besides very few Au single sites, Au nanoparticles with different sizes are formed (**Fig. 1e2**).

**Geometric structure identification.** The Co K-edge X-ray absorption near-edge structure (XANES) spectra and Fourier transformed- (FT-) extended X-ray absorption fine structure (EXAFS) spectra of  $\text{Pt}_{0.06}\text{Co}_{2.94}\text{O}_4$  show that the Co species are in similar valence state and coordination environment with

that of pure  $\text{Co}_3\text{O}_4$  (Fig. S4). Pt  $L_3$ -edge XANES spectra of  $\text{Pt}_{0.06}\text{Co}_{2.94}\text{O}_4$  exhibit high Pt valence state close to those in  $\text{PtO}_2$  (Fig. S5), indicating that the Pt species locate in the  $\text{Co}_3\text{O}_4$  lattice rather than being supported on the surface as Pt nanoparticles or single atoms, which tend to exhibit much smaller Pt valence states<sup>20,21</sup>. The Pt  $L_3$ -edge FT-EXAFS spectra of  $\text{Pt}_{0.06}\text{Co}_{2.94}\text{O}_4$  and the corresponding fitting results demonstrate the coexistence of Pt–Co and Pt–Pt scatterings in the second shell at interatomic distances of 2.88Å and 2.75Å with a large coordination number (CN) value of 7.0 (4.1+2.9) (**Fig. 2a**, Fig. S6-7 and Table S1). These parameters are close to those of  $\text{Co}_{\text{oct}}\text{--Co}_{\text{oct}}$  (interatomic distance: 2.90 Å, CN: 6.0) in  $\text{Co}_3\text{O}_4$ , supporting our proposed geometric structure that Pt locates in the  $\text{Co}_{\text{oct}}$  sites in the  $\text{Co}_3\text{O}_4$  lattice. Additionally, the existence of Pt–Pt pairing path indicates that the substituted Pt in the spinel structure is in the form of locally clustered Pt sites instead of fully isolated ones. Similar results can be obtained for  $\text{Ru}_{0.06}\text{Co}_{2.94}\text{O}_4$  and  $\text{Pd}_{0.08}\text{Co}_{2.92}\text{O}_4$ , demonstrating that Ru and Pd ions are incorporated into the spinel oxide lattice and occupy the  $\text{Co}_{\text{oct}}$  sites. In contrast, XANES and EXAFS spectra of  $\text{Au-Co}_3\text{O}_4$  indicate that Au sites exist mainly as Au nanoparticle with the typical Au–Au bond, which agrees well with the DFT and HRSTEM observations (Fig. S5 and **Fig. 2b**).

Taking  $\text{Pt}_{0.06}\text{Co}_{2.94}\text{O}_4$  as a model sample, we further performed detailed analysis on the atomic-resolution HRSTEM image along  $\langle 233 \rangle$  projection, where a few distinctive doping configurations were identified and labelled by dashed rectangles with different colors (**Fig. 2c**). The simulated  $Z^2$ -maps based on geometry with correlated Pt substitution at  $\text{Co}_{\text{oct}}$  sites matches well with the experimental observations (**Fig. 2d**). Therefore, it is clearly visualized that Pt atoms occupy the  $\text{Co}_{\text{oct}}$  sites in the  $\text{Co}_3\text{O}_4$  lattice and suggests that the Pt substitutions are in a unique spatial correlation. Importantly, the XRD pattern of  $\text{M}_x\text{Co}_{3-x}\text{O}_4$  samples exhibit characteristic peaks of Co spinel oxide in an  $Fd3m$  symmetry and a weak additional peak at  $2\theta$  of  $\sim 16^\circ$ , which corresponds to the (110) reflection of a cubic structure and originates from the breakage of diamond glide plane symmetry of the  $\text{Co}_3\text{O}_4$  lattice due to noble metal substitutions<sup>18,22</sup> (**Fig. 2e**). Therefore, benefiting from the well-designed ion exchange-pyrolysis strategy

with MOFs as host, the Pt, Ru and Pd ions can be accommodated in the  $\text{Co}_{\text{oct}}$  sites of  $\text{Co}_3\text{O}_4$  lattice to form correlated substitutions. To investigate the electrocatalytic performance of  $\text{M}_x\text{Co}_{3-x}\text{O}_4$  samples, we performed HER measurements in Argon saturated 0.1 M  $\text{HClO}_4$  electrolyte. As is shown in **Fig. 2f**, the  $\text{Pt}_{0.06}\text{Co}_{2.94}\text{O}_4$  catalyst demonstrates a promising HER electrocatalytic activity that outperforms those of the others.

**Electrocatalytic HER/HOR performance evaluation.** To further evaluate the catalytic performance of the  $\text{Pt}_{0.06}\text{Co}_{2.94}\text{O}_4$  catalyst toward HER and HOR, we conducted electrocatalytic experiments in  $\text{H}_2$ -saturated 0.1 M  $\text{HClO}_4$  electrolyte with commercial 20 wt% Pt/C as references. In addition, to investigate the effect of spatial correlation of Pt substitutions we also prepared the isolated Pt single atom substituted  $\text{Co}_3\text{O}_4$  (Pt SA- $\text{Co}_3\text{O}_4$ ) and a hybrid material with Pt nanoparticles supported on the surface of  $\text{Co}_3\text{O}_4$  (Pt NP@ $\text{Co}_3\text{O}_4$ ) as references. As illustrated in **Fig. 3a**, the  $\text{Pt}_{0.06}\text{Co}_{2.94}\text{O}_4$  catalyst exhibits a remarkable apparent HER/HOR activity with an onset potential closing to 0 V *vs.* reversible hydrogen electrode (RHE) and large anode/cathode current densities at 1600 rpm (Fig. S8). By contrast, Pt NP@ $\text{Co}_3\text{O}_4$  and Pt SA- $\text{Co}_3\text{O}_4$  exhibit much poorer catalytic performance with substantial onset potentials and limited HER/HOR current densities. This observation suggests that the remarkable catalytic activity of  $\text{Pt}_{0.06}\text{Co}_{2.94}\text{O}_4$  derives from the Pt substitutions with unique spatial correlation in the  $\text{Co}_3\text{O}_4$  lattice. Further, to evaluate the intrinsic activity of the catalysts, we normalized the polarization curves to their electrochemical active surface areas (ECSAs), which was determined by CO stripping voltammograms (Fig. S9). Significantly, the  $\text{Pt}_{0.06}\text{Co}_{2.94}\text{O}_4$  catalyst exhibits a remarkable intrinsic activity greatly exceeding that of the state-of-the-art 20 wt% Pt/C and Pt NP@ $\text{Co}_3\text{O}_4$  catalysts with lower onset potential and much higher intrinsic current densities. As is shown in **Fig. 3b**, the polarization curves at different rotating speeds were collected for  $\text{Pt}_{0.06}\text{Co}_{2.94}\text{O}_4$  and Pt/C catalysts and the Koutecky–Levich plots were constructed accordingly (Fig. S10). Linear relationships are demonstrated between inverse of the limiting specific current density (@ 0.6 V *vs.* RHE) and the square root of rotation speed with slopes of 14.612 and 13.125  $\text{cm}_{\text{Pt}}^2 \text{mA}^{-1} \text{s}^{-1/2}$  obtained for  $\text{Pt}_{0.06}\text{Co}_{2.94}\text{O}_4$  and Pt/C, respectively. Then we calculated the



kinetic current densities ( $j_k$ ) for both catalysts and extracted the exchange current densities ( $j_0$ ) by fitting with the Butler-Volmer equation (**Fig. 3c**)<sup>23</sup>. Significantly, the Pt<sub>0.06</sub>Co<sub>2.94</sub>O<sub>4</sub> catalyst delivers a specific  $j_0$  of 3.78 mA cm<sub>Pt</sub><sup>-2</sup>, more than one order of magnitude higher than that of Pt/C (0.38 mA cm<sub>Pt</sub><sup>-2</sup>) and Pt NP@Co<sub>3</sub>O<sub>4</sub> (0.15 mA cm<sub>Pt</sub><sup>-2</sup>) catalysts. Additionally, the mass activity of Pt<sub>0.06</sub>Co<sub>2.94</sub>O<sub>4</sub> catalyst, determined by the mass of Pt, greatly outperforms that of Pt NP@Co<sub>3</sub>O<sub>4</sub> and Pt/C catalysts (Fig. S11). The mass activity recorded at 0.5 V vs. RHE for the three catalysts was 235, 151 and 141 A g<sub>Pt</sub><sup>-1</sup>, respectively. The catalytic activity of Pt<sub>0.06</sub>Co<sub>2.94</sub>O<sub>4</sub> catalyst represents an unprecedented performance among previously reported Pt-based catalysts and offers a promising solution for cost-effective HER/HOR catalysts in acidic environments.

In order to explore the effect of the correlated Pt substitutions in hybrid catalysts on their catalytic performance, we synthesized a series of Pt-substituted Co<sub>3</sub>O<sub>4</sub> catalysts with different incorporation ratios of Pt (Pt<sub>n</sub>Co<sub>3-n</sub>O<sub>4</sub>, n = 0.01, 0.04, 0.06 and 0.14, determined by ICP-MS). Adjusting the ratios of Pt substitutions integrated in the Co<sub>3</sub>O<sub>4</sub> lattice is expected to regulate the degree of spatial correlation of Pt sites and lead to different catalytic performance. As illustrated in the XRD patterns (Fig. S12a), all the Pt<sub>n</sub>Co<sub>3-n</sub>O<sub>4</sub> catalysts show the identical peaks of Co<sub>3</sub>O<sub>4</sub> phase with no Pt or Pt oxide phase formed, which confirms that the Pt substitutions are accommodated in the Co<sub>3</sub>O<sub>4</sub> lattice. In addition, the Raman spectra of the Pt<sub>n</sub>Co<sub>3-n</sub>O<sub>4</sub> catalysts exhibit typical characteristic bands of Co<sub>3</sub>O<sub>4</sub> with an observable redshift of the A<sub>1g</sub> band, which demonstrates a preferential occupation of Pt at the octahedral Co(III) sites (Co<sub>oct</sub>) instead of the tetrahedral Co(II) sites (Co<sub>tet</sub>) in Co<sub>3</sub>O<sub>4</sub> lattice (Fig. S12b)<sup>24</sup>. The HER/HOR catalytic activity of the Pt<sub>n</sub>Co<sub>3-n</sub>O<sub>4</sub> catalysts were investigated under the same testing conditions as described above. The trend of apparent activity on Pt<sub>n</sub>Co<sub>3-n</sub>O<sub>4</sub> catalysts matches with the ratio of Pt because of the different spatial correlation of Pt substitutions in the catalysts and the different loading amounts of Pt on the electrodes (**Fig. 3d**). Upon normalization to ECSAs, the intrinsic activity of the Pt<sub>n</sub>Co<sub>3-n</sub>O<sub>4</sub> catalysts improved with the n increases from 0.01 to 0.06 yet slightly decreased when the n further increased to

0.14 (Fig. S13, 14a). When the mass of Pt in the catalysts was taken into consideration, a similar mass activity trend of  $\text{Pt}_{0.06}\text{Co}_{2.94}\text{O}_4 > \text{Pt}_{0.14}\text{Co}_{2.86}\text{O}_4 > \text{Pt}_{0.04}\text{Co}_{2.96}\text{O}_4 > \text{Pt}_{0.01}\text{Co}_{2.99}\text{O}_4$  can be delivered (Fig. S14b). In addition, we established the Tafel plots for the  $\text{Pt}_n\text{Co}_{3-n}\text{O}_4$  catalysts and extracted the  $j_0$  by fitting with the Butler-Volmer equation (**Fig. 3e**). It is demonstrated that the  $j_0$  of the  $\text{Pt}_n\text{Co}_{3-n}\text{O}_4$  catalysts increases from 0.75, 1.04 to 3.90  $\text{mA cm}_{\text{Pt}}^{-2}$  with the increased Pt ratio in  $\text{Pt}_{0.01}\text{Co}_{2.99}\text{O}_4$ ,  $\text{Pt}_{0.04}\text{Co}_{2.96}\text{O}_4$ ,  $\text{Pt}_{0.06}\text{Co}_{2.94}\text{O}_4$  and remained at 3.90  $\text{mA cm}_{\text{Pt}}^{-2}$  for the  $\text{Pt}_{0.14}\text{Co}_{2.86}\text{O}_4$  (**Fig. 3f** and Table S2). This result suggests that the  $\text{Pt}_n\text{Co}_{3-n}\text{O}_4$  catalysts exhibit promoted HER/HOR intrinsic activity in comparison with state-of-the-art Pt/C catalyst and the catalytic performance is closely related to the spatial correlation among Pt substitutions in the catalysts.

**Spatial structure analyses on Pt substitutions.** To elucidate the spatial correlation of Pt substitutions, we analyzed a large number of Pt substitutions to label and measure the coordinates of individual Pt sites and projected distances for the correlated Pt sites (a representative image is shown **Fig. 4a**). The location and size of such “clusters” defined by short-range correlated Pt sites can be well determined based on the projected nearest neighbor distances between  $\text{Co}_{\text{oct}}$  sites. After proper labelling and classification of these sites with short-range order, a demonstrative cluster distribution graph along  $\langle 233 \rangle$  projection can be produced as shown in **Fig. 4b** inset. It indicates that the distribution of nanodomains with correlated Pt substitution is inhomogeneous within the  $\text{Co}_3\text{O}_4$  spinel framework. Furthermore, the relative population of clusters with a certain size can be statistically analyzed and evaluated in the mass fractions (**Fig. 4b**). Generally, it is found that the majority of Pt sites adopt short-range order rather than exist as single sites within the cationic lattice of  $\text{Co}_3\text{O}_4$  and moreover the mass fraction of clusters decreases as cluster size increases.

Further, we performed detailed HRSTEM imaging and analyses on other catalysts to determine the spatial correlation of Pt substitutions. The HRSTEM analysis shows that the majority of Pt atoms in the Pt SA- $\text{Co}_3\text{O}_4$  exist as isolated sites (**Fig. 4c**), while almost all the Pt atoms in the Pt NP@ $\text{Co}_3\text{O}_4$  exist as

randomly distributed Pt nanoparticles on the surface of  $\text{Co}_3\text{O}_4$  (Fig. S15), which are very different from those of Pt substituted  $\text{Co}_3\text{O}_4$ . For the  $\text{Pt}_n\text{Co}_{3-n}\text{O}_4$  catalysts, with the increase of Pt ratio integrated in the  $\text{Co}_3\text{O}_4$  lattice, the cluster distribution graph exhibits a larger population of correlated Pt clusters in addition to isolated Pt sites (**Fig. 4d-f**). Specifically, the  $\text{Pt}_{0.01}\text{Co}_{2.99}\text{O}_4$  catalyst exhibits dominant isolated Pt single atoms together with Pt clusters with size of 2-4 atoms. By contrast, the mass fractions of Pt clusters were observed to increase significantly in the sequence of  $\text{Pt}_{0.04}\text{Co}_{2.96}\text{O}_4$ ,  $\text{Pt}_{0.06}\text{Co}_{2.94}\text{O}_4$  and  $\text{Pt}_{0.14}\text{Co}_{2.86}\text{O}_4$ .

**Electronic structure identification and exploration of activity origin.** To further investigate the electronic structure of the correlated Pt substitutions in  $\text{Co}_3\text{O}_4$  lattice and to explore the origin of remarkable catalytic activity achieved on the  $\text{Pt}_n\text{Co}_{3-n}\text{O}_4$  catalysts, we performed a series of density functional theory (DFT) calculations on  $\text{Co}_3\text{O}_4$  based models. The (110) facet of  $\text{Co}_3\text{O}_4$  was selected because it is composed mainly of  $\text{Co}_{\text{oct}}$  cations, which has been proved by experimental studies<sup>25</sup>. Following the observations from the experiment, we substituted  $\text{Co}_{\text{oct}}$  atoms with one Pt atom to represent the Pt single atom substitution ( $\text{Pt}_1\text{-Co}_3\text{O}_4$ ) and with 2-4 Pt atoms to represent the clustered Pt substitutions in various sizes ( $\text{Pt}_n\text{-Co}_3\text{O}_4$ ,  $n = 2-4$ ). As is illustrated in **Fig. 5a** (upper) and Fig. S16, we compared the free energies of various configurations for models with different Pt cluster sizes. Further, we evaluated the strength of hydrogen adsorption on these Pt sites by the free energy change for the intermediate adsorption step and denoted as  $\Delta G_{\text{H}^*}$ . The  $|\Delta G_{\text{H}^*}|$  has been widely considered as a major descriptor of HER activity in acidic environments, where a smaller  $|\Delta G_{\text{H}^*}|$  indicates an improved activity<sup>26</sup>. We computed and compared the  $\Delta G_{\text{H}^*}$  of correlated Pt substituted  $\text{Co}_3\text{O}_4$  with the pure  $\text{Co}_3\text{O}_4$  and Pt (1 1 1) as references (**Fig. 5a** lower, **Fig. 5b** and Fig. S17). As is demonstrated, the pure  $\text{Co}_3\text{O}_4$  exhibits the greatest  $\Delta G_{\text{H}^*}$  of +0.42 eV, indicating a too weak hydrogen adsorption on the surface. By contrast, the Pt single atom substituted  $\text{Co}_3\text{O}_4$  ( $\text{Pt}_1$ ) shows a largely negative  $\Delta G_{\text{H}^*}$  of -0.41 eV and suggests an over strong hydrogen adsorption. Significantly, as demonstrated by the values of the most

stable configurations, the correlated Pt sites exhibit much smaller values of  $\Delta G_{H^*}$  of -0.12, +0.36 and -0.10 (-0.11) eV for the surface Pt sites in Pt<sub>2</sub>, Pt<sub>3</sub> and Pt<sub>4</sub>, respectively. The  $|\Delta G_{H^*}|$  values for correlated Pt<sub>n</sub> (n = 2-4) configurations are not only smaller than the pure Co<sub>3</sub>O<sub>4</sub> and Pt single atom configuration but are even more optimized in comparison with that of Pt (1 1 1). This result demonstrates the well optimized hydrogen adsorption strength on the correlated Pt substituted Co<sub>3</sub>O<sub>4</sub> surface and explains the experimental observations that catalysts with more correlated Pt sites exhibit higher intrinsic catalytic activity.

In addition, we carried out density of states (DOS) analyses on these Pt-substituted Co<sub>3</sub>O<sub>4</sub> models. The pure Co<sub>3</sub>O<sub>4</sub> exhibits a semiconducting feature with a bandgap in the DOS curve (Fig. S18a). In contrast, the Pt<sub>1</sub>-Co<sub>3</sub>O<sub>4</sub> shows additional Pt-5d states within the bandgap (**Fig. 5c**), indicating that the Pt substitution facilitates the charge transfer of Co spinel oxide<sup>27</sup>. Significantly, the Pt<sub>n</sub>-Co<sub>3</sub>O<sub>4</sub> (n = 2-4) exhibit much more evident additional Pt-5d states and a nearly disappeared bandgap, which is close to that of conductive Pt metal (Fig. S18b). This observation demonstrates the metal-like behavior of clustered Pt substitutions in the lattice of Co<sub>3</sub>O<sub>4</sub>, which is expected to facilitate Pt-Pt interaction and modify hydrogen adsorption strength on the Pt substitutions.

## Conclusions

In summary, we report a facile strategy to integrate Pt atomic substitutions with adjustable spatial structure in the Co<sub>oct</sub> sites of cobalt spinel oxide lattice. As evidenced by HRSTEM imaging and analysis on Pt<sub>n</sub>Co<sub>3-n</sub>O<sub>4</sub> catalysts, with the increase of Pt concentration, a larger ratio of correlated Pt substitutions can be observed in comparison with the Pt SA-Co<sub>3</sub>O<sub>4</sub> catalyst with almost 100% Pt single atoms. The Pt<sub>0.06</sub>Co<sub>2.94</sub>O<sub>4</sub> catalyst with optimized Pt spatial correlation exhibits a remarkable specific activity with an exchange current density of 3.78 mA cm<sub>Pt</sub><sup>-2</sup>, more than one order of magnitude higher than those of state-of-the-art commercial Pt/C catalyst (0.38 mA cm<sub>Pt</sub><sup>-2</sup>) and the Co<sub>3</sub>O<sub>4</sub> catalyst with surface supported Pt nanoparticle (Pt NP@Co<sub>3</sub>O<sub>4</sub>, 0.15 mA cm<sub>Pt</sub><sup>-2</sup>). The DFT investigations attribute this exceptional

performance of  $\text{Pt}_{0.06}\text{Co}_{2.94}\text{O}_4$  catalyst to the favorable hydrogen adsorption strength induced by correlated Pt substitutions. This work provides a great promise for the design of noble metal analogues with tunable geometries towards extensive applications.

## Methods

**Material synthesis.** Co-based zeolitic imidazolate framework (ZIF-67) nanocubes were synthesized by a surfactant-mediated method reported previously<sup>28</sup>. Afterwards an ion exchange process was conducted on the obtained ZIF-67 nanocubes with the existence of platinum precursor in aqueous solution. Typically, 100 mg of ZIF-67 nanocubes was first dispersed in 50 mL of DI water, then 10 mL of aqueous solution containing 9.7 mg of potassium hexachloroplatinate (IV) ( $\text{K}_2\text{PtCl}_6$ ) was added under stirring conditions. The suspension was centrifuged 3 hours later, the precipitate was collected and repeatedly washed with ethanol and DI water. After being dried overnight in a vacuum oven at 60 °C, the precipitate was pyrolyzed at 300°C in air for 4 hours. The obtained hybrid oxide was determined to be  $\text{Pt}_{0.06}\text{Co}_{2.94}\text{O}_4$  by inductively coupled plasma mass spectrometry (ICP-MS). The Pt SA- $\text{Co}_3\text{O}_4$ ,  $\text{Pt}_{0.01}\text{Co}_{2.99}\text{O}_4$ ,  $\text{Pt}_{0.04}\text{Co}_{2.96}\text{O}_4$  and  $\text{Pt}_{0.14}\text{Co}_{2.86}\text{O}_4$  were synthesized by similar procedure with different addition doses of  $\text{K}_2\text{PtCl}_6$  of 0.38 mg, 1.9 mg, 5.8 mg and 19.4 mg, respectively. The  $\text{Ru}_{0.06}\text{Co}_{2.94}\text{O}_4$ ,  $\text{Pd}_{0.08}\text{Co}_{2.92}\text{O}_4$  and Au- $\text{Co}_3\text{O}_4$  nanocrystals were synthesized by similar procedure with addition of 4.2 mg of ruthenium (III) chloride hydrate ( $\text{RuCl}_3 \cdot x\text{H}_2\text{O}$ ), 5.9 mg of sodium tetrachloropalladate (II) ( $\text{Na}_2\text{PdCl}_4$ ) and 7.9 mg of gold (III) chloride ( $\text{HAuCl}_4$ ). The pure  $\text{Co}_3\text{O}_4$  was synthesized by pyrolyzing ZIF-67 nanocubes under similar procedure without performing the ion exchange process. The Pt NP@ $\text{Co}_3\text{O}_4$  was synthesized by adding 10 mL of aqueous solution containing 7.5 mg of  $\text{K}_2\text{PtCl}_6$  into 50 mL of aqueous solution containing 100 mg of  $\text{Co}_3\text{O}_4$  nanoparticles. Later 10 mL of aqueous solution containing 11.4 mg of sodium borohydride was added into the mixture to reduce  $\text{K}_2\text{PtCl}_6$  and immobilize Pt species on the surface of  $\text{Co}_3\text{O}_4$  nanoparticles.

**Materials characterization.** ICP-MS analysis was conducted to detect the amounts of platinum and cobalt in catalysts using an Agilent 7500cx instrument with attached laser ablation system. X-ray diffraction (XRD) data was collected on a Rigaku MiniFlex 600 X-Ray Diffractometer. Raman spectra were collected using a HORIBA Scientific Raman Spectroscopy instrument (laser excitation at 532 nm). The NEXAFS and EXAFS measurements were performed at the beamline 14W1 in the Shanghai Synchrotron Radiation Facility. For Pt, Ir and Au L<sub>3</sub>-edge, the X-ray was monochromatized by a double-crystal Si (111) monochromator, while for Pd and Ru K-edge, the X-ray was monochromatized by a double-crystal Si (311) monochromator. The monochromator was detuned to reject higher harmonics. The raw absorption data were first background subtracted by fitting the pre-edge using a least-squares method and then all spectra were normalized to one at energies far from the edge. The fitting was made in the k-space in the ranges of 2.6-13.8 Å<sup>-1</sup>, 2.6-13.0 Å<sup>-1</sup>, 2.5-12.8 Å<sup>-1</sup>, 2.6-13.0 Å<sup>-1</sup> and 2.3-13.8 Å<sup>-1</sup> for Ir, Pt, Ru, Pd and Au-edges, respectively.

**HRSTEM imaging and analysis.** HAADF-STEM images were recorded using a FEI Titan G2 80-300 microscope at 300 kV equipped with a probe corrector. Projected Z<sup>2</sup>-map simulations were carried out by using the qSTEM program<sup>29</sup>. After flat-field correction and background subtraction, the position searching, refining and labelling of projected Ir sites with brighter contrast in the HRSTEM image were carried out using CalAtom software<sup>30</sup> with a Multiple-Ellipse-Fitting (MEF) Method<sup>31</sup>. The coordinates of refined positions for those projected Ir sites were manually checked to exclude mis-labelled sites and then extracted for future analysis.

**Electrochemical measurements.** Electrocatalyst ink was prepared by dispersing a freshly synthesized catalyst powder (1 mg) and carbon black (Vulcan-XC72, 1 mg) in a solution containing distilled water (Milli-Q, 965 µL) and 5 weight % Nafion solution (35 µL) followed by ultrasonication for 2 hr. 40 µL of catalyst ink was then deposited onto a polished glassy carbon electrode (diameter = 5 mm, area = 0.196 cm<sup>2</sup>, Pine Research Instrument). As a reference, 2mg of commercial 20 wt% Pt/C catalyst was prepared as ink in a similar procedure and 10 µL of the ink was used to prepare the working electrode. All

electrochemical experiments were carried out using rotating disk electrode method in a three-electrode glass cell with an Au-wire as the counter electrode and an Ag/AgCl as the reference electrode (Pine Research Instrument). The 0.1 M HClO<sub>4</sub> electrolyte solution was prepared by diluting 70 % HClO<sub>4</sub> with Milli-Q water. The reference electrode was calibrated in H<sub>2</sub>-saturated 0.1 M HClO<sub>4</sub> solution. All potentials were converted to RHE and corrected for iR-compensation. The HER and HOR measurements were conducted in H<sub>2</sub>-saturated 0.1 M HClO<sub>4</sub> electrolyte with a CHI potentiostat (CHI 760D) at different rotating speeds. The polarization curves of the catalysts were obtained with scan rates of 2 mV s<sup>-1</sup>. The ECSAs of the catalysts were determined by CO stripping voltammograms<sup>32</sup>. The electrolyte was bubbled with 20% CO in argon for 30 min with the working electrode held at 0.1 V vs. RHE, followed by argon purging for 20 min to remove the excess CO. Then the CO stripping voltammograms were collected in the potential range from around 0V to 1.2V vs. RHE during argon bubbling.

The kinetic current density was calculated based on the Koutecky–Levich equation,

$$\frac{1}{j} = \frac{1}{j_k} + \frac{1}{j_d} = \frac{1}{j_k} + \frac{1}{BC_0\omega^{1/2}}$$

where  $j$  is the measured current density,  $j_k$  is the kinetic current density,  $j_d$  is the diffusion limited current density,  $\omega$  is the rotation rate, and  $BC_0$  is a constant associated with the electron transfer number, the gas concentration and the electrolyte kinematic viscosity<sup>33</sup>. Exchange current densities,  $j_0$ , of the HOR/HER were obtained by fitting the experimental data to the Butler–Volmer equation,

$$j_k = j_0 \left[ \exp\left(\frac{\alpha F \eta}{RT}\right) - \exp\left(\frac{(\alpha-1)F \eta}{RT}\right) \right]$$

where  $\alpha$  is the transfer coefficient,  $\eta$  is the overpotential,  $F$  is Faraday's constant (96 485 C mol<sup>-1</sup>),  $R$  is the universal gas constant (8.314 J mol<sup>-1</sup> K<sup>-1</sup>) and  $T$  is the thermodynamic temperature.

**DFT calculations.** DFT calculations were carried out using the Vienna ab-initio Simulation Package (VASP)<sup>34,35</sup>. The exchange-correlation interaction was described by generalized gradient approximation (GGA) with the Perdew-Burke-Ernzerhof (PBE) functional<sup>36</sup>. The DFT-TS method of Grimme was employed to treat the VDW interaction<sup>37</sup>. The GGA+U calculations were performed using the model

proposed based on the TEM images with the  $U_{\text{eff}}$  ( $U_{\text{eff}} = \text{Coulomb } U - \text{exchange } J$ ) values of 3.5 and 3.2 eV for Co and Pt, respectively<sup>38-40</sup>. For the plane-wave expansion, a kinetic energy cut-off of 600 eV was used after testing a series of different cut-off energies. The force and energy convergence tolerance values were set to be 0.01 eV  $\text{\AA}^{-1}$  and  $10^{-5}$  eV, respectively. A Gaussian smearing of 0.1 eV was applied during the geometry optimization, whilst for the accurate density of states computations a tetrahedron method with Blöchl correction was employed. The K-points were set to be  $2 \times 2 \times 1$  for the unit cells. Denser  $8 \times 8 \times 2$  K-points were used for the density of states (DOS) calculations. 20 K-points along each high-symmetry line in the Brillouin zone were used to obtain the band structures. All periodic slabs have a vacuum spacing of at least 15  $\text{\AA}$ . The structural model of  $\text{Co}_3\text{O}_4$  (110) facet contains three Co-O layers (88 atoms), with a supercell size of  $a = 16.80 \text{ \AA}$ ,  $b = 11.88 \text{ \AA}$ ,  $c = 17.97 \text{ \AA}$ ,  $\alpha = \beta = \gamma = 90^\circ$ . In calculations, the bottom layer was kept fixed, whereas the rest of atoms were allowed to relax.

In acidic solution, a simple method was used to compute the free energy based on the hydrogen adsorption strength, as in previous calculations:<sup>41</sup>

$$\Delta G_{\text{H}^*} = \Delta E_{\text{H}} + 0.24 \text{ eV}$$

$$\Delta E_{\text{H}} = E_{\text{total}} - 1/2E_{\text{H}_2} - E_{\text{s}}$$

where  $E_{\text{total}}$ ,  $E_{\text{H}_2}$  and  $E_{\text{s}}$  are the energies of the whole system, hydrogen and substrate, respectively.

## Acknowledgments

DFT computations were performed by using services offered from the National Computational Infrastructure (NCI) and Phoenix High Performance Computing, which are supported by the Australian Government and the University of Adelaide. This work was financially supported by the Australian Research Council (FL170100154, DP160104866 and DP170104464). Y.H.Z. acknowledges financial support from Zhejiang Provincial Natural Science Foundation of China (LR18B030003), National Natural Science Foundation of China (51701181, 21771161) and the Thousand Talents Program for Distinguished Young Scholars.



**Author contributions**

Y.Z., Y.H.Z. and S.Q. conceived the concept. J.S. prepared the materials and performed electrochemical measurements. C.Y. conducted DFT calculations. Y.H.Z carried out HRSTEM imaging and analysis. J.S., Y.H.Z., Y.Z. and S.Q. wrote the manuscript. All authors contributed to the interpretation of data and preparation of the final manuscript.

**Competing interests**

Authors declare no competing interests.

**Data and materials availability**

All data is available in the main text or the supplementary materials.

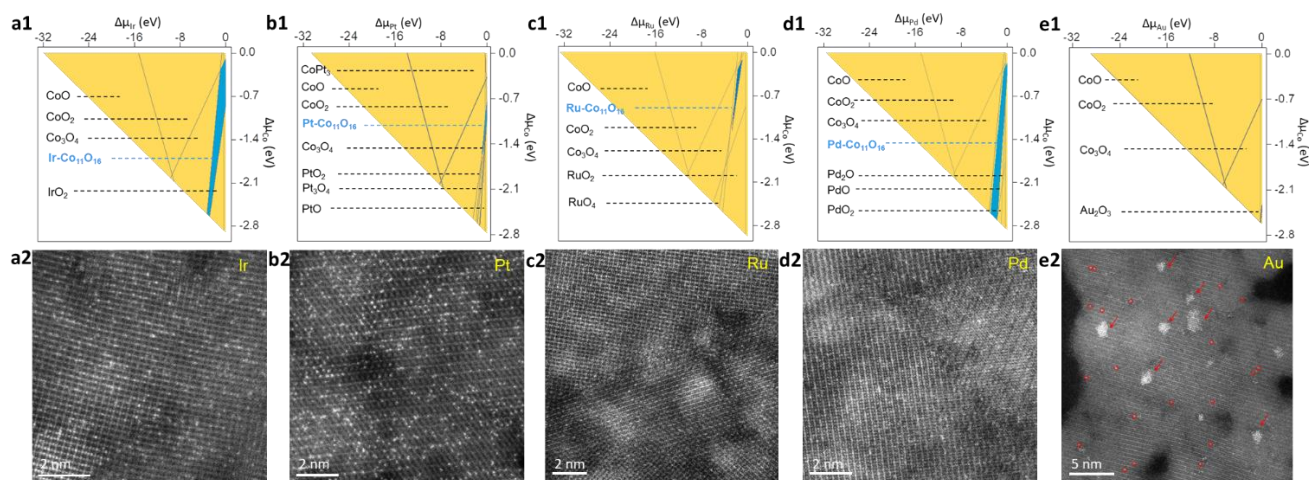


**Fig. 1. Structure prediction and HRSTEM images of  $M_x\text{Co}_{3-x}\text{O}_4$  catalysts.** (a1-d1) The projected ternary phase diagrams for M-Co-O ( $M=\text{Ir, Pt, Ru, Pd}$  for a1-d1, respectively) in the  $(\Delta\mu_{\text{Co}}, \Delta\mu_{\text{M}})$  plane in which the blue regions represent the existence of stable  $\text{M-Co}_{11}\text{O}_{16}$ . See Methods in SI for the ranges that stable  $\text{M-Co}_{11}\text{O}_{16}$  catalysts can exist against all the competing phases. (e1) The projected ternary phase diagrams for Au-Co-O in the  $(\Delta\mu_{\text{Co}}, \Delta\mu_{\text{Au}})$  plane, the  $\text{Au-Co}_{11}\text{O}_{16}$  cannot exist under this concentration. (a2-d2) HRSTEM images of  $M_x\text{Co}_{3-x}\text{O}_4$  catalysts, almost all the M atoms are incorporated in the  $\text{Co}_3\text{O}_4$  lattice. (e2) HRSTEM images of  $\text{Au-Co}_3\text{O}_4$ , the coexistence of Au nanoparticles (indicated by red arrows) and Au single atoms (indicated by red circles) can be clearly observed.

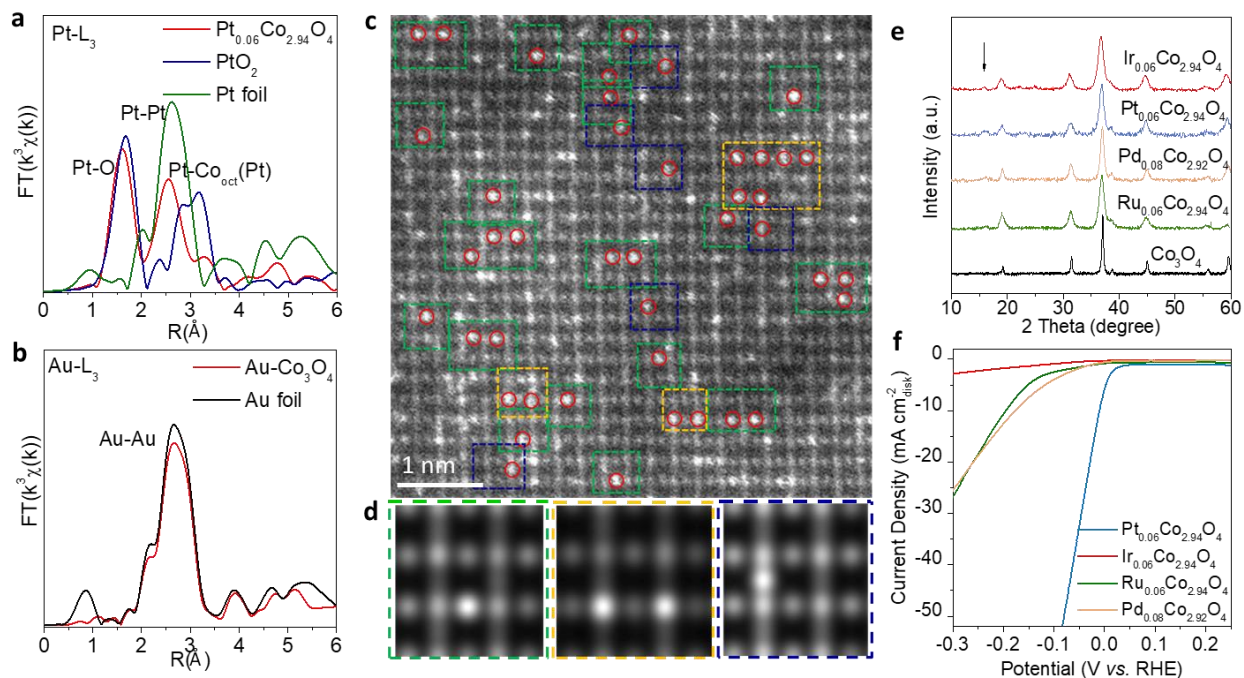


**Fig. 2. Geometric structure identification and catalytic performance evaluation of  $M_x\text{Co}_{3-x}\text{O}_4$  catalysts.** (a) Pt  $L_3$ -edge FT-EXAFS spectra of  $\text{Pt}_{0.06}\text{Co}_{2.94}\text{O}_4$  and the references. (b) Au  $L_3$ -edge FT-EXAFS spectra of  $\text{Au-Co}_3\text{O}_4$  and the reference. (c) Experimental atomic-resolution HRSTEM image of  $\text{Pt}_{0.06}\text{Co}_{2.94}\text{O}_4$  catalyst with Pt sites labelled by red circles and image motifs labelled by dashed rectangles with different colors. (d) Simulated projected  $Z^2$ -maps along symmetry-related  $\langle 233 \rangle$  directions, which match the image motifs marked in (c). (e) XRD patterns of  $M_x\text{Co}_{3-x}\text{O}_4$  catalysts. (f) HER performance of  $M_x\text{Co}_{3-x}\text{O}_4$  catalysts in Ar-saturated 0.1 M  $\text{HClO}_4$  electrolyte, sweep rate:  $10 \text{ mV s}^{-1}$ , rotation speed: 1600 rpm.

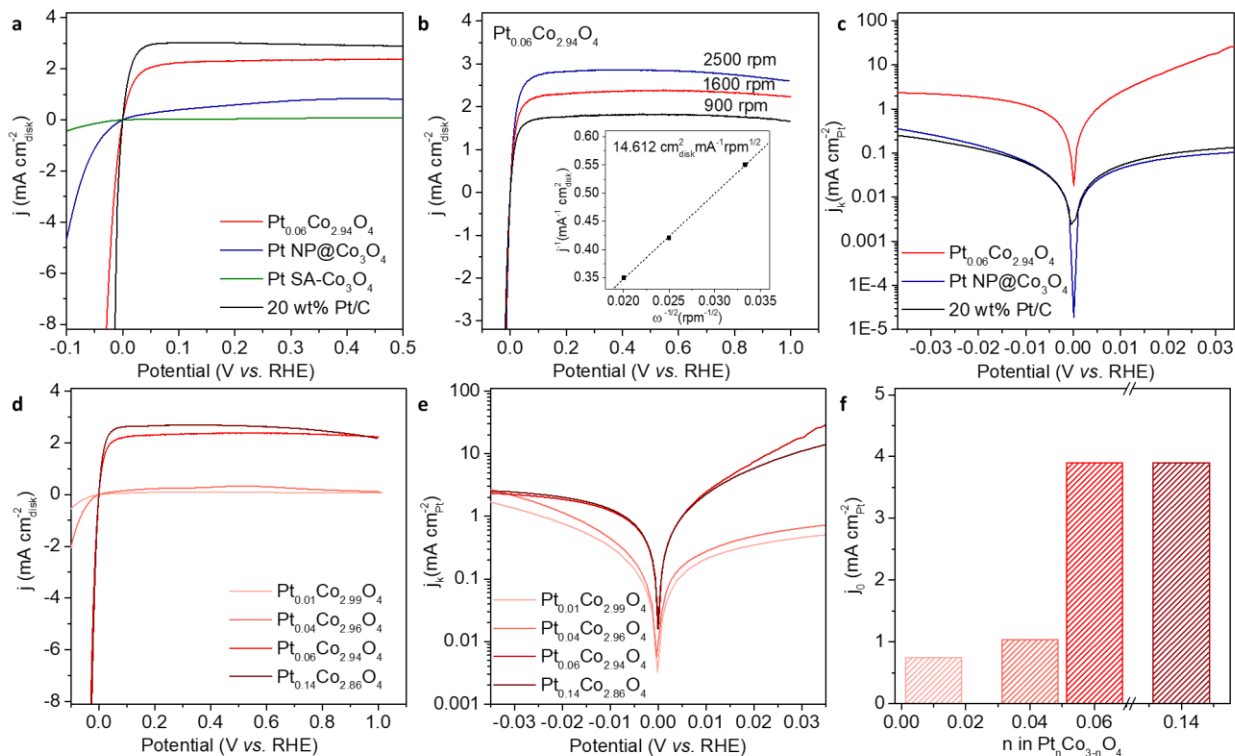


**Fig. 3. HER/HOR performance evaluation of  $\text{Pt}_n\text{Co}_{3-n}\text{O}_4$  catalysts.** (a) Polarization curves normalized to surface area of disk electrodes made from various catalysts in  $\text{H}_2$ -saturated 0.1 M  $\text{HClO}_4$ , sweep rate:  $2 \text{ mV s}^{-1}$ , rotation speed: 1600 rpm. (b) Polarization curves for  $\text{Pt}_{0.06}\text{Co}_{2.94}\text{O}_4$  at different rotation speeds and the corresponding the Koutecky–Levich plot (inset). (c) Tafel plots of the HER/HOR kinetic current density for  $\text{Pt}_{0.06}\text{Co}_{2.94}\text{O}_4$ , Pt NP@ $\text{Co}_3\text{O}_4$  and Pt/C catalysts. (d) Polarization curves normalized to ECSAs of electrodes made from  $\text{Pt}_n\text{Co}_{3-n}\text{O}_4$  catalysts in  $\text{H}_2$ -saturated 0.1 M  $\text{HClO}_4$ , sweep rate:  $2 \text{ mV s}^{-1}$ , rotation speed: 1600 rpm. (e) Tafel plots of the HER/HOR kinetic current density for  $\text{Pt}_n\text{Co}_{3-n}\text{O}_4$  catalysts. (f) Comparison of exchange current density on  $\text{Pt}_n\text{Co}_{3-n}\text{O}_4$  catalysts.

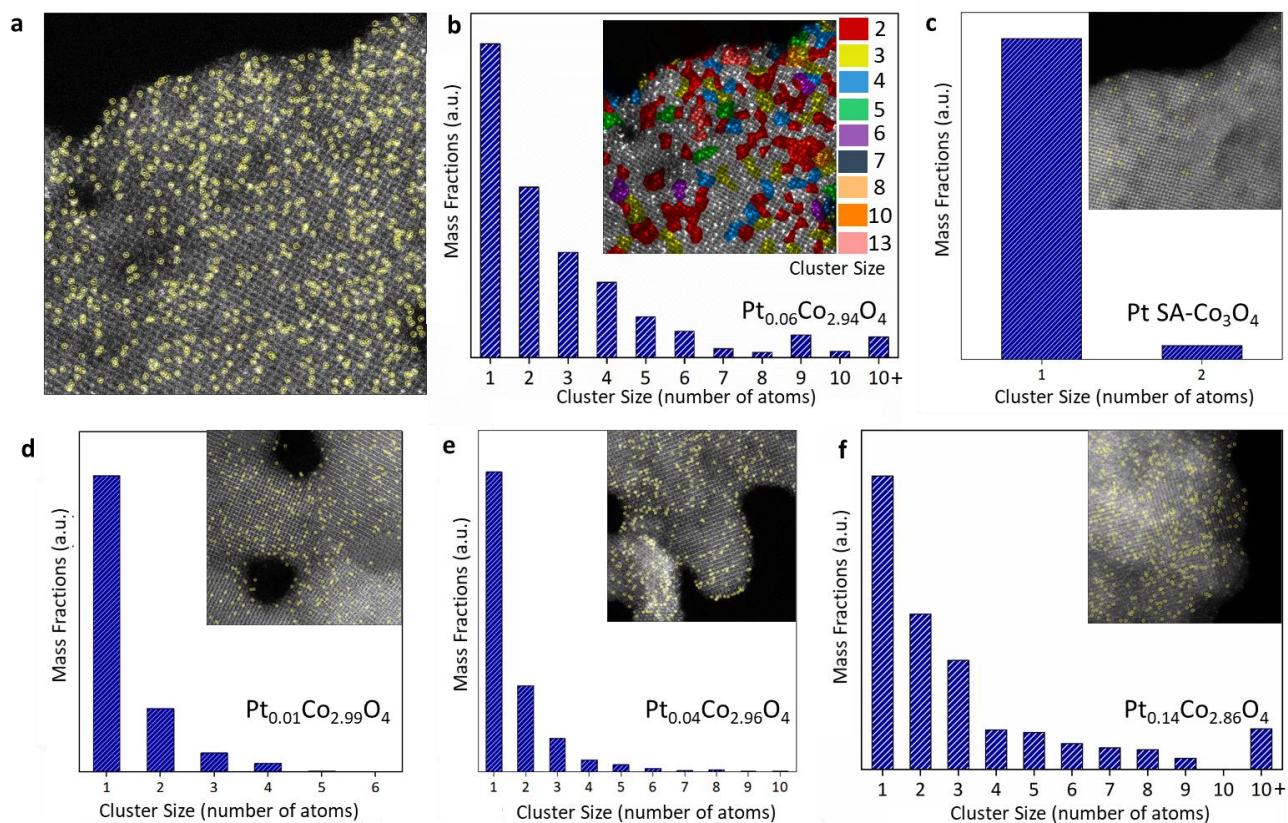


**Fig. 4. Spatial structure analyses on Pt substitutions in  $Pt_nCo_{3-n}O_4$  catalysts.** (a) HRSTEM image of a typical  $Pt_{0.06}Co_{2.94}O_4$  nanocrystal projected along  $\langle 233 \rangle$  direction with Pt sites searched and labelled by yellow circles. (b) Mass fraction histogram of identified projected clusters in the  $Pt_{0.06}Co_{2.94}O_4$  catalyst with different numbers of correlated Pt dopant sites. Inset shows the the distribution map for those correlated Pt sites. Mass fraction histogram of identified isolated Pt sites and projected clusters with different numbers of correlated Pt dopant sites in the (c) Pt SA- $Co_3O_4$ , (d)  $Pt_{0.01}Co_{2.99}O_4$ , (e)  $Pt_{0.04}Co_{2.96}O_4$ , and (c)  $Pt_{0.14}Co_{2.86}O_4$  catalysts.

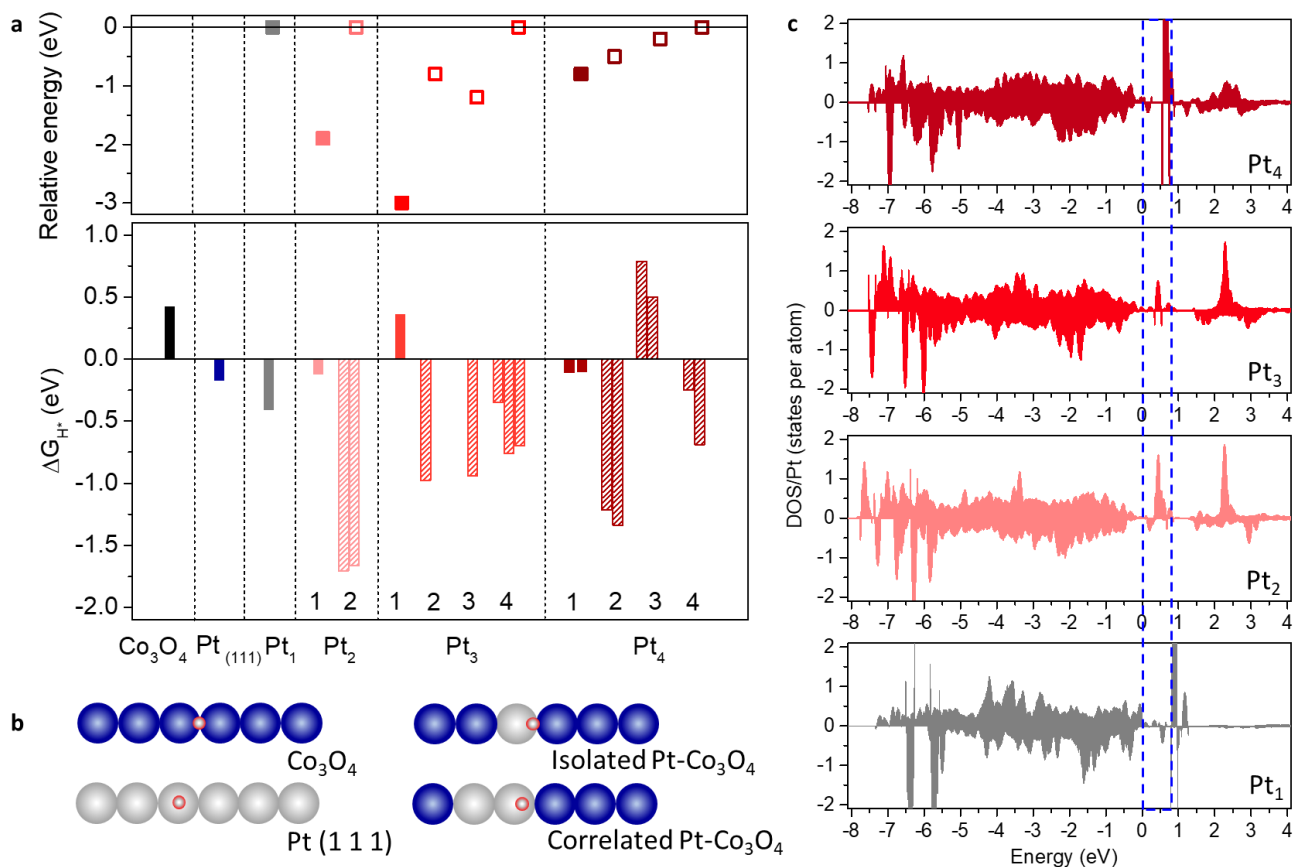


**Fig. 5. Theoretical investigations on correlated Pt substituted  $\text{Co}_3\text{O}_4$  for HER.** (a) Upper: Calculated relative energies of various configurations for  $\text{Co}_3\text{O}_4$  models with different Pt cluster sizes ( $\text{Pt}_1$ - $\text{Pt}_4$ ). The configuration with the lowest free energy is defined as 0 eV and the relative energies of the other configurations are determined accordingly. Lower: The calculated hydrogen adsorption energy on various configurations. The solid bars represent the values for the most stable configurations of each Pt cluster size. (b) The schematic hydrogen adsorption configurations for pure  $\text{Co}_3\text{O}_4$ ,  $\text{Pt}(111)$ , isolated Pt substituted  $\text{Co}_3\text{O}_4$ , and correlated Pt substituted  $\text{Co}_3\text{O}_4$  models. (d) Calculated Pt pDOS curves for Pt single atom ( $\text{Pt}_1$ ) substituted  $\text{Co}_3\text{O}_4$  and correlated Pt substituted  $\text{Co}_3\text{O}_4$  with Pt cluster size of 2-4 atoms ( $\text{Pt}_2$ - $\text{Pt}_4$ ).

## References

1. Liu, L. & Corma, A. Metal Catalysts for Heterogeneous Catalysis: From Single Atoms to Nanoclusters and Nanoparticles. *Chem. Rev.* **118**, 4981-5079 (2018).
2. Seh, Z. W. *et al.* Combining theory and experiment in electrocatalysis: Insights into materials design. *Science* **355**, eaad4998 (2017).
3. Mavrikakis, M., Stoltze, P. & Nørskov, J. K. Making gold less noble. *Catalysis Letters* **64**, 101-106 (2000).
4. Li, Y. *et al.* Recent Advances on Water-Splitting Electrocatalysis Mediated by Noble-Metal-Based Nanostructured Materials. *Advanced Energy Materials* **10** (2020).
5. Tian, X., Zhao, P. & Sheng, W. Hydrogen Evolution and Oxidation: Mechanistic Studies and Material Advances. *Adv Mater* **31**, e1808066 (2019).
6. Yang, J., Li, W., Wang, D. & Li, Y. Electronic Metal-Support Interaction of Single-Atom Catalysts and Applications in Electrocatalysis. *Adv Mater*, e2003300 (2020).
7. Li, X. *et al.* Supported Noble-Metal Single Atoms for Heterogeneous Catalysis. *Adv Mater*, e1902031 (2019).
8. Stamenkovic, V. R. *et al.* Improved Oxygen Reduction Activity on Pt<sub>3</sub>Ni(111) via Increased Surface Site Availability. *Science* **315**, 493-497 (2007).
9. Greeley, J. *et al.* Alloys of platinum and early transition metals as oxygen reduction electrocatalysts. *Nat. Chem.* **1**, 552-556 (2009).
10. Lee, S. W. *et al.* Roles of Surface Steps on Pt Nanoparticles in Electro-oxidation of Carbon Monoxide and Methanol. *J. Am. Chem. Soc.* **131**, 15669–15677 (2009).
11. Tsung, C. *et al.* Sub-10 nm Platinum Nanocrystals with Size and Shape Control: Catalytic Study for Ethylene and Pyrrole Hydrogenation. *J. Am. Chem. Soc.* **131**, 5816-5822 (2009).
12. Lykhach, Y. *et al.* Counting electrons on supported nanoparticles. *Nat Mater* **15**, 284-288 (2016).
13. Xiaofeng Yang *et al.* Single-Atom Catalysts: A New Frontier in Heterogeneous Catalysis. *Acc Chem Res* **46**, 1740–1748 (2013).
14. Chen, Y. *et al.* Single-Atom Catalysts: Synthetic Strategies and Electrochemical Applications. *Joule* **2**, 1242-1264 (2018).
15. Tian, S. *et al.* Regulating the Catalytic Performance of Single-Atomic-Site Ir Catalyst for Biomass Conversion by Metal–Support Interactions. *ACS Catal.* **9**, 5223-5230 (2019).
16. Li, J. *et al.* Highly Active and Stable Metal Single-Atom Catalysts Achieved by Strong Electronic Metal-Support Interactions. *J. Am. Chem. Soc.* **141**, 14515-14519 (2019).
17. Dong, C. *et al.* Supported Metal Clusters: Fabrication and Application in Heterogeneous Catalysis. *ACS Catalysis* **10**, 11011-11045 (2020).
18. Shan, J. *et al.* Short-Range Ordered Iridium Single Atoms Integrated into Cobalt Oxide Spinel Structure for Highly Efficient Electrocatalytic Water Oxidation. *Journal of the American Chemical Society* (2021).

19. Ling, T., Jaroniec, M. & Qiao, S. Z. Recent Progress in Engineering the Atomic and Electronic Structure of Electrocatalysts via Cation Exchange Reactions. *Adv Mater*, e2001866 (2020).
20. Liu, D. *et al.* Atomically dispersed platinum supported on curved carbon supports for efficient electrocatalytic hydrogen evolution. *Nature Energy* **4**, 512-518 (2019).
21. Zhang, Q. *et al.* In situ DRIFT spectroscopy insights into the reaction mechanism of CO and toluene co-oxidation over Pt-based catalysts. *Catalysis Science & Technology* **9**, 4538-4551 (2019).
22. Liu, L. *et al.* Imaging defects and their evolution in a metal-organic framework at sub-unit-cell resolution. *Nat. Chem.* **11**, 622-628 (2019).
23. Sheng, W. *et al.* Non-precious metal electrocatalysts with high activity for hydrogen oxidation reaction in alkaline electrolytes. *Energy Environ. Sci.* **7**, 1719-1724 (2014).
24. Hosterman, B. D. Raman Spectroscopic Study of Solid Solution Spinel Oxides.
25. Xie, X. *et al.* Low-temperature oxidation of CO catalysed by Co<sub>3</sub>O<sub>4</sub> nanorods. *Nature* **458**, 746 (2009).
26. Jiao, Y., Zheng, Y., Davey, K. & Qiao, S.-Z. Activity origin and catalyst design principles for electrocatalytic hydrogen evolution on heteroatom-doped graphene. *Nature Energy* **1** (2016).
27. Choi, W. S. *et al.* Wide bandgap tunability in complex transition metal oxides by site-specific substitution. *Nat Commun* **3**, 689 (2012).
28. Hu, H., Guan, Bu Y. & Lou, Xiong W. Construction of Complex CoS Hollow Structures with Enhanced Electrochemical Properties for Hybrid Supercapacitors. *Chem* **1**, 102-113 (2016).
29. Koch, C. *Determination of core structure periodicity and point defect density along dislocations* Ph. D. thesis, Arizona State University, (2002).
30. Zhang, Q. *et al.* CalAtom: A software for quantitatively analysing atomic columns in a transmission electron microscope image. *Ultramicroscopy* **202**, 114-120 (2019).
31. Zhang, Q. *et al.* Multiple-ellipse fitting method to precisely measure the positions of atomic columns in a transmission electron microscope image. *Micron* **113**, 99-104 (2018).
32. Durst, J., Simon, C., Hasché, F. & Gasteiger, H. A. Hydrogen Oxidation and Evolution Reaction Kinetics on Carbon Supported Pt, Ir, Rh, and Pd Electrocatalysts in Acidic Media. *Journal of The Electrochemical Society* **162**, F190-F203 (2014).
33. Sheng, W., Gasteiger, H. A. & Shao-Horn, Y. Hydrogen Oxidation and Evolution Reaction Kinetics on Platinum: Acid vs Alkaline Electrolytes. *Journal of The Electrochemical Society* **157** (2010).
34. G. Kresse & Furthmüller, J. Efficient iterative schemes for ab initio total-energy calculations using a plane-wave basis set. *Phys. Rev. B* **54**, 11169-11186 (1996).
35. G. Kresse & Furthmüller, J. Efficiency of ab-initio total energy calculations for metals and semiconductors using a plane-wave basis set. *Comp. Mater. Sci.* **6**, 15-50 (1996).
36. John P. Perdew, Kieron Burke & Ernzerhof, M. Generalized Gradient Approximation Made Simple. *Phys. Rev. Lett.* **77**, 3865-3868 (1996).



37. Tkatchenko, A. & Scheffler, M. Accurate Molecular Van Der Waals Interactions from Ground-State Electron Density and Free-Atom Reference Data. *Phys. Rev. Lett.* **102**, 073005 (2009).
38. Chen, J., Wu, X. & Selloni, A. Electronic structure and bonding properties of cobalt oxide in the spinel structure. *Phys. Rev. B* **83**, 245204 (2011).
39. Lan, G., Song, J. & Yang, Z. A linear response approach to determine Hubbard U and its application to evaluate properties of Y2B2O7, B = transition metals 3d, 4d and 5d. *J. Alloy. Compd.* **749**, 909-925 (2018).
40. Sclauzero, G. & Dal Corso, A. Efficient DFT+U calculations of ballistic electron transport: Application to Au monatomic chains with a CO impurity. *Phys. Rev. B* **87**, 085108 (2013).
41. Nørskov, J. K. *et al.* Trends in the Exchange Current for Hydrogen Evolution. *Journal of The Electrochemical Society* **152**, J23 (2005).

# Supporting Information

## Spatial Structure Tuning of Correlated Single-Atom Platinum Sites for Acidic Hydrogen Evolution and Oxidation Electrocatalysis

Jieqiong Shan<sup>1,2,†</sup>, Chao Ye<sup>1,2,†</sup>, Yihan Zhu<sup>3\*</sup>, Yao Zheng<sup>1,2\*</sup> and Shi-Zhang Qiao<sup>1,2\*</sup>

<sup>1</sup> School of Chemical Engineering and Advanced Materials, The University of Adelaide, Adelaide, SA5005, Australia.

<sup>2</sup> Centre for Materials in Energy and Catalysis, The University of Adelaide, Adelaide, SA 5005, Australia.

<sup>3</sup> Center for Electron Microscopy, State Key Laboratory Breeding Base of Green Chemistry Synthesis Technology and College of Chemical Engineering, Zhejiang University of Technology, Hangzhou 310014, China.

\*Correspondence to: [yihanzhu@zjut.edu.cn](mailto:yihanzhu@zjut.edu.cn); [yao.zheng01@adelaide.edu.au](mailto:yao.zheng01@adelaide.edu.au); [s.qiao@adelaide.edu.au](mailto:s.qiao@adelaide.edu.au).

## Methods

### Construction of ternary phase diagrams

The formation energy ( $\Delta G_f$ ) was introduced to describe the thermodynamic stability of the compounds used. For  $M\text{-Co}_{11}\text{O}_{16}$  at standard conditions,

$$\Delta G_f(M\text{-Co}_{11}\text{O}_{16}) = G_{M\text{-Co}_{11}\text{O}_{16}} - \mu_{M(s)} - 11\mu_{\text{Co}(s)} - 16\mu_{\text{O}(g)}$$

where  $G_{M\text{-Co}_{11}\text{O}_{16}}$  is the Gibbs free energy of  $M\text{-Co}_{11}\text{O}_{16}$ ,  $\mu_{M(s)}$ ,  $\mu_{\text{Co}(s)}$  and  $\mu_{\text{O}(g)}$  are the atomic chemical potentials of elemental M, Co and oxygen gas, respectively. To maintain a stable compound, the sum of atomic chemical potentials of all atoms equals to the Gibbs free energy of  $\text{Ir-Co}_{11}\text{O}_{16}$ , namely,  $G_{M\text{-Co}_{11}\text{O}_{16}} = \mu_M + 11\mu_{\text{Co}} + 16\mu_{\text{O}}$ , in which  $\mu_M$ ,  $\mu_{\text{Co}}$  and  $\mu_{\text{O}}$  are the atomic chemical potentials of M, Co and O atoms in the compound, respectively. In general, the atomic chemical potentials can vary within a range in near-equilibrium states of the compound<sup>3</sup>. Herein, at standard conditions,  $\mu_M$ ,  $\mu_{\text{Co}}$  and  $\mu_{\text{O}}$  can be redefined as

$$\mu_M = \mu_{M(s)} + \Delta\mu_M;$$

$$\mu_{\text{Co}} = \mu_{\text{Co}(s)} + \Delta\mu_{\text{Co}};$$

$$\mu_{\text{O}} = \mu_{\text{O}(g)} + \Delta\mu_{\text{O}};$$

where  $\Delta\mu_M$ ,  $\Delta\mu_{\text{Co}}$  and  $\Delta\mu_{\text{O}}$  are the varying ranges of  $\mu_M$ ,  $\mu_{\text{Co}}$  and  $\mu_{\text{O}}$ , respectively. To determine the chemical potential of a solid element  $i$  ( $\mu_{i(s)}$ ) through DFT calculation, we assign the enthalpy and entropy as  $H_{i(s)} = E_{i(s)}^{\text{DFT}}$  and  $S_{i(s)} = 0$  (at standard conditions)<sup>4</sup>. As a result,  $\mu_{i(s)}$  equals to  $E_{i(s)}^{\text{DFT}}$ . To determine the atomic chemical potential of the oxygen gas ( $\mu_{\text{O}(g)}$ ), we assign  $\mu_{\text{O}(g)}$  and Gibbs free energy of the oxygen ( $G_{\text{O}_2(g)}$ ) at the standard state as  $2\mu_{\text{O}(g)} = G_{\text{O}_2(g)} = E_{\text{O}_2(g)}^{\text{DFT}} + E_{\text{O}_2(g)}^{\text{ZPE}} + RT - TS_{\text{O}_2(g)}^{\text{exp}}$ , where  $S_{\text{O}_2(g)}^{\text{exp}} = 205.152 \text{ J mol}^{-1} \text{ K}^{-1}$  is an experimental entropy<sup>5</sup>. As a result,  $\mu_{\text{O}(g)} = -4.63 \text{ eV}$  is obtained.

Assuming  $\text{Ir-Co}_{11}\text{O}_{16}$  is a stable compound, we have

$$\Delta G_f(\text{Ir-Co}_{11}\text{O}_{16}) = 11\Delta\mu_{\text{Co}} + \Delta\mu_{\text{Ir}} + 16\Delta\mu_{\text{O}}.$$

There are some thermodynamic limitations to determine  $\Delta\mu_{\text{Co}}$ ,  $\Delta\mu_{\text{Ir}}$ ,  $\Delta\mu_{\text{O}}$  and the stability of  $\text{Ir-Co}_{11}\text{O}_{16}$ .

Firstly,  $\mu_M$ ,  $\mu_{\text{Co}}$  and  $\mu_{\text{O}}$  should be smaller than  $\mu_{M(s)}$ ,  $\mu_{\text{Co}(s)}$  and  $\mu_{\text{O}(g)}$  to avoid formation of elemental metal

Ir, Co and oxygen gas. Furthermore,  $\mu_M$ ,  $\mu_{Co}$  and  $\mu_O$  are restricted by possible competing phases including CoO, CoO<sub>2</sub>, Co<sub>3</sub>O<sub>4</sub> and IrO<sub>2</sub><sup>3</sup>. Here, tetrahedral site substitution of Ir in Co spinel oxide lattice (Ir-Co<sub>11</sub>O<sub>16\_tet</sub>) was also considered as a competing phase. The following equations can be solved to obtain the varying ranges of  $\Delta\mu_M$ ,  $\Delta\mu_{Co}$  and  $\Delta\mu_O$ :

$$\Delta\mu_{Co} \leq 0;$$

$$\Delta\mu_{Ir} \leq 0;$$

$$\Delta\mu_O \leq 0;$$

$$11\Delta\mu_{Co} + \Delta\mu_{Ir} + 16\Delta\mu_O \leq \Delta G_f(\text{Ir-Co}_{11}\text{O}_{16\_tet});$$

$$\Delta\mu_{Co} + \Delta\mu_O \leq \Delta G_f(\text{CoO});$$

$$\Delta\mu_{Co} + 2\Delta\mu_O \leq \Delta G_f(\text{CoO}_2);$$

$$4\Delta\mu_{Co} + 3\Delta\mu_O \leq \Delta G_f(\text{Co}_3\text{O}_4);$$

$$\Delta\mu_{Ir} + 2\Delta\mu_O \leq \Delta G_f(\text{IrO}_2).$$

Using the approach, the thermodynamic stable conditions of Ir-Co<sub>11</sub>O<sub>16</sub>, Pt-Co<sub>11</sub>O<sub>16</sub>, Ru-Co<sub>11</sub>O<sub>16</sub>, Pd-Co<sub>11</sub>O<sub>16</sub> and Au-Co<sub>47</sub>O<sub>64</sub> can be determined.

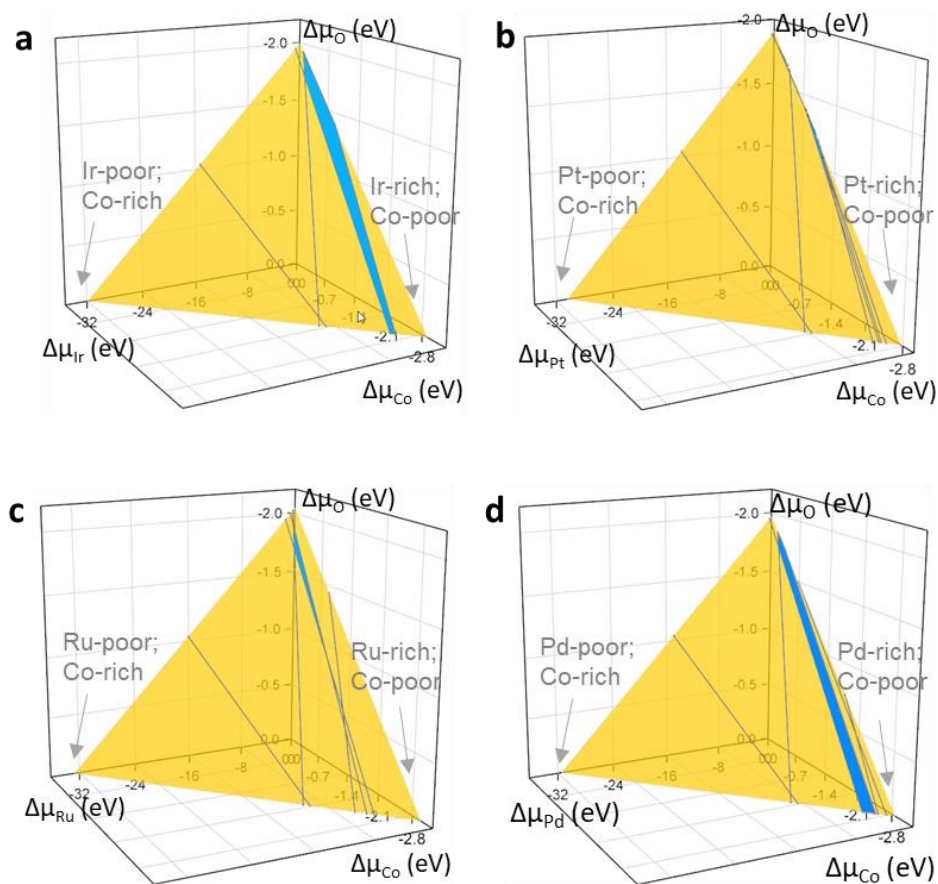


**Fig. S1.** The calculated stability triangles for  $M\text{-Co}_{11}\text{O}_{16}$  in the  $(\Delta\mu_{\text{Co}}, \Delta\mu_{\text{M}}, \Delta\mu_{\text{O}})$  spaces. The  $\text{Ir-Co}_{11}\text{O}_{16}$  catalyst is thermodynamically stable against all the competing phases in the ranges of  $-2.65 \leq \Delta\mu_{\text{Co}} \leq 0.09$ ,  $-3.26 \leq \Delta\mu_{\text{Ir}} \leq 0.00$  and  $-1.93 \leq \Delta\mu_{\text{O}} \leq 0.00$ ; the  $\text{Pt-Co}_{11}\text{O}_{16}$  catalyst is thermodynamically stable against all the competing phases in the ranges of  $-1.55 \leq \Delta\mu_{\text{Co}} \leq -0.76$ ,  $-0.80 \leq \Delta\mu_{\text{Pt}} \leq -0.79$  and  $-1.38 \leq \Delta\mu_{\text{O}} \leq -0.79$ ; the stable  $\text{Ru-Co}_{11}\text{O}_{16}$  and  $\text{Pd-Co}_{11}\text{O}_{16}$  catalysts can exist against all the competing phases with the ranges of  $-1.26 \leq \Delta\mu_{\text{Co}} \leq -0.12$ ,  $-2.70 \leq \Delta\mu_{\text{Ru}} \leq -0.90$ ,  $-1.91 \leq \Delta\mu_{\text{O}} \leq -1.01$  and  $-2.71 \leq \Delta\mu_{\text{Co}} \leq -0.17$ ,  $-2.88 \leq \Delta\mu_{\text{Pd}} \leq 0.00$ ,  $-1.85 \leq \Delta\mu_{\text{O}} \leq 0.00$ , respectively. The stable  $\text{Au-Co}_{47}\text{O}_{64}$  catalyst can exist against all the competing phases in the ranges of  $-2.54 \leq \Delta\mu_{\text{Co}} \leq -1.22$ ,  $-1.30 \leq \Delta\mu_{\text{Au}} \leq 0.00$ ,  $-0.98 \leq \Delta\mu_{\text{O}} \leq 0.00$ .

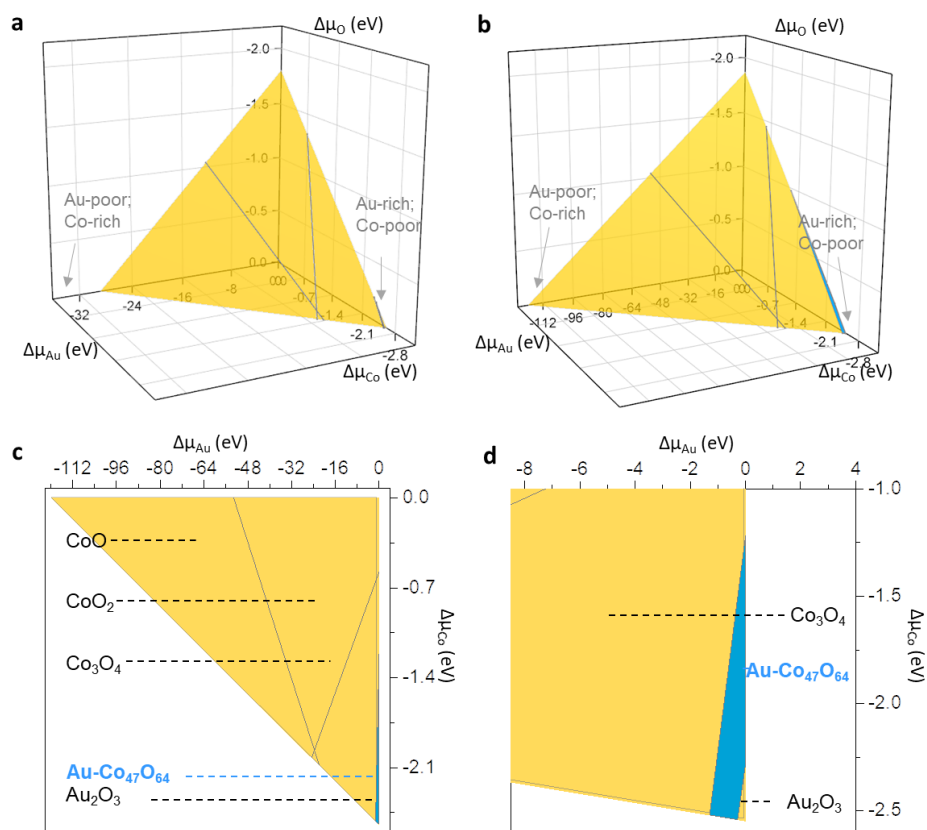


**Fig. S2.** (a) The calculated stability triangle for  $\text{Au-Co}_{11}\text{O}_{16}$  in the  $(\Delta\mu_{\text{Co}}, \Delta\mu_{\text{Au}}, \Delta\mu_{\text{O}})$  space; (b) The calculated stability triangle for  $\text{Au-Co}_{47}\text{O}_{64}$  in the  $(\Delta\mu_{\text{Co}}, \Delta\mu_{\text{Au}}, \Delta\mu_{\text{O}})$  space; (c) The projected triangle in the  $(\Delta\mu_{\text{Co}}, \Delta\mu_{\text{Au}})$  plane; (d) The enlarged projected triangle (c) in the  $(\Delta\mu_{\text{Co}}, \Delta\mu_{\text{Au}})$  plane in which the blue region represents the existence of stable  $\text{Au-Co}_{47}\text{O}_{64}$ . The stable  $\text{Au-Co}_{47}\text{O}_{64}$  catalyst can exist against all the competing phases in the ranges of  $-2.54 \leq \Delta\mu_{\text{Co}} \leq -1.22$ ,  $-1.30 \leq \Delta\mu_{\text{Au}} \leq 0.00$ ,  $-0.98 \leq \Delta\mu_{\text{O}} \leq 0.00$ .

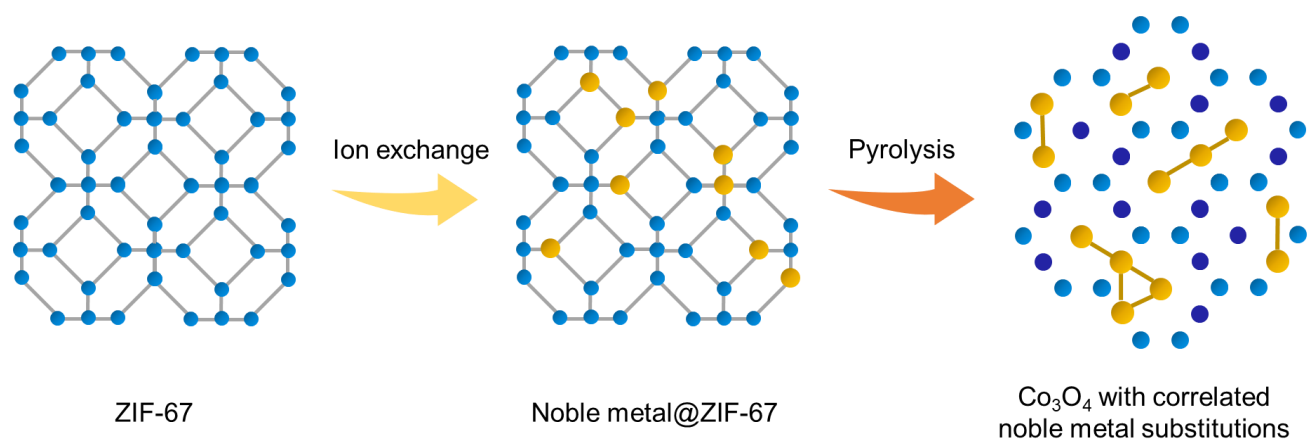


**Fig. S3.** Schematic illustration of ion exchange-pyrolysis strategy. Blue, yellow and navy dots refer to Co(II), Co(III) and noble metal ions, respectively.

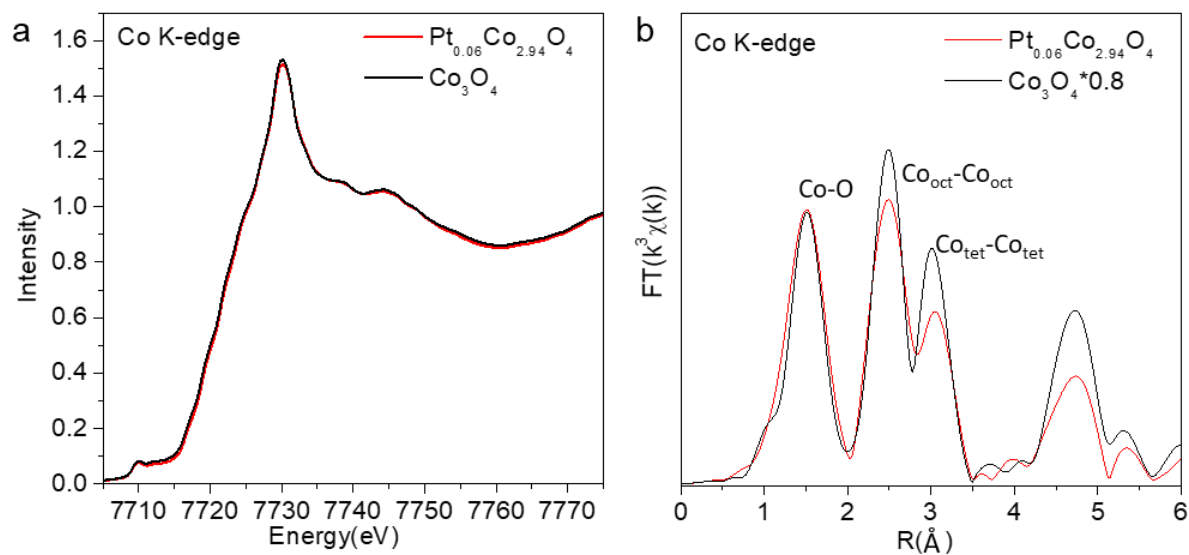


**Fig. S4.** Co K-edge (a) XANES spectra and (b) FT-EXAFS spectra of Pt<sub>0.06</sub>Co<sub>2.94</sub>O<sub>4</sub> and Co<sub>3</sub>O<sub>4</sub>.

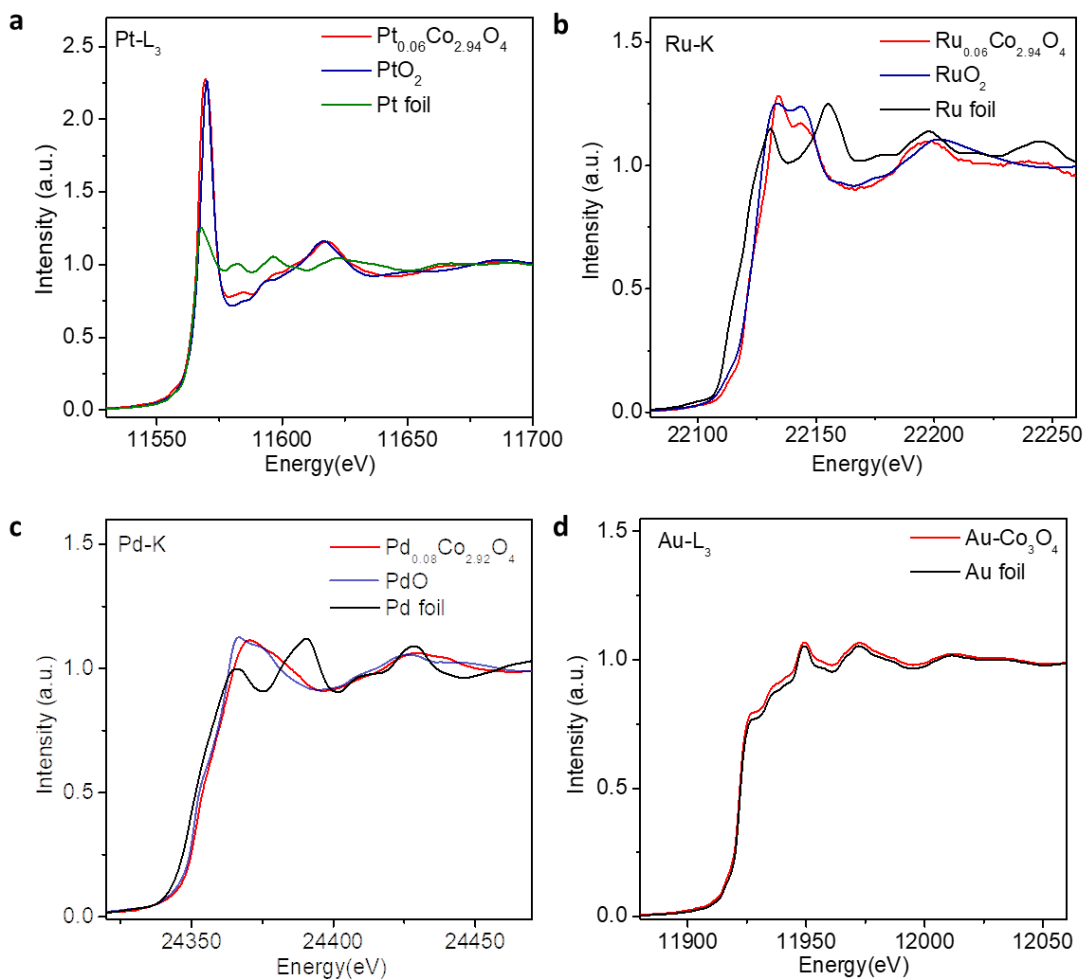


**Fig. S5.** (a) Pt L<sub>3</sub>-edge XANES spectra of Pt<sub>0.06</sub>Co<sub>2.94</sub>O<sub>4</sub> and the references; (b) Ru K-edge XANES spectra of Ru<sub>0.06</sub>Co<sub>2.94</sub>O<sub>4</sub> and the references; (c) Pd K-edge XANES spectra of Pd<sub>0.08</sub>Co<sub>2.92</sub>O<sub>4</sub>; (d) Au L<sub>3</sub>-edge XANES spectra of Au-Co<sub>3</sub>O<sub>4</sub> and the references. Pt, Ru and Pd exhibit high valence states like those of oxides, respectively. This suggests that the Pt, Ru and Pd ions are incorporated into the spinel oxide lattice and directly coordinated with O sites. In contrast, Au-Co<sub>3</sub>O<sub>4</sub> shows a low valence state close to that of Au foil, suggesting that the majority Au atoms exist as nanoparticles rather than dopants.



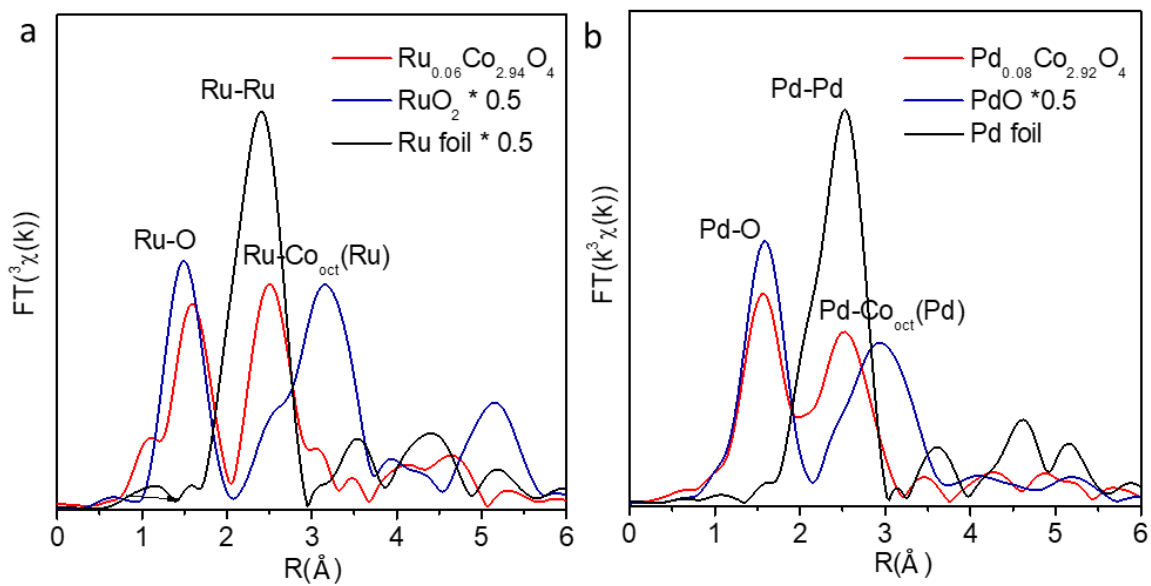


**Fig. S6.**  $k^3$ -weighted FT-EXAFS spectra of (a) Ru K-edge data for  $\text{Ru}_{0.06}\text{Co}_{2.94}\text{O}_4$  and (b) Pd K-edge data for  $\text{Pd}_{0.08}\text{Co}_{2.92}\text{O}_4$  and the corresponding references.

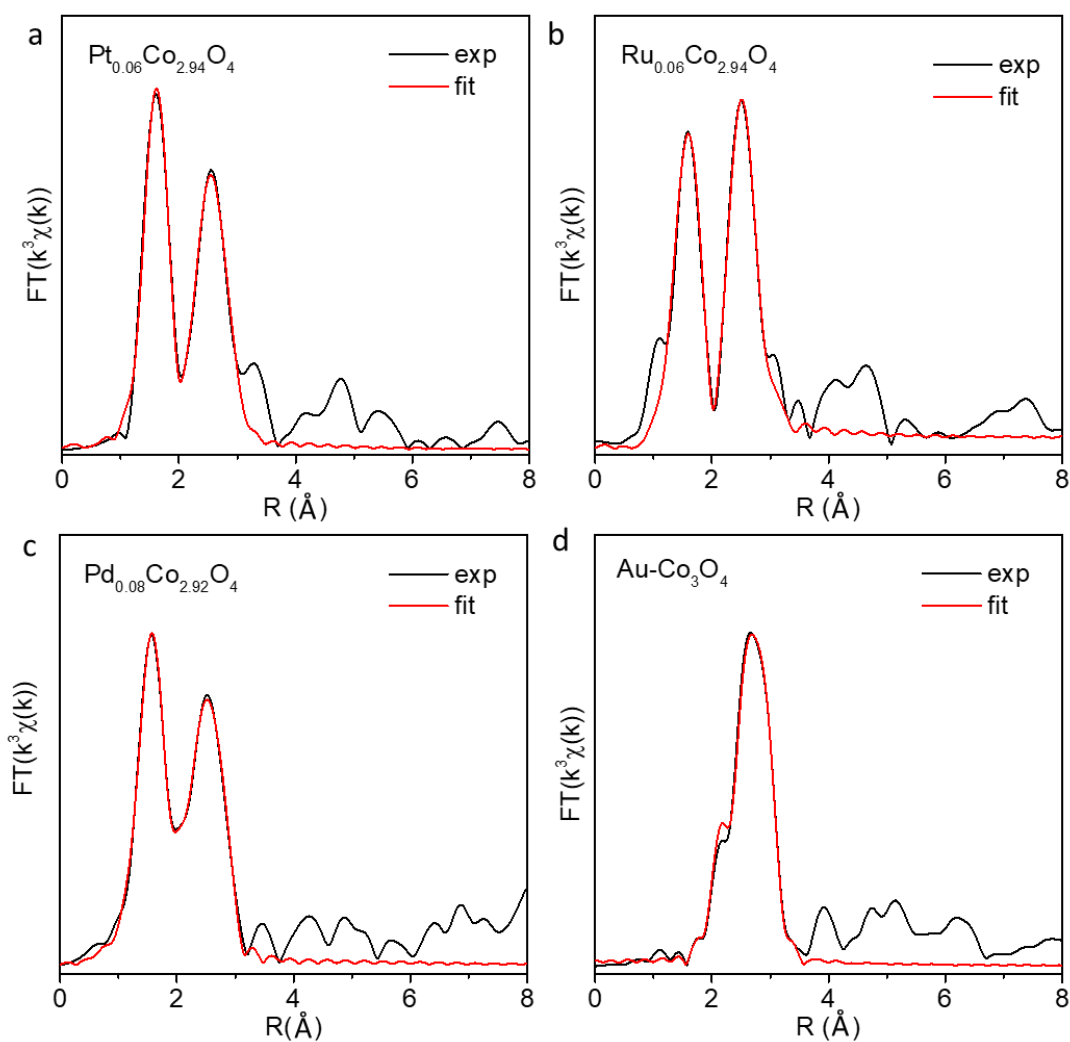


**Fig. S7.**  $k^3$ -weighted Fourier transform of Pt L<sub>3</sub>-edge, Ru K-edge, Pd K-edge and Au L<sub>3</sub>-edge experimental data (denoted as exp) and fitting data (denoted as fit) for (a) Pt<sub>0.06</sub>Co<sub>2.94</sub>O<sub>4</sub>, (b) Ru<sub>0.06</sub>Co<sub>2.94</sub>O<sub>4</sub>, (c) Pd<sub>0.08</sub>Co<sub>2.92</sub>O<sub>4</sub> and (d) Au-Co<sub>3</sub>O<sub>4</sub>, respectively. Au-Co<sub>3</sub>O<sub>4</sub> shows only one interatomic distance of Au-Au with CN close to that of Au foil, which suggests the formation of Au nanoparticles.

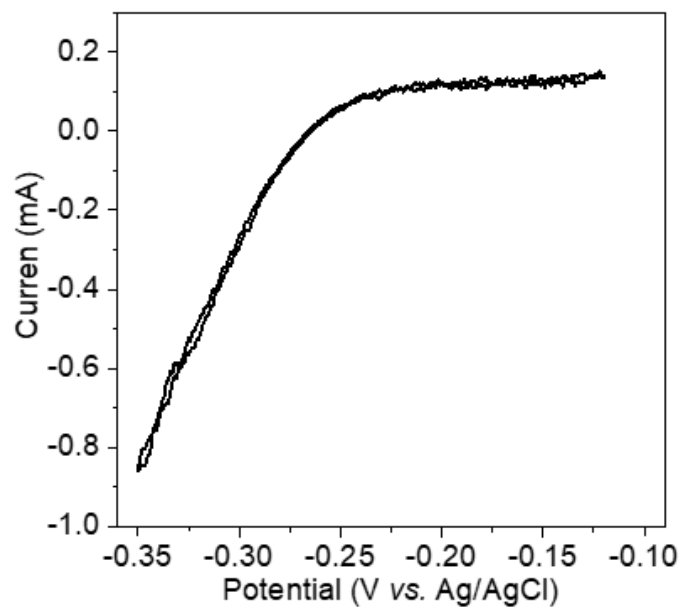


**Fig. S8.** Potential calibration of the Ag/AgCl reference electrode in H<sub>2</sub>-saturated 0.1 M HClO<sub>4</sub>.

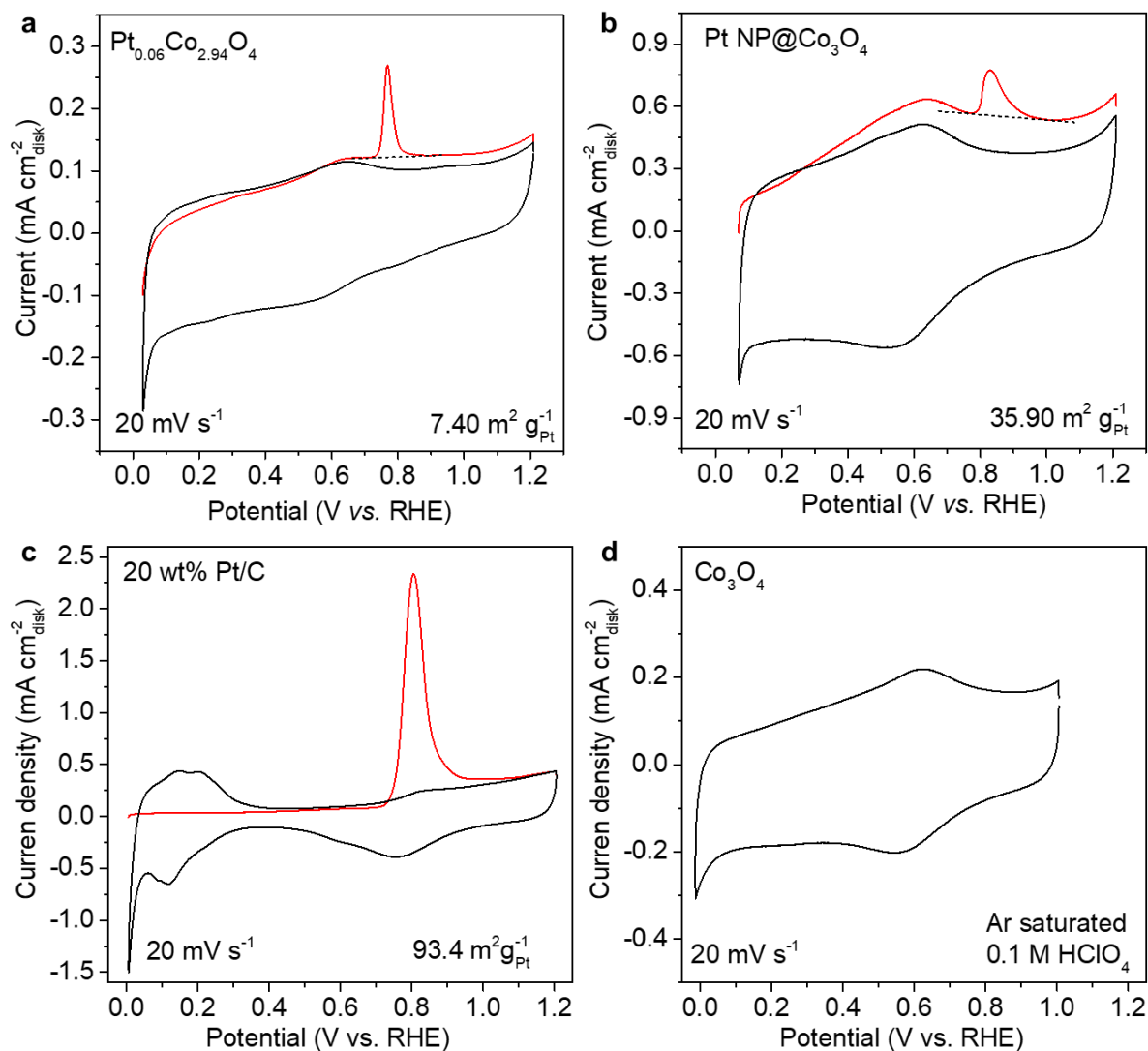


**Fig. S9.** CO stripping voltammograms of (a) Pt<sub>0.06</sub>Co<sub>2.94</sub>O<sub>4</sub>, (b) Pt NP@Co<sub>3</sub>O<sub>4</sub> and (c) Pt/C catalysts in 0.1M HClO<sub>4</sub> electrolytes. The scan rate is 20 mV s<sup>-1</sup>. The CV curve of pure Co<sub>3</sub>O<sub>4</sub> in Ar-saturated 0.1M HClO<sub>4</sub> is provided in panel d for comparison.

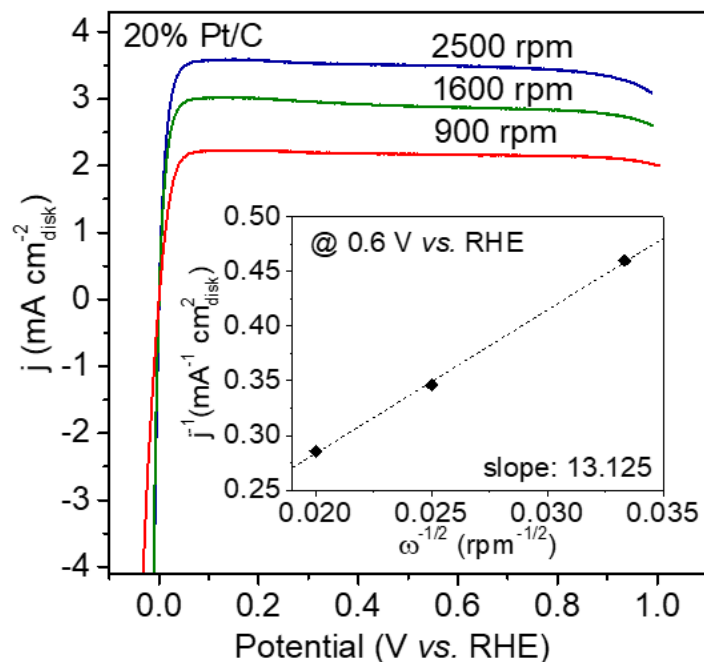


**Fig. S10.** Polarization curves for Pt/C catalyst at different rotation speeds and the corresponding the Koutecky–Levich plot (inset).

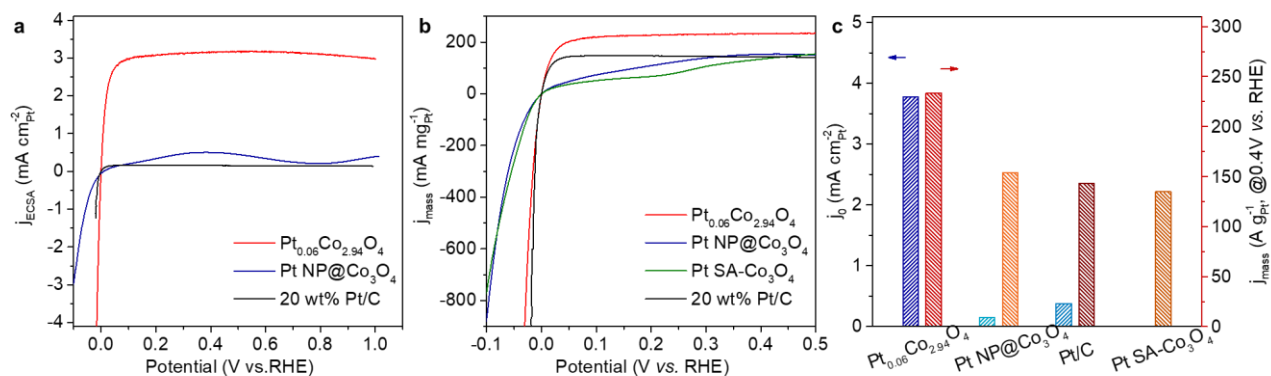


**Fig. S11.** (a) Polarization curves normalized to ECSA of Pt<sub>0.06</sub>Co<sub>2.94</sub>O<sub>4</sub>, Pt NP@Co<sub>3</sub>O<sub>4</sub> and Pt/C catalysts. (b) Polarization curves normalized to mass of Pt loaded on the electrodes of Pt<sub>0.06</sub>Co<sub>2.94</sub>O<sub>4</sub>, Pt NP@Co<sub>3</sub>O<sub>4</sub>, Pt SA-Co<sub>3</sub>O<sub>4</sub> and Pt/C catalysts. (c) Comparison of exchange current density (left y-axis) and mass activity (right y axis, determined @ 0.4 V vs. RHE) on Pt<sub>0.06</sub>Co<sub>2.94</sub>O<sub>4</sub>, Pt NP@Co<sub>3</sub>O<sub>4</sub>, Pt SA-Co<sub>3</sub>O<sub>4</sub> and Pt/C catalysts.

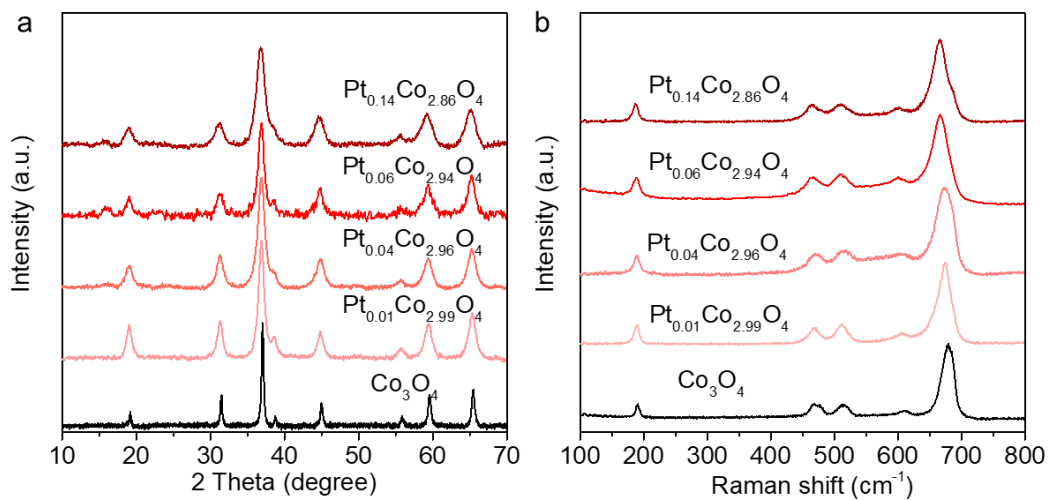


**Fig. S12.** (a) XRD patterns and (b) Raman spectra of Pt<sub>n</sub>Co<sub>3-n</sub>O<sub>4</sub> catalysts.

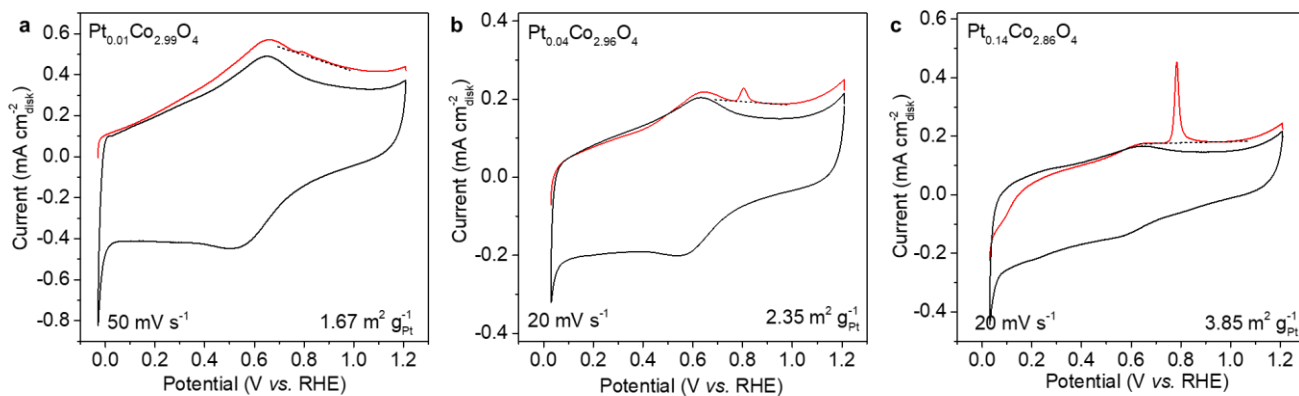


**Fig. S13** CO stripping voltammograms of (a) Pt<sub>0.01</sub>Co<sub>2.99</sub>O<sub>4</sub>, (b) Pt<sub>0.04</sub>Co<sub>2.96</sub>O<sub>4</sub>, and (c) Pt<sub>0.14</sub>Co<sub>2.86</sub>O<sub>4</sub> catalysts in 0.1M HClO<sub>4</sub> electrolytes. The scan rate is 50 mV s<sup>-1</sup> for Pt<sub>0.01</sub>Co<sub>2.99</sub>O<sub>4</sub> and 20 mV s<sup>-1</sup> for the other catalysts.

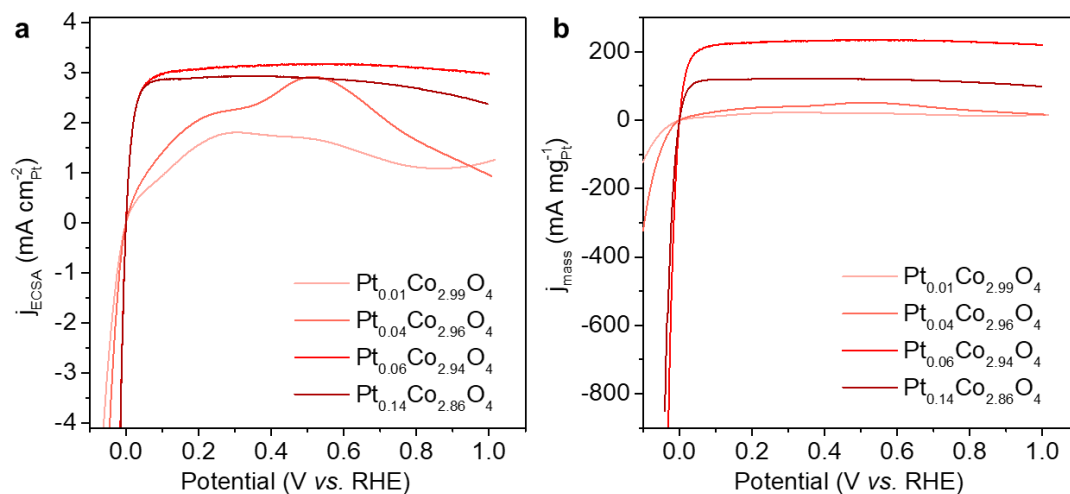


**Fig. S14** (a) Polarization curves normalized to surface areas of disk electrodes made from Pt<sub>n</sub>Co<sub>3-n</sub>O<sub>4</sub> catalysts in H<sub>2</sub>-saturated 0.1 M HClO<sub>4</sub>, (b) the corresponding polarization curves normalized to mass of Pt loaded on the electrodes, sweep rate: 2 mV s<sup>-1</sup>, rotation speed: 1600 rpm.

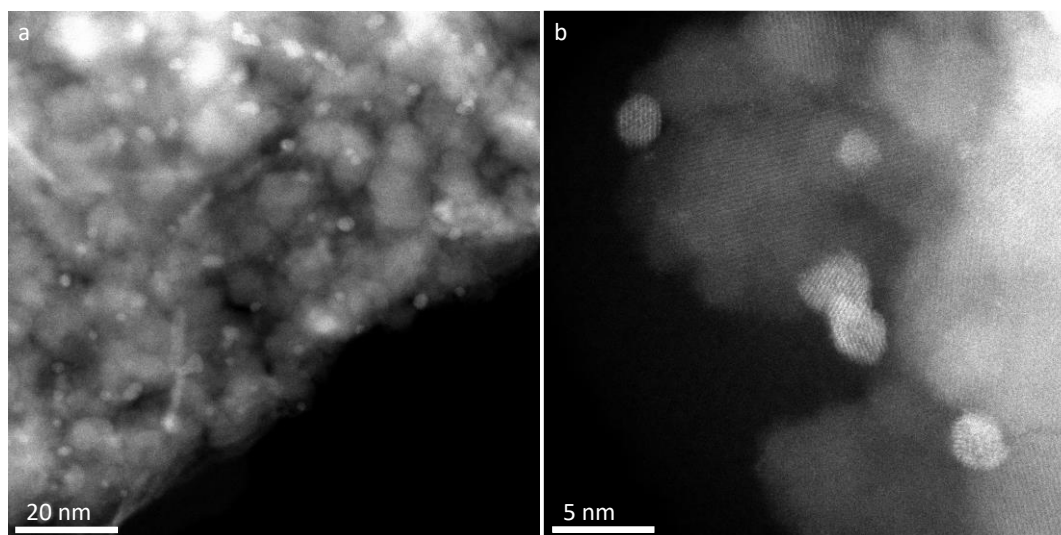


**Fig. S15.** STEM images of the Pt NP@Co<sub>3</sub>O<sub>4</sub> catalyst.

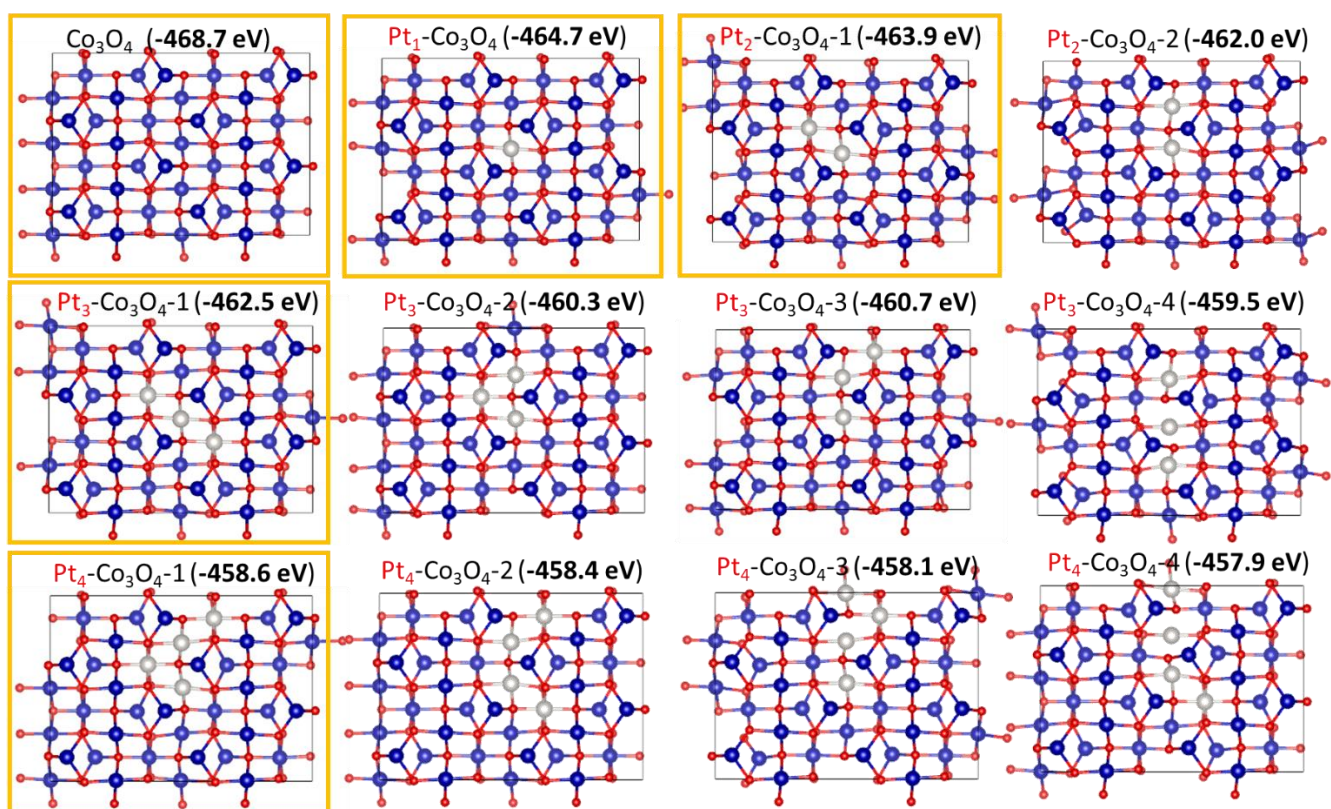


**Fig. S16.**  $\text{Co}_3\text{O}_4$  and  $\text{Pt}_n\text{-Co}_3\text{O}_4$  configurations and the corresponding free energies. The most stable configurations for model with various Pt cluster sizes have been highlighted with yellow boxes.

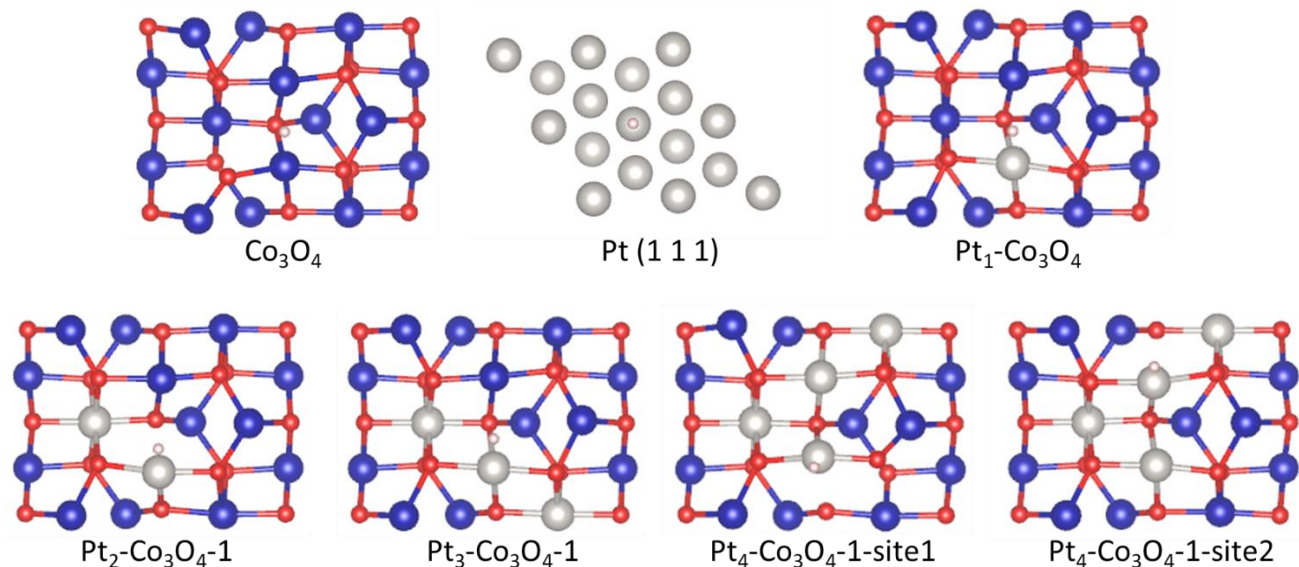


**Fig. S17.** Hydrogen adsorption on surfaces of  $\text{Co}_3\text{O}_4$ , Pt (1 1 1) and the most stable configurations with various Pt cluster sizes.



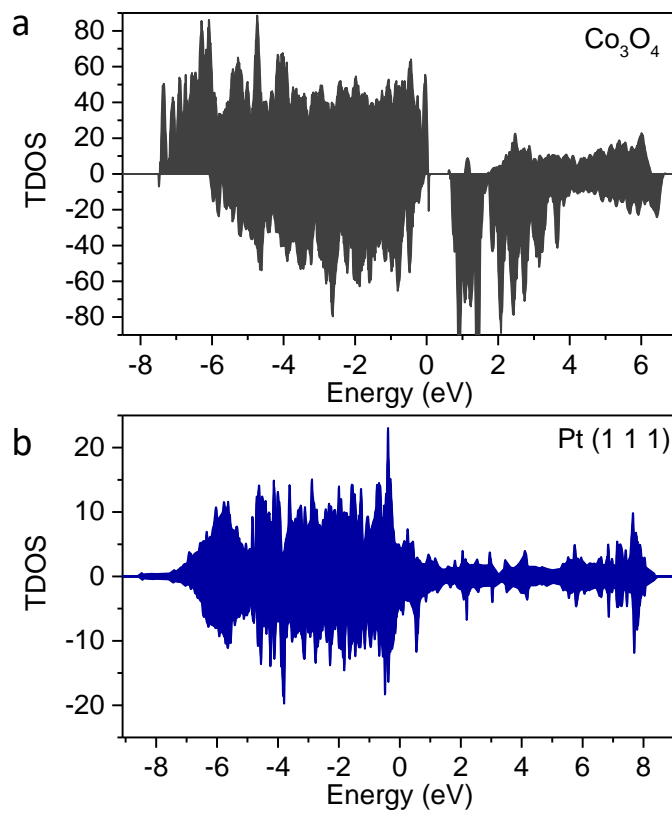


**Fig. S18.** Total DOS of (a) pure  $\text{Co}_3\text{O}_4$  and (b) Pt (1 1 1).

**Table S1** Fitting parameters of Fourier transform Pt L<sub>3</sub>-edge, Ru K-edge, Pd K-edge and Au L<sub>3</sub>-edge EXAFS data for Pt<sub>0.06</sub>Co<sub>2.94</sub>O<sub>4</sub>, Ru<sub>0.06</sub>Co<sub>2.94</sub>O<sub>4</sub>, Pd<sub>0.08</sub>Co<sub>2.92</sub>O<sub>4</sub>, Au-Co<sub>3</sub>O<sub>4</sub> and the references.

	Samples	Bond	CN	Bond length	$\sigma^2 (10^{-3} \text{ \AA}^2)$
<b>Pt-L<sub>3</sub> edge</b>	Pt <sub>0.06</sub> Co <sub>2.94</sub> O <sub>4</sub>	Pt-O	5.9	2.00	4.4
		Pt-Co	4.1	2.88	3.8
		Pt-Pt	2.9	2.75	5.0
	Pt foil	Pt-Pt	12*	2.77	4.9
	PtO <sub>2</sub>	Pt-O	6*	2.03	3.0
<b>Ru-K edge</b>	Ru <sub>0.06</sub> Co <sub>2.94</sub> O <sub>4</sub>	Ru-O	5.2	2.02	3.6
		Ru-Co	4.9	2.92	3.5
		Ru-Ru	2.5	2.98	5.9
	Ru foil	Ru-Ru	12*	2.68	4.1
	RuO <sub>2</sub>	Ru-O	6*	1.97	1.5
<b>Pd-K edge</b>	Pd <sub>0.08</sub> Co <sub>2.92</sub> O <sub>4</sub>	Pd-O	4.2	2.01	5.8
		Pd-Co	1.2	2.91	3.1
		Pd-Pd	5.6	2.72	10.8
	Pd foil	Pd-Pd	12*	2.74	5.5
	PdO	Pd-O	4*	2.02	1.8
<b>Au-L<sub>3</sub> edge</b>	Au-Co <sub>3</sub> O <sub>4</sub>	Au-Au	10.3	2.85	7.5
	Au foil	Au-Au	12*	2.86	7.8

CN, coordination number;  $\sigma^2$ , Debye-Waller factor; Error limits (accuracies) were estimated as follows: CN,  $\pm 10\%$ ; bond length,  $\pm 1\%$ ;  $\sigma^2$ ,  $\pm 10\%$ . \* refers to the fixed coordination number according to the standard crystal structure.

**Table S2** Comparison of exchange current density ( $j_0$ ) for Pt<sub>n</sub>Co<sub>3-n</sub>O<sub>4</sub> and Pt/C catalysts.

Samples	Pt <sub>0.01</sub> Co <sub>2.99</sub> O <sub>4</sub>	Pt <sub>0.04</sub> Co <sub>2.96</sub> O <sub>4</sub>	Pt <sub>0.06</sub> Co <sub>2.94</sub> O <sub>4</sub>	Pt <sub>0.14</sub> Co <sub>2.86</sub> O <sub>4</sub>	Pt/C	Pt NP@ Co <sub>3</sub> O <sub>4</sub>
$j_0$ (mA cm <sub>r</sub> <sup>-2</sup> )	0.75	1.04	3.78	3.90	0.38	0.15

## Chapter 7 Conclusions and perspectives

This thesis is devoted to the development of noble metal electrocatalysts with well-designed surface/interface structure and unique spatial topologies as high-efficiency candidates in key energy conversion reactions including OER, HER and HOR in acidic environments. Through a judicious combination of experimental methodologies, advanced characterization techniques and fundamental theoretical investigations, some major conclusions have been made in promoting the research understanding of this topic:

- (1) In the Ru@IrO<sub>x</sub> core-shell nanocrystals, the strong charge-redistribution across the core-shell heterojunction helps to break the activity and stability limits of RuO<sub>2</sub> and IrO<sub>2</sub> simultaneously and represents a promising strategy in facilitating catalytic performance.
- (2) The surface dopants in RuIr alloy catalysts exhibit dual effect in modifying surface intermediate species for OER and regulating surface valence states for HER. A linear activity dependence on the binding strength of reaction intermediates is demonstrated, which highlights the chemical/valence states of catalysts as a good indication of activity at the fundamental level.
- (3) A simple ion exchange-pyrolysis strategy has been adopted to allocate noble metal atoms with identical atomic spatial correlations in transition metal oxide host structures, which greatly diversifies the noble metal geometry structures and offers promising electronic properties towards acidic OER electrocatalysis.
- (4) A series of Pt-substituted cobalt spinel oxide was synthesized to illustrate the effect of spatial structure of correlated Pt substitutions on the physical properties and catalytic performance. The optimized Pt<sub>0.069</sub>Co<sub>2.931</sub>O<sub>4</sub> catalyst exhibited more than one order of

magnitude enhanced HER/HOR specific catalytic performance in acidic environment in comparison with that of commercial 20 wt% Pt/C catalyst.

Although progresses have been achieved in the development of noble metal electrocatalysts, some fundamental challenges remain to be investigated and point out the future perspectives in this topic, including the following:

(1) Substantial improvement in catalytic activity is required for the future electrocatalyst design towards PEM devices, especially acidic OER. The sluggish reaction kinetics of OER and the limited choices in catalyst design have significantly impeded the application of PEM water electrolyzers and the fast production of hydrogen fuel. More efficient strategies focusing on increasing the number of active sites and improving the specific activity of each active site should be investigated.

(2) One of the greatest challenges for energy conversion reactions in acidic environments is the long-term stability due to the harsh acidic operating conditions. Fundamental understanding of catalytic stability has often been overlooked because of a major emphasis on catalytic activity. Greater in-depth experimental and theoretical study is therefore needed to reveal the origin of stability fading and the structure – stability relationship. Further, it would practically guide the future design of catalysts if a quantitative descriptor dealing with the catalyst stability could be raised.

(3) It is increasingly recognized that some catalyst surfaces can be changed dynamically during electrocatalysis under acidic conditions, mainly because of oxidized potential and/or acid corrosion. This makes it difficult to precisely identify the active sites and to determine the reaction mechanisms based on characterizations upon freshly prepared catalysts. Therefore, the

fundamental understanding of well-established catalysts would require the combination of advanced *in-situ* analytical techniques and *operando* theoretical computations.

(4) Although a new geometric structure of allocating various noble metal atoms with identical spatial correlations in the lattice of transition metal oxides has been proposed in this thesis, more efforts would be devoted to extending this strategy to wider options of host materials and to more energy conversion applications. In addition, further studies to investigate both the synergistic effect among correlated noble metal substitutions and the interactions between the noble metal substitutions and the transition metal oxide (or other) host materials are still needed.

## Appendix: Publications during Ph.D. Candidature

- [1] **Shan, J.**, Guo, C., Zhu, Y., Chen, S., Song, L., Jaroniec, M., Zheng, Y. and Qiao, S. Z. (2019). Charge-Redistribution-Enhanced Nanocrystalline Ru@IrO<sub>x</sub> Electrocatalysts for Oxygen Evolution in Acidic Media. *Chem*, 5(2), 445-459.
- [2] **Shan, J.**, Ling, T., Davey, K., Zheng, Y. and Qiao, S. Z. (2019). Transition-Metal-Doped RuIr Bifunctional Nanocrystals for Overall Water Splitting in Acidic Environments. *Advanced Materials*, 31(17), 1900510.
- [3] **Shan, J.**, Zheng, Y., Shi, B., Davey, K. and Qiao, S. Z. (2019). Regulating Electrocatalysts via Surface and Interface Engineering for Acidic Water Electrooxidation. *ACS Energy Letters*, 4(11), 2719-2730.
- [4] **Shan, J.**, Ye, C., Chen, S., Sun, T., Jiao, Y., Liu, L., Zhu, C., Song, L., Han, Y., Jaroniec, M., Zhu, Y., Zheng, Y. and Qiao, S. Z. Short-Range Ordered Iridium Single Atoms Integrated into Cobalt Oxide Spinel Structure for Highly Efficient Electrocatalytic Water Oxidation. *Journal of the American Chemical Society*, 143, DOI: 10.1021/jacs.1c01525.
- [5] **Shan, J.**, Ye, C., Zhu, Y., Zheng, Y. and Qiao, S. Z. Spatial Structure Tuning of Correlated Single-Atom Platinum Sites for Acidic Hydrogen Evolution and Oxidation Electrocatalysis. To be submitted.
- [6] Ye, C., Jiao, Y., Chao, D., Ling, T., **Shan, J.**, Zhang, B., Gu, Q., Davey, K., Wang, H., and Qiao, S. Z. (2020). Electron-State Confinement of Polysulfides for Highly Stable Sodium-Sulfur Batteries. *Advanced Materials*, 32(13), 1907557.
- [7] Ye, C., Chao, D., **Shan, J.**, Li, H., Davey, K., and Qiao, S. Z. (2020). Unveiling the Advances of 2D Materials for Li/Na-S Batteries Experimentally and Theoretically. *Matter*, 2(2),

323-344.

[8] Ran, J., Zhang, H., Qu, J., **Shan, J.**, Chen, S., Yang, F., Zheng, R., Cairney, J., Song, L., Jing, L., and Qiao, S. Z. (2020). Atomic-Level Insights into the Edge Active ReS<sub>2</sub> Ultrathin Nanosheets for High-Efficiency Light-to-Hydrogen Conversion. *ACS Materials Letters*, 2(11), 1484-1494.